SYNTHESIS, CHARACTERIZATION, PROPERTIES AND APPLICATION OF NOVEL NANO MATERIALS

ABSTRACT
OF
THESIS

SUBMITTED FOR THE AWARD OF THE DEGREE OF

Doctor of Philosophy

IN

CHEMISTRY

BY

ZEBA NASIR

Under the Supervision of

PROF. LUTFULLAH

DEPARTMENT OF CHEMISTRY
ALIGARH MUSLIM UNIVERSITY
ALIGARH (INDIA)

2017

Nanomaterials are cornerstones of nanoscience and nanotechnology. Nanoscale materials are defined as a set of substances where at least one dimension is less than approximately 100 nanometers. A nanometer is one millionth of a millimeter approximately 100,000 times smaller than the diameter of a human hair. Nanomaterials are of interest because at this scale unique optical, magnetic, electrical, and other properties emerge. These emergent properties have the potential for great impacts in electronics, medicine and other fields. Engineered nanomaterials are resources designed at the molecular (nanometre) level to take advantage of their small size and novel properties which are generally not seen in their conventional, bulk counterparts. The two main reasons why materials at the nanoscale can have different properties as increased relative surface area and new quantum effects. Our laboratory from the past is concerned mainly with the synthesis of novel nanomaterials. In continuation of the aforesaid studies, the present work embodied the design and synthesis of nanoparticles along with their catalytic and biological behavior. The identification of newly synthesized nanoparticles has been ascertained by X-ray diffraction (XRD), scanning electron microscopy (SEM), transmission electron microscopy (TEM), high resolution transmission electron microscopy (HR-TEM), vibrating sample magnetometer (VSM) and fourier transform infrared spectroscopy (FT-IR). The whole work of thesis has been divided into five chapters namely:

Chapter 1: *Introduction and literature review.*

Chapter 2: *Study on immobilization of yeast alcohol dehydrogenase on nanocrystalline Ni-Co ferrites as magnetic support.*

Chapter 3: *Co-precipitation synthesis and characterization of Co doped SnO_2 NPs, HSA interaction via various spectroscopic techniques and their antimicrobial and photocatalytic activities.*

Chapter 4: *Silica supported NiO nanocomposite prepared via sol-gel technique and its excellent catalytic performance for one-pot multicomponent synthesis of benzodiazepine derivatives under microwave irradiation.*

Chapter 5: *Immobilization of glucose oxidase enzyme on silica coated Ni-Co ferrite nanocomposites as a magnetic support.*

The results are summarized as follows:

CHAPTER-1

Introduction and literature review

Nanotechnology and nanoscience is the most dependable branch of science and technology in the recent years which is extensively used due to its great applications in the life days. Nanostructured materials have certainly turn out to be a very dynamic research field in the expanse of materials science containing organic, inorganic and composite materials. Nanostructured materials made of nanosized grains or nanoparticles as building blocks have a substantial segment of grain boundaries with a high degree of disorder of atoms beside the grain boundaries (or particle surfaces), and a large ratio of interface (or surface) area to volume. Chemical composition of the phases and the interfaces, between nano-grains, must be coordinated too for obtaining required properties in the material. The properties of materials can be different at the nanoscale for two main reasons. First, nanomaterials have a relatively larger surface area when compared to the same mass of material produced in a larger form. This can make materials more chemically reactive (in some cases materials that are inert in their larger form are reactive when produced in their nanoscale form), and affect their strength or electrical properties. Second, quantum effects can begin to dominate the behaviour of matter at the nanoscale particularly at the lower end-affecting the optical, electrical and magnetic behaviour of materials. Materials can be produced that are nanoscale in one dimension (for example, very thin surface coatings), in two dimensions (for example, nanowires and nanotubes) or in all three dimensions (for example, nanoparticles). Nanomaterials can be constructed by ‘top down’ techniques, producing very small structures from larger pieces of material, for example by etching to create circuits on the surface of a silicon microchip. They may also be constructed by ‘bottom up’ techniques, atom by atom or molecule by molecule. One way of doing this is self-assembly, in which the atoms or molecules arrange themselves into a structure due to their natural properties. Crystals grown for the semiconductor industry provide an example of self-assembly, as does chemical synthesis of large molecules. A second way is to use tools to move each atom or molecule individually. Although this ‘positional assembly’ offers greater control over construction, it is currently very laborious and not suitable for industrial applications.

CHAPTER-2

Study on immobilization of yeast alcohol dehydrogenase on nanocrystalline Ni-Co ferrites as magnetic support[1]

In this chapter, I have explained the binding of YADH to Ni-Co nanoferrites *via* carbodiimide and the possible binding mechanism have been proposed by comparing the FT-IR results. The binding properties of the immobilized YADH enzyme were also studied by kinetic parameters, optimum operational pH, temperature, thermal stability and reusability. The immobilized YADH exhibits enhanced thermal stability as compared to the free enzyme over a wide range of temperature and pH, and showed good durability after recovery by magnetic separation for repeated use. Several characterization were performed such as structural analysis, morphology and magnetic properties of Ni-Co nanoferrites were determined by XRD, SEM, EDS, VSM, HR-TEM and FT-IR. The morphological investigation displayed that the prepared materials were in the range of 20-30 nm.

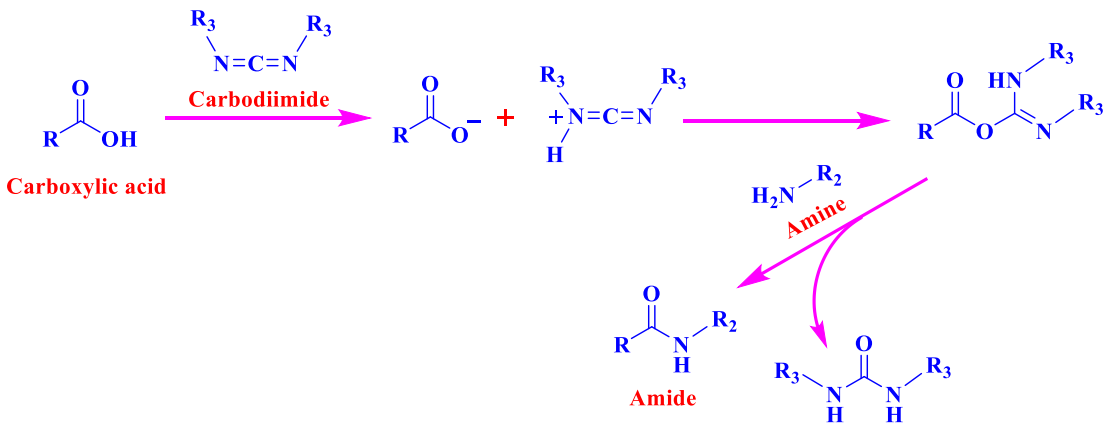

[1] *Int. J. Biol. Macromolec.*, 2015, **72**, 1196-1204.

CHAPTER-3

Co-precipitation synthesis and characterization of Co doped SnO_2 NPs, HSA interaction via various spectroscopic techniques and their antimicrobial and photocatalytic activities[2]

Herein, I have explained the synthesis of Co doped SnO_2 NPs by co-precipitation method. The interaction of Co doped SnO_2 NPs with human serum albumin (HSA) and their photocatalytic and antimicrobial properties were studied. The structural analysis and morphology of Co doped SnO_2 NPs were analyzed by XRD, SEM, EDS, HR-TEM and FT-IR. Besides the structural and morphological analysis, the interaction of Co doped SnO_2 NPs with HSA were studied by UV-vis, circular dichroism (CD) and fluorescence spectroscopy. The photocatalytic activities of the NPs with increased doping concentration were evaluated through a degradation process in the presence of methylene blue (MB) dye under UV light irradiation, which exhibited that the surface area of NPs with increased doping concentration plays a major role in improving the photocatalytic activity. The antimicrobial effect of undoped and Co-doped SnO_2 NPs was determined using agar-well diffusion method and analyzed against gram-positive bacteria (*Bacillus Cereus* MC 2434). In present results, I have found that as the doping concentration increases into NPs, zone of inhibition increases, which could be ascribed to the production of ROS and large surface area of the NPs.

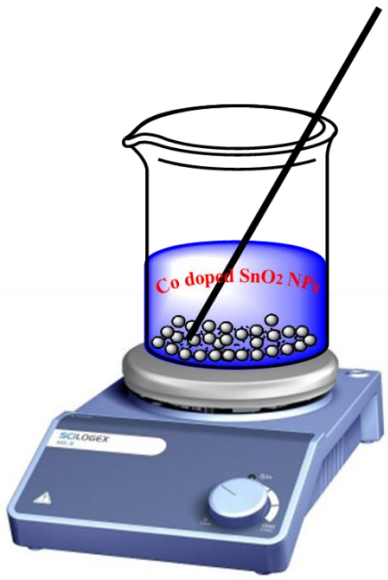

[2] *Int. J. Biol. Macromolec.*, 2017, **94**, 554-565.

CHAPTER-4

Silica supported NiO nanocomposite prepared via sol-gel technique and its excellent catalytic performance for one-pot multicomponent synthesis of benzodiazepine derivatives under microwave irradiation[3]

In this chapter, a heterogeneous versatile NiO@SiO_2 NCs were synthesized by a sol-gel technique and used as a catalyst for the synthesis of one-pot multicomponent benzodiazepine derivatives (**4a-u**) from a mixture of *o*-phenylenediamine, aromatic aldehydes and dimedone under microwave irradiation. Tetraethyl orthosilicate (TEOS) used as a source of SiO_2 for the creation of NiO@SiO_2 NCs. The structure and morphology of the prepared nanocatalyst was characterized by using elemental analysis, SEM, TEM, XRD, EDS and FT-IR. ^{1}H NMR, ^{13}C NMR and MS analyses were performed for the confirmation of the synthesized compounds (**4a-u**). Moreover, the remarkable catalytic properties of NiO@SiO_2 NCs permit easy separation of the catalyst from the reaction mixture without significant loss of catalytic activity.

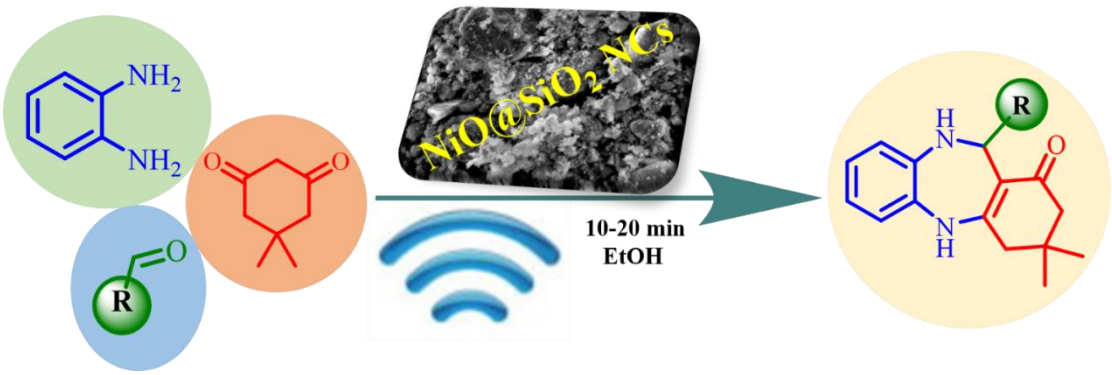

[3] Communicated.

CHAPTER-5

Immobilization of glucose oxidase enzyme on silica coated Ni-Co ferrite nanocomposites as a magnetic support[4]

In this last chapter of the thesis, I have explained the synthesis of silica coated Ni-Co ferrite NCs by sol-gel auto-combustion method to be used as a support for enzyme immobilization. GOx (Glucose oxidase) was covalently immobilized on this magnetic support using glutaraldehyde as a coupling agent. The structural analysis and morphology of silica coated Ni-Co ferrite NCs were determined by XRD, SEM, EDS, HR-TEM and FT-IR. The binding of GOx to silica coated Ni-Co ferrite NCs were confirmed by FT-IR spectra and had loading efficiency around 85%. Immobilized GOx enzyme showed higher catalytic activity at alkaline pH and higher temperature. It retained 69% catalytic activity after 10 times of reuses. The overall results showed that the immobilized GOx had higher operational stability than the free enzyme over wider temperature and pH ranges and good reusability after recovery by magnetic separation.

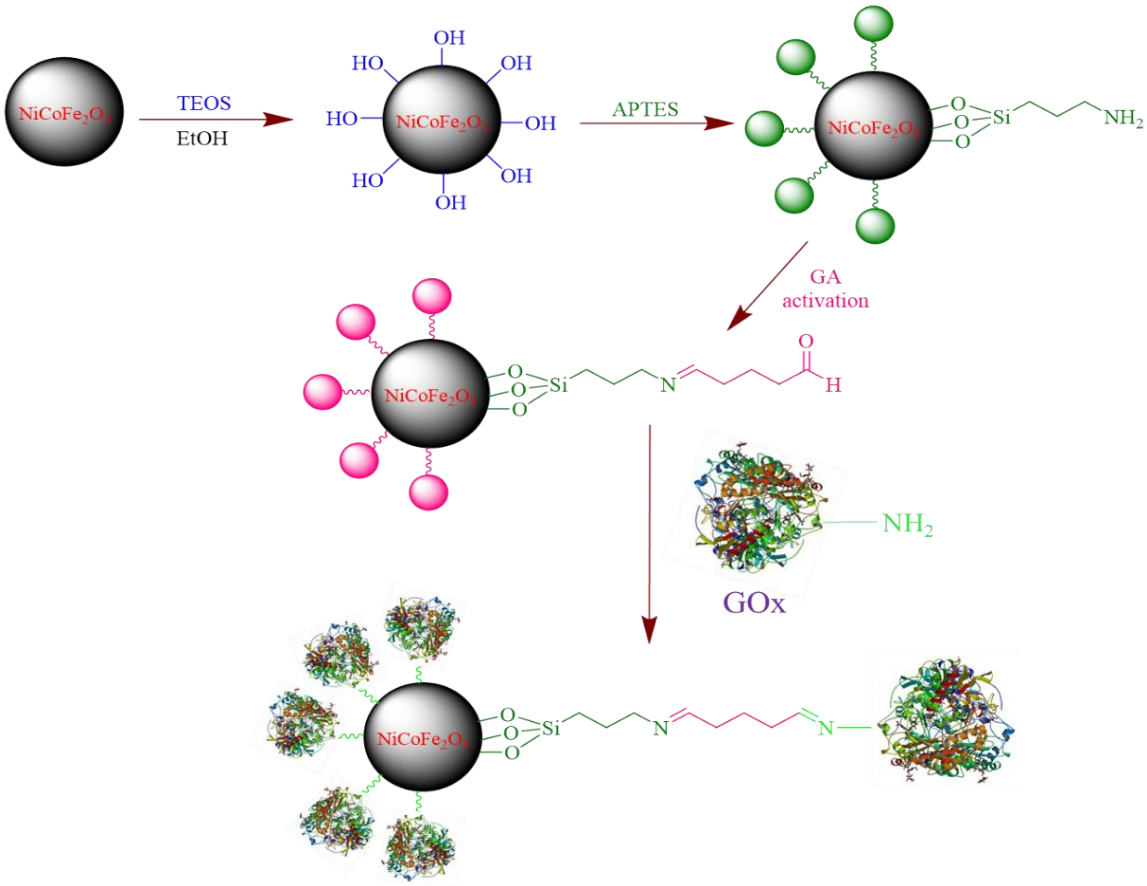

[4] Communicated.

SYNTHESIS, CHARACTERIZATION, PROPERTIES AND APPLICATION OF NOVEL NANO MATERIALS

THESIS

SUBMITTED FOR THE AWARD OF THE DEGREE OF

Doctor of Philosophy

IN

CHEMISTRY

BY

ZEBA NASIR

Under the Supervision of

PROF. LUTFULLAH

DEPARTMENT OF CHEMISTRY
ALIGARH MUSLIM UNIVERSITY
ALIGARH (INDIA)

2017

CANDIDATE'S DECLARATION

I, **Zeba Nasir**, Department of **Chemistry** certify that work embodied in this Ph.D thesis is my own bonafide work carried out by me under the supervision of **Prof. Lutfullah** at Aligarh Muslim University, Aligarh. The matter embodied in this Ph.D thesis has not been submitted for the award of any other degree.

I declare that I have faithfully acknowledged, given credit to and referred to the research workers wherever their works have been cited in the text and the body of the thesis. I further certify that I have not willfully lifted up some other's work, para, text, data, results, etc. reported in the journals, books, magazines, reports, dissertations, thesis, etc., or available at web-sites and included them in this Ph.D thesis and cited as my own work.

Date: ..... **(Signature of the candidate)**

Zeba Nasir
(Name of the candidate)

Certificate from the Supervisor

This is to certify that the above statement made by the candidate is correct to the best of my knowledge.

Signature of the supervisor…….

Name & Designation: Dr. Lutfullah

Professor

Department: CHEMISTRY

(Signature of the Chairperson of the Department with seal)

COURSE/ COMPREHENSIVE EXAMINATION/ PRE-SUBMISSION SEMINAR COMPLETION CERTIFICATE

This is to certify that Miss. **Zeba Nasir**, Department of Chemistry has satisfactorily completed the course work/ comprehensive examination and pre-submission seminar requirement which is part of her Ph.D. programme.

Date: …….. **(Signature of the Chairperson of the Department)**

COPYRIGHT TRANSFER CERTIFICATE

Title of the Thesis: **SYNTHESIS, CHARACTERIZATION, PROPERTIES AND APPLICATION OF NOVEL NANO MATERIALS**

Candidate's Name: **ZEBA NASIR**

Copyright Transfer

The undersigned hereby assigns to the Aligarh Muslim University, Aligarh, copyright that may exist in and for the above thesis submitted for the award of Ph.D. degree.

(Signature of the Candidate)

Dedicated to.....

My beloved father & Mother

Mr **Nasiruddin**

Mrs **Asma Khan**

Acknowledgments

All praise and thanks belong to ALLAH (SWT) Alone, The Exalted, Almighty, All-Glorious, as befits His glory and the greatness of His power. I thank Him for the blessing which He has bestowed upon me, and for honouring me with His aid to accomplish this research work.

*I wish to express the deep sense of gratitude to my research advisor, **Prof. Lutfullah** whose encouragement and guidance were a source of great inspiration to me. It was his constant support, supervision, advice and kind co-operation which helped me to build an optimistic attitude towards my research work. His invaluable helpful suggestions, enlightening explanations and assistance were indispensable throughout the work.*

I wish to convey my sincere thanks to the chairman department of Chemistry, Aligarh Muslim University, Aligarh for constant support and encouragement and for providing necessary research facilities.

*Of course, I would not be where I am today without the great love and support from my family. My parents have been encouraging from the beginning, allowing me to choose my own path. My pursuit of higher education has been a long journey, and for the opportunities afforded to me by my Father (**Nasiruddin**) and Mother (**Asma Khan**), I am forever grateful. I am also very grateful to my brothers (**Bilal** and **Amaan**), sister (**shaiba** and **nida**) and brother-in-law (**Talha**) for their support throughout my research and for their help during the challenging time.*

*I wish to convey my heartiest thanks to **Prof. Jawaid Iqbal, Prof. Abdul Rauf, Prof. Shamsuzzaman, Prof. Mehtab Parveen, Prof. Zeba N. Siddique, Prof. M. Muneer, Prof. Sartaj Tabassum, Prof. Farukh Arjmand,***

Prof. Nafisur Rahman, Dr. Anamika Gupta, Dr. Md. Musawwer Khan, Dr. M. Shahid, Dr. Mohd. Khalid and Dr. Shafiullah for their gracious support.

I wish to convey my heartiest thanks to my friends and members non-teaching staff of the department who were always with me throughout this tenure, helping me in all situations especially Shaista, Sabiha, Saira, Shahnaz, Shama, Mumtaz, Abad Ali, Mohd Asif, Samim Hasan, Babar Ali, Wajid Ali, Ajhar Khan, Mohd Rehan, Arafat Arif, Parvez Ishtiaque, Imran Khan and Raisuddin. Their constant help, support, trust and moral boost together with enormous motivation proved to be priceless.

I would like to acknowledge University Grants Commission (UGC) New Delhi India, for providing Non-NET fellowship during this tenure.

I also acknowledge Instrumentation Centre Department of Chemistry, USIF, Aligarh Muslim University, Aligarh, SAIF Punjab University chandigarh for providing spectral and analytical data.

"Science is a way of thinking much more than it is a body of knowledge"

-Carl Sagan

Zeba Nasir

CONTENTS

LIST TABLES i-ii
LIST OF FIGURES iii-xi
LIST OF SCHEMES xii-xiii
SUMMARY xiv-xix

CHAPTER 1: Introduction and literature review 1-68
1.1. Introduction to nanomaterials 1-4
1.2. Various types of nanostructured materials (NSMs) 4-5
1.3. Synthesis methods of nanomaterials 6-16
1.4. Properties of nanomaterials 17-20
1.5. Ni-Co nanoferrites: A brief review 21-22
1.6. Tin oxide (SnO_2) NPs: A brief review 22-24
1.7. Silica coated nickel oxide (NiO) NCs: A brief review 25-26
1.8. Characterization techniques 27-43
1.9. Applications of nanomaterials 43-56
1.10. Aim of the present work and thesis outlines 57
1.11. References 58-68

CHAPTER 2: Study on immobilization of yeast alcohol dehydrogenase on nanocrystalline Ni-Co ferrites as magnetic support 69-93
2.1. Introduction 69-70
2.2. Results and discussion 70-84
2.3. Experimental 85-88
2.4. Conclusion 89
2.5. References 90-93

CHAPTER 3: Co-precipitation synthesis and characterization of Co doped SnO_2 NPs, HSA interaction via various spectroscopic techniques and their antimicrobial and photocatalytic activities 94-127
3.1. Introduction 94-96
3.2. Results and discussion 96-117
3.3. Experimental 117-121
3.4. Conclusion 122
3.5. References 123-127

CHAPTER 4: Silica supported NiO nanocomposite prepared via sol-gel technique and its excellent catalytic performance for one-pot multicomponent synthesis of benzodiazepine derivatives under microwave irradiation 128-173
4.1. Introduction 128-129
4.2. Results and discussion 129-157
4.3. Experimental 157-168
4.4. Conclusion 169
4.5. References 170-173

CHAPTER 5: Immobilization of glucose oxidase enzyme on silica coated Ni-Co ferrite nanocomposites as a magnetic support 174-194
5.1. Introduction 174-175
5.2. Results and discussion 175-186
5.3. Experimental 186-190
5.4. Conclusion 191
5.5. References 192-194

LIST OF ABBREVIATIONS AND SYMBOLS
LIST OF PUBLICATIONS

LIST OF TABLES

Table No.	Title	Page No.
Table 1.1.	Properties of SnO_2 NPs	24
Table 1.2.	Properties of NiO NPs	26
Table 2.1.	Structural parameters of nanocrystalline Ni-Co ferrites	71
Table 2.2.	EDS analysis (weight % and atomic %) of $Ni_xCo_{1-x}Fe_2O_4$ at different compositions	76
Table 2.3.	Magnetic data of nanocrystalline Ni-Co ferrites	79
Table 2.4.	The kinetic parameters for free and immobilized YADH	83
Table 2.5.	Comparison of different systems of immobilization of YADH on magnetic NPs	84
Table 3.1.	Structural parameters of $Sn_{1-x}Co_xO_2$ (x = 0.00, 0.01, 0.03, 0.05) NPs	97
Table 3.2.	EDS analysis (weight % and atomic %) of $Sn_{1-x}Co_xO_2$ (x = 0.00, 0.01, 0.03, 0.05) NPs at different compositions	101
Table 3.3.	Stern-Volmer quenching constants and binding parameters for HSA with undoped SnO_2 NPs and Co doped SnO_2 NPs at 298 K	106
Table 4.1.	Structural parameters of NiO@SiO_2 NCs	131
Table 4.2.	Comparison of the catalytic efficiency of NiO@SiO_2 NCs with other catalysts 4e[a]	136

Table 4.3.	*Effect of solvent and temperature on the model reaction 4e[a]*	*138*
Table 4.4.	*Synthesis of benzodiazepine derivatives (4a-u) in the presence of $NiO@SiO_2$ NCs*	*139-141*
Table 4.5.	*Composition of $NiO@SiO_2$ NCs determined by XRF analysis*	*157*
Table 5.1.	*Structural parameters of $Ni_xCo_{1-x}Fe_2O_4/SiO_2$ NCs*	*176*
Table 5.2.	*EDS analysis (weight % and atomic %) of $Ni_xCo_{1-x}Fe_2O_4/SiO_2$ NCs at different compositions*	*180*
Table 5.3.	*The kinetic parameters for free and immobilized GOx*	*185*

LIST OF FIGURES

Figure No.	Title	Page No.
Figure 1.1.	Electronic bands in bulk metals, semiconductors and insulator	2
Figure 1.2.	Propagation of a slip plane across a grain boundary in a crystal	3
Figure 1.3.	Schematic representation of top-down and bottom-up approaches for synthesis of nanomaterials	6
Figure 1.4.	Schematic diagram of the experimental setup of inert gas condensation process	8
Figure 1.5.	Chemical vapor synthesis process	10
Figure 1.6.	Microwave (Monowave 300 & Masterwave BTR) synthesis instruments	11
Figure 1.7.	Schematic representation of hydrothermal technology	13
Figure 1.8.	Schematic representation of the different stages and routes of the sol-gel process	14
Figure 1.9.	Co-precipitation method for nanoparticle synthesis	16
Figure 1.10.	Suspensions of gold nanoparticles of various sizes	18
Figure 1.11.	The schematic diagram of spinel structure of ferrite with tetrahedral and octahedral sites	22

Figure 1.12.	*The schematic diagram of rutile type tetragonal structure and powder form of SnO_2 nanoparticle*	*23*
Figure 1.13.	*The schematic diagram and powder form of NiO nanoparticles*	*25*
Figure 1.14.	*Geometrical illustrations of crystal planes and Bragg's law*	*28*
Figure 1.15.	*X-ray Diffraction (XRD) machine*	*29*
Figure 1.16.	*Schematic details of X-ray Diffraction (XRD)*	*29*
Figure 1.17.	*Schematic representation of scanning electron microscope (SEM)*	*32*
Figure 1.18.	*Schematic view of XPS*	*33*
Figure 1.19.	*Ejection of photoelectrons*	*33*
Figure 1.20.	*Schematic representation of transmission electron microscope (TEM)*	*35*
Figure 1.21.	*Schematic representation of UV-visible spectrophotometer*	*38*
Figure 1.22.	*UV-Visible spectrophotometer*	*38*
Figure 1.23.	*TGA/DTA analyzer*	*41*
Figure 1.24.	*Schematic details of IR spectroscopy*	*42*
Figure 1.25.	*The mechanism of photocatalysis*	*56*
Figure 2.1.	*XRD patterns of $Ni_xCo_{1-x}Fe_2O_4$ (x = 0.0, 0.2, 0.5, 0.8, 1.0)*	*71*

Figure 2.2.	*FT-IR spectra of naked $Ni_xCo_{1-x}Fe_2O_4$ (x = 0.0, 0.2, 0.5, 0.8, 1.0), immobilized $Ni_xCo_{1-x}Fe_2O_4$ and free YADH.*	*74*
Figure 2.3.	*SEM images (left side) and EDS spectrum (right side) of $Ni_xCo_{1-x}Fe_2O_4$ (x = 0.0, 0.2, 0.5, 0.8, 1.0): (a) $CoFe_2O_4$ (b) $Ni_{0.2}Co_{0.8}Fe_2O_4$ (c) $Ni_{0.5}Co_{0.5}Fe_2O_4$ (d) $Ni_{0.8}Co_{0.2}Fe_2O_4$ (e) $NiFe_2O_4$*	*75*
Figure 2.4.	*TEM images of magnetic Ni-Co nanoferrites without YADH (a) and with YADH (b) and their statistical analysis*	*77*
Figure 2.5.	*Magnetization curves for $Ni_xCo_{1-x}Fe_2O_4$ (x = 0.0, 0.2, 0.5, 0.8, 1.0)*	*79*
Figure 2.6.	*Effect of pH on the activity of soluble enzyme (sol) and immobilized YADH on $Ni_xCo_{1-x}Fe_2O_4$ (x = 0.0, 0.2, 0.5, 0.8, 1.0): (a) $CoFe_2O_4$ (b) $Ni_{0.2}Co_{0.8}Fe_2O_4$ (c) $Ni_{0.5}Co_{0.5}Fe_2O_4$ (d) $Ni_{0.8}Co_{0.2}Fe_2O_4$ (e) $NiFe_2O_4$*	*80*
Figure 2.7.	*Effect of temperature on the activity of soluble enzyme (sol) and immobilized YADH on $Ni_xCo_{1-x}Fe_2O_4$ (x = 0.0, 0.2, 0.5, 0.8, 1.0): (a) $CoFe_2O_4$ (b) $Ni_{0.2}Co_{0.8}Fe_2O_4$ (c) $Ni_{0.5}Co_{0.5}Fe_2O_4$ (d) $Ni_{0.8}Co_{0.2}Fe_2O_4$ (e) $NiFe_2O_4$*	*81*
Figure 2.8.	*Thermal stability of soluble enzyme (sol) and immobilized YADH on $Ni_xCo_{1-x}Fe_2O_4$ (x = 0.0, 0.2, 0.5, 0.8, 1.0): (a) $CoFe_2O_4$ (b) $Ni_{0.2}Co_{0.8}Fe_2O_4$ (c) $Ni_{0.5}Co_{0.5}Fe_2O_4$ (d) $Ni_{0.8}Co_{0.2}Fe_2O_4$ (e) $NiFe_2O_4$*	*82*
Figure 2.9.	*Double reciprocal plots for soluble and immobilized YADH*	*83*

Figure 2.10.	*Reusability of the immobilized YADH on $Ni_xCo_{1-x}Fe_2O_4$ (x = 0.0, 0.2, 0.5, 0.8, 1.0): (a) $CoFe_2O_4$ (b) $Ni_{0.2}Co_{0.8}Fe_2O_4$ (c) $Ni_{0.5}Co_{0.5}Fe_2O_4$ (d) $Ni_{0.8}Co_{0.2}Fe_2O_4$ (e) $NiFe_2O_4$*	84
Figure 3.1.	*XRD patterns of $Sn_{1-x}Co_xO_2$ (x = 0.00, 0.01, 0.03, 0.05) NPs: (a) SnO_2 (b) $Sn_{0.99}Co_{0.01}O_2$ (c) $Sn_{0.97}Co_{0.03}O_2$ and (d) $Sn_{0.95}Co_{0.05}O_2$*	96
Figure 3.2.	*FT-IR spectra of $Sn_{1-x}Co_xO_2$ (x = 0.00, 0.01, 0.03, 0.05) NPs: (a) SnO_2 (b) $Sn_{0.99}Co_{0.01}O_2$ (c) $Sn_{0.97}Co_{0.03}O_2$ and (d) $Sn_{0.95}Co_{0.05}O_2$*	98
Figure 3.3.	*FT-IR spectra of (a) free HSA (b) HSA bound with undoped SnO_2 NPs and (c) HSA bound with Co doped SnO_2 NPs*	99
Figure 3.4.	*SEM images (left side) and EDS spectrum (right side) of $Sn_{1-x}Co_xO_2$ (x = 0.00, 0.01, 0.03, 0.05) NPs: (a) SnO_2 (b) $Sn_{0.99}Co_{0.01}O_2$ (c) $Sn_{0.97}Co_{0.03}O_2$ and (d) $Sn_{0.95}Co_{0.05}O_2$*	100
Figure 3.5.	*HR-TEM images of Co doped SnO_2 NPs without HSA (a_1, a_2) and with HSA (b_1, b_2) and their SAED pattern of Co doped SnO_2 NPs without HSA (a_3) and with HSA (b_3)*	101
Figure 3.6.	*Fluorescence quenching spectra of HSA with increasing concentration of (a) undoped SnO_2 NPs and (b) Co doped SnO_2 NPs*	102-103
Figure 3.7.	*Stern-Volmer plot and modified Stern-Volmer plot of HSA with undoped SnO_2 NPs (A) and (B), respectively*	104
Figure 3.8.	*Stern-Volmer plot and modified Stern-Volmer plot of HSA with Co doped SnO_2 NPs (A) and (B), respectively*	105-106

Figure 3.9.	*UV-Visible absorption spectra of HSA in absence and presence of (A) undoped SnO_2 NPs and (B) Co doped SnO_2 NPs*	*107-108*
Figure 3.10.	*Far UV-CD spectra of (A) HSA bound with undoped SnO_2 NPs and (B) HSA bound with Co doped SnO_2 NPs*	*109*
Figure 3.11.	*Photocatalytic degradation of MB dye under the irradiation of UV light over undoped SnO_2 NPs, Co doped SnO_2 NPs and without any catalysts*	*110*
Figure 3.12.	*Plot of $ln(C_0/C)$ as a function of UV irradiation time for photocatalysis of MB dye containing Co doped SnO_2 NPs and undoped SnO_2 NPs*	*111*
Figure 3.13.	*Photocatalytic degradation of MB dye in the presence of undoped SnO_2 NPs and Co doped SnO_2 NPs in the dark condition*	*112*
Figure 3.14.	*A comparison of % photodegradation of MB dyes in aqueous solution at different concentration of Co doping in SnO_2 NPs matrix*	*113*
Figure 3.15.	*TOC of MB dye over undoped SnO_2 NPs and Co doped SnO_2 NPs*	*114*
Figure 3.16.	*Zone of inhibition formed by $Sn_{0.95}Co_{0.05}O_2$ NPs at 100, 200, 300 and 400 µg mL^{-1} in disc diffusion test*	*115*
Figure 3.17.	*Comparative analysis of the antibacterial activity of undoped SnO_2 NPs and Co doped SnO_2 NPs at different concentration against Bacillus Cereus bacteria*	*116*

Figure 3.18.	*Schematic diagram of the mechanistic principles of the antibacterial action indicating ROS generation induced by Co doped SnO_2 NPs*	*117*
Figure 4.1.	*FT-IR spectra of (a) NiO@SiO_2 NCs and (b) SiO_2*	*130*
Figure 4.2.	*XRD patterns of NiO@SiO_2 NCs*	*131*
Figure 4.3.	*SEM images of (a) freshly synthesized NiO@SiO_2 NCs and (b) NiO@SiO_2 NCs after seven catalytic cycles*	*131*
Figure 4.4.	*EDS spectrum of NiO@SiO_2 NCs*	*132*
Figure 4.5.	*HR-TEM images of NiO@SiO_2 NCs (a and b) and their statistical analysis (c and d)*	*133*
Figure 4.6.	*SAED pattern of NiO@SiO_2 NCs*	*133*
Figure 4.7.	*Effects of catalyst dose (0.01-0.06 g) on the production yield of benzodiazepine 4e under microwave irradiation*	*135*
Figure 4.8.	*Effects of temperature with 0.05 g of the catalyst on the production yield of benzodiazepine 4e under microwave irradiation*	*137*
Figure 4.9.	*HRMS spectrum of 11-(3,5-difluorophenyl)-3,3-dimethyl-2,3,4,5,10,11-hexahydro-1H-dibenzo[b,e][1,4]diazepin-1-one (4a)*	*150*
Figure 4.10.	*HRMS spectrum of 3,3-dimethyl-11-(pyridin-2-yl)-2,3,4,5,10,11-hexahydro-1H-dibenzo[b,e][1,4]diazepin-1-one (4b)*	*150*

Figure 4.11. *HRMS spectrum of 11-(4-(dimethylamino)phenyl)-3,3-dimethyl-2,3,4,5,10,11-hexahydro-1H-dibenzo[b,e][1,4]diazepin-1-one (4e)* 151

Figure 4.12. *HRMS spectrum of 11-(furan-2-yl)-3,3-dimethyl-2,3,4,5,10,11-hexahydro-1H-dibenzo[b,e][1,4]diazepin-1-one (4f)* 151

Figure 4.13. *HRMS spectrum of 3,3-dimethyl-11-(thiophen-2-yl)-2,3,4,5,10,11-hexahydro-1H-dibenzo[b,e][1,4]diazepin-1-one (4g)* 152

Figure 4.14. *HRMS spectrum of 11-(2-hydroxy-3-methoxyphenyl)-3,3-dimethyl-2,3,4,5,10,11-hexahydro-1H-dibenzo[b,e][1,4]diazepin-1-one (4h)* 152

Figure 4.15. *HRMS spectrum of 11-(4-chloro-3-nitrophenyl)-3,3-dimethyl-2,3,4,5,10,11-hexahydro-1H-dibenzo[b,e][1,4]diazepin-1-one (4j)* 153

Figure 4.16. *HRMS spectrum of 3,3-dimethyl-11-(p-tolyl)-2,3,4,5,10,11-hexahydro-1H-dibenzo[b,e][1,4]diazepin-1-one (4k)* 153

Figure 4.17. *HRMS spectrum of 11-(4-methoxyphenyl)-3,3-dimethyl-2,3,4,5,10,11-hexahydro-1H-dibenzo[b,e][1,4]diazepin-1-one (4l)* 154

Figure 4.18. *HRMS spectrum of 11-(4-chlorophenyl)-3,3-dimethyl-2,3,4,5,10,11-hexahydro-1H-dibenzo[b,e][1,4]diazepin-1-one (4o)* 154

Figure 4.19. *HRMS spectrum of 11-(2,4-dichlorophenyl)-3,3-dimethyl-2,3,4,5,10,11-hexahydro-1H-dibenzo[b,e][1,4]diazepin-1-one (4q)* 155

Figure 4.20.	*HRMS spectrum of 11-(3-hydroxyphenyl)-3,3-dimethyl-2,3,4,5,10,11-hexahydro-1H-dibenzo[b,e][1,4]diazepin-1-one (4u)*	*155*
Figure 5.1.	*Representation of GOx reaction*	*174*
Figure 5.2.	*XRD patterns of silica coated Ni-Co ferrite NCs*	*176*
Figure 5.3.	*FT-IR spectra of silica coated Ni-Co ferrite NCs*	*178*
Figure 5.4.	*FT-IR spectra of pure GOx and immobilized silica coated Ni-Co ferrite NCs*	*178*
Figure 5.5.	*SEM images (right side) and EDS spectrum (left side) of silica coated Ni-Co ferrite NCs*	*179*
Figure 5.6.	*TEM images of (a) $CoFe_2O_4/SiO_2$ NCs (b) $NiCoFe_2O_4/SiO_2$ NCs (c) $NiFe_2O_4/SiO_2$ NCs (d) immobilized $CoFe_2O_4/SiO_2$ NCs (e) immobilized $NiCoFe_2O_4/SiO_2$ NCs (f) immobilized $NiFe_2O_4/SiO_2$ NCs*	*181*
Figure 5.7.	*Effect of pH on the activity of soluble enzyme (sol) and immobilized GOx on SiO_2 coated Ni-Co ferrite NCs*	*182*
Figure 5.8.	*Effect of temperature on the activity of soluble enzyme (sol) and immobilized GOx on SiO_2 coated Ni-Co ferrite NCs*	*183*
Figure 5.9.	*Thermal stability of soluble enzyme (sol) and immobilized GOx on SiO_2 coated Ni-Co ferrite NCs*	*184*
Figure 5.10.	*Double reciprocal plots for soluble and immobilized GOx*	*185*

Figure 5.11. Reusability of the immobilized GOx on silica coated Ni-Co ferrite NCs **186**

LIST OF SCHEMES

Scheme No.	Title	Page No.
Scheme 2.1.	Synthesis involving amide bond formation via carbodiimide activation	73
Scheme 4.1.	$NiO@SiO_2$ NCs catalyzed benzodiazepine reaction	135
Scheme 4.2.	Proposed fragmentation mechanisms of molecular ion $[M^{+\cdot}]$ of compounds (4a-e, 4j-s and 4u)	143
Scheme 4.3.	Proposed fragmentation mechanisms of molecular ion $[M^{+\cdot}]$ of compounds (4a-e, 4j-s and 4u)	144
Scheme 4.4.	Proposed fragmentation mechanisms of molecular ion $[M^{+\cdot}]$ of compounds (4f, 4g and 4i)	145
Scheme 4.5.	Proposed fragmentation mechanisms of molecular ion $[M^{+\cdot}]$ of compounds (4f, 4g and 4i)	146
Scheme 4.6.	Proposed fragmentation mechanisms of molecular ion $[M^{+\cdot}]$ of compounds (4h and 4t)	147
Scheme 4.7.	Plausible reaction mechanism for the synthesis of benzodiazepines 4a-u	149
Scheme 4.8.	Schematic representation of reusability of $NiO@SiO_2$ NCs for the model reaction 4e	156

Scheme 5.1. *Schematic diagram for the immobilization of glucose oxidase enzyme on silica coated Ni-Co ferrite NCs using glutaraldehyde as a cross-linker* 177

Summary

Nanomaterials are cornerstones of nanoscience and nanotechnology. Nanoscale materials are defined as a set of substances where at least one dimension is less than approximately 100 nanometers. A nanometer is one millionth of a millimeter approximately 100,000 times smaller than the diameter of a human hair. Nanomaterials are of interest because at this scale unique optical, magnetic, electrical, and other properties emerge. These emergent properties have the potential for great impacts in electronics, medicine and other fields. Engineered nanomaterials are resources designed at the molecular (nanometre) level to take advantage of their small size and novel properties which are generally not seen in their conventional, bulk counterparts. The two main reasons why materials at the nanoscale can have different properties as increased relative surface area and new quantum effects. Our laboratory from the past is concerned mainly with the synthesis of novel nanomaterials. In continuation of the aforesaid studies, the present work embodied the design and synthesis of nanoparticles along with their catalytic and biological behavior. The identification of newly synthesized nanoparticles has been ascertained by X-ray diffraction (XRD), scanning electron microscopy (SEM), transmission electron microscopy (TEM), high resolution transmission electron microscopy (HR-TEM), vibrating sample magnetometer (VSM) and fourier transform infrared spectroscopy (FT-IR). The whole work of thesis has been divided into five chapters namely:

Chapter 1: *Introduction and literature review.*

Chapter 2: *Study on immobilization of yeast alcohol dehydrogenase on nanocrystalline Ni-Co ferrites as magnetic support.*

Chapter 3: *Co-precipitation synthesis and characterization of Co doped SnO_2 NPs, HSA interaction via various spectroscopic techniques and their antimicrobial and photocatalytic activities.*

Chapter 4: *Silica supported NiO nanocomposite prepared via sol-gel technique and its excellent catalytic performance for one-pot multicomponent synthesis of benzodiazepine derivatives under microwave irradiation.*

Chapter 5: *Immobilization of glucose oxidase enzyme on silica coated Ni-Co ferrite nanocomposites as a magnetic support.*

The results are summarized as follows:

CHAPTER-1

Introduction and literature review

Nanotechnology and nanoscience is the most dependable branch of science and technology in the recent years which is extensively used due to its great applications in the life days. Nanostructured materials have certainly turn out to be a very dynamic research field in the expanse of materials science containing organic, inorganic and composite materials. Nanostructured materials made of nanosized grains or nanoparticles as building blocks have a substantial segment of grain boundaries with a high degree of disorder of atoms beside the grain boundaries (or particle surfaces), and a large ratio of interface (or surface) area to volume. Chemical composition of the phases and the interfaces, between nano-grains, must be coordinated too for obtaining required properties in the material. The properties of materials can be different at the nanoscale for two main reasons. First, nanomaterials have a relatively larger surface area when compared to the same mass of material produced in a larger form. This can make materials more chemically reactive (in some cases materials that are inert in their larger form are reactive when produced in their nanoscale form), and affect their strength or electrical properties. Second, quantum effects can begin to dominate the behaviour of matter at the nanoscale particularly at the lower end-affecting the optical, electrical and magnetic behaviour of materials. Materials can be produced that are nanoscale in one dimension (for example, very thin surface coatings), in two dimensions (for example, nanowires and nanotubes) or in all three dimensions (for example, nanoparticles). Nanomaterials can be constructed by ‘top down’ techniques, producing very small structures from larger pieces of material, for example by etching to create circuits on the surface of a silicon microchip. They may also be constructed by ‘bottom up’ techniques, atom by atom or molecule by molecule. One way of doing this is self-assembly, in which the atoms or molecules arrange themselves into a structure due to their natural properties. Crystals grown for the semiconductor industry provide an example of self-assembly, as does chemical synthesis of large molecules. A second way is to use tools to move each atom or molecule individually. Although this ‘positional assembly’ offers greater control over construction, it is currently very laborious and not suitable for industrial applications.

CHAPTER-2

Study on immobilization of yeast alcohol dehydrogenase on nanocrystalline Ni-Co ferrites as magnetic support[1]

In this chapter, I have explained the binding of YADH to Ni-Co nanoferrites *via* carbodiimide and the possible binding mechanism have been proposed by comparing the FT-IR results. The binding properties of the immobilized YADH enzyme were also studied by kinetic parameters, optimum operational pH, temperature, thermal stability and reusability. The immobilized YADH exhibits enhanced thermal stability as compared to the free enzyme over a wide range of temperature and pH, and showed good durability after recovery by magnetic separation for repeated use. Several characterization were performed such as structural analysis, morphology and magnetic properties of Ni-Co nanoferrites were determined by XRD, SEM, EDS, VSM, HR-TEM and FT-IR. The morphological investigation displayed that the prepared materials were in the range of 20-30 nm.

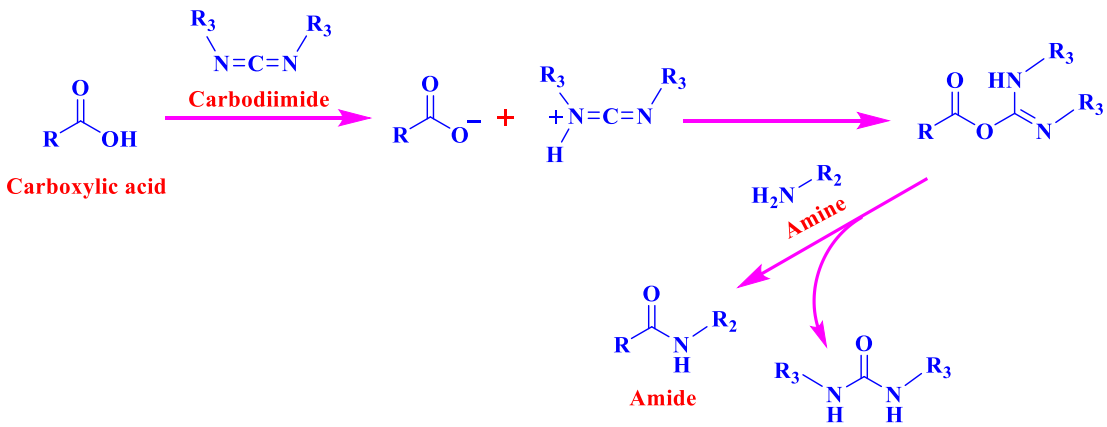

[1] *Int. J. Biol. Macromolec.*, 2015, **72**, 1196-1204.

CHAPTER-3

Co-precipitation synthesis and characterization of Co doped SnO_2 NPs, HSA interaction via various spectroscopic techniques and their antimicrobial and photocatalytic activities[2]

Herein, I have explained the synthesis of Co doped SnO_2 NPs by co-precipitation method. The interaction of Co doped SnO_2 NPs with human serum albumin (HSA) and their photocatalytic and antimicrobial properties were studied. The structural analysis and morphology of Co doped SnO_2 NPs were analyzed by XRD, SEM, EDS, HR-TEM and FT-IR. Besides the structural and morphological analysis, the interaction of Co doped SnO_2 NPs with HSA were studied by UV-vis, circular dichroism (CD) and fluorescence spectroscopy. The photocatalytic activities of the NPs with increased doping concentration were evaluated through a degradation process in the presence of methylene blue (MB) dye under UV light irradiation, which exhibited that the surface area of NPs with increased doping concentration plays a major role in improving the photocatalytic activity. The antimicrobial effect of undoped and Co-doped SnO_2 NPs was determined using agar-well diffusion method and analyzed against gram-positive bacteria (*Bacillus Cereus* MC 2434). In present results, I have found that as the doping concentration increases into NPs, zone of inhibition increases, which could be ascribed to the production of ROS and large surface area of the NPs.

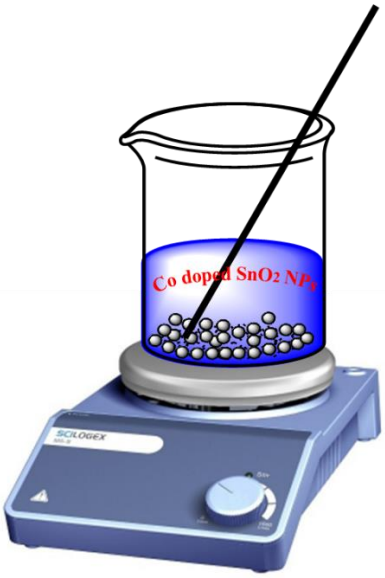

[2] *Int. J. Biol. Macromolec.*, 2017, **94**, 554-565.

CHAPTER-4

Silica supported NiO nanocomposite prepared via sol-gel technique and its excellent catalytic performance for one-pot multicomponent synthesis of benzodiazepine derivatives under microwave irradiation[3]

In this chapter, a heterogeneous versatile NiO@SiO_2 NCs were synthesized by a sol-gel technique and used as a catalyst for the synthesis of one-pot multicomponent benzodiazepine derivatives (**4a-u**) from a mixture of *o*-phenylenediamine, aromatic aldehydes and dimedone under microwave irradiation. Tetraethyl orthosilicate (TEOS) used as a source of SiO_2 for the creation of NiO@SiO_2 NCs. The structure and morphology of the prepared nanocatalyst was characterized by using elemental analysis, SEM, TEM, XRD, EDS and FT-IR. ^{1}H NMR, ^{13}C NMR and MS analyses were performed for the confirmation of the synthesized compounds (**4a-u**). Moreover, the remarkable catalytic properties of NiO@SiO_2 NCs permit easy separation of the catalyst from the reaction mixture without significant loss of catalytic activity.

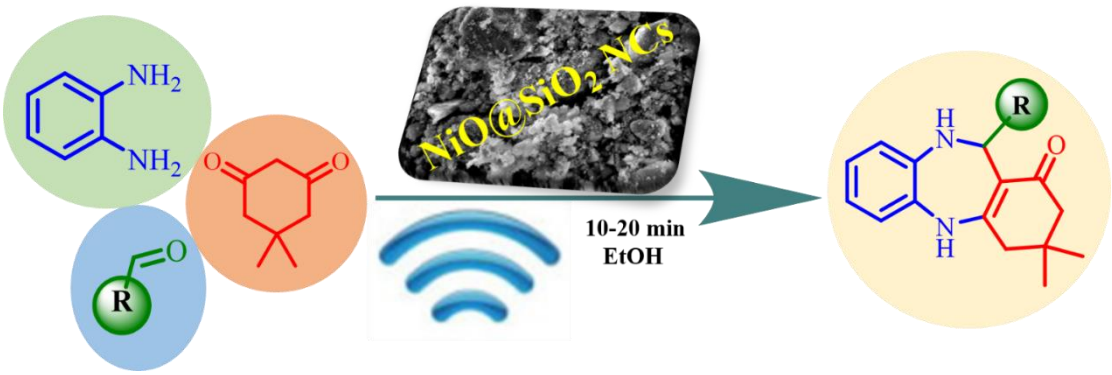

[3] Communicated.

CHAPTER-5

Immobilization of glucose oxidase enzyme on silica coated Ni-Co ferrite nanocomposites as a magnetic support[4]

In this last chapter of the thesis, I have explained the synthesis of silica coated Ni-Co ferrite NCs by sol-gel auto-combustion method to be used as a support for enzyme immobilization. GOx (Glucose oxidase) was covalently immobilized on this magnetic support using glutaraldehyde as a coupling agent. The structural analysis and morphology of silica coated Ni-Co ferrite NCs were determined by XRD, SEM, EDS, HR-TEM and FT-IR. The binding of GOx to silica coated Ni-Co ferrite NCs were confirmed by FT-IR spectra and had loading efficiency around 85%. Immobilized GOx enzyme showed higher catalytic activity at alkaline pH and higher temperature. It retained 69% catalytic activity after 10 times of reuses. The overall results showed that the immobilized GOx had higher operational stability than the free enzyme over wider temperature and pH ranges and good reusability after recovery by magnetic separation.

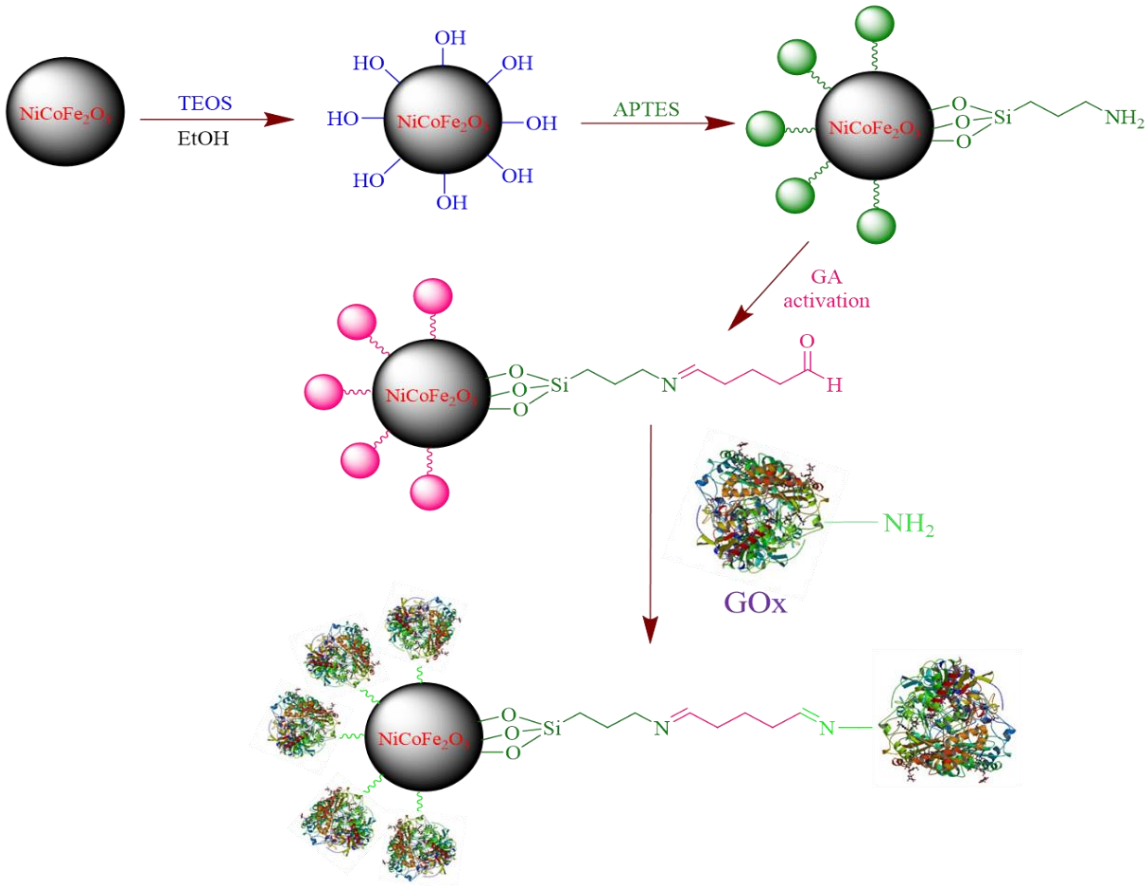

[4] Communicated.

Chapter 1

Introduction and literature review

1.1. Introduction to nanomaterials

Nanotechnology and nanoscience is the interdisciplinary science which connects the basic science and engineering for making and using materials, functional structures and devices on the order of nanometer scale. In the recent years, the technology extensively used due to its versatile applications in daily life. Earlier, nanotechnology is defined as the design and fabrication of materials, devices, and systems to control at the nanometer scale up to 100 nanometers while is defined in later as focus towards the observations, study of the phenomenon at nanometer scale and ways of manipulating matter at these scales, at which many properties of matter vary from those of bulk counterpart.[1] There is an immense elevation in the ratio of surface area to volume at the nanoscale.

As a result of this, materials at the nanoscale exhibit numerous properties when juxtaposed with microscale, which facilitate unique applications.[2] This technology seldom referred to as 'converging technology' as it elucidates the formation/incorporation and consumption of materials, devices, and systems through the control of nanometer-sized materials and their new applications to physics, chemistry, biology, engineering, materials science, medicine and other activities. Sometimes it is called as 'enabling technology', due to it permits new scientific and technological developments in an extensive range of disciplines and fields of application.[2]

Materials at the nanoscale can have diverse properties due to their increased relative surface area and new quantum effects. Nanomaterials comprises large surface area to volume ratio comparatively with their standard form, which can steer to better chemical reactivity and influence their strength. Quantum effects can become much more prominent for defining the materials properties and characteristics, directing to novel optical, electrical and magnetic behaviours. The quantum size effect in metallic nanoparticles (NPs) is well acknowledged in the literature.[3]

In metal and semiconductor NPs, there is completely an electronic effect. The band structure progresses with increasing particle size, *i.e*. molecular orbital convert into delocalized band states. In a metal, the quasi-continuous density of states in the valence and the conduction bands splits into discrete electronic levels, the spacing between these levels and the band gap increasing with decreasing particle size.[4,5] The gap noticed in metal NPs can be equivalent in size to that perceived in semiconductors

(< 2 eV) or even insulators (> 2 eV).[3] A diagram of the electronic bands in bulk metals, semiconductors, and insulator can be seen in **Fig. 1.1**.

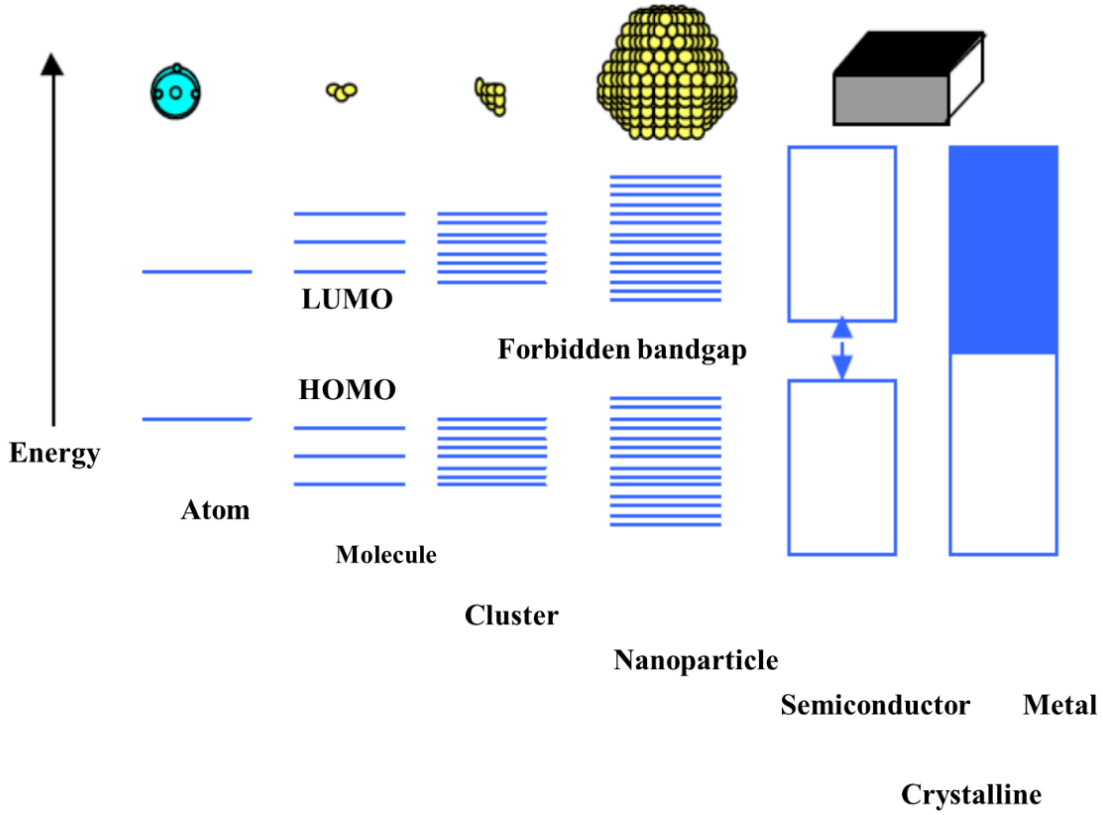

Figure 1.1. Electronic bands in bulk metals, semiconductors and insulator.

The altering of materials on the near-atomic (nanoscale) level has confirmed to be a precious contrivance in the accomplishment of essential properties of bulk materials. For paradigm, to adapt mechanical properties minor changes at the atomic level in bulk materials takes place and in specific such modifications are frequently performed to construct stronger materials. In case of single-phase materials, strengthening can be attained by grain size diminution and solid-solution strengthening or alloying. Grain size diminution acts to strengthen materials by creating it arduous for defects in crystals such as slip planes or dislocations to carry on propagation, because the slip plane or dislocation will have to adjust direction once crossing the grain boundary, as shown in **Fig. 1.2**.

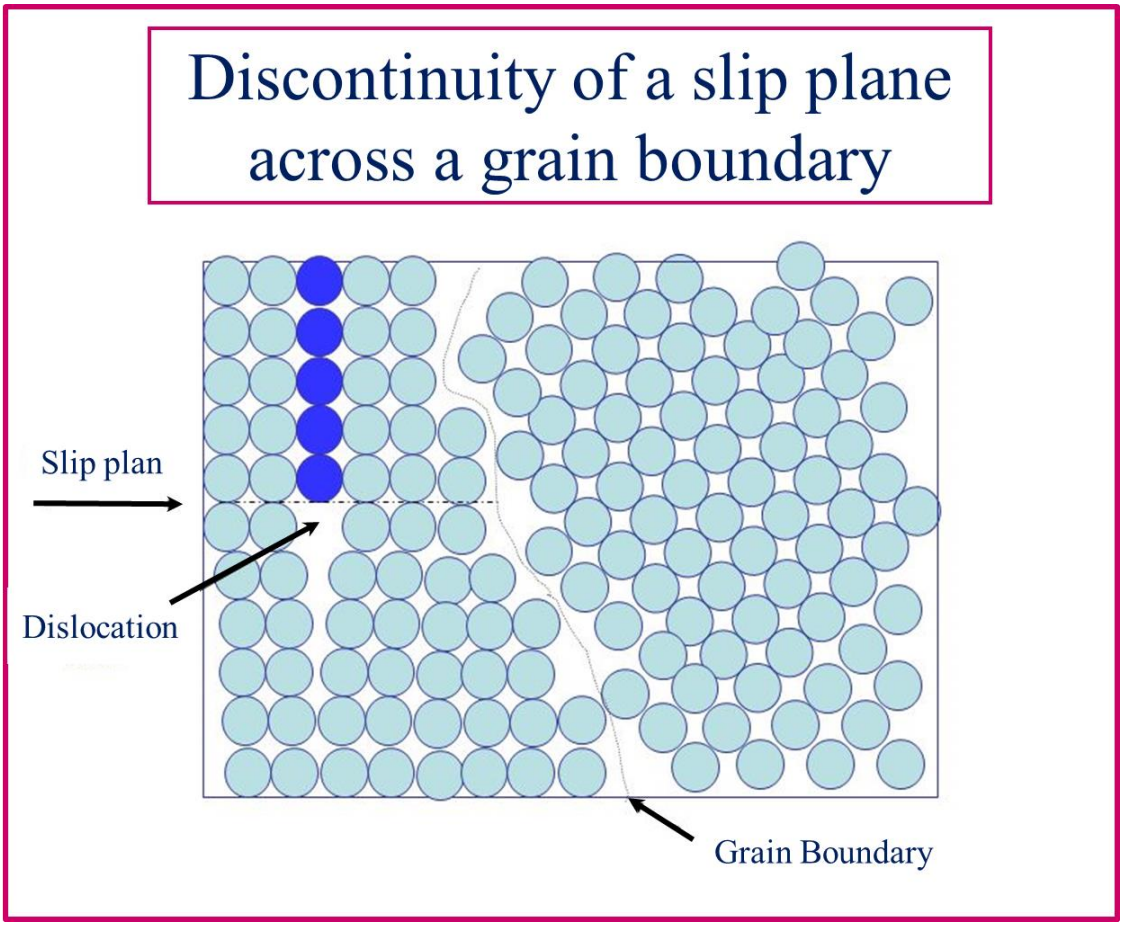

Figure 1.2. Propagation of a slip plane across a grain boundary in a crystal.

If the crystal increases in disorientation this becomes more difficult. The existence of smaller grains develops a large grain boundary area to hinder dislocation motion.

Nanostructured materials have certainly turn out to be a very dynamic research field in the expanse of materials science containing organic, inorganic and composite materials. Nanostructured materials made of nanosized grains or NPs as building blocks have a substantial segment of grain boundaries with a high degree of disorder of atoms beside the grain boundaries (or particle surfaces), and a large ratio of interface (or surface) area to volume. Chemical composition of the phases and the interfaces, between nano-grains, must be coordinated too for obtaining required properties in the material. One of the most eminent features of nanostructured materials is the significant need of several properties upon the size in the nanoscale region. For example, electronic property, with quantum size effects, instigated by spatial confinement of delocalized valence electrons, is unswervingly reliant on the particle size. Small particle size facilitates usual limitations of phase equilibrium and kinetics to be prevail during the synthesis and processing by the combination of short diffusion distances and high

driving forces of accessible large surfaces and interfaces. A wide range of materials, including metals, ceramics and metal oxides in crystalline, quasi crystalline, or amorphous phases have been synthesized as nanosized or nanostructured materials. The large surface area provides higher reactivity and diffusivity. Thus novel properties may result from surface "defects".[6–8]

1.2. Various types of nanostructured materials (NSMs)

Nanostructure is an intermediate size between microscopic and molecular structures. NSMs as a subject of nanotechnology are low dimensional materials comprising of building units of a submicron or nanoscale size at least in one direction and exhibiting size effects. There are four different types of nanostructured materials are given as:

- Zero dimensional nanostructured materials (0D NSMs)
  - For example: Nanoparticles, Colloids, Nanodots, Nanoclusters.
- One dimensional nanostructured materials (1D NSMs)
  - For example: Nanowires, Nanotubes, Nanobelts, Nanorods.
- Two dimensional nanostructured materials (2D NSMs)
  - For example: Quantum wells, Super lattices, Thin films.
- Three dimensional nanostructured materials (3D NSMs)
  - For example: Nanocomposites, Porous materials, Hybrids, Nanocrystal arrays *etc*.

All the four nanostructures are enclosed with distinct properties.[9,10] 0D NSMs contain single crystal, polycrystalline and amorphous particles with all possible morphologies such as spheres, cubes and platelets. Normally, the characteristic dimension of NPs ranges from 1-100 nm. If the NPs are single crystalline, they are often referred to as nanocrystals. When the characteristic dimension of the NPs is sufficiently small and quantum effects are observed, they are described as quantum dots. 1D NSMs are ideal systems for exploring a large number of novel phenomena at the nanoscale and investigating the size and dimensionality dependence of functional properties. 1D NSMs contains whiskers, fibers, nanowires and nanorods. Although the whiskers and nanorods are in general considered to be shorter than fibers and nanowires, the definition is slight arbitrary. In addition, one-dimensional structures with diameters ranging from several nanometers to several hundred microns (μ) were referred to as

whiskers and fibers in the early literature, whereas nanowires and nanorods with diameters not exceeding a few hundred nanometers are used predominantly in the current literature. Nanowires in general have a high aspect ratio than that of nanorods. 2D NSMs are ultrathin nanomaterials with a high degree of anisotropy and chemical functionality.[11] Research on 2D nanomaterials is still in its infancy, with the majority of research focusing on elucidating the unique material characteristics and few reports focusing on biomedical applications of 2D nanomaterials.[12] Nonetheless, recent rapid advances in 2D nanomaterials have raised important yet exciting questions about their interactions with biological moieties. 2D nanomaterials are highly diverse in terms of their mechanical, chemical and optical properties, as well as in size, shape, biocompatibility and degradability.[13] These diverse properties make 2D nanomaterials suitable for a wide range of applications, including drug delivery, imaging, tissue engineering and biosensors *etc*.[14] However, their low-dimension nanostructure gives them some common characteristics. For example, 2D nanomaterials are the thinnest materials known, which means that they also possess the highest specific surface areas of all known materials. This characteristic makes these materials invaluable for applications requiring high levels of surface interactions on a small scale. Owing to the large specific surface area and other superior properties over their bulk counterparts arising from quantum size effect, 3D NSMs have attracted significant research interest and various 3D NSMs have been synthesized in the past 10 years.[15–25] It is well known that the behaviors of NSMs strongly depend on the sizes, shapes, dimensionality and morphologies, which are thus the key factors to their ultimate performance and applications. Therefore it is of great interest to synthesize 3D NSMs with a controlled structure and morphology. In addition, 3D nanostructures are an important material due to its wide range of applications in the area of catalysis, magnetic material and electrode material for batteries.[15–25] Moreover, the 3D NSMs have recently attracted intensive research interests because the nanostructures have higher surface area and supply enough absorption sites for all involved molecules in a small space.[26] On the other hand, such materials with porosity in three dimensions could lead to a better transport of the molecules.[26–28]

1.3. Synthesis methods of nanomaterials

The process to manufacture of nanomaterials and nanostructures are the first step in nanotechnology to discover their unique physical properties and phenomena and comprehend potential applications. There are several methods to synthesize the nanomaterials which are classified in two techniques.

- "Top-down" approach
- "Bottom-up" approach

In "top-down" process bulk material is converted to fine particle. This approach comprises of solid state route and ball milling techniques. The second "bottom-up" approach, involves the reduction of atoms or molecular entities in a gas phase or in solution to form the nanomaterial in the nanometer range. The bottom-up approach is more advantageous than the top-down approach because the bottom-up approach has a better chance of producing nanostructures with less defects, more homogenous chemical composition, and better short- and long-range ordering. **Fig. 1.3**, reveals the general summary of the two approaches.

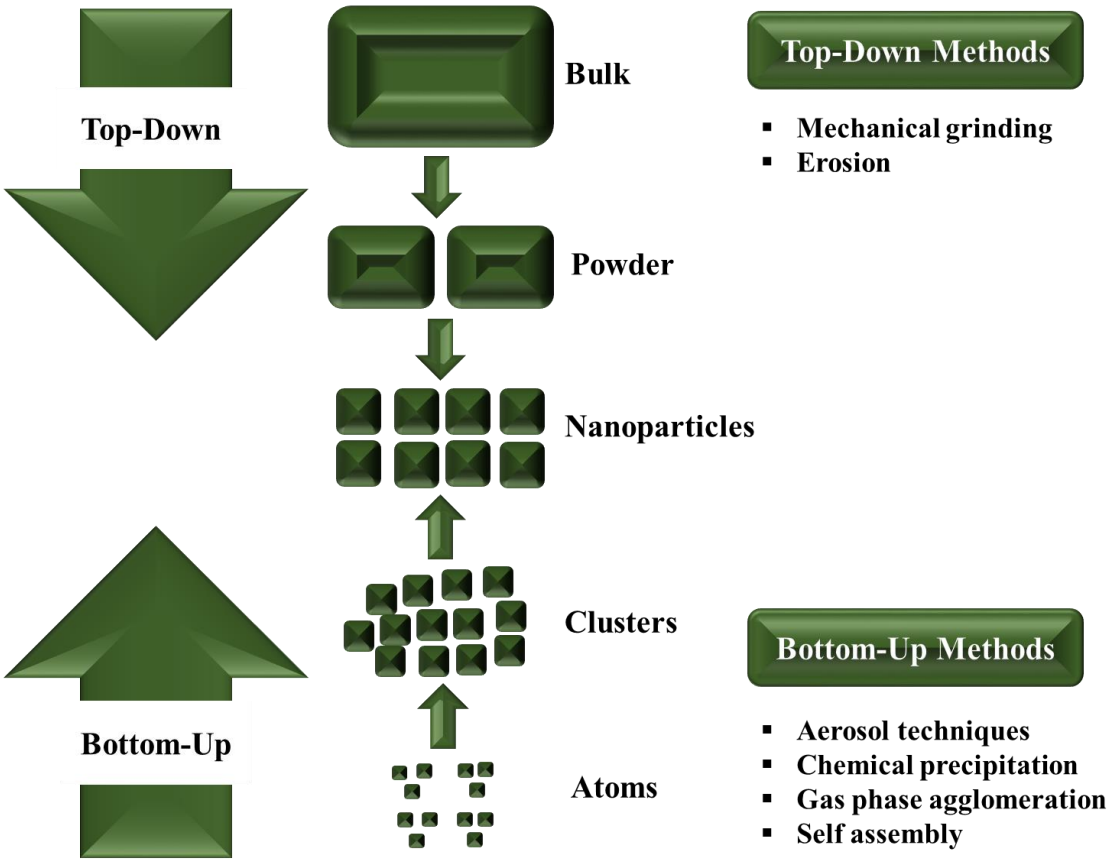

Figure 1.3. Schematic representation of top-down and bottom-up approaches for synthesis of nanomaterials.

There are various "bottom-up" methods of synthesizing nanomaterials such as:

- Combustion synthesis
- Gas-phase methods
- Microwave synthesis
- Hydrothermal method
- Solvothermal synthesis
- Sol-gel processing
- Co-precipitation method, *etc*.

1.3.1. Combustion synthesis

Combustion synthesis (CS) or self-propagating high-temperature synthesis (SHS) is an effective, low-cost method for production of various industrially useful materials. Combustion synthesis leads to highly crystalline particles with large surface areas.[29,30] The process involves prompt heating of a solution containing redox groups.[31] The temperature reaches almost 650 °C for one or two minutes resulted in the formation of crystalline material in combustion synthesis. Therefore, combustion synthesis of nanomaterials are classified on the basis of the physical nature of the initial reaction medium:[32]

- Conventional SHS of nanoscale materials, *i.e.* initial reactants are in solid state (condensed phase combustion).
- Solution-combustion synthesis (SCS) of nanosized powders, *i.e.* initial reaction medium is aqueous solution.
- Synthesis of nanoparticles in flame, *i.e.* gas-phase combustion.

1.3.2. Gas-phase methods

Gas phase NP preparation methods have attracted huge interest over the years due to number of benefits that they can deliver over other methods.[33,34] These techniques are typically characterized by the ability to accurately control the process parameters to be able to tune shape, size and chemical composition of the nanostructures.[35] Although, means and methods can differ, almost all gas phase nanomaterial production methods follows following sequence:

- Suspending the precursor materials in a gas phase.

- Transforming the precursor material to small clusters.
- Enforcing the growth of these clusters to a NPs.
- Method to collect prepared NPs.

The growth of small nuclei clusters to NPs is referred to as condensation and it occurs only when the precursor vapor is supersaturated. Condensation process can be driven by both physical and chemical methods and will be discussed in the following:

❖ ***Inert gas condensation*:** This method is the most rudimentary of all the gas phase fabrication techniques. The method is simple as heating a material inside a furnace usually under an inert gas such as Nitrogen or Helium.[36] This method however, is only appropriate for the materials that have low vapor pressure. An overview of the inert gas condensation process is illustrated in **Fig. 1.4**.

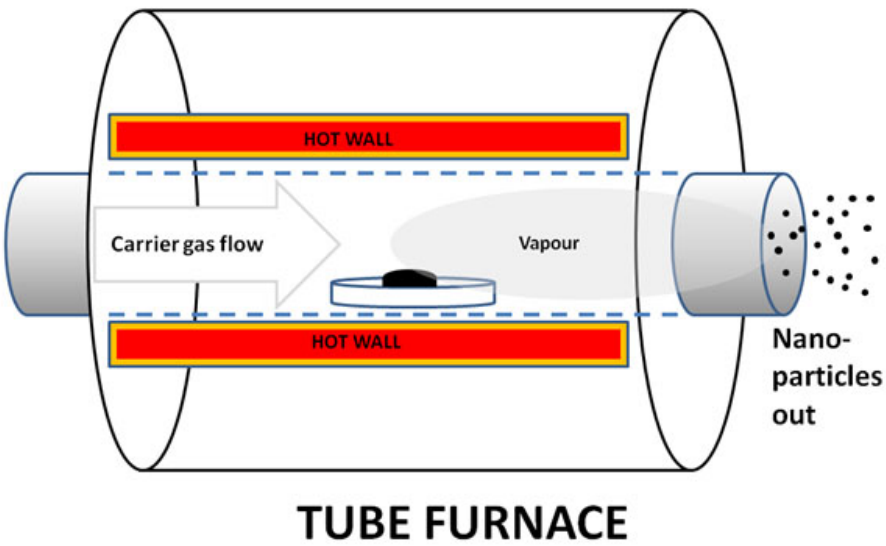

Figure 1.4. Schematic diagram of the experimental setup of inert gas condensation process.

❖ ***Pulsed laser ablation*:** In pulse laser ablation technique, more confined plume of the material is vaporized instead of the entire sample to produce vapor. To achieve this, high energy laser is focused on to a much localized position.[37,38] The laser exposure is made in pulses thus the name pulsed laser. This rapidly heats up a small spot of the material to very high temperature at which the material is vaporized. Due to the small weight size of the sample being vaporized, this generally can be used to make small amount of nanomaterials. However, the technique is quite useful in synthesizing nanomaterials of the

materials that cannot be evaporated otherwise. The method is excessively used to make metal oxide NPs than other types.

- ***Chemical vapor synthesis (CVS)*:** In chemical vapor synthesis (CVS), chemical vapors of precursor materials are brought to reaction in a reaction chamber. The reaction chamber is typically heated using joule heating.[39] The method is similar to chemical vapor deposition (CVD), however instead of deposition of nanomaterial as a thin film, CVS process encourage formation of NPs. Hence, the process parameters are adjusted appropriately during the synthesis in order to suppress film formation and to encourage nucleation of particles in the gas phase. Typically, the resident time of the precursor in the reaction chamber is the most critical parameter to determine whether the film or parameter will be formed.

  The main parameters of the CVS process are the residence time of precursors, gas flow rate, pressure different between inlet and the main chamber and temperature of the hot wall. In the simplest form of CVS, metal organic precursor is introduced to the hot wall reactor at a controlled rate.

  The reactor chamber can be filled with reactive gases to produce the respective metal oxide, halide, nitride or carbide during the process. In other technique, mixtures of NPs of two phases can be fabricated by supplying two or more precursors simultaneously. The same strategy was used to make doped nanomaterials as well. Some researchers have used CVS process to make coated or core shell NPs. This is typically achieved by supplying the second precursor at a later stage of the reactor. CVS is also regarded as a high throughput process as the production is continuous. Even a small scale reactor can produce considerably high amount of nanomaterials compared to other manufacturing techniques. An overview of the chemical vapor synthesis is illustrated in **Fig. 1.5**.

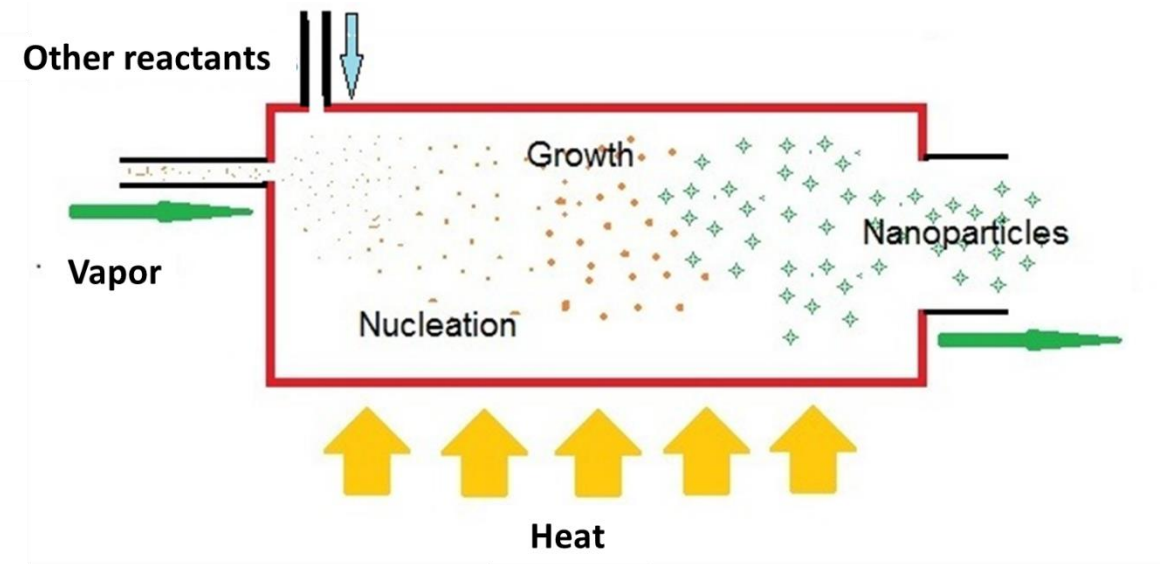

Figure 1.5. Chemical vapor synthesis process.

- ***Flame assisted synthesis*:** In flame assisted synthesis process, the energy required to particle nucleation is given by a flame instead of a supplying the energy externally from a secondary heat source. In the flame assisted synthesis method, particle nucleation and the growth will occur inside the flame.[40]
- ***Sputtering*:** Sputtering is a gas phase method of fabrication of nanomaterials that involves vaporizing of a solid precursor material by bombarding with a high velocity ions of an inert gas. This produce a cloud of atoms and atom clusters that get deposited into a substrate subsequently.[41] Sputtering is typically carried out under vacuum environment as at higher pressures mobility of sputtered materials are hindered. The most commonly used sputter sources are ion guns or hollow cathode plasma generators. This method is advantages as the composition of the sputtered material is same as the target material.

1.3.3. Microwave synthesis

Microwave-assisted synthesis is popular in areas ranging from biochemical processes to nanotechnology.[42–48] Chemical reactions are often faster than traditional convection heating methods, and have higher yields and fewer side products.[49,50] Using microwave irradiation it is possible to synthesize NPs with exact parameter control in a short time and also change particle properties and particle size as required. Microwave techniques eliminate the use of high temperature calcination for extended periods of time and allow

for fast, reproducible synthesis of crystalline metal oxide nanomaterials. Utilizing microwave energy for the thermal treatment generally leads to a very fine particle in the nanocrystalline regime because of the shorter synthesis time and a highly focused local heating **(Fig. 1.6)**.

Figure 1.6. Microwave (Monowave 300 & Masterwave BTR) synthesis instruments.

1.3.4. Hydrothermal method

Hydrothermal synthesis is generally operated in steel pressure vessels called autoclaves with or without Teflon liners under regulated temperature and/or pressure with the reaction in aqueous solutions.[51–53] The temperature can be elated above the boiling point of water, attaining the pressure of vapor saturation. Hydrothermal synthesis is widely used for the preparation of important inorganic materials, super ionic conductor, chemical sensors, electronically conducting solids, complex oxide ceramics and fluorides, magnetic materials and luminescence phosphors *etc*. Advantages of the hydrothermal synthesis method over other types of crystal growth include the ability to synthesize crystals of substances which are unstable near the melting point, and the ability to synthesize large crystals of high quality. Disadvantages are the high cost of equipment and the inability to monitor crystals in the process of their growth.

Hydrothermal synthesis can be effected both under temperatures and pressures below the critical point for a specific solvent above which differences between liquid and vapor disappear, and under supercritical conditions. The solubility of many oxides in hydrothermal solutions of salts is much higher than in pure water; such salts are called mineralizers.[54] There is also a group of solvothermal synthesis methods, relational to hydrothermal methods; this group of methods is based on the use of organic solvents and supercritical CO_2. One of the most widely known nanomaterials produced by the hydrothermal method are synthetic zeolites. A necessary condition for their production is the presence in the solution of some surface active agents (SAA) that actively influence morphological evolution of oxide compounds in hydrothermal solutions. The choice of synthesis conditions and type of surfactants can ensure the production of targeted porous nanomaterials with given pore size controlled in a fairly wide range of values.[55] Furthermore, with an ever-increasing demand for composite nanostructures, the hydrothermal technique offers a unique method for coating of various compounds on metals, polymers and ceramics as well as for the fabrication of powders or bulk ceramic bodies. It has now emerged as a frontline technology for the processing of advanced materials for nanotechnology. On the whole, hydrothermal technology offered a new perspective which is illustrated in **Fig. 1.7**. It links all the important technologies like geotechnology, biotechnology, nanotechnology and advanced materials technology.[56]

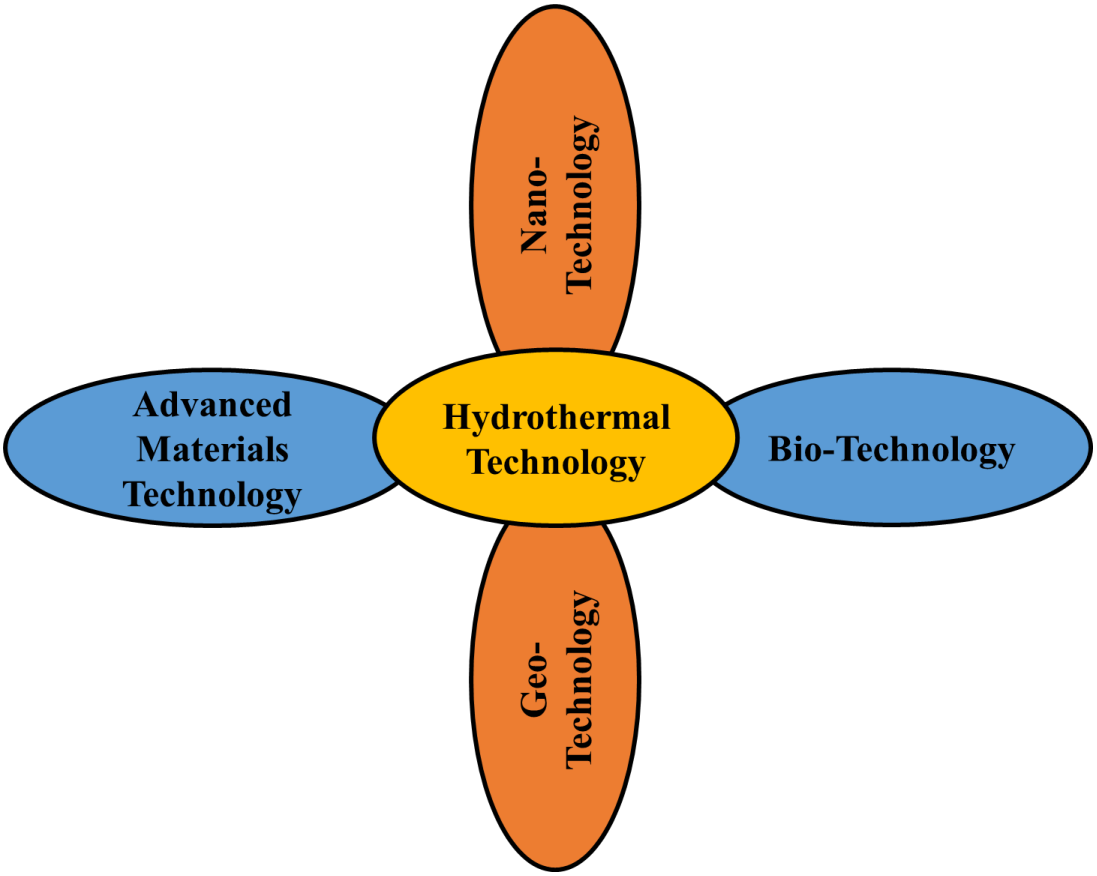

Figure 1.7. Schematic representation of hydrothermal technology.

1.3.5. Solvothermal synthesis

Solvothermal synthesis is a particularly versatile low-temperature route, in which polar solvents, under pressure and at temperatures above their boiling point, are used.[57] Under solvothermal conditions, the solubility of the reactants increases significantly, enabling reaction to take place at considerably lower temperatures than in conventional synthetic techniques. This type of soft-chemistry approach is mild enough to allow "molecular" building blocks such as chains and rings to form and participate in the formation of nanostructures.

1.3.6. Sol-gel processing

The sol-gel technique is a long-established industrial process for the generation of colloidal NPs from liquid phase that has been further developed in last years for the production of advanced nanomaterials and coatings. Sol-gel-processes are well adapted for oxide NPs and composites nanopowders synthesis. The main advantages of sol-gel techniques for the preparation of materials are low temperature of processing,

versatility, and flexible rheology allowing easy shaping and embedding. They offer unique opportunities for access to organic-inorganic materials. The most commonly used precursors of oxides are alkoxides, due to their commercial availability and to the high liability of the M-OR bond allowing facile tailoring in situ during processing. An overview of the sol-gel process is illustrated in **Fig. 1.8**.

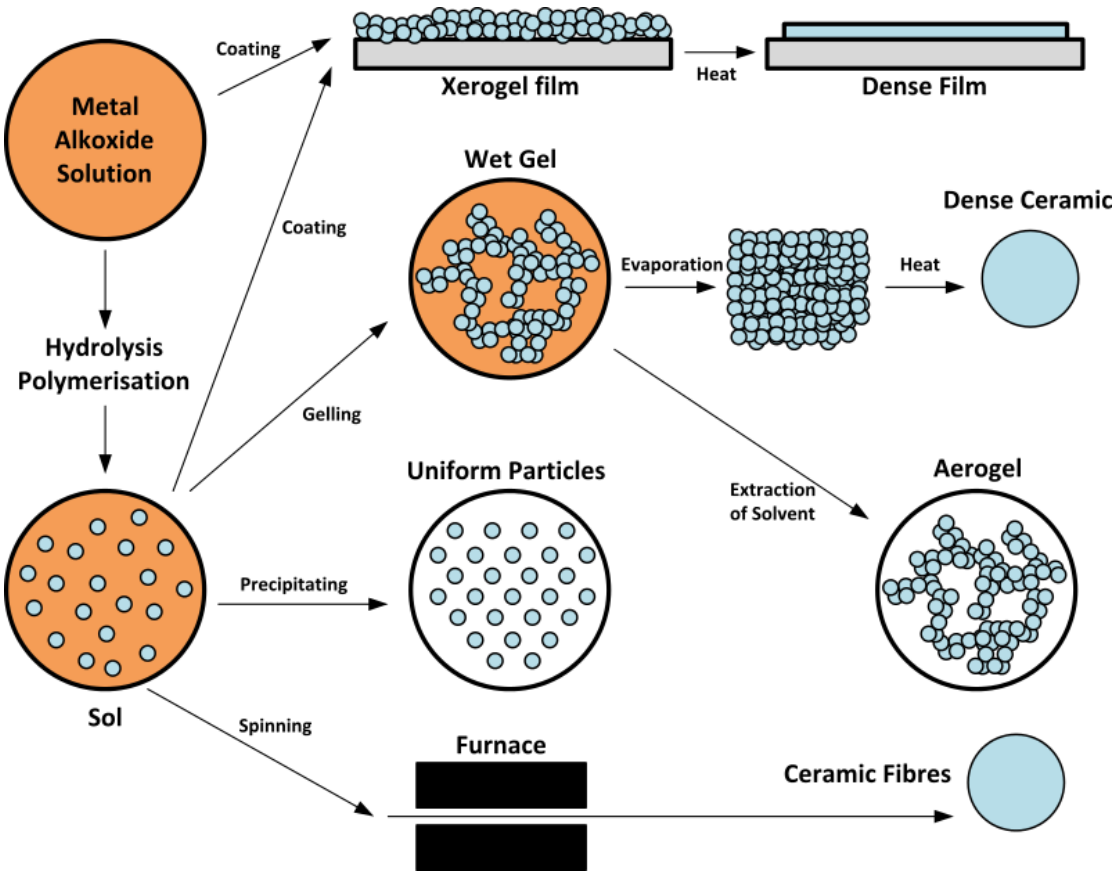

Figure 1.8. Schematic representation of the different stages and routes of the sol-gel process.

The starting materials used in the preparation of the sol are usually inorganic metal salts or metal organic compounds, which by hydrolysis and polycondensation reactions form the sol.[58–60] Further processing of the sol enables one to make ceramic materials in different forms. Thin films can be produced by spin-coating or dip-coating. When the sol is cast into a mould, a wet gel will form. By drying and heat-treatment, the gel is converted into dense ceramic or glass materials. If the liquid in a wet gel is removed under a supercritical condition, a highly porous and extremely low density aerogel material is obtained. As the viscosity of a sol is adjusted into a suitable viscosity range, ceramic fibres can be drawn from the sol. Ultrafine and uniform ceramic powders are formed by precipitation, spray pyrolysis, or emulsion techniques.

Sol-gel derived products have numerous applications. One of the promising application areas is for coatings and thin films used in electronics, optical and electro-optical components and devices, such as substrates, capacitors, memory devices, infrared (IR) detectors and wave guides. Anti-reflection coatings are also used for automotive and architectural applications. Submicron particle size powders of single and multicomponent composition can be made for structural, electronic, dental and biomedical applications. Composite powders can also be used as agrochemicals or herbicides. Optical and refractory fibers are used for fiber optics sensors and thermal insulation, respectively. In addition, sol-gel techniques can be used to infiltrate fiber performs to make composites. Glass monoliths and coating and organic/inorganic hybrids are under development for lenses, mirror substrates, graded index optics, optical filters, chemical sensors, passive and nonlinear active waveguides and lasers. Membranes for separation and filtration processes also are being investigated, as well as catalysts. Biomolecules (such as proteins, enzymes, antibodies, *etc*.) are incorporated into sol-gel matrices, which can be used for the monitoring of biochemical processes, environmental testing, food processing and drug delivery for medicine or agriculture.

1.3.7. Co-precipitation method

Co-precipitation is the least expensive and the simplest approach for making NPs. This method produces NPs in large quantities (order of grams) in a relatively short interval of time and utilizes inexpensive and readily available chemicals as precursors. The synthesis of NPs by co-precipitation method consists of several steps including:[61,62]

- Nucleation
- Growth
- Coarsening
- Agglomeration

For the fabrication of monodispersed NPs, the nucleation and growth stages must be under precise control (**Fig. 1.9**). The rapid nucleation and relatively slow growth will lead to the formation of monodispersed NPs. In the slow growth mode, molecules of NPs generally follow the Oswald ripening process, whereas the rapid growth mode will always lead to an irregular morphology and scattered size distribution for the NPs.[63]

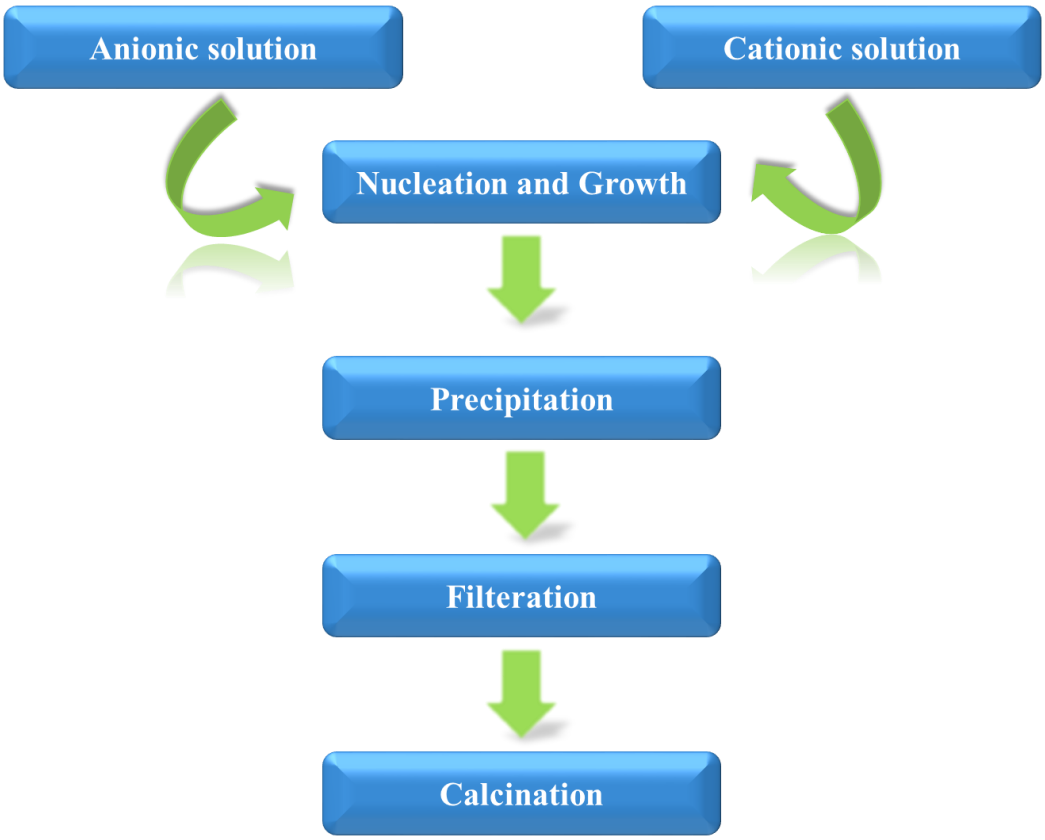

Figure 1.9. Co-precipitation method for nanoparticle synthesis.

Co-precipitation method gives an amorphous product and subsequent calcinations or annealing is necessary in order to render the crystalline NPs, in which some agglomeration will be unavoidable. The crystalline NPs are rarely precipitated for aqueous solution therefore, the non-aqueous approach using organic solvent may be used to overcome some of these issues of aqueous solutions in the synthesis of metal oxide NPs.[64,65]

There are three main mechanisms of co-precipitation:[66]

- Inclusion
- Occlusion
- Adsorption

An **inclusion** occurs when the impurity occupies a lattice site in the crystal structure of the carrier, resulting in a crystallographic defect; this can happen when the ionic radius and charge of the impurity are similar to those of the carrier. An **adsorbate** is an impurity that is weakly bound (adsorbed) to the surface of the precipitate. An **occlusion** occurs when an adsorbed impurity gets physically trapped inside the crystal as it grows.

1.4. Properties of nanomaterials

Nanoparticles have one dimension that measures 100 nanometers or less. The properties of many conventional materials change when formed from NPs. This is typically because NPs have a greater surface area per weight than larger particles which causes them to be more reactive to some other molecules.

There are several properties of nanomaterials follows as:

- Physical properties
- Chemical properties

1.4.1. Physical properties

Nanomaterials displays some characteristic physical properties including electrical, catalytic, magnetic, mechanical, thermal or imaging features as compare to normal bulk particles which make the nanomaterials a significant area in medical, pharmaceutical and different engineering sectors. The nanomaterials acquire some incredible and specific peculiar properties which may be considerably different from the physical properties of bulk materials.[67,68] The specific features of those physical properties are as follows:

- ***Color*:** There are some materials which show different color when they are changed to NPs like gold materials which turn into red when they are converted to nanomaterials. Gold NPs in contact with light is powerfully controlled by the particle sizes of the materials. Small particle sizes (~2-150 nm) have high surface electron densities which are called as surface plasmons undergo a collective oscillation when they are excited by light at specific wavelengths.[69–71] This oscillation is described as a surface plasmon resonance (SPR). For small (~30 nm) monodisperse gold NPs the surface plasmon resonance phenomena is responsible for an absorption of the blue-green portion of the spectrum (~450 nm) while red light (~700 nm) is reflected, producing a rich red color (**Fig. 1.10**).

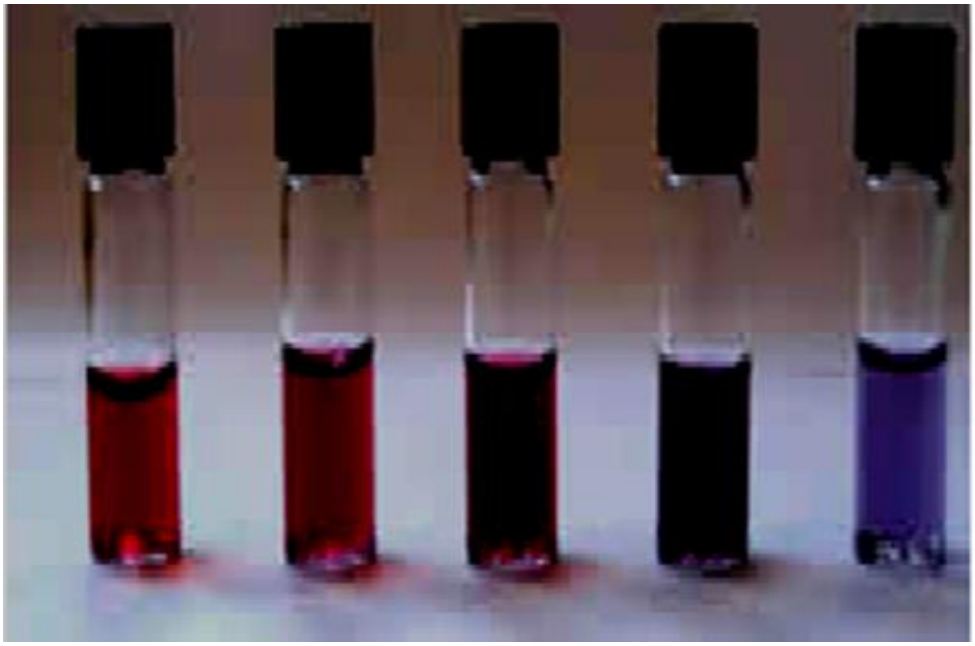

Figure 1.10. Suspensions of gold nanoparticles of various sizes.

- ***Melting point*:** The melting point drastically falls when the particle size of the material approaches to the nanoscale ranges. This phenomenon related to melting point depression is very prominent in nanoscale materials which melt at temperature hundreds of degrees lower than bulk materials. Melting point depression is most evident in nanowires, nanotubes and nanoparticles, which all melt at lower temperatures than bulk form of the same material. Changes in melting point occur because nanoscale materials have a much larger surface to volume ratio than bulk materials, drastically altering their thermodynamic and thermal properties.[72]
- ***Mechanical strength*:** All the nanomaterials possess high mechanical strength as compared to their conventional counterparts. The mechanical strength of nanomaterials may be one or two times higher in magnitude than that of single crystals in the bulk form. Defects in the form of atomic vacancies can lower the tensile strength of the materials by up to 85 %. Conversion of materials into nanoscale increases crystal perfection or reduction of defects, which would result the enhancement in mechanical strength. Cutting tools which should be harder than the material which is to be cut are made of nanomaterials, such as tungsten carbide, tantalum carbide and titanium carbide. These cutting tools are much more erosion-resistant and durable than their conventional large grained bulk materials. In general, hardness of metals (e.g. Cu) increases linearly with

increase of grain size. However, in case of nanomaterial, the hardness increases linearly with decrease of particle size.[73]

- ***Electrical properties*:** This is quite complex phenomenon. Reduction in material's dimensions would have two different contrasting effects on electrical conductivity. By its property nanoparticle product enhance the crystal perfection and as well as it reduce the defects. As a result electron scattering phenomenon due to crystal defects are also reduced and a reduction in resistivity is experienced. However, at room temperature the defect scattering incident contributes a minor influence on the total electrical resistibility of various metals. On the other hand surface scattering phenomenon which is highly increased due to reduction of particle size is one of the prominent reasons for increase of the total resistivity. In addition a reduction in particle size below a critical dimension, (*i.e.* electron de Broglie wavelength), would result in a modified electronic structure with wide and discrete band gap. The reduction of particle size into this range would result in an increased electrical resistivity.[74]
- ***Optical properties*:** Optical properties exhibited by nanomaterials are quite different from their bulk counterpart. The reason behind this change in property is mainly due to the effect of the surface plasmon resonance. In addition, the increased energy level spacing is also an important criterion for this changing behavior. Due to increased band gap for semiconductor NPs absorption edge is shifted toward shorter wavelengths. Surface plasmon resonance effect changes due to change in particle size which in turn changes the color of metallic NPs.[70] The coherent excitation of entire free electrons in the conduction band may produce an in-phase oscillation, called surface plasmon resonance. When the size of a metal nanocrystal is smaller than the wavelength of incident radiation, a surface plasmon resonance is generated. On resonance, light is tightly confined to the surface of the nanostructure, until it gets eventually absorbed inside the metal, or scattered back into photons.[74]
- ***Magnetic properties*:** Reducing the size of the magnetic systems changes the electronic properties by reducing the symmetry of the system and by introducing a quantum confinement.[75] The strength of a magnet is measured in terms of coercivity and saturation magnetization value. These values increase with decrease in the grain size and an increase in specific surface area (surface area per unit volume) of the grain.

Nanoparticles exhibit magnetic properties that are different from bulk materials. These are due to the following reasons:

- As the size of these system reaches the typical lengths of few nanometers, it is expected that the response of the system depends on the boundary conditions (which no longer periodic, but determined by the particle size) and therefore, to be different from bulk materials.
- Because of the large ratio of surface to volume atoms in NPs, the surface energy becomes important when compared with volume energy, and therefore, the equilibrium situation can be different that for bulk materials. In the case of NPs, the volume is so small, therefore the thermal energy (K_BT) is enough to invert the magnetization with relaxation times as low as few seconds. Thus, the material looses coercivity and remanence, giving rise to the so-called super paramagnetic behavior.

1.4.2. Chemical properties

Chemical properties of the materials are also changed when it converts to nano range. Due to increase of exposed surface area of the NPs as compared with conventional bulk objects, reactivity of those particles increase enormously.

Some important chemical properties of the NP are as follows:

- In case of NPs 50 % of all the atoms are surface atoms and as a result electric transport properties of these particles are no longer dependent on solid state bulk phenomenon. Electrical properties are directly related to chemical properties.
- Due to larger proportion of surface atoms, the atoms present in nanomaterials posses a higher energy as compare to atoms present in bulk structure.
- The interactions between NPs depend on the chemical nature of the surface. Due to large surface area high quantity charge species defects and impurities may be easily attracted to surfaces and interfaces of NPs and thus chemical nature of the surfaces changes abruptly as compare to their bulk counterpart.
- Surface properties of the NPs and their interaction can be modified or altered by using molecular monolayer.

1.5. Ni-Co nanoferrites: A brief review

Ferrites are chemical compounds obtained as powder or ceramic bodies with ferrimagnetic properties formed by iron oxides as their main component, Fe_2O_3 and FeO, which can be partly changed by other transition metal oxides.[76] Spinel ferrites have general formula AB_2O_4, where A is divalent and B is trivalent metal cations, respectively (**Fig. 1.11**). The Oxygen forms an *fcc* crystal lattice with $32O^{2-}$, which has 64 tetrahedral and 32 octahedral vacancies, wherein, 1/8 of tetrahedral and 1/2 of octahedral sites are occupied by A and B metal cations.[77–79] The magnetic and electrical properties of ferrites are highly sensitive to the cation distribution among tetrahedral and octahedral sites, which in turn can be governed by the choice of synthesis route and sintering conditions. Super paramagnetism, spin canting, core/shell structure, metastable cation distribution *etc*. are some of the phenomena, which have been observed in NPs of various ferrites.[80–82]

Cobalt ferrite is a well-known hard magnetic material with relatively high coercivity and saturation magnetization while nickel ferrite is a soft material with low coercivity and saturation magnetization. These (hard and soft magnetic) properties make them very promising candidates for a variety of applications in biomedical, electronic as well recording technologies.[83–86] Many technological applications require magnetic NPs to be embedded in a nonmagnetic matrix. Over the past few years, increased attention has been focused on the preparation of various nanostructures with magnetic nanoparticulate components and on understanding the magnetic behavior of NPs due to new possible surface, interparticle, and exchange interactions in magnetic/nonmagnetic matrix.[87]

Encapsulating magnetic NPs in silica is a promising and important approach in the development of magnetic NPs for technological and biomedical applications. For magneto-electronic applications, silica-coated NPs could be used to form ordered arrays with interparticle magnetic couplings controlled through the silica shell thickness.[88] The rich and well documented biocompatible chemistry of silica colloids may allow for practical implementation of magnetic NPs in magnetically guided drug delivery, tumor targeting, and magnetically assisted chemical separation of cells and/or protein.[89–91]

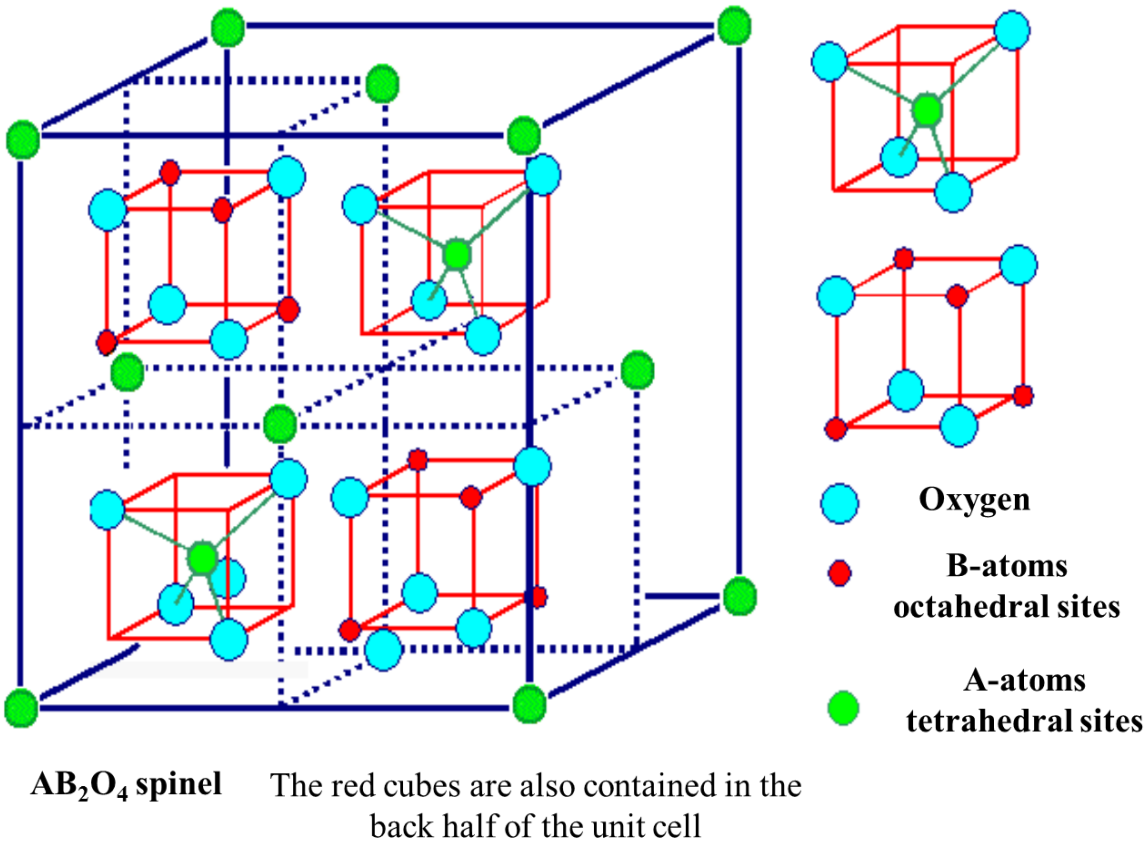

Figure 1.11. The schematic diagram of spinel structure of ferrite with tetrahedral and octahedral sites.

1.5.1. Applications of ferrite

- Spinel ferrites ceramic are widely used in microwave devices to control transmission path, frequency, amplitude and phase of microwave signals.
- The structured magnetic materials have an interesting area of study because of its possible applications in a variety of widely areas ranging from information technology to biotechnology.
- Ferrites are excellent soft magnetic materials in high-frequency devices due to their low cost, high resistivity and low eddy current losses, which have been studied extensively for multilayer chip inductor application.

1.6. Tin oxide (SnO_2) NPs: A brief review

SnO_2 is a wide band-gap metal oxide semiconductor (**Table 1.1**) in which inherent oxygen vacancies act as *n*-type dopants.[92,93] It belongs to a class of materials that combines high electrical conductivity with optical transparency and thus constitutes an important component for optoelectronic applications.[94] The

study of SnO_2 is motivated by its applications as a solid state gas sensor material, oxidation catalyst, and transparent conductor.[95–100] The key for understanding many aspects of SnO_2 surface properties is the dual valency of Sn. The dual valency facilitates a reversible transformation of the surface composition from stoichiometric surfaces with Sn^{4+} surface cations into a reduced surface with Sn^{2+} surface cations depending on the oxygen chemical potential of the system.[101] SnO_2 has the rutile type tetragonal structure belonging to the *P42/mnm* space group (**Fig. 1.12**). The lattice parameters are a = b = 4.7382 Å and c = 3.1871 Å, and the band-gap energy is in the ultraviolet range between 3.5 and 3.8 eV as estimated from experimental results and theoretical calculations.[102] Its high optical transparency, electrical conductivity, and chemical stability make it a very attractive material for solar cells, heat mirrors, catalysis and gas sensing applications.

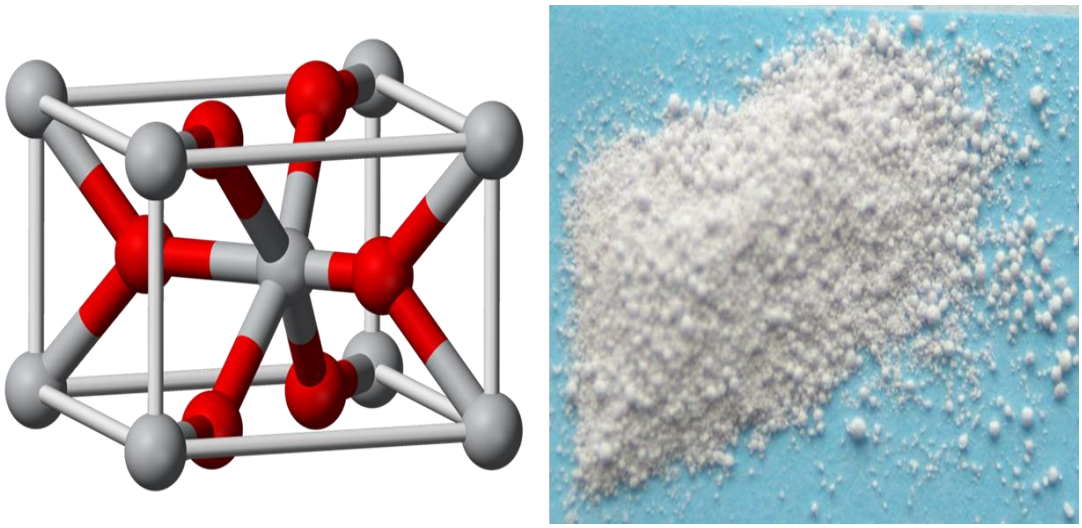

Figure 1.12. The schematic diagram of rutile type tetragonal structure and powder form of SnO_2 nanoparticle.

Table 1.1. Properties of SnO_2 NPs.

S.No.	Properties	Values
1.	Chemical formula	SnO_2
2.	Molar mass	150.71 g mol^{-1}
3.	Melting point	1630 °C
4.	Boiling point	1900 °C
5.	Density	6.95 g cm^{-3}
6.	Appearance	White or light grey powder
7.	Odor	Odorless
8.	Solubility in water	Insoluble
9.	Solubility	Soluble in hot concentrated alkalis, Concentrated acids, Insoluble in alcohol
10.	Magnetic susceptibility (χ)	-4.1×10^{-5} cm^3 mol^{-1}
11.	Refractive index	2.006
12.	Crystal structure	Rutile tetragonal
13.	Electronic configuration	Tin [Kr] $4d^{10}$ $5s^2$ $5p^2$ Oxygen [He] $2s^2$ $2p^4$

1.6.1. Applications of SnO_2 NPs

- SnO_2 NPs, as one of the most important semiconductor oxides, has been used as photocatalyst for photodegradation of organic compounds.
- SnO_2 NPs also used as catalysts, energy-saving coatings and anti-static coatings, in the making of optoelectronic devices and resistors.
- SnO_2 layers have been used as transparent and electrically conducting coatings on glass. These films have a high mechanical and chemical stability. Due to the mechanical stability of the SnO_2 they are used in hot end coatings on bottles.
- SnO_2 NPs has very good transparent mirror properties, due to this property they are used as electrodes and anti-reflection coatings in solar cells, as heat shields in electronic devices, in thermal insulation, in solar head collectors, in photovoltaic cells, in double glazing lamps.
- SnO_2 NPs are widely used in sensing applications due to its semiconductor properties like in smoke sensors, humidity sensors, gas sensors *etc*. The transparent electrical conduction property of SnO_2 NPs are mostly used in transparent ovens and in liquid crystal displays.

1.7. Silica coated nickel oxide (NiO) NCs: A brief review

NiO NPs are one such momentous metal oxide that tend to be *p*-type semiconductor with a wide band-gap (**Fig. 1.13**).[103] It has tremendous application in science and technology (**Table 1.2**). It can be used as a transparent *p*-type semiconducting layer[104,105] and as an antiferromagnetic film[106] and can also be extensively used in smart windows,[107] electrochemical supercapacitor,[108–110] and dye-sensitized photocathode.[111] It exhibits anodic electrochromism. Due to excellent durability and electrochemical stability, low material cost as an ion storage material, large-spin optical density, and various manufacturing possibilities, NiO semiconductors become interesting topics for scientists. Different methods have already been reported for the synthesis of NiO NPs such as evaporation,[112,113] magnetron sputtering,[114–116] and sol-gel.[117] Particularly, the optical behavior of NiO under different circumstances is becoming one of the prime searches of the scientists. Professor Guerra *et al.*[118] investigated the cathodoluminescence and photoluminescence of NiO whereas Professor Kuzmin and his group[119] examined the effect of doping in the origin of visible photoluminescence in NiO. Even the NiO nanowires are also under observation for their emission property.[120] However, the complexity remains in the synthesis technique as well as in the limitation of tailoring the optical properties of NiO NPs. Especially the optical response of bare NiO NPs cannot be tailored much for their large band-gap energy. Keeping this in mind, scientists have proposed to oxidize Ni nanoparticle within insulating medium by ion implantation method in search of better stability and novel optical properties.[121] Effort has been also delivered to synthesize NiO NPs within insulating silica matrix to form nanocomposite (NC) films leading toward optical gas sensor.[122,123]

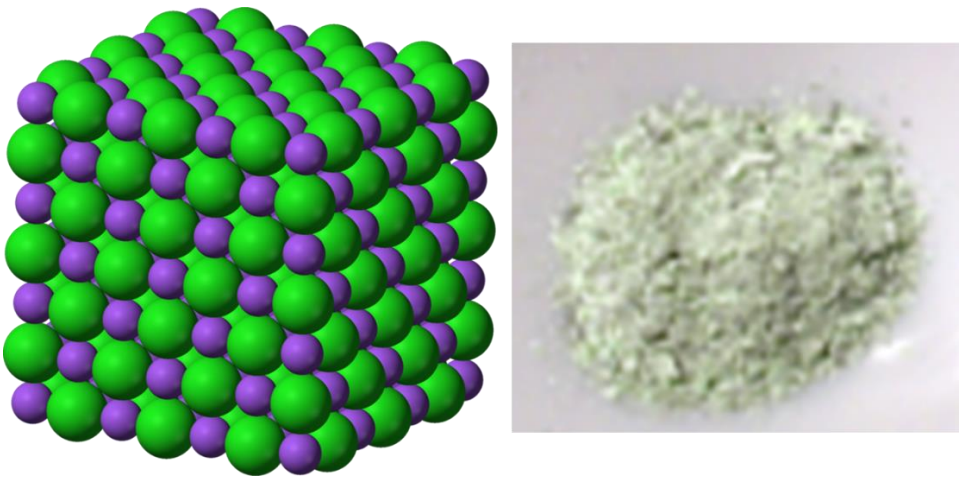

Figure 1.13. The schematic diagram and powder form of NiO nanoparticles.

Table 1.2. Properties of NiO NPs.

S.No.	Properties	Values
1.	Chemical formula	NiO
2.	Molar mass	74.6928 g mol^{-1}
3.	Appearance	Green crystalline solid
4.	Density	6.67 g cm^{-3}
5.	Melting point	1955 °C
6.	Solubility in water	Negligible
7.	Solubility	Soluble in KCN
8.	Magnetic susceptibility (χ)	660×10^{-6} cm^3 mol^{-1}
9.	Refractive index	2.1818

1.7.1. Applications of NiO NPs

The key applications of NiO NPs are as follows:

- In preparation of Ni cermet for the anode layer of solid oxide fuel cells.
- In lithium NiO cathodes for lithium ion microbatteries.
- In electrochromic coatings, plastics and textiles.
- In nanowires, nanofibers and specific alloy and catalyst applications.
- As a catalyst and as anti-ferromagnetic layers.
- In light weight structural components in aerospace.
- Adhesive and coloring agents for enamels.
- In active optical filters.
- In ceramic structures.
- In automotive rear-view mirrors with adjustable reflectance.
- In cathode materials for alkaline batteries.
- Electrochromic materials.
- Energy efficient smart windows.
- P-type transparent conductive films.
- Materials for gas or temperature sensors, such as CO sensor, H_2 sensor, and formaldehyde sensors.
- As a counter electrodes.

1.8. Characterization techniques

There are several techniques used to understand these characterization parameters in NPs. They include:

- X-ray diffraction (XRD)
- Scanning electron microscopy (SEM)
- Energy dispersive X-ray analysis (EDS)
- X-ray photoelectron spectroscopy (XPS)
- Transmission electron microscopy (TEM)
- High resolution transmission electron microscopy (HR-TEM)
- Optical spectroscopy
- UV-Visible (UV-Vis) spectroscopy
- Differential thermal analysis (DTA)/Thermogravimetric analysis (TGA)
- Infrared spectroscopy (IR)

1.8.1. X-ray diffraction (XRD)

The X-ray diffraction is a conventional technique for determination of crystallographic structure and compositional analysis of the materials. There is increase or decrease in intensity with the amount of constituent. This technique is used to establish the metallic nature of particles gives information on translational symmetry size and shape of the unit cell from peak positions and information on electron density inside the unit cell, namely where the atoms are located from peak intensities.[124]

The interaction of X-ray radiation with crystalline sample is governed by Bragg's law, which depicts a relationship between the diffraction angles (Bragg angle), X-ray wavelength, and interplanar spacing of the crystal planes. According to Bragg's law, the X-ray diffraction can be visualized as X-rays reflecting from a series of crystallographic planes as shown in **Fig. 1.14**. The path differences introduced between a pair of waves travelled through the neighboring crystallographic planes are determined by the interplanar spacing. If the total path difference is equal to $n\lambda$ (n being an integer), the constructive interference will occur and a group of diffraction peaks can be observed, which give rise to X-ray patterns. The quantitative account of Bragg's law can be expressed as:

$$2d_{hkl}sin\theta = n\lambda$$

Where d is the interplanar spacing for a given set of hkl and θ is the Bragg angle.

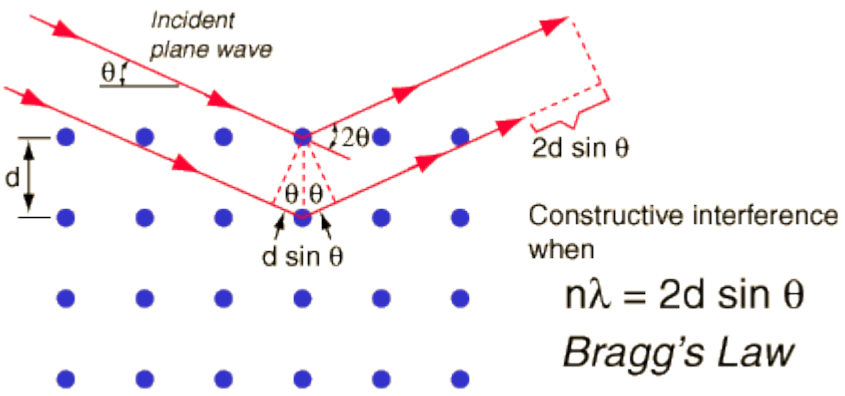

Figure 1.14. Geometrical illustrations of crystal planes and Bragg's law.

The XRD measurements were carried out using Rigaku X-ray diffractometer with Cu Kα (λ = 1.54187Å) radiation at room temperature, shown in **Fig. 1.15** and **Fig. 1.16**, and operated at a voltage of 30 kV and filament current of 40 mA.

The diffraction method is based on the effect of broadening of diffraction reflections associated with the size of the particles (crystallites). All types of defects cause displacement of the atoms from the lattice sites. M.A. Krivoglaz[125] in 1969 derived an equation for the intensity of the Bragg reflections from a crystal defect, which enabled all the defects to be derived conventionally into two groups. The defects in the first group only lower the intensity of the diffraction reflections but do not cause the reflection broadening. The broadening of the reflections is caused by the defects of second group. These defects are micro-deformations, inhomogeneity (non-uniform composition of the substance over their volume) and the small particle size. The size of nanomaterials can be derived from the peak broadening and can be calculated by using the Scherrer equation, provided that the nanocrystalline size is less than 100 nm.

$$D = \frac{k\lambda}{\beta COS\theta}$$

Where D is the average crystallite dimension perpendicular to the reflecting phases, λ is the X-ray wavelength, k is the Scherrer constant which equals to 0.9 for spherical particles, whose value depends on the shape of the particle (crystallite, domain) and on diffraction reflection indices (*hkl*), and β is the full width half maximum of the peaks.

The Scherrer formula is quite satisfactory for small grains (large broadening) in the absence of significant microstrain. A microstrain describes the relative mean square deviation of the lattice spacing from its mean value. Based on the grain size dependence

of the strain it is reasonable to assume that there is a radial strain gradient, but from X-ray diffraction only a homogeneous, volume averaged value is obtained.

Figure 1.15. X-ray Diffraction (XRD) machine.

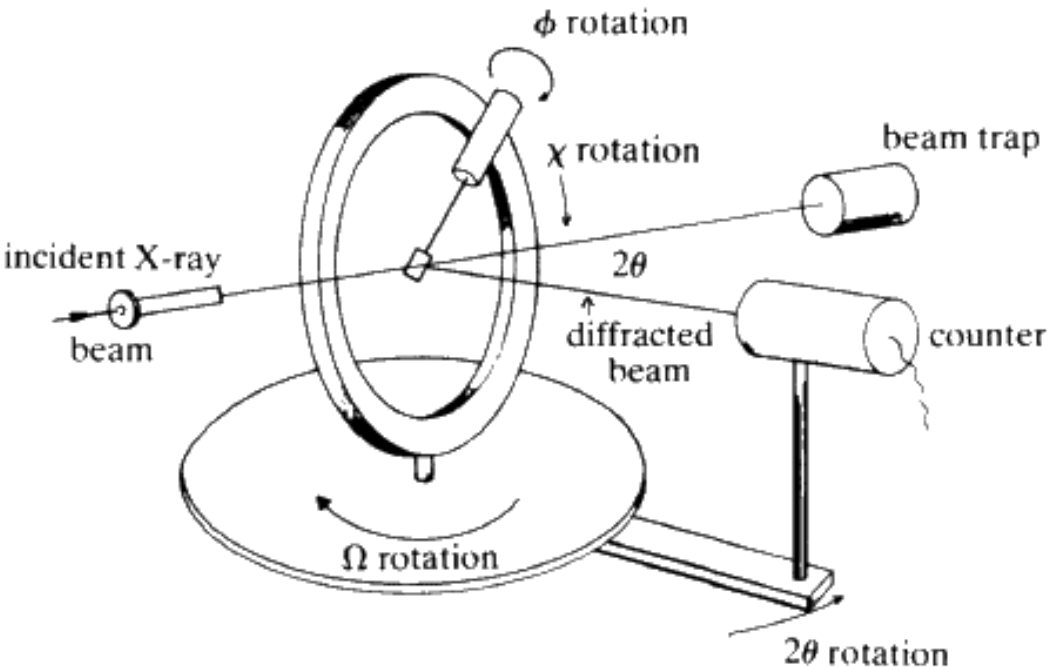

Figure 1.16. Schematic details of X-ray Diffraction (XRD).

Therefore, X-ray diffraction is most widely used for the identification of unknown crystalline materials (e.g. minerals, inorganic compounds). Determination of unknown solids is critical to studies in geology, environmental science, material science, engineering and biology.

Other applications include:

- Characterization of crystalline materials
- Identification of fine-grained minerals such as clays and mixed layer clays that are difficult to determine optically
- Determination of unit cell dimensions
- Measurement of sample purity

With specialized techniques, XRD can be used to:

- Determine crystal structures using Rietveld refinement
- Determine modal amounts of minerals (quantitative analysis)
- Characterize thin films samples by:
    - Determining lattice mismatch between film and substrate and to inferring stress and strain
    - Determining dislocation density and quality of the film by rocking curve measurements
    - Measuring superlattices in multilayered epitaxial structures
    - Determining the thickness, roughness and density of the film using glancing incidence X-ray reflectivity measurements
- Make textural measurements, such as the orientation of grains, in a polycrystalline sample.

1.8.2. Scanning electron microscopy (SEM)

The scanning electron microscope (**Fig. 1.17**) is an electron microscope that determines the size, shape and surface morphology with direct visualization of the NPs. Therefore scanning electron microscopy offer several advantages in morphological and sizing analysis. However they provide limited information about the size distribution and true population average. During the process of SEM characterization, solution of NPs should be initially converted into a dry powder. This dry powder is then further mounted on a sample holder followed by coating with a conductive metal (e.g. gold) using a sputter coater. Whole sample is then analyzed by scanning with a focused fine beam of

electrons.[126] Secondary electrons emitted from the sample surface determine the surface characteristics of the sample. This electron beam can often damage the polymer of the NPs which must be able to withstand vacuum. Average mean size evaluated by SEM is comparable with results obtained by dynamic light scattering (DLS). In addition these techniques are time consuming, costly and frequently need complementary information about sizing distribution.[127]

The basic principle behind the SEM is that when the beam of electrons strikes the surface of the specimen and interacts with the atoms of the sample, signals in the form of secondary electrons, back scattered electrons and characteristic X-rays are generated that contain information about the sample's surface topography, composition, *etc*. The SEM can produce very high-resolution images of a sample surface, revealing details about 1-5 nm in size in its primary detection mode *i.e.* secondary electron imaging. Characteristic X-rays are the second most common imaging mode for an SEM. These characteristic X-rays are used to identify the elemental composition of the sample by a technique known as energy dispersive X-ray (EDS). Back-scattered electrons (BSE) that come from the sample may also be used to form an image. BSE images are often used in analytical SEM along with the spectra made from the characteristic X-rays as clues to the elemental composition of the sample.[128]

In a typical SEM, the beam passes through pairs of scanning coils or pairs of deflector plates in the electron column to the final lens, which deflect the beam horizontally and vertically so that it scans in a raster fashion over a rectangular area of the sample surface. Electronic devices are used to detect and amplify the signals and display them as an image on a cathode ray tube in which the raster scanning is synchronized with that of the microscope. The image displayed is therefore a distribution map of the intensity of the signal being emitted from the scanned area of the specimen.

SEM requires that the specimens should be conductive for the electron beam to scan the surface and that the electrons have a path to ground for conventional imaging. Non-conductive solid specimens are generally coated with a layer of conductive material by low vacuum sputter coating or high vacuum evaporation. This is done to prevent the accumulation of static electric charge on the specimen during electron irradiation. Non-conducting specimens may also be imaged uncoated using specialized SEM instrumentation such as the "Environmental SEM" (ESEM) or in field emission gun (FEG) SEM operated at low voltage, high vacuum or at low vacuum, high voltage.

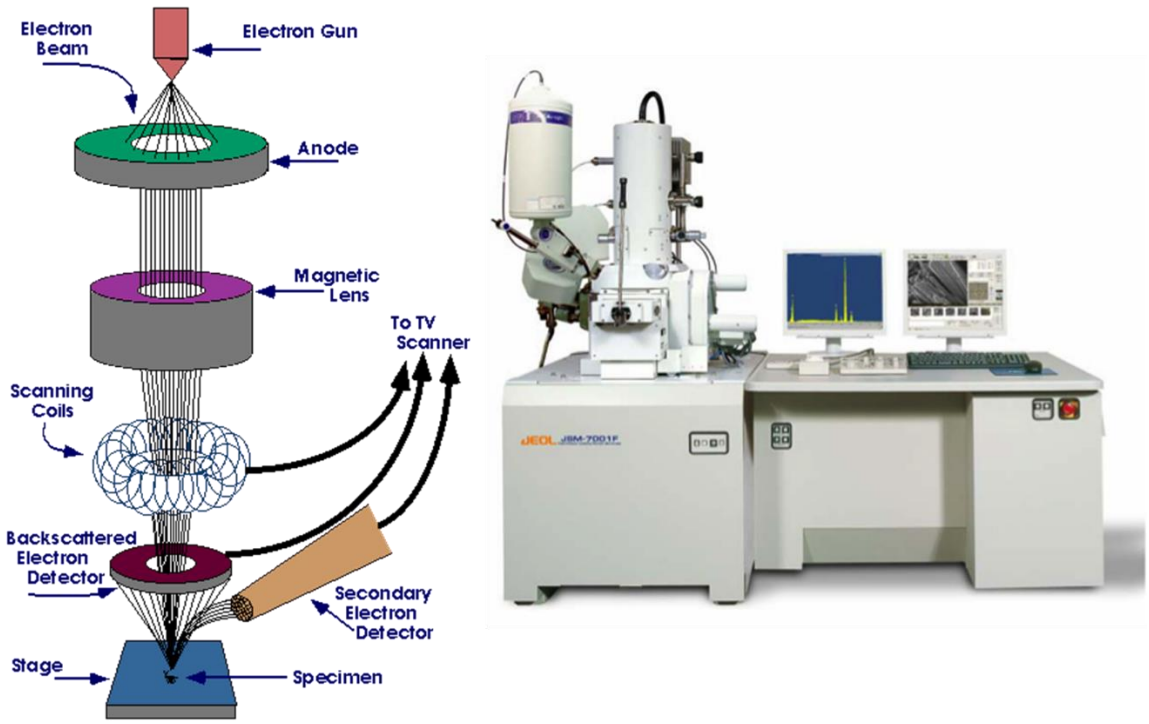

Figure 1.17. Schematic representation of scanning electron microscope (SEM).

1.8.3. Energy dispersive X-ray analysis (EDS)

EDS analysis is a technique to analyze near surface elements and estimate their proportion at different position, thus giving an overall mapping of the sample.

This technique is used in conjunction with SEM. An electron beam strikes the surface of a conducting sample. The energy of the beam is typically in the range 10-20 keV. This causes X-rays to be emitted from the material. The energy of the X-rays emitted depends on the material under examination. The X-rays are generated in a region about 2 microns (µ) in depth, and thus EDS is not truly a surface science technique. By moving the electron beam across the material an image of each element in the sample can be obtained. Due to the low X-ray intensity, images usually take a number of hours to acquire.

The composition or the amount of NPs near and at the surface can be estimated using the EDS, provided they contain some heavy metal ions. Elements of low atomic number are difficult to detect by EDS. The Si-Li detector protected by a beryllium (Be) window cannot detect elements below an atomic number of 11 (Na). In windowless systems, elements with as low atomic number as 4 (Be) can be detected. EDS spectra have to be taken by focusing the beam at different regions of the same sample to verify spatially uniform composition of the bimetallic materials.

1.8.4. X-ray photoelectron spectroscopy (XPS)

The X-ray photoelectron spectroscopy (**Fig. 1.18**) also known as electron spectroscopy for chemical analysis (ESCA) is the most widely used surface analysis technique because it can be applied to a broad range of materials and provides valuable quantitative and chemical state information from the surface of the material being studied. The average depth of analysis for an XPS measurement is approximately 5 nm. XPS is typically accomplished by exciting a samples surface with monoenergetic Al kα X-rays causing photoelectrons to be emitted from the sample surface. An electron energy analyzer is used to measure the energy of the emitted photoelectrons (**Fig. 1.19**). From the binding energy and intensity of a photoelectron peak, the elemental identity, chemical state, and quantity of a detected element can be determined.

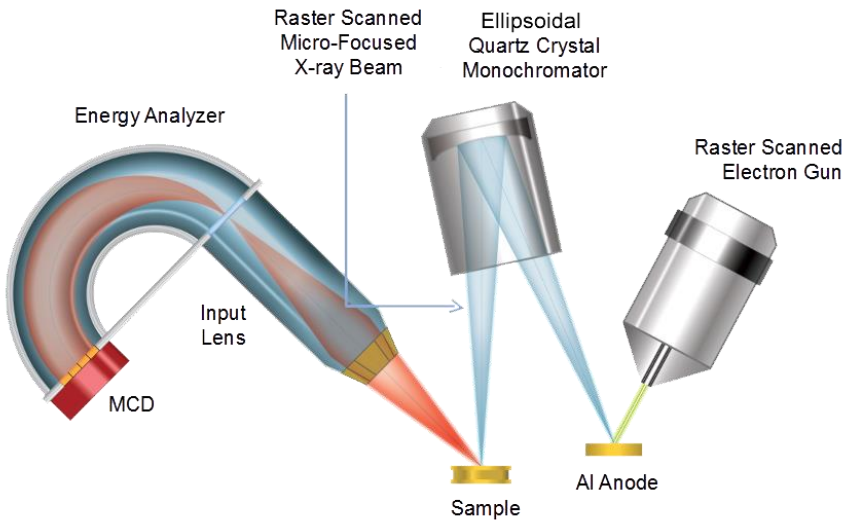

Figure 1.18. Schematic view of XPS.

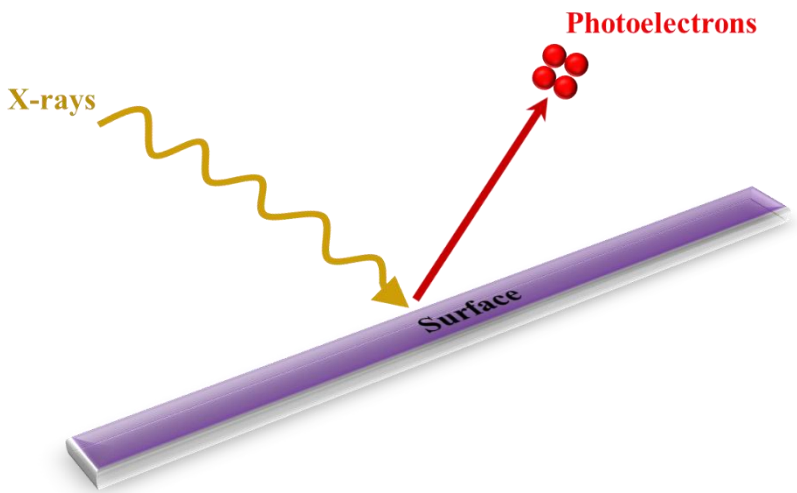

Figure 1.19. Ejection of photoelectrons.

As the demand for high performance materials increases, so does the importance of surface engineering. Many of the problems associated with modern materials can be solved only by understanding the physical and chemical interactions that occur at the surface or at the interfaces of a material's layers. The surface chemistry will influence such factors as corrosion rates, catalytic activity, adhesive properties, wettability, contact potential and failure mechanisms.

The material's surface is the point of interaction with the external environment and other materials. Therefore, surface modification can be used in a wide variety of applications to alter or improve the performance and behavior of a material. XPS can be used to analyze the surface chemistry of a material after an applied treatment such as fracturing, cutting or scraping. From non-stick cookware coatings to thin film electronics and bioactive surfaces, XPS is the standard tool for surface material characterization.

1.8.5. Transmission electron microscopy (TEM)

Transmission electron microscopy (**Fig. 1.20**) is a microscopy technique whereby a beam of electrons is transmitted through an ultra-thin specimen and interacts as passes through the sample. An image is formed from the electrons transmitted through the specimen, magnified and focused by an objective lens and appears on an imaging device, such as a fluorescent screen, on a layer of photographic film, or to be detected by a sensor such as a charge-coupled device (CCD).

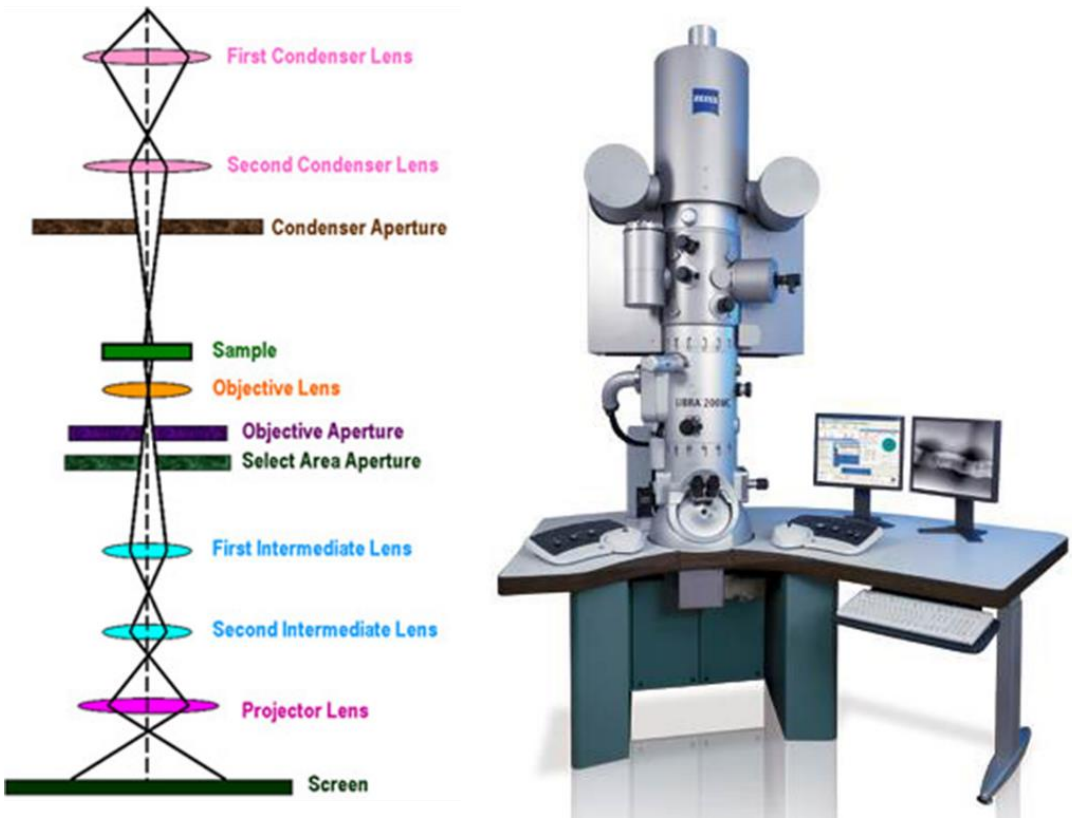

Figure 1.20. Schematic representation of transmission electron microscope (TEM).

TEM forms a major analysis method in a range of scientific fields, in both physical and biological sciences. TEMs find application in cancer research, virology, materials science as well as pollution, nanotechnology and semiconductor research.

The TEM operates on the same basic principles as the light microscope but uses electrons instead of light. Because the wavelength of electrons is much smaller than that of light, the optimal resolution attainable for TEM images is many orders of magnitude better than that from a light microscope.

Modern TEMs are equipped with specimen holders that allow to tilt the specimen to a range of angles in order to obtain specific diffraction conditions. Therefore, a high contrast image can be formed by blocking electrons deflected away from the optical axis of the microscope by placing the aperture to allow only unscattered electrons through. This produces a variation in the electron intensity that reveals information on the crystal structure. This technique, particularly sensitive to extended crystal lattice defects, is known as ‘bright field’ or ‘light field’. It is also possible to produce an image from electrons deflected by a particular crystal plane which is known as a dark field image.

The specimens must be prepared as a thin foil so that the electron beam can penetrate. Materials that have dimensions small enough to be electron transparent, such as powders or nanotubes, can be quickly produced by the deposition of a dilute sample containing the specimen onto support grids.

The TEM is used widely both in material science/metallurgy and biological sciences. In both cases the specimens must be very thin and able to withstand the high vacuum present inside the instrument. For biological specimens, the maximum specimen thickness is roughly 1 µm. To withstand the instrument vacuum, biological specimens are typically held at liquid nitrogen temperatures after embedding in vitreous ice, or fixated using a negative staining material such as uranyl acetate or by plastic embedding. The properties of nanocomposites (NCs) depend to a large extent on successful nano-level dispersion or intercalation/exfoliation of nanoclays, therefore monitoring their morphology and dispersion is very crucial.

1.8.6. High resolution transmission electron microscopy (HR-TEM)

HR-TEM is an imaging mode of the transmission electron microscope that allows the imaging of the crystallographic structure of a sample at an atomic scale.[129,130] HR-TEM is a powerful tool to study properties of materials on the atomic scale, such as semiconductors, metals, nanoparticles and sp^2-bonded carbon (e.g. graphene, carbon nanotubes). While HR-TEM is often also used to refer to high resolution scanning TEM (STEM, mostly in high angle annular dark field mode), this article describes mainly the imaging of an object by recording the 2D spatial wave amplitude distribution in the image plane, in analogy to a “classic” light microscope. For disambiguation, the technique is also often referred to as phase contrast TEM. At present, the highest point resolution realized in phase contrast TEM is around 0.5 Å (0.050 nm).[131] At these small scales, individual atoms of a crystal and its defects can be resolved. For 3-dimensional crystals, it may be necessary to combine several views, taken from different angles, into a 3D map. This technique is called electron crystallography.

One of the difficulties with HR-TEM is that image formation relies on phase contrast. In phase-contrast imaging, contrast is not necessarily intuitively interpretable, as the image is influenced by aberrations of the imaging lenses in the microscope. The largest contributions for uncorrected instruments typically come from defocus and

astigmatism. The latter can be estimated from the so-called "Thon ring pattern" appearing in the fourier transform modulus of an image of a thin amorphous film.

As opposed to conventional microscopy, HR-TEM does not use absorption by the sample for image formation, but the contrast arises from the interference in the image plane of the electron wave with itself. Each imaging electron interacts independently with the sample. As a result of the interaction with the sample, the electron wave passes through the imaging system of the microscope where it undergoes further phase change and interferes as the image wave in the imaging plane. It is important to realize that the recorded image is not a direct representation of the samples crystallographic structure.

1.8.7. Optical spectroscopy

Optical spectroscopy has been extensively used for the characterization of nanomaterials and the techniques can be generally categorized into two groups:

- Absorption and emission spectroscopy
- Vibrational spectroscopy.

The former determines the electronic structures of atoms, ions, molecules or crystals through exciting electrons from the ground to excited states (absorption) and relaxing from the excited to ground states (emission). The vibrational techniques may be summarized as involving the interactions of photons with species in a sample that results in energy transfer to or from the sample *via* vibrational excitation or de-excitation. The vibrational frequencies provide the information of chemical bonds in the detecting samples. IR and Raman spectroscopy are the examples of vibrational spectroscopy.

1.8.8. UV-Visible (UV-Vis) spectroscopy

Ultraviolet spectrophotometers (**Fig. 1.21**) consist of a light source, reference and sample beams, a monochromator and a detector. The ultraviolet spectrum for a compound is obtained by exposing a sample of the compound to ultraviolet light from a light source, such as a Xenon lamp (**Fig. 1.22**).

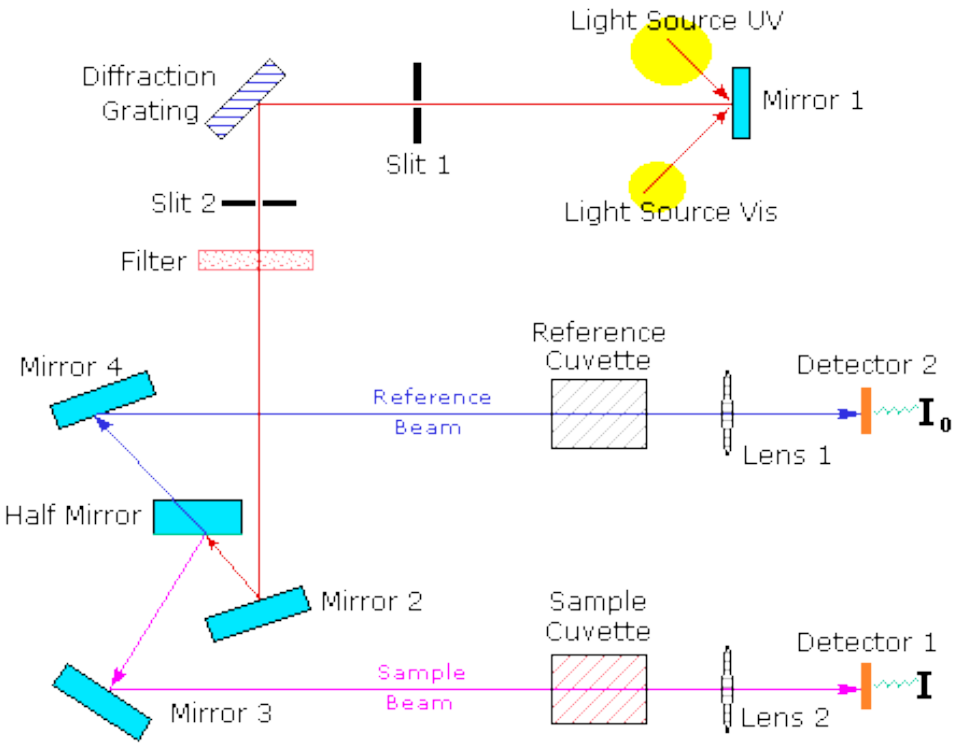

Figure 1.21. Schematic representation of UV-visible spectrophotometer.

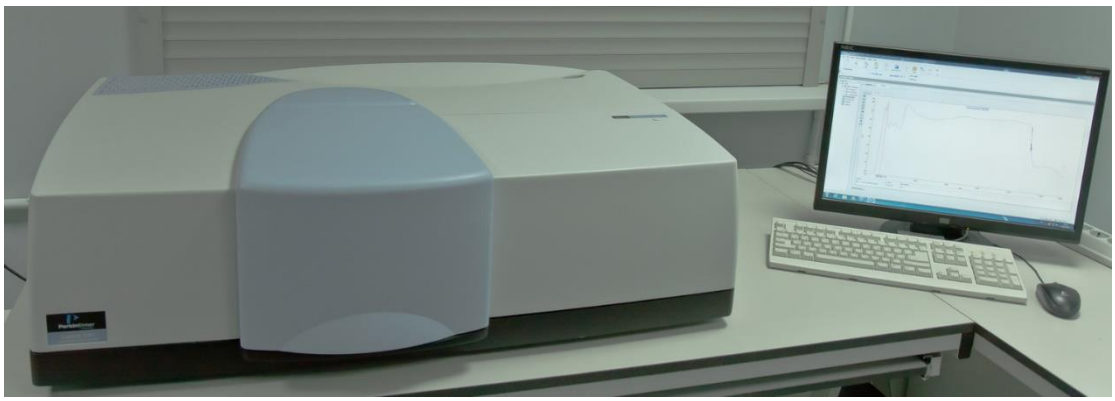

Figure 1.22. UV-Visible spectrophotometer.

The reference beam in the spectrophotometer travels from the light source to the detector without interacting with the sample. The sample beam interacts with the sample exposing it to ultraviolet light of continuously changing wavelength. When the emitted wavelength corresponds to the energy level which promotes an electron to a higher molecular orbital, energy is absorbed. The detector records the ratio between reference and sample beam intensities (I_0/I). The computer determines at what wavelength the sample absorbed a large amount of ultraviolet light by scanning for the largest gap between the two beams. When a large gap between intensities is found,

where the sample beam intensity is significantly weaker than the reference beam, the computer plots this wavelength as having the highest ultraviolet light absorbance when it prepares the ultraviolet absorbance spectrum.

UV-Vis spectroscopy is routinely used in analytical chemistry for the quantitative determination of different analytes, such as transition metal ions, highly conjugated organic compounds and biological macromolecules. Spectroscopic analysis is commonly carried out in solutions but solids and gases may also be studied.

- Solutions of transition metal ions can be colored (*i.e.* absorb visible light) because d electrons within the metal atoms can be excited from one electronic state to another. The color of metal ion solutions is strongly affected by the presence of other species, such as certain anions or ligands. For instance, the color of a dilute solution of copper sulfate is a very light blue; adding ammonia intensifies the color and changes the wavelength of maximum absorption (λ_{max}).
- Organic compounds, especially those with a high degree of conjugation, also absorb light in the UV or visible regions of the electromagnetic spectrum. The solvents for these determinations are often water for water-soluble compounds, or ethanol for organic-soluble compounds. Organic solvents may have significant UV absorption; not all solvents are suitable for use in UV spectroscopy. Ethanol absorbs very weakly at most wavelengths. Solvent polarity and pH can affect the absorption spectrum of an organic compound. Tyrosine, for example, increases in absorption maxima and molar extinction coefficient when pH increases from 6 to 13 or when solvent polarity decreases.
- While charge transfer complexes also give rise to colors, the colors are often too intense to be used for quantitative measurement.

1.8.9. Differential thermal analysis (DTA)/Thermogravimetric analysis (TGA)

Thermal analysis is the analysis of a change in a property of a sample, which is related to an imposed change in the temperature. The sample is usually in the solid state and the changes that occur on heating include melting, phase transition, sublimation, and decomposition.

The analysis of the change in the mass of a sample on heating is known as thermogravimetric analysis (TGA). TGA measures mass changes in a material as a

function of temperature (or time) under a controlled atmosphere. Its principal uses include measurement of a materials thermal stability and composition. TGA is most useful for dehydration, decomposition, desorption and oxidation processes.[132]

Common applications of TGA are:

- Materials characterization through analysis of characteristic decomposition patterns.
- Studies of degradation mechanisms and reaction kinetics.
- Determination of organic content in a sample.
- Determination of inorganic (e.g. ash) content in a sample, which may be useful for corroborating predicted material structures or simply used as a chemical analysis.

It is an especially useful technique for the study of polymeric materials, including thermoplastics, thermosets, elastomers, composites, plastic films, fibers, coatings and paints.

The most widely used thermal method of analysis is DTA. In DTA, the temperature of a sample is compared with that of an inert reference material during a programmed change of temperature. The temperature should be the same until thermal event occurs, such as melting, decomposition or change in the crystal structure. In an endothermic event takes place within the sample, the temperature of the sample will lag behind that of the reference and a minimum will be observed on the curve. On the contrary, if an exothermal event takes place, then the temperature of the sample will exceed that of the reference and a maximum will be observed on the curve. The area under the endotherm or exotherm is related to the enthalpy of the thermal event, ΔH. **Fig. 1.23,** shows a typical TGA/DTA system.

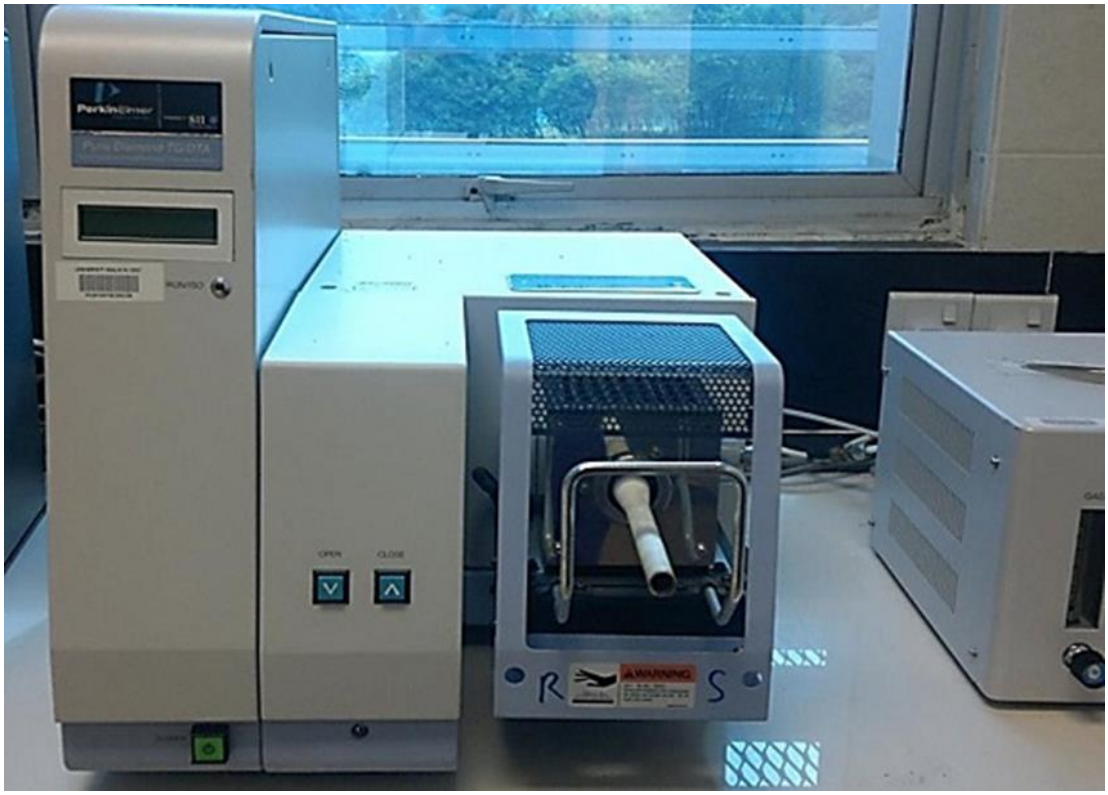

Figure 1.23. TGA/DTA analyzer.

For many problems, it is advantageous to use both DTA and TGA, because the DTA events can then be classified into those which do or do not involve mass change.

TGA-DTA modes can be used to determine the following:

- Melting points
- Glass transition temperatures
- Crystallinity
- Moisture/volatile content
- Thermal and oxidative stability
- Purity
- Transformation temperatures

1.8.10. Infrared spectroscopy (IR)

Measures infrared intensity *vs* wavelength of light, it is used to determine the nature of associated functional groups and structural features of NPs.[133] IR spectroscopy (**Fig.1.24**) is a popular characterization technique in which a sample is placed in the path of an IR radiation source and its absorption of different IR frequencies is measured. Solid, liquid and gaseous samples can all be characterized by this technique. IR photons

energies, in a range between 1 to 15 kcal mol^{-1}, are insufficient to excite electrons to higher electronic energy states, but transitions in vibrational energy states.

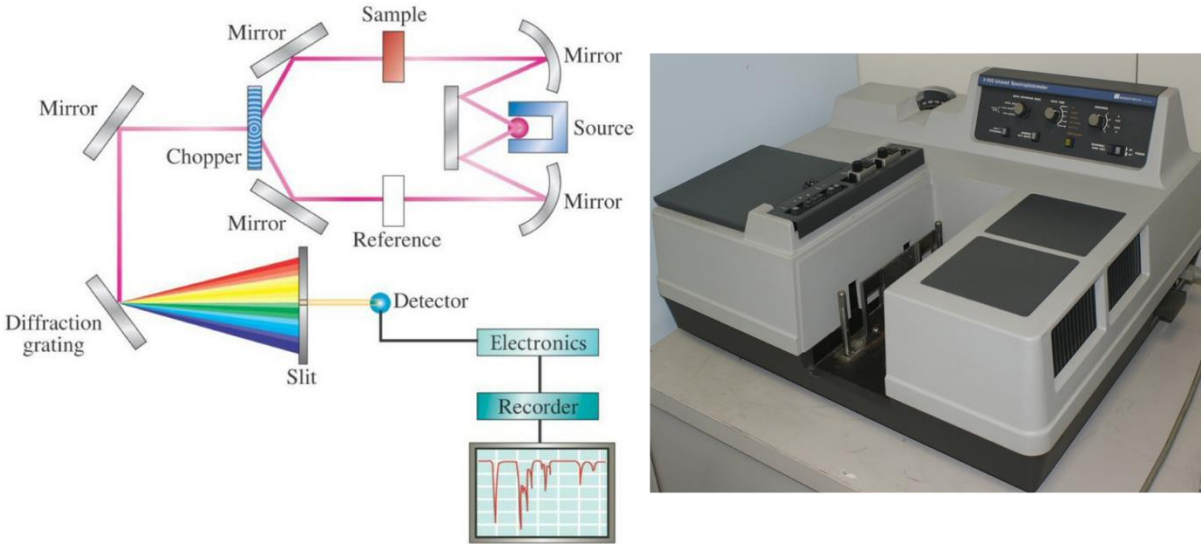

Figure 1.24. Schematic details of IR spectroscopy.

Each molecule has its own unique signatures. Therefore, IR spectroscopy may be employed to identify the type of bond between two or more atoms and consequently identify functional groups. IR spectroscopy is also widely used to characterize the attachment of organic ligands to organic/inorganic NPs and surfaces. Because IR spectroscopy is quantitative, the number of a type of bond may be determined. Virtually all organic compounds absorb IR radiation, but inorganic materials are less commonly characterized, as heavy atoms show vibrational transitions in the far IR region, with some having extremely broad peaks that hampers the identification of the functional groups. Furthermore, the peak intensities of some ionic inorganic compounds may be too weak to be measured.[134,135] The covalent bonds that hold molecules together are neither stiff nor rigid, but rather they vibrate at specific frequencies corresponding to their vibrational energy levels. The vibration frequencies depend on several factors including bond strength and the atomic mass. The bonds can be modified in different ways, in a similar manner to a spring. Chemical bonds may be contorted in six different ways:

- Stretching (both symmetrical and asymmetrical)
- Scissoring
- Rocking
- Wagging

- Twisting

Absorption of IR radiation causes the bond to move from the lowest vibrational state to the next highest, and the energy associated with absorbed IR radiation is converted into these types of motions.[136–138] Other rotational motions usually accompany these individual vibrational motions. These combinations lead to absorption bands, not discrete lines, which are commonly observed in the mid IR region.[138] Weaker bonds require less energy to be absorbed and behave as though the bonds are springs that have different strengths. More complex molecules contain dozens or even hundreds of different possible bond stretches and bending motions, which implies the spectrum may contain dozens or hundreds of absorption lines. This means that the IR absorption spectrum can be its unique fingerprint for identification of a molecule.[139] The fingerprint region contains wavenumbers between 400 and 1500 cm^{-1}. A diatomic molecule, that has only one bond, can only vibrate in one direction. For a linear molecule (e.g. hydrocarbons) with *n* atoms, there are 3*n*-5 vibrational modes. If the molecule is non-linear (such as methane, aromatics *etc*.), then there will be 3*n*-6 modes. Samples can be prepared in several ways for an IR measurement. For powders, a small amount of the sample is added to KBr, after which this mixture is ground into a fine powder and subsequently compressed into a small, thin, quasi-transparent disc. For liquids, a drop of sample may be sandwiched between two salt plates, such as NaCl, KBr and NaCl are chosen as neither of these compound shows an IR active stretch in the region typically observed for organic and some inorganic molecules.

1.9. Applications of nanomaterials

The nanomaterials possessed exceptional, useful chemical, physical and mechanical properties, which can be exploited for a broad spectrum of applications in diverse fields such as:[140]

- Medicine and drug
- Electronics
- Food
- Fuel cells
- Solar cells
- Batteries
- Space

- Better air quality
- Cleaner water
- Chemical sensors
- Fabric
- Enzyme immobilization
- Protein-nanoparticle interaction
- Catalysis
- Photocatalysis

1.9.1. Medicine and drug

Researchers are developing customized NPs the size of molecules that can deliver drugs directly to affected cells in human body. When its perfected, this method should greatly reduce the damage treatment such as chemotherapy does to a patient's healthy cells.

- ***Drug delivery*:** Nanotechnology in medicine currently being developed involves employing NPs to deliver drugs, heat, light or other substances to specific types of cells (such as cancer cells). Particles are engineered so that they are attracted to affected cells, which allows direct treatment of those cells. This technique reduces damage to healthy cells in the body and allows for earlier detection of disease. For example, NPs that deliver chemotherapeutic drugs directly to cancer cells are under development.
- ***Therapy techniques*:** In this techniques researchers have developed "nanosponges" that absorb toxins and remove them from the bloodstream. The nanosponges are polymer NPs coated with a red blood cell membrane. The red blood cell membrane allows the nanosponges to travel freely in the bloodstream and attract the toxins.
- ***Diagnostic techniques*:** Researchers have developed a sensor using carbon nanotubes embedded in a gel; that can be injected under the skin to monitor the level of nitric oxide in the bloodstream. The level of nitric oxide is important because it indicates inflammation, allowing easy monitoring of inflammatory diseases.

1.9.2. Electronics

Nanoelectronics holds some answers for how we might increase the capabilities of electronics devices while we reduce their weight and power consumption. Electrodes made from nanowires that would enable flat panel displays to be flexible as well as thinner than current flat panel displays. Semiconductor nanowires to build transistors and integrated circuits. Transistors built in single atom thick graphene film to enable very high speed transistors.[141]

1.9.3. Food

Nanotechnology is having an impact on several aspects of food science, from how food is grown to how it is packaged. Companies are developing nanomaterials that will make a difference not only in the taste of food, but also in food safety, and the health benefits that food delivers.

Clay NCs are being used to provide an impermeable barrier to gases such as O_2 or CO_2 in lightweight bottles, cartons and packaging films. Storage bins are being produced with silver NPs embedded in the plastic. The silver NPs kill bacteria from any material that was previously stored in the bins, minimizing health risks from harmful bacteria. ZnO NPs can be incorporated into plastic packaging to block UV rays and provide antibacterial protection, while improving the strength and stability of the plastic film.

Nanosensors are being developed that can detect bacteria and other contaminates, such as salmonella, at a packaging plant. This will allow for frequent testing at a much lower cost than sending samples to a lab for analysis. This point-of-packaging testing, if conducted properly, has the potential to dramatically reduce the chance of contaminated food reaching grocery store shelves.

1.9.4. Fuel cells

Nanotechnology is being used to reduce the cost of catalysts used in fuel cells to produce hydrogen ions from fuel such as methanol and to improve the efficiency of membranes used in fuel cells to separate hydrogen ions from other gases such as oxygen. Catalysts are used with fuels such as hydrogen or methanol to produce hydrogen ions. Platinum, which is very expensive, is the catalyst typically used in this process. Companies are using NPs of platinum to reduce the amount of platinum needed, or using NPs of other materials to replace platinum entirely and thereby lower

costs. Fuel cells contain membranes that allow hydrogen ions to pass through the cell but do not allow other atoms or ions, such as oxygen, to pass through. Companies are using nanotechnology to create more efficient membranes; this will allow them to build lighter weight and longer lasting fuel cells. Fuel cells that can replace batteries in electric cars are also under development. Hydrogen is the fuel most researchers propose for use in fuel cell powered cars. In addition to the improvements to catalysts and membranes, it is necessary to develop a lightweight and safe hydrogen fuel tank to hold the fuel and build a network of refueling stations. To build these tanks, researchers are trying to develop lightweight nanomaterials that will absorb the hydrogen and only release it when needed.

1.9.5. Solar cells

Companies have developed nanotech solar cells that can be manufactured at significantly lower cost than conventional solar cells. Researchers at Michigan Technological University have developed a honeycomb like structure of graphene in which the graphene sheets are held apart by lithium carbonate (Li_2CO_3). They have used this "3D graphene" to replace the platinum in a dye sensitized solar cell and achieved 7.8 % conversion of sunlight to electricity. Researchers are studying solar cells made from single molecule thick sheets of graphene and materials such as molybdenum diselenide ($MoSe_2$). They are predicting that this type of solar cells could produce up to 1000 times as much more power for a given weigh of material than conventional solar cells. They have completed computer modeling and are working on building the solar cells.

1.9.6. Batteries

Companies are currently developing batteries using nanomaterials. One such battery will be a good as new after sitting on the shelf for decades. Researchers have demonstrated the use of silicon coated carbon nanotubes for in anodes for Li-ion batteries. They are predicting that the use of silicon can increase the capacity of Li-ion batteries by up to 10 times.

Using nanotechnology in the manufacture of batteries offers the following benefits:

- Reducing the possibility of batteries catching fire by providing less flammable electrode material.

- Increasing the available power from a battery and decreasing the time required to recharge a battery. These benefits are achieved by coating the surface of an electrode with NPs. This increases the surface area of the electrode thereby allowing more current to flow between the electrode and the chemicals inside the battery. This technique could increase the efficiency of hybrid vehicles by significantly reducing the weight of the batteries needed to provide adequate power.
- Increasing the shelf life of a battery by using nanomaterials to separate liquids in the battery from the solid electrodes when there is no draw on the battery. This separation prevents the low level discharge that occurs in a conventional battery, which increases the shelf life of the battery dramatically.

1.9.7. Space

Nanotechnology may hold the key to making space-flight more practical. Advancements in nanomaterials make lightweight spacecraft and a cable for the space elevator possible. By significantly reducing the amount of rocket fuel required, these advances could lower the cost of reaching orbit and traveling in space.

1.9.8. Better air quality

Nanotechnology can improve the performance of catalysts used to transform vapors escaping from cars or industrial plants into harmless gases. That's because catalysts made from NPs have a greater surface area to interact with the reacting chemicals than catalysts made from larger particles. The larger surface area allows more chemicals to interact with the catalyst simultaneously, which makes the catalyst more effective.

1.9.9. Cleaner water

Nanotechnology is being used to develop solutions to three very different problems in water quality. One challenge is the removal of industrial wastes, such as a cleaning solvent called TCE (trichloroethylene), from groundwater. NPs can be used to convert the contaminating chemical through a chemical reaction to make it harmless. Studies have shown that this method can be used successfully to reach contaminates dispersed in underground ponds and at much lower cost than methods which require pumping the water out of the ground for treatment.

1.9.10. Chemical sensors

Nanotechnology can enable sensors to detect very small amounts of chemical vapors. Various types of detecting elements, such as carbon nanotubes, ZnO nanowires or Pd NPs can be used in nanotechnology based sensors. Because of the small size of nanotubes, nanowires, or NPs, a few gas molecules are sufficient to change the electrical properties of the sensing elements. This allows the detection of a very low concentration of chemical vapors.

1.9.11. Fabric

Making composite fabric with nano-sized particles or fibers allows improvement of fabric properties without a significant increase in weight, thickness, or stiffness as might have been the case with previously used techniques.

1.9.12. Enzyme immobilization

The definition of immobilization is to fix something preventing it from moving. In enzyme technology, this term refers to the physical confinement or localization in a certain region of space with retention of their catalytic activities. By immobilizing an enzyme, some structural changes can occur, thereby changing its properties[142,143] and activity to some extent.[144,145] Immobilized proteins and enzymes have also been found useful in many bioanalytical and biomedical applications. These applications include the use of immobilized antibodies or antigens in bioaffinity chromatography, immobilized receptors or ligands in the study of their interactions and immobilized cells in biosensors.[146,147] Irreversible immobilizations involve the covalent attachment of the enzyme to the surface, or the entrapment within a matrix or micro-encapsulation. For the covalent attachment, the support must have a reactive group (*i.e.* amine, carboxylate, thiol) or must be activated in order to perform the immobilization. The immobilization procedure gives rise to a stable amide bond between the support and the enzyme (*i.e.* carbodiimide).[148–156] When the support is aminated, a cross-linker such as glutaraldehyde, is commonly used, forming imine bonds between the biomolecule and the support.

1.9.12.1. Salient features of enzyme immobilization

- The enzyme phase is called as carrier phase which is water insoluble but hydrophilic porous polymeric matrix, *e.g*. agarose, cellulose, *etc*.

- The enzyme phase may be in the form of fine particulate, membranous, or microcapsule.
- The enzyme in turn may be bound to another enzyme *via* cross linking.
- A special module is produced employing immobilization techniques through which fluid can pass easily, transforming substrate into product and at the same time facilitating the easy removal of catalyst from the product as it leaves the reactor.
- The support or carrier utilized in immobilization technique is not stable at particular pH, ionic strength or solvent conditions. Hence, may be disrupted or dissolved releasing the enzyme component after the reaction.

1.9.12.2. Advantages of enzyme immobilization

- Multiple or repetitive use of a single batch of enzymes.
- Immobilized enzymes are usually more stable.
- Ability to stop the reaction rapidly by removing the enzyme from the reaction solution.
- Product is not contaminated with the enzyme.
- Easy separation of the enzyme from the product.
- Allows development of a multi-enzyme reaction system.
- Reduces effluent disposal problems.

1.9.12.3. Disadvantages of enzyme immobilization

- It gives rise to an additional bearing on cost.
- It invariably affects the stability and activity of enzymes.
- The technique may not prove to be of any advantage when one of the substrate is found to be insoluble.
- Certain immobilization protocols offer serious problems with respect to the diffusion of the substrate to have an access to the enzyme.

1.9.12.4. Technique of enzyme immobilization

- Carrier binding
  - Physical adsorption
  - Covalent bonding
  - Ionic bonding
- Cross linking
- Entrapment

- Occlusion within a cross linked gel
- Microencapsulation

■ ***Carrier binding***

❖ ***Physical adsorption*:** This method is based on the physical adsorption of enzyme protein on the surface of water-insoluble carriers. Examples of suitable adsorbents are ion-exchange matrices, porous carbon, clay, hydrous metal oxides, glasses and polymeric aromatic resins.

The bond between the enzyme and carrier molecule may be ionic, covalent, hydrogen, coordinated covalent or even combination of any of these. Immobilization can be brought about by coupling an enzyme either to external or internal surface of the carrier. The external surface binding method is advantageous as it does not involve conditions like pore diffusion. The disadvantages, however, include exposure of enzymes to microbial attack, physical abrasion of enzyme due to turbulence associated with the bulk solution. The major disadvantage of the internal immobilization method is the pore diffusion.

➢ ***Advantages of adsorption***

- Little or no confirmation change of the enzyme.
- Simple and cheap.
- No reagents are required.
- Wide applicability and capable of high enzyme loading.

➢ ***Disadvantages of adsorption***

- Desorption of the enzyme protein resulting from changes in temperature, pH and ionic strength.
- Slow method.

❖ ***Covalent bonding*:** Covalent binding is the most widely used method for immobilizing enzymes. The covalent bond between enzyme and a support matrix forms a stable complex. The functional group present on enzyme, through which a covalent bond with support could be established, should be non-essential for enzymatic activity.

The protein functional groups which could be utilized in covalent coupling include:

- Amino group
- Carboxylic group
- Phenol ring
- Indole group

➢ ***Advantages of covalent coupling***

- The strength of binding is very strong, so, leakage of enzyme from the support is absent or very little.
- This is a simple, mild and often successful method of wide applicability.

➢ ***Disadvantages of covalent coupling***

- Enzymes are chemically modified and so many are denatured during immobilization.
- Only small amounts of enzymes may be immobilized (about 0.02 grams per gram of matrix).

■ ***Cross linking***

This method is based on the formation of covalent bonds between the enzyme molecules, by means of multifunctional reagents, leading to three dimensional cross linked aggregates.

The most common reagent used for cross-linking is glutaraldehyde.

➢ ***Advantages of cross linking***

- Very little desorption (enzyme strongly bound).
- Best used in conjunction with other methods.

➢ ***Disadvantages of cross linking***

- Cross linking may cause significant changes in the active site.

■ ***Entrapment***

In entrapment, the enzymes or cells are not directly attached to the support surface, but simply trapped inside the polymer matrix. Entrapment is carried out by mixing the biocatalyst into a monomer solution, followed by polymerization initiated by a change in temperature or by a chemical reaction.

Polymers like polyacrylamide, collagen, cellulose acetate, calcium alginate or carrageenan *etc*. are used as the matrices.

- ***Advantages of entrapment***
  - Loss of enzyme activity upon immobilization is minimized.
- ***Disadvantages of entrapment***
  - The enzyme can leak into the surrounding medium.
  - Another problem is the mass transfer resistance to substrates and products.
  - Substrate cannot diffuse deep into the gel matrix.

- ***Occlusion within a cross linked gel*:** In this entrapment method, a highly cross-linked gel is formed as a result of the polymerization which has a fine "wire mesh" structure and can more effectively hold smaller enzymes in its cages. Amounts in excess of 1 g of enzyme per gram of gel or fibre may be entrapped. Some synthetic polymers such as polyarylamide, polyvinylalcohol, *etc*. and natural polymer (starch) have been used to immobilize enzymes using this technique.
- ***Microencapsulation*:** This entrapment involves the formation of spherical particle called as "microcapsule" in which a liquid or suspension of biocatalyst is enclosed within a semi permeable polymeric membrane.

1.9.12.5. Applications of enzyme immobilization

- ***Industrial production*:** Industrial production of antibiotics, beverages, amino acids *etc*. uses immobilized enzymes or whole cells.
- ***Biomedical applications*:** Immobilized enzymes are widely used in the diagnosis and treatment of many diseases. Immobilized enzymes can be used to overcome inborn metabolic disorders by the supply of immobilized enzymes. Immobilization techniques are effectively used in drug delivery systems especially to oncogenic sites.
- ***Food industry*:** Enzymes like pectinases and cellulases immobilized on suitable carriers are successfully used in the production of jams, jellies and syrups from fruits and vegetables.
- ***Research*:** A research activity extensively uses many enzymes. The use of immobilized enzyme allow researcher to increase the efficiency of different

enzymes such as Horse Radish Peroxidase (HRP) in blotting experiments and different proteases for cell or organelle lysis.

- ***Production of biodiesel*:** From vegetable oils.
- ***Waste water management*:** Treatment of sewage and industrial effluents.
- ***Textile industry*:** Scouring, biopolishing and desizing of fabrics.
- ***Detergent industry*:** Immobilization of lipase enzyme for effective dirt removal from cloths.

1.9.13. Protein-nanoparticle interaction

Nanoparticles and other nanomaterials are increasingly considered for use in biomedical applications such as imaging, drug delivery, and hyperthermic therapies. Thus, understanding the interaction of nanomaterials with biological systems becomes key for their safe and efficient application. It is increasingly being accepted that the surface of nanomaterials would be covered by protein corona upon their entrance to the biological medium. The biological medium will then see the achieved modified surface of nanomaterials, and therefore further cellular/tissue responses depend on the composition of corona.[157]

In a biological medium, NPs may interact with biomolecules such as proteins, nucleic acids, lipids and even biological metabolites due to their nano-size and large surface-to-mass ratio. Of particular importance is the adsorption of proteins on the NP surface. The formation of NP-protein complexes is commonly referred to as the nanoparticle-protein corona (NP-PC). A number of consequences of protein adsorption on the NP surface can be speculated. Overall, the NP-PC can influence the biological reactivity of the NP.[158,159] The protein corona may influence cellular uptake, inflammation, accumulation, degradation and clearance of the NPs. Furthermore, the NP surface can induce conformational changes in adsorbed protein molecules which may affect the overall bio-reactivity of the NP. In depth understanding of such interactions can be directed towards generating bio-compatible nanomaterials with controlled surface characteristics in a biological environment.[160,161] Adsorption of proteins at the nano-bio interface is aided by several forces such as hydrogen bonds, solvation forces, Van der Waals interactions, *etc*. The overall NP-PC formation is a multifactorial process and not only depends on the characteristics of the NP, but also on the interacting proteins and the medium. Specific association and dissociation rates for each protein decide

longevity of their interaction with the NP surface. Irreversible (or at least long-term) binding of proteins on the NP leads to formation of a "hard corona" whereas quick reversible binding of proteins that have faster exchange rates defines a "soft corona".[162–166]

1.9.14. Catalysis

During the twentieth century, chemists have made considerable achievements in heterogeneous catalysis,[167–178] whereas homogeneous catalysis[179–182] progressed after world war-II (hydroformylation) and especially since the early 1970s (hydrogenation). Heterogeneous catalysis that benefits from easy removal of catalyst materials and possible use of high temperatures suffered for a long time from lack of selectivity and understanding of the mechanistic aspects that are indispensable for parameter improvements. Homogeneous catalysis is very efficient and selective, and is used in a few industrial processes, but it suffers from the impossibility of removal of the catalyst from the reaction media and its limited thermal stability. Green catalysis aspects now obviously require that environmentally friendly (for example phosphine-free) catalysts be designed for easy removal from the reaction media and recycling many times with very high efficiency. These demanding conditions bring a new research impetus for catalyst development at the interface between homogeneous and heterogeneous catalysis, gathering the sophisticated fulfilment of all the constraints that were far from being fully taken into account by the pioneers and even the specialists in each catalytic discipline in the former decades. Yet the considerable knowledge gained from the past research in homogeneous, heterogeneous, supported and biphasic catalysis, including also studies in non-classical conditions (solvent-free, aqueous, use of ionic liquids, fluorine chemistry, micro-emulsions, micelles, reverse micelles, vesicles, surfactants, aerogels). In this context, the use of transition-metal NPs in catalysis[183,184] is crucial as they mimic metal surface activation and catalysis at the nanoscale and thereby bring selectivity and efficiency to heterogeneous catalysis. Transition-metal NPs are clusters containing from a few tens to several thousand metal atoms, stabilized by ligands, surfactants, polymers or dendrimers protecting their surfaces. Their sizes vary between the order of one nanometer to several tens or hundreds of nanometers, but the most active in catalysis are only one or a few nanometers in diameter, *i.e*. they contain a few tens to a few hundred atoms only.[185–187] This approach is also relevant to homogeneous

catalysis, because there is a full continuum between small metal clusters and large metal clusters, the latter being also called colloids, sols or NPs. NPs are also well soluble in classic solvents (unlike metal chips in heterogeneous catalysis) and can often be handled and even characterized as molecular compounds by spectroscopic techniques that are well known to molecular chemists, such as ^{1}H and multinuclear NMR, IR and UV-Vis spectroscopy and cyclic voltammetry. Molecular mechanisms involving the NP surfaces in catalytic reactions are much more difficult to elucidate, however, than those of monometallic catalysts, and the size and shape of the NP catalysts are key aspects of the catalytic steps. NPs themselves can also be used as catalysts in homogeneous systems or alternatively they can be heterogenized by fixation onto a heterogeneous support such as silica, alumina, other oxides or carbon, for example carbon nanotubes. Thus, the field of nanoparticle catalysis involves both the homogeneous and heterogeneous catalysis communities, and these catalysts are sometimes therefore called "semi-heterogeneous".[188–193]

1.9.15. Photocatalysis

Photocatalysis is a branch of science which employes catalyst that is utilized for speeding up chemical reactions that requires or engages light. A photocatalyst is defined as a material that is capable of absorbing light, producing electron-hole pairs that enable chemical transformations of the reaction participants and regenerate its chemical composition after each cycle of such interactions.[194–199] There are two types of photocatalytic reactions.

- Homogeneous photocatalysis
- Heterogeneous photocatalysis

The significant features of the photocatalytic system are the desired band gap, suitable morphology, high surface area, stability and reusability.[195–198,200] Metal oxides such as oxides of vanadium, chromium, titanium, zinc, tin and cerium having these characteristics follow similar primary photocatalytic processes such as light absorption, which induces a charge separation process with the formation of positive holes that are able to oxidize organic substrates.[195,196,198,200] In this process, a metal oxide is activated with either UV light, visible light or a combination of both, and photoexcited electrons are promoted from the valence band to the conduction band, forming an electron/hole pair (e^-/h^+). The photogenerated pair (e^-/h^+) is able to reduce and/or oxidize a

compound adsorbed on the photocatalyst surface. The photocatalytic activity of metal oxide comes from two sources: **(i)** generation of $^{\bullet}OH$ radicals by oxidation of OH^- anions, **(ii)** generation of $O_2^{\bullet -}$ radicals by reduction of O_2. Both the radicals and anions can react with pollutants to degrade or otherwise transform them to lesser harmful byproducts (**Fig. 1.25**).[196,198,200]

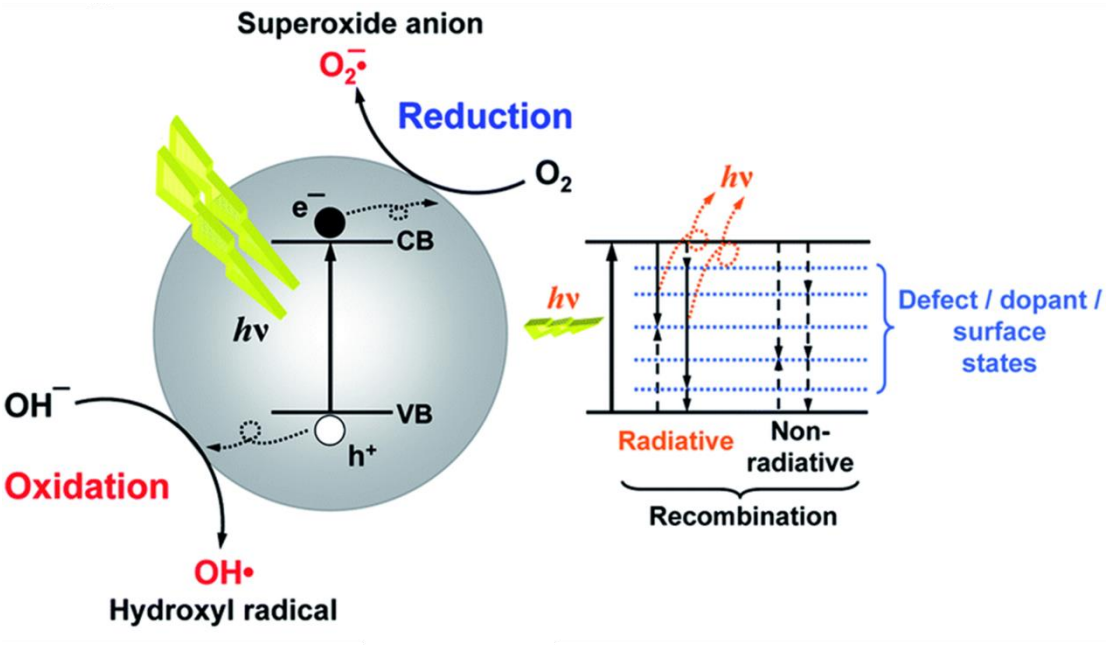

Figure 1.25. The mechanism of photocatalysis.

There are many catalysts reported in the literature for this exciting process. Among these metal oxides (TiO_2, ZnO, SnO_2 and CeO_2), which are abundant in nature, have also been extensively used as photocatalysts, particularly as heterogeneous photocatalyst since several decades.[196,200,201] This is because of their biocompatibility, exceptional stability in a variety of conditions and capability to generate charge carriers when stimulated with required amount of light energy. The favourable combination of electronic structure, light absorption properties, charge transport characteristics and excited lifetimes of metal oxides has made it possible for their application as photocatalyst.[195–198,200,202] Heterogeneous photocatalysis employing metal oxides such as TiO_2, ZnO, SnO_2 and CeO_2 has proved its efficiency in degrading a wide range of distinct pollutants into biodegradable compounds and eventually mineralizing them to harmless CO_2 and H_2O.[203–209]

1.10. Aim of the present work and thesis outlines

The goal of the present work was to study physical properties for different types of nanomaterials with different synthetic routes (*i.e.* sol-gel auto-combustion and co-precipitation) and various characterization techniques. In the present work the structural analysis, morphology and magnetic properties of selected system will be studied using XRD, SEM, EDS, VSM, HR-TEM and FT-IR spectroscopy. First chapter is dealing with the general introduction of nanomaterials, second chapter is concerned with the synthesis of Ni-Co nanoferrites by sol-gel auto-combustion method to study their structural, optical, morphological and magnetic properties and to provide magnetic support for immobilization of yeast alcohol dehydrogenase enzyme (YADH), and third chapter is accredited to the synthesis of Co doped SnO_2 NPs by co-precipitation technique to determine their particle size, structure, morphology, elemental composition and its interaction with human serum albumin (HSA) *via* various spectroscopic techniques and their antimicrobial and photocatalytic activities while as the fourth chapter is associated with the synthesis of silica supported NiO nanocomposite *via* sol-gel auto-combustion method to investigate their particle size, structure, morphology and elemental composition and its catalytic performance for one-pot multicomponent synthesis of benzodiazepine derivatives under microwave irradiation. The fifth chapter is concerned with the synthesis of silica coated Ni-Co ferrite nanocomposites *via* sol-gel auto-combustion method to study their structural, optical and morphological properties and immobilization of glucose oxidase enzyme as a magnetic support.

1.11. References

1 J. Ramsden, *Nanotechnology: An Introduction*, William Andrew, 2011.

2 O. P. Singh and R. M. Nehru, *Asian J. Exp. Sci.*, 2008, **22**, 45–50.

3 M. C. Daniel and D. Astruc, *Chem. Rev.*, 2004, **104**, 293–346.

4 G. Schön and U. Simon, *Colloid Polym. Sci.*, 1995, **273**, 101–117.

5 B. N. Gaponik, I. L. Radtchenko, G. B. Sukhorukov, H. Weller and A. L. Rogach, *Adv. Mater.*, 2002, **14**, 879–882.

6 H. Gleiter, *Adv. Struct. Funct. Mater.*, 1991, 1–37.

7 R. W. Siegel and F. E. Fujita, *Springer Ser. Mater. Sci.*, 1994, **27**.

8 C. Hayashi, *Phys. Today*, 1987, **40**, 44.

9 S. Xu, Y. Qin, C. Xu, Y. Wei, R. Yang and Z. L. Wang, *Nat. Nanotechnol.*, 2010, **5**, 366–373.

10 P. W. May, *Philos. Trans. R. Soc. London. Ser. A Math. Phys. Eng. Sci.*, 2000, **358**, 473–495.

11 X. Huang, C. Tan, Z. Yin and H. Zhang, *Adv. Mater.*, 2014, **26**, 2185–2204.

12 P. Kerativitayanan, J. K. Carrow and A. K. Gaharwar, *Adv. Healthc. Mater.*, 2015, **4**, 1600–1627.

13 J. K. Carrow and A. K. Gaharwar, *Macromol. Chem. Phys.*, 2015, **216**, 248–264.

14 A. K. Gaharwar, N. A. Peppas and A. Khademhosseini, *Biotechnol. Bioeng.*, 2014, **111**, 441–453.

15 J. N. Tiwari, R. N. Tiwari and K. S. Kim, *Prog. Mater. Sci.*, 2012, **57**, 724–803.

16 X. M. Ren, P. Zelenay, S. Thomas, J. Davey and S. Gottesfeld, *S0378-7753 (99)*, 2000, 403–407.

17 S. K. Kamarudin, F. Achmad and W. R. W. Daud, *Int. J. Hydrogen Energy*, 2009, **34**, 6902–6916.

18 A. S. Arico, P. Bruce, B. Scrosati, J. M. Tarascon and W. van Schalkwijk, *Nat Mater*, 2005, **4**, 366–377.

19 Y. H. Jin, S. H. Lee, H. W. Shim, K. H. Ko and D. W. Kim, *Electrochim. Acta*, 2010, **55**, 7315–7321.

20 Z. Dong, S. J. Kennedy and Y. Wu, *J. Power Sources*, 2011, **196**, 4886–4904.

21 M. Mastragostino and F. Soavi, *J. Power Sources*, 2007, **174**, 89–93.

22 M. Winter and R. J. Brodd, *Chem. Rev.*, 2004, **104**, 4245–4269.

23 M. Armand and J. M. Tarascon, *Nature*, 2008, **451**, 652–657.

24 P. Simon and Y. Gogotsi, *Nat. Mater.*, 2008, **7**, 845–854.

25 C. C. Hu, K. H. Chang, M. C. Lin and Y. T. Wu, *Nano Lett.*, 2006, **6**, 2690–2695.

26 Q. Shen, Q. Min, J. Shi, L. Jiang, J. R. Zhang, W. Hou and J. J. Zhu, *J. Phys. Chem. C*, 2009, **113**, 1267–1273.

27 X. Teng, S. Maksimuk, S. Frommer and H. Yang, *Chem. Mater.*, 2007, **19**, 36–41.

28 H. Lee, S. E. Habas, S. Kweskin, D. Butcher, G. A. Somorjai and P. Yang, *Angew. Chemie Int. Ed.*, 2006, **45**, 7824–7828.

29 W. N. Wang, I. W. Lenggoro, Y. Terashi, T. O. Kim and K. Okuyama, *Mater. Sci. Eng. B*, 2005, **123**, 194–202.

30 S. Watson, D. Beydoun, J. Scott and R. Amal, *J. Nanoparticle Res.*, 2004, **6**, 193–207.

31 K. Nagaveni, M. S. Hegde, N. Ravishankar, G. N. Subbanna and G. Madras, *Langmuir*, 2004, **20**, 2900–2907.

32 S. T. Aruna and A. S. Mukasyan, *Curr. Opin. Solid State Mater. Sci.*, 2008, **12**, 44–50.

33 H. Hahn, *Nanostructured Mater.*, 1997, **9**, 3–12.

34 *Gas phase synthesis*, Ninithi.co.

35 P. Reactions, *AIChE J.*, 1987, **33**, 2037–2046.

36 Lee, K. Min, Juhng, W. Nam, Choi and B. Young, *J. Nanosci. Nanotechnol.*, 2006, **6**, 3433–3437(5).

37 M. I. Mendivil, L. V García, B. Krishnan, D. Avellaneda, J. A. Martinez and S. Shaji, *Mater. Res. Bull.*, 2015, **72**, 106–115.

38 D. Amans, C. Malaterre, M. Diouf, C. Mancini, F. Chaput, G. Ledoux, G. Breton, Y. Guillin, C. Dujardin, K. Masenelli-Varlot and P. Perriat, *J. Phys. Chem. C*, 2011, **115**, 5131–5139.

39 M. T. Swihart, *Curr. Opin. Colloid Interface Sci.*, 2003, **8**, 127–133.

40 O. Arutanti, A. B. D. Nandiyanto, T. Ogi, F. Iskandar, T. O. Kim and K. Okuyama, *J. Alloys Compd.*, 2014, **591**, 121–126.

41 P. Shah and A. Gavrin, *J. Magn. Magn. Mater.*, 2006, **301**, 118–123.

42 M. Nuchter, B. Ondruschka, W. Bonrath and A. Gum, *Green Chem.*, 2004, **6**, 128–141.

43 M. Damm, T. N. Glasnov and C. O. Kappe, *Org. Process Res. Dev.*, 2010, **14**,

215–224.

44 M. Baghbanzadeh, L. Carbone, P. D. Cozzoli and C. O. Kappe, *Angew. Chem. Int. Ed. Engl.*, 2011, **50**, 11312–11359.

45 I. Bilecka and M. Niederberger, *Nanoscale*, 2010, **2**, 1358–1374.

46 Y. J. Zhu and F. Chen, *Chem. Rev.*, 2014, **114**, 6462–6555.

47 M. B. Gawande, S. N. Shelke, R. Zboril and R. S. Varma, *Acc. Chem. Res.*, 2014, **47**, 1338–1348.

48 M. N. Nadagouda, T. F. Speth and R. S. Varma, *Acc. Chem. Res.*, 2011, **44**, 469–478.

49 J. Jacob, L. H. L. Chia and F. Y. C. Boey, *J. Mater. Sci.*, 1995, **30**, 5321–5327.

50 M. J. J. Collins, *Future Med. Chem.*, 2010, **2**, 151–155.

51 K. Nagaveni, G. Sivalingam, M. S. Hegde and G. Madras, *Appl. Catal. B Environ.*, 2004, **48**, 83–93.

52 S. Ge, X. Shi, K. Sun, C. Li, C. Uher, J. R. Baker, M. M. Banaszak Holl and B. G. Orr, *J. Phys. Chem. C*, 2009, **113**, 13593–13599.

53 C. C. Wang and J. Y. Ying, *Chem. Mater.*, 1999, **11**, 3113–3120.

54 S. Komarneni, Q. Li, K. M. Stefansson and R. Roy, *J. Mater. Res.*, 1993, **8**, 3176–3183.

55 P. E. Meskin, V. K. Ivanov, A. E. Barantchikov, B. R. Churagulov and Y. D. Tretyakov, *Ultrason. Sonochem.*, 2006, **13**, 47–53.

56 K. Byrappa and T. Adschiri, *Prog. Cryst. Growth Charact. Mater.*, 2007, **53**, 117–166.

57 R. I. Walton, *Chem. Soc. Rev.*, 2002, **31**, 230–238.

58 C. J. Brinker and G. W. Scherer, *Sol-gel science: the physics and chemistry of sol-gel processing*, Academic press, 2013.

59 C. J. Brinker, B. C. Bunker, D. R. Tallant, K. J. Ward and R. J. Kirkpatrick, *Inorg. Organomet. Polym.*, 1988, **360**, 314–332.

60 R. W. Jones, *Inst. Met.*, 1990, **1990**, 128.

61 S. Irfan, M. Ajaz-un-Nabi, Y. Jamil and N. Amin, *IOP Conf. Ser. Mater. Sci. Eng.*, 2014, **60**, 12048.

62 M. G. Naseri, E. Saion and N. K. Zadeh, *Int. Nano Lett.*, 2013, **3**, 1–8.

63 N. T. K. Thanh, N. Maclean and S. Mahiddine, *Chem. Rev.*, 2014, **114**, 7610–7630.

64 H. Kumar, Manisha and P. Sangwan, *Int. J. Chem. Chem. Eng.*, 2013, **3**, 155–

160.

65 T. D. Nguyen and T. O. Do, *Size- and Shape-Controlled Synthesis of Monodisperse Metal Oxide and Mixed Oxide Nanocrystals*, 2009.

66 D. Harvey, *Modern analytical chemistry*, 2000.

67 N. Lubick and K. Betts, *Silver socks have cloudy lining| Court bans widely used flame retardant*, ACS Publications, 2008.

68 D. Vollath, *Environ. Eng. Manag. J.*, 2008, **7**, 865–870.

69 D. P. Puzzo, L. D. Bonifacio, J. Oreopoulos, C. M. Yip, I. Manners and G. A. Ozin, *J. Mater. Chem.*, 2009, **19**, 3500–3506.

70 L. M. Liz-Marzán, *Mater. Today*, 2004, **7**, 26–31.

71 A. L. González, C. Noguez, J. Beránek and A. S. Barnard, *J. Phys. Chem. C*, 2014, **118**, 9128–9136.

72 H. Li, P. D. Han, X. B. Zhang and M. Li, *Mater. Chem. Phys.*, 2013, **137**, 1007–1011.

73 D. Guo, G. Xie and J. Luo, *J. Phys. D. Appl. Phys.*, 2014, **47**, 13001.

74 G. Y. Yurkov, A. S. Fionov, Y. A. Koksharov, V. V Koleso and S. P. Gubin, *Inorg. Mater.*, 2007, **43**, 834–844.

75 J. T. Lue, *Encycl. Nanosci. Nanotechnolog*, 2007, 1–46.

76 N. D. S. Mohallem, G. L. T. Nascimento, J. B. Silva and V. L. Guimarães, *Study of Multifunctional Nanocomposites Formed by Cobalt Ferrite Dispersed in a Silica Matrix Prepared by Sol-Gel Process*, INTECH Open Access Publisher, 2012.

77 B. D. Cullity and C. D. Graham, *Introduction to magnetic materials*, John Wiley & Sons, 2011.

78 A. Goldman, *Modern ferrite technology*, Springer Science & Business Media, 2006.

79 A. E. Clark, *Handb. Ferromagn. Mater.*, 1980, **1**, 531–589.

80 Q. A. Pankhurst, J. Connolly, S. K. Jones and J. Dodson, *J Phys D Appl Phys*, 2003, **36**, R167.

81 R. H. Kodama, *J. Magn. Magn. Mater.*, 1999, **200**, 359–372.

82 X. Batlle and A. lcar Labarta, *J. Physics-London-D Appl. Phys.*, 2002, **35**, R15–R42.

83 K. Maaz, S. Karim, A. Mashiatullah, J. Liu, M. D. Hou, Y. M. Sun, J. L. Duan, H. J. Yao, D. Mo and Y. F. Chen, *Phys. B Condens. Matter*, 2009, **404**, 3947–

3951.

84 S. D. Bader, *Rev. Mod. Phys.*, 2006, **78**, 1–15.

85 C. A. Ross, *Annu. Rev. Mater. Res.*, 2001, **31**, 203–235.

86 R. W. Wood, J. Miles and T. Olson, *IEEE Trans. Magn.*, 2002, **38**, 1711–1718.

87 F. Caruso, *Adv. Mater.*, 2001, **13**, 11–22.

88 P. R. Krauss and S. Y. Chou, *Appl. Phys. Lett.*, 1997, **71**, 3174–3176.

89 M. Qhobosheane, S. Santra, P. Zhang and W. Tan, *Analyst*, 2001, **126**, 1274–1278.

90 D. Gerion, F. Pinaud, S. C. Williams, W. J. Parak, D. Zanchet, S. Weiss and A. P. Alivisatos, *J. Phys. Chem. B*, 2001, **105**, 8861–8871.

91 L. Levy, Y. Sahoo, K. S. Kim, E. J. Bergey and P. N. Prasad, *Chem. Mater.*, 2002, **14**, 3715–3721.

92 S. W. Lee, Y. W. Kim and H. Chen, *Appl. Phys. Lett.*, 2001, **78**, 350–352.

93 M. G. Mason, L. S. Hung, C. W. Tang, S. T. Lee, K. W. Wong and M. Wang, *J. Appl. Phys.*, 1999, **86**, 1688–1692.

94 S. de Monredon, A. Cellot, F. Ribot, C. Sanchez, L. Armelao, L. Gueneau and L. Delattre, *J. Mater. Chem.*, 2002, **12**, 2396–2400.

95 K. Sekizawa, H. Widjaja, S. Maeda, Y. Ozawa and K. Eguchi, *Appl. Catal. A Gen.*, 2000, **200**, 211–217.

96 G. E. Patil, D. D. Kajale, D. N. Chavan, N. K. Pawar, P. T. Ahire, S. D. Shinde, V. B. Gaikwad and G. H. Jain, *Bull. Mater. Sci.*, 2011, **34**, 1–9.

97 A. Tabet-Aoul, F. Saidani, D. Rochefort and M. Mohamedi, *Int. J. Electrochem. Sci*, 2011, **6**, 6385–6397.

98 Y. Zhang, A. Kolmakov, S. Chretien, H. Metiu and M. Moskovits, *Nano Lett.*, 2004, **4**, 403–407.

99 T. T. Emons, J. Li and L. F. Nazar, *J. Am. Chem. Soc.*, 2002, **124**, 8516–8517.

100 S. Nakao, N. Yamada, T. Hitosugi, Y. Hirose, T. Shimada and T. Hasegawa, *Phys. status solidi*, 2011, **8**, 543–545.

101 M. Batzill and U. Diebold, *Prog. Surf. Sci.*, 2005, **79**, 47–154.

102 V. Kumar, S. Sen, K. P. Muthe, N. K. Gaur, S. K. Gupta and J. V Yakhmi, *Sensors Actuators B Chem.*, 2009, **138**, 587–590.

103 B. Subramanian, M. Mohamed Ibrahim, V. Senthilkumar, K. R. Murali, V. S. Vidhya, C. Sanjeeviraja and M. Jayachandran, *Phys. B Condens. Matter*, 2008, **403**, 4104–4110.

104 X. Wang, J. Song, L. Gao, J. Jin, H. Zheng and Z. Zhang, *Nanotechnology*, 2004, **16**, 37.

105 B. Sasi, K. G. Gopchandran, P. K. Manoj, P. Koshy, P. Prabhakara Rao and V. K. Vaidyan, *Vacuum*, 2002, **68**, 149–154.

106 S. R. Krishnakumar, M. Liberati, C. Grazioli, M. Veronese, S. Turchini, P. Luches, S. Valeri and C. Carbone, *J. Magn. Magn. Mater.*, 2007, **310**, 8–12.

107 C. G. Granqvist, *Handbook of inorganic electrochromic materials*, Elsevier, 1995.

108 X. Wang, L. Li, Y. Zhang, S. Wang, Z. Zhang, L. Fei and Y. Qian, *Cryst. Growth Des.*, 2006, **6**, 2163–2165.

109 T. Nathan, A. Aziz, A. F. Noor and S. R. S. Prabaharan, *J. Solid State Electrochem.*, 2008, **12**, 1003–1009.

110 M. Wu, J. Gao, S. Zhang and A. Chen, *J. Power Sources*, 2006, **159**, 365–369.

111 L. Li, E. A. Gibson, P. Qin, G. Boschloo, M. Gorlov, A. Hagfeldt and L. Sun, *Adv. Mater.*, 2010, **22**, 1759–1762.

112 T. Kado and T. Yamada, *J. Appl. Phys.*, 1995, **77**, 6651–6657.

113 W. Wang, Y. Liu, C. Xu, C. Zheng and G. Wang, *Chem. Phys. Lett.*, 2002, **362**, 119–122.

114 G. H. Yu, L. R. Zeng, F. W. Zhu, C. L. Chai and W. Y. Lai, *J. Appl. Phys.*, 2001, **90**, 4039–4043.

115 S. Nandy, U. N. Maiti, C. K. Ghosh and K. K. Chattopadhyay, *J. Phys. Condens. Matter*, 2009, **21**, 115804.

116 H. Hahn and R. S. Averback, *J. Appl. Phys.*, 1990, **67**, 1113–1115.

117 L. Xiang, X. Y. Deng and Y. Jin, *Scr. Mater.*, 2002, **47**, 219–224.

118 C. Díaz-Guerra, A. Remon, J. A. Garcia and J. Piqueras, *Phys. status solidi*, 1997, **163**, 497–503.

119 A. Kuzmin, N. Mironova-Ulmane and S. Ronchin, *Adv. Org. Inorg. Opt. Mater.*, 2003, 61–67.

120 H. Cao, X. Qiu, Y. Liang, L. Zhang, M. Zhao and Q. Zhu, *ChemPhysChem*, 2006, **7**, 497–501.

121 H. Amekura, Y. Takeda, K. Kono, H. Kitazawa and N. Kishimoto, *Rev. Adv. Mater. Sci.*, 2003, **5**, 178–182.

122 A. Martucci, N. Bassiri, M. Guglielmi, L. Armelao, S. Gross and J. C. Pivin, *J. Sol-Gel Sci. Technol.*, 2003, **26**, 993–996.

123 L. Zbroniec, A. Martucci, T. Sasaki and N. Koshizaki, *Appl. Phys. A*, 2004, **79**, 1303–1305.

124 P. Heera and S. Shanmugam, *Int.J.Curr.Microbiol.App.Sci*, 2015, **4**, 379–386.

125 M. A. Krivoglaz, *Theory of X-ray and thermal-neutron scattering by real crystals*, 1969, (Plenum press, New York), 1969.

126 K. Jores, W. Mehnert, M. Drechsler, H. Bunjes, C. Johann and K. Mäder, *J. Control. Release*, 2004, **95**, 217–227.

127 J. Molpeceres, M. R. Aberturas and M. Guzman, *J. Microencapsul.*, 2000, **17**, 599–614.

128 M. Joshi, A. Bhattacharyya and S. W. Ali, *Indian J. Fibre Text. Res.*, 2008, **33**, 304–317.

129 J. C. H. Spence, H. R. Kolar, G. Hembree, C. J. Humphreys, J. Barnard, R. Datta, C. Koch, F. M. Ross and J. F. Justo, *Philos. Mag.*, 2006, **86**, 4781–4796.

130 J. C. H. Spence, *Experimental high-resolution electron microscopy*, Oxford University Press, 1988.

131 C. Kisielowski, B. Freitag, M. Bischoff, H. van Lin, S. Lazar, G. Knippels, P. Tiemeijer, M. van der Stam, S. von Harrach, M. Stekelenburg, M. Haider, S. Uhlemann, H. Müller, P. Hartel, B. Kabius, D. Miller, I. Petrov, E. A. Olson, T. Donchev, E. A. Kenik, A. R. Lupini, J. Bentley, S. J. Pennycook, I. M. Anderson, A. M. Minor, A. K. Schmid, T. Duden, V. Radmilovic, Q. M. Ramasse, M. Watanabe, R. Erni, E. A. Stach, P. Denes and U. Dahmen, *Microsc. Microanal.*, 2008, **14**, 469–477.

132 D. F. Shriver, *Shriver & Atkins' Inorganic Chemistry*, Oxford University Press, 2006.

133 A. Murugan and K. kumari Shanmugasundaram, *World J. Pharm. Pharm. Sci.*, 2014, **3**, 1385–1393.

134 A. Seigneur, S. Hou, R. A. Shaw, J. T. McClure, H. Gelens and C. B. Riley, *Vet. Immunol. Immunopathol.*, 2015, **163**, 8–15.

135 N. Ferrer, *Practical fourier transform infrared spectroscopy. Industrial and laboratory chemical analysis: John R. Ferraro and K. Krishnan (Eds.), Academic Press, New York, 1990 (ISBN 0-12-254125-1). 534 pp.*, Elsevier, 1994.

136 H. Hausdorff, in *Analytical Chemistry*, Amer Chemical Soc 1155 16TH ST, NW, Washington, DC 20036, 1951, vol. 23, p. 683.

137 J. J. van der Maas, *Basic infrared spectroscopy*, Heyden & Son, 1972.

138 C. P. S. Hsu, *Infrared spectroscopy*, Prentice Hall: Englewood Cliffs, NJ, 1997, vol. 249.

139 J. McMurry, *Organic Chemistry*, Pacific Grove, Calif: Brooks/Cole Pub, 1992.

140 *Nanoparticle Applications and Uses*, UnderstandingNano.com.

141 J. E. Millstone, D. F. J. Kavulak, C. H. Woo, T. W. Holcombe, E. J. Westling, A. L. Briseno, M. F. Toney and J. M. J. Fréchet, *Langmuir*, 2010, **26**, 13056–13061.

142 S. Nisha, A. S. Karthick and N. Gobi, *Chem. Sci. Rev. Lett.*, 2012, **1**, 148–155.

143 J. Kim, J. W. Grate and P. Wang, *Chem. Eng. Sci.*, 2006, **61**, 1017–1026.

144 A. Sharma, Y. Qiang, J. Antony, D. Meyer, P. Kornacki and A. Paszczynski, *IEEE Trans. Magn.*, 2007, **43**, 2418–2420.

145 J. Ge, D. Lu, Z. Liu and Z. Liu, *Biochem. Eng. J.*, 2009, **44**, 53–59.

146 T. Bahar and S. S. Çelebi, *Enzyme Microb. Technol.*, 1998, **23**, 301–304.

147 N. Schultz, G. Metreveli, M. Franzreb, F. H. Frimmel and C. Syldatk, *Colloids Surfaces B Biointerfaces*, 2008, **66**, 39–44.

148 F. Šulek, M. Drofenik, M. Habulin and Ž. Knez, *J. Magn. Magn. Mater.*, 2010, **322**, 179–185.

149 Z. Bílková, M. Slováková, A. Lyčka, D. Horák, J. Lenfeld, J. Turková and J. Churáček, *J. Chromatogr. B*, 2002, **770**, 25–34.

150 J. Hong, D. Xu, P. Gong, H. Ma, L. Dong and S. Yao, *J. Chromatogr. B*, 2007, **850**, 499–506.

151 D. Demirel and M. Mutlu, *J. Food Eng.*, 2005, **70**, 1–6.

152 D. Demirel, A. R. Özdural and M. Mutlu, *J. Food Eng.*, 2004, **64**, 417–421.

153 L. Zeng, K. Luo and Y. Gong, *J. Mol. Catal. B Enzym.*, 2006, **38**, 24–30.

154 Z. Guo, S. Bai and Y. Sun, *Enzyme Microb. Technol.*, 2003, **32**, 776–782.

155 M. Iman, S. S. Çelebi and A. R. Özdural, *React. Polym.*, 1992, **17**, 325–330.

156 C. Pan, B. Hu, W. Li, Y. Sun, H. Ye and X. Zeng, *J. Mol. Catal. B Enzym.*, 2009, **61**, 208–215.

157 I. Lynch and K. A. Dawson, *Nano Today*, 2008, **3**, 40–47.

158 Y. Kim, S. M. Ko and J. M. Nam, *Chem. Asian J.*, 2016, **11**, 1869–1877.

159 E. Casals, T. Pfaller, A. Duschl, G. J. Oostingh and V. Puntes, *ACS Nano*, 2010, **4**, 3623–3632.

160 S. R. Saptarshi, A. Duschl and A. L. Lopata, *J. Nanobiotechnology*, 2013, **11**,

26.

161 P. Wang, X. Wang, L. Wang, X. Hou, W. Liu and C. Chen, *Sci. Technol. Adv. Mater.*, 2015, **16**, 34610.

162 T. Cedervall, I. Lynch, M. Foy, T. Berggård, S. C. Donnelly, G. Cagney, S. Linse and K. A. Dawson, *Angew. Chem. Int. Ed. Engl.*, 2007, **46**, 5754–5756.

163 R. Landsiedel, L. Ma-Hock, A. Kroll, D. Hahn, J. Schnekenburger, K. Wiench and W. Wohlleben, *Adv. Mater.*, 2010, **22**, 2601–2627.

164 M. Lundqvist, I. Sethson and B. H. Jonsson, *Langmuir*, 2004, **20**, 10639–10647.

165 M. Lundqvist, I. Sethson and B.-H. Jonsson, *Biochemistry*, 2005, **44**, 10093–10099.

166 S. S. Karajanagi, A. A. Vertegel, R. S. Kane and J. S. Dordick, *Langmuir*, 2004, **20**, 11594–11599.

167 V. Ponec and G. C. Bond, *Catalysis by metals and alloys*, Elsevier, 1995, vol. 95.

168 G. C. Bond, *Heterogeneous catalysis*, Oxford University Press, New York, NY, 1987.

169 A. Baiker, H. U. Blaser, G. Ertl, H. Knözinger and J. Weitkamp, *Ertl, G., Knözinger, H., Weitkamp, J., Eds*, 1997, 2422.

170 R. J. Farrauto and C. H. Bartholomew, *Fundamental of Industrial Catalytic Processes, Blackie Academic and Professional, London, 1997*, 1997.

171 C. R. Henry, *Appl. Surf. Sci.*, 2000, **164**, 252–259.

172 T. P. St.Clair and D. W. Goodman, *Top. Catal.*, 2000, **13**, 5–19.

173 M. Bowker, A. Dickinson, D. James, R. D. Smith, P. Stone and R. A. Bennett, *Stud. Surf. Sci. Catal.*, 2001, **133**, 3–17.

174 M. Králik and A. Biffis, *J. Mol. Catal. A Chem.*, 2001, **177**, 113–138.

175 J. M. Thomas and R. Raja, *Chem. Rec.*, 2001, **1**, 448–466.

176 C. Mohr and P. Claus, *Sci. Prog.*, 2001, **84**, 311–334.

177 J. M. Thomas, B. F. G. Johnson, R. Raja, G. Sankar and P. A. Midgley, *Acc. Chem. Res.*, 2003, **36**, 20–30.

178 O. S. Alexeev and B. C. Gates, *Ind. Eng. Chem. Res.*, 2003, **42**, 1571–1587.

179 B. Cornils and W. A. Herrmann, *Applied homogeneous catalysis with organometallic compounds*, VCH Weinheim, 1996, vol. 2.

180 D. Astruc, F. Lu and J. R. Aranzaes, *Angew. Chem. Int. Ed. Engl.*, 2005, **44**, 7852–7872.

181 J. A. Gladysz, *Pure Appl. Chem.*, 2001, **73**, 1319–1324.

182 D. Astruc, *Organometallic chemistry and catalysis*, Springer, 2007, vol. 291.

183 C. Ornelas, D. Méry, J. Blais, E. Cloutet, J. Ruiz Aranzaes and D. Astruc, *Angew. Chemie Int. Ed.*, 2005, **44**, 7399–7404.

184 M. J. Jin and D. H. Lee, *Angew. Chemie Int. Ed.*, 2010, **49**, 1119–1122.

185 J. H. Fendler, *Nanoparticles and nanostructured films: preparation, characterization, and applications*, John Wiley & Sons, 2008.

186 M. Faraji, Y. Yamini and M. Rezaee, *J. Iran. Chem. Soc.*, 2010, **7**, 1–37.

187 A. Wieckowski, E. R. Savinova and C. G. Vayenas, *Catalysis and electrocatalysis at nanoparticle surfaces*, CRC Press, New York, 2003.

188 Y. Shiraishi and N. Toshima, *Colloids Surfaces A Physicochem. Eng. Asp.*, 2000, **169**, 59–66.

189 E. B. M. Doesburg, R. H. Hoppener, B. De Koning, X. Xiaoding, J. J. F. Scholten, B. Delmon, P. Grange, P. A. Jacobs and G. Poncelet, *Preparation of Catalysts IV*, 1987, vol. 767.

190 G. Schmid, *Nanostructured Mater.*, 1995, **6**, 15–24.

191 J. S. Bradley and G. Schmid, *Cluster and Colloids*, 1994, vol. 459.

192 N. Toshima and T. Yonezawa, *New J. Chem.*, 1998, **22**, 1179–1201.

193 Y. Shiraishi and N. Toshima, *J. Mol. Catal. A Chem.*, 1999, **141**, 187–192.

194 S. H. S. Chan, T. Yeong Wu, J. C. Juan and C. Y. Teh, *J. Chem. Technol. Biotechnol.*, 2011, **86**, 1130–1158.

195 T. Hisatomi, J. Kubota and K. Domen, *Chem. Soc. Rev.*, 2014, **43**, 7520–7535.

196 M. R. Hoffmann, S. T. Martin, W. Choi and D. W. Bahnemann, *Chem. Rev.*, 1995, **95**, 69–96.

197 E. Pelizzetti and C. Minero, *Comments Inorg. Chem.*, 1994, **15**, 297–337.

198 A. B. Djurisic, Y. H. Leung and A. M. Ching Ng, *Mater. Horizons*, 2014, **1**, 400–410.

199 M. M. Khan, S. F. Adil and A. Al-Mayouf, *J. Saudi Chem. Soc.*, 2015, **19**, 462–464.

200 A. Hernández-Ramírez and I. Medina-Ramírez, *Photocatalytic semiconductors: synthesis, characterization, and environmental applications*, Springer, 2014.

201 A. Fujishima and K. Honda, *Nature*, 1972, **238**, 37–38.

202 H. Wang, L. Zhang, Z. Chen, J. Hu, S. Li, Z. Wang, J. Liu and X. Wang, *Chem. Soc. Rev.*, 2014, **43**, 5234–5244.

203 M. M. Khan, S. A. Ansari, D. Pradhan, M. O. Ansari, D. H. Han, J. Lee and M. H. Cho, *J. Mater. Chem. A*, 2014, **2**, 637–644.

204 S. A. Ansari, M. M. Khan, S. Kalathil, A. Nisar, J. Lee and M. H. Cho, *Nanoscale*, 2013, **5**, 9238–9246.

205 S. Kalathil, M. M. Khan, S. A. Ansari, J. Lee and M. H. Cho, *Nanoscale*, 2013, **5**, 6323–6326.

206 S. A. Ansari, M. M. Khan, M. Omaish Ansari, J. Lee and M. H. Cho, *New J. Chem.*, 2014, **38**, 2462–2469.

207 C. Sun, H. Li and L. Chen, *Energy Environ. Sci.*, 2012, **5**, 8475–8505.

208 S. A. Ansari, M. M. Khan, M. O. Ansari, S. Kalathil, J. Lee and M. H. Cho, *RSC Adv.*, 2014, **4**, 16782–16791.

209 M. Pelaez, N. T. Nolan, S. C. Pillai, M. K. Seery, P. Falaras, A. G. Kontos, P. S. M. Dunlop, J. W. J. Hamilton, J. A. Byrne and K. O'shea, *Appl. Catal. B Environ.*, 2012, **125**, 331–349.

****

Chapter 2

Study on immobilization of yeast alcohol dehydrogenase on nanocrystalline Ni-Co ferrites as magnetic support

2.1. Introduction

Nanocrystalline ferrites have fascinated much interest in various fields such as some examples including biomedical and environmental applications during the last decade because of their small size, high specific surface area and low cellular toxicity with strong magnetic properties extending applications in intracellular uptake and separation,[1–5] drug delivery,[6] hyperthermia,[4,7] magnetic resonance imaging contrast enhancement,[4,8] enzyme and protein immobilization[9,10] and protein purification.[11] A number of synthetic routes have been adopted for the synthesis of nanoferrites such as mechanical milling, co-precipitation, thermal decomposition, sol-gel, auto-combustion and hydrothermal methods.[1] over various synthesis approach auto-combustion synthesis provides numerous distinct advantages over co-precipitation and ceramic techniques as it does not involve any pH control or a consequent annealing step in synthesis of phase pure and highly crystalline ferrite nanoparticles (FNPs).[12]

Although alcohol dehydrogenase which catalyzes the oxidation of alcohols and the reduction of carbonyl compounds attracted the attention of chemists due to its potential applications in the production of various starting materials and intermediates in chemical industry viz., the synthesis of chiral compounds, regeneration of coenzymes NAD(P) and NAD(P)H and biosensors[13–15] but the poor stability limits its practical applications.[16,17] Therefore, the efforts have been directed towards the immobilization of bioactive materials onto insoluble organic and inorganic supports which not only offered a path to enhance stability and reusability, but also altered the catalytic properties, enzymatic activity or selectivity in some cases.[18–23]

Magnetic supports for biological and biomedical materials are of particular interest amongst various supports due to their inherent characteristics, including non-toxicity, large surface area, and capacity to generate required magnetic properties and their ability to be separated with magnets and recycled. A number of techniques have been adopted for immobilization such as physical adsorption technique is one of the most widely used techniques in which the enzymes and the supports interact *via* vander Waals, ionic, covalent and hydrogen bonding.[9,24–31] It is a simple technique and rarely affects the basic structure of enzymes, reducing the loss of activity. It is important for the sustenance of enzymes that the interactions are firm in order to warrant their reusability. However, there have been reports where covalent binding may result in loss of activity, but it is still suitable for industrial applications in view of advantages such

as prevention of enzyme loss from the support and improved reusability and stability.[32,33] The binding between ferrites and bioactive materials such as enzymes, proteins, antibodies, and anticancer agents have been commonly accomplished through the surface coating with polymers, use of coupling agents or cross linking agents and encapsulation.[2,26,34–46] An appropriate method for the direct binding of proteins such as bovine serum albumin (BSA) *via* carbodiimide activation was reported.[9,47] This technique of binding is prominent as it is simple and extremely efficient. Although immobilization of the yeast alcohol dehydrogenase enzyme (YADH) complex on magnetic supports has been reported previously, but there are no studies made on immobilization of the alcohol dehydrogenase system on Ni-Co nanoferrites.[16,48–50]

Herein, we report the synthesis of Ni-Co nanoferrites, $Ni_xCo_{1-x}Fe_2O_4$ (x = 0.0, 0.2, 0.5, 0.8, 1.0) to study their particle size, structure, morphology, elemental composition and magnetic properties through XRD, SEM, EDS, VSM, HR-TEM, and FT-IR analysis. The prime objective was to investigate the covalent interaction of YADH immobilized on magnetic nanoferrites *via* carbodiimide activation. The covalent bonding of YADH to nanoferrite was confirmed by comparing the results of FT-IR spectroscopy and HR-TEM with that of bare nanoferrites. The comparative assessment of operating parameters such as kinetic constants, varying thermal and pH stability and reusability of free YADH and immobilized YADH helped to determine optimum operating conditions.

2.2. Results and discussion

2.2.1. Structural analysis

X-ray diffraction patterns for $Ni_xCo_{1-x}Fe_2O_4$ (x = 0.0, 0.2, 0.5, 0.8, 1.0) demonstrated in the **Fig. 2.1**, showed the reflection planes: (220), (311), (222), (400), (422), (533) and (440) comparably close with those of reported reflection planes of Ni-Co ferrites.[54] The d-spacing of peaks was confirmed with standard data (JCPDS card No. 77-0426) and the above mentioned reflection planes suggested a face-centered cubic spinel for all nanoferrites having Fd3m space group. It is evident from the diffraction lines that ferrite phase was formed in all the samples. All the peaks in the diffraction pattern have been indexed and refinement of their lattice parameter was done by using Powder-X software. The variation in FWHM is in agreement with the crystallite size reckoned by Debye-Scherrer's formula:

$$D = \frac{0.9\lambda}{\beta COS\theta}$$

Where, λ is the wavelength of Cu Kα radiation, D is the particle size, β is the full width half maximum intensity, and θ is the position of peak.

The crystallite size was determined from main diffraction peak (311) and the calculation outputs are summarized in **Table 2.1**.

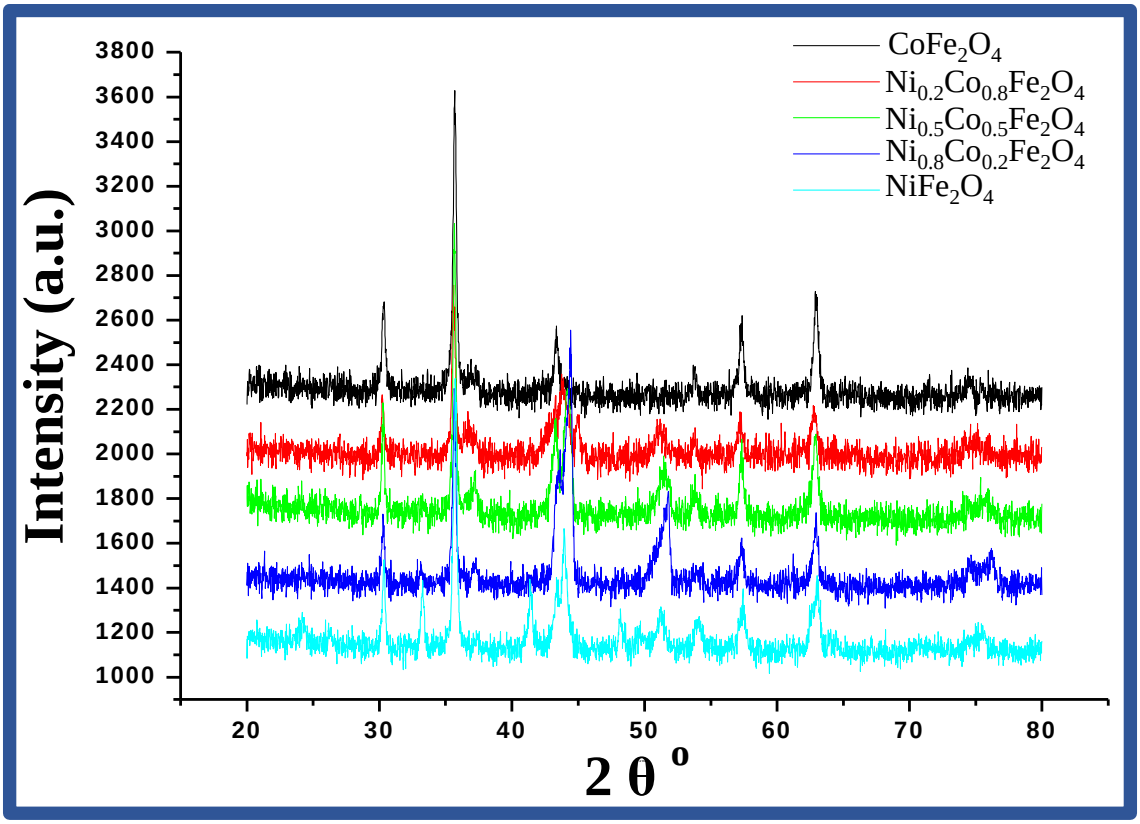

Figure 2.1. XRD patterns of $Ni_xCo_{1-x}Fe_2O_4$ (x = 0.0, 0.2, 0.5, 0.8, 1.0).

Table 2.1. Structural parameters of nanocrystalline Ni-Co ferrites.

S.No.	Sample	2θ	FWHM (β)	Crystallite Size (nm)	Lattice Parameter (a)
1.	$CoFe_2O_4$	35.684	0.3157	26.433	8.40
2.	$Ni_{0.2}Co_{0.8}Fe_2O_4$	35.598	0.3518	23.71	8.390
3.	$Ni_{0.5}Co_{0.5}Fe_2O_4$	35.667	0.2788	29.93	8.370
4.	$Ni_{0.8}Co_{0.2}Fe_2O_4$	44.409	0.7230	11.86	8.365
5.	$NiFe_2O_4$	35.731	0.3604	23.13	8.62

2.2.2. Fourier transform infrared (FT-IR) spectroscopic studies

The FT-IR spectra presented in **Fig. 2.2**, facilitated in assessing the pattern of the spinel structure in the nanocrystalline Ni-Co ferrite samples. The FT-IR spectra of the samples revealed important signals at 3421 and 1600 cm^{-1} which were attributed to the stretching modes and H-O-H bending vibration of the free or absorbed water which suggested that hydroxyl groups are retained in the ferrites during their preparation following the low temperature soft chemistry routes. The retention of water in nanocrystalline ferrites up to 873 K have been reported in some ferrite samples.[55–57] The band observed at 1465 cm^{-1} assigned to the antisymmetric NO-stretching vibration of the nitrate group persisted even after the combustion of the sample. The IR bands of solids in the range 1000-400 cm^{-1} are generally assigned to vibration of inorganic ions in the crystal lattice. Two strong absorption bands in the higher frequency ranges from 551-587 cm^{-1} and lower frequency range 470-430 cm^{-1} were clearly examined in the FT-IR spectra of spinels particularly in ferrites. These bands were attributed to the vibrations of the metal ion-oxygen complexes in the tetrahedral and octahedral sites, respectively.[58] The presence of tetrahedral vibrations suggested the formation of ferrite phase. The YADH enzyme complex exhibited the characteristic IR frequencies at 1639 and 1376 cm^{-1} which were also shown on the nanoferrites containing immobilized YADH thus signifying attachment of the enzyme to Ni-Co nanoferrites. These characteristic frequencies specifically correspond to the stretching modes of C=O and C-O groups. A negative shift in frequency from 1376 to 1306 cm^{-1} on the immobilized enzyme was probably due to the formation of an amide bond (**Scheme 2.1**) resulted from the reaction between a carboxyl group on the enzyme and an amine group on the NPs surface (specifically, the C-O to C-N conversion).

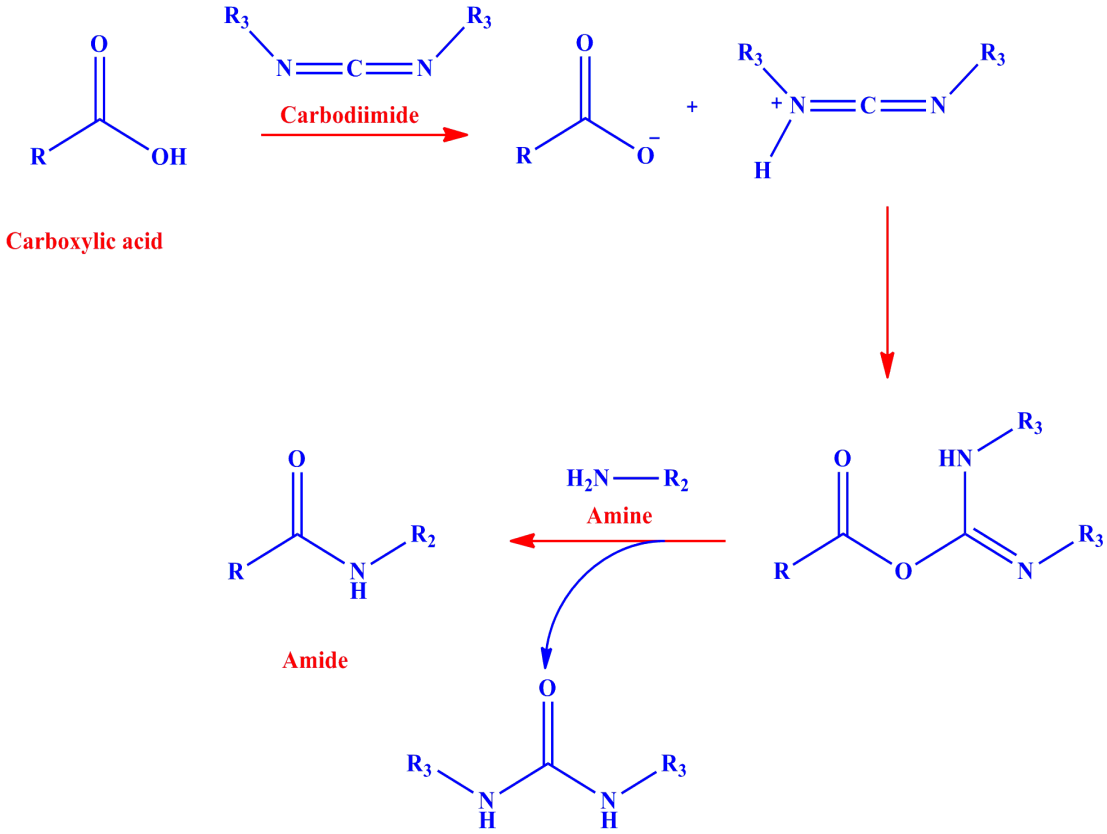

Scheme 2.1. Synthesis involving amide bond formation *via* carbodiimide activation.

The prominent band in the range 2900-2800 cm^{-1} possibly due to stretching of C-H bond.[59,60] The naked $Ni_xCo_{1-x}Fe_2O_4$ (x = 0.0, 0.2, 0.5, 0.8, 1.0) also show a characteristic frequency at 1623 cm^{-1} which may be due to N-H stretching of the amine functional group. This peak disappeared after binding with the immobilized YADH enzyme, suggesting that the binding was achieved by the reaction between the amine group on nanoferrites and carboxyl group of YADH activated by carbodiimide. The weaker bands for the immobilized YADH are basically an effect of low enzyme loading on the NP surface.[51]

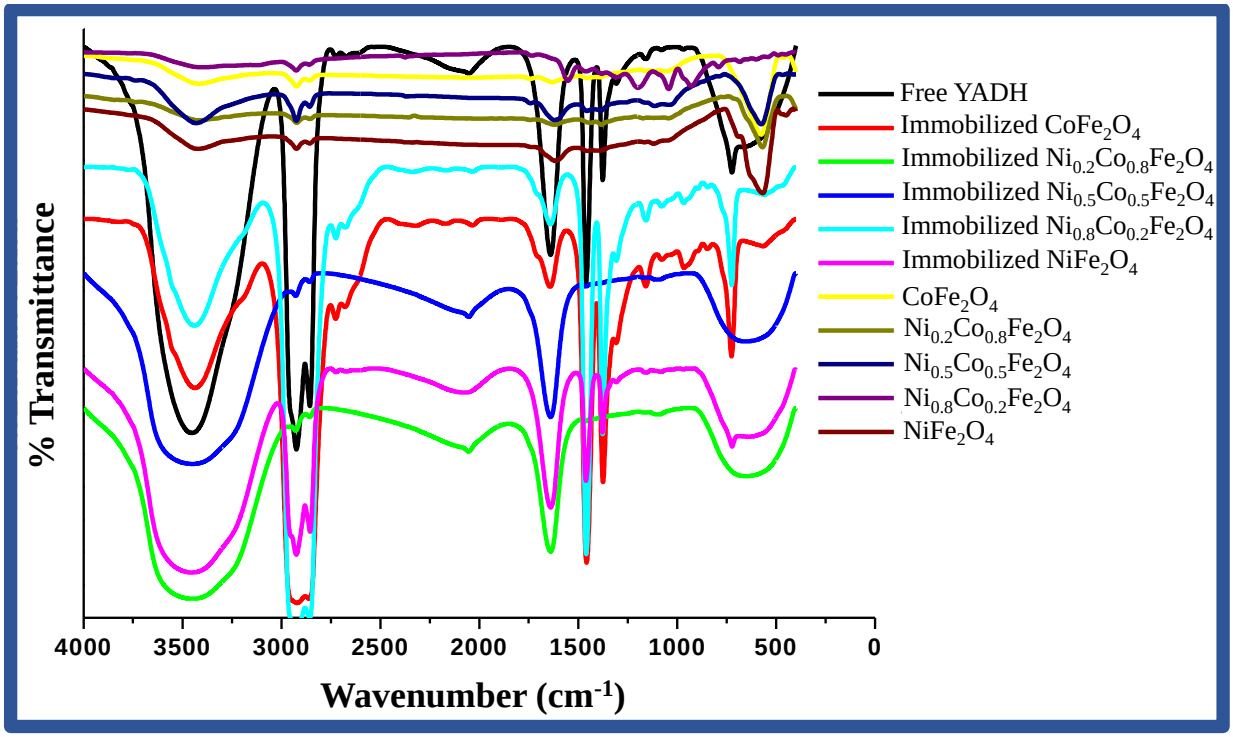

Figure 2.2. FT-IR spectra of naked $Ni_xCo_{1-x}Fe_2O_4$ (x = 0.0, 0.2, 0.5, 0.8, 1.0), immobilized $Ni_xCo_{1-x}Fe_2O_4$ and free YADH.

2.2.3. Surface morphology and compositional analysis

The SEM images and EDS spectra of the prepared samples were taken at 4000 × magnification (**Fig. 2.3**). The SEM images of $CoFe_2O_4$ revealed that the particles are not well distributed and show relatively diffused patterns of particles whereas other samples of Ni-Co nanoferrites exhibit a uniform particle distribution. The compositions of different ferrite samples, $Ni_xCo_{1-x}Fe_2O_4$ (x = 0.0, 0.2, 0.5, 0.8, 1.0) have been analyzed by EDS for the various elements in terms of weight % and atomic % (**Table 2.2**) which revealed that Ni, Co, Fe and O are present approximately as per the expected stoichiometry.

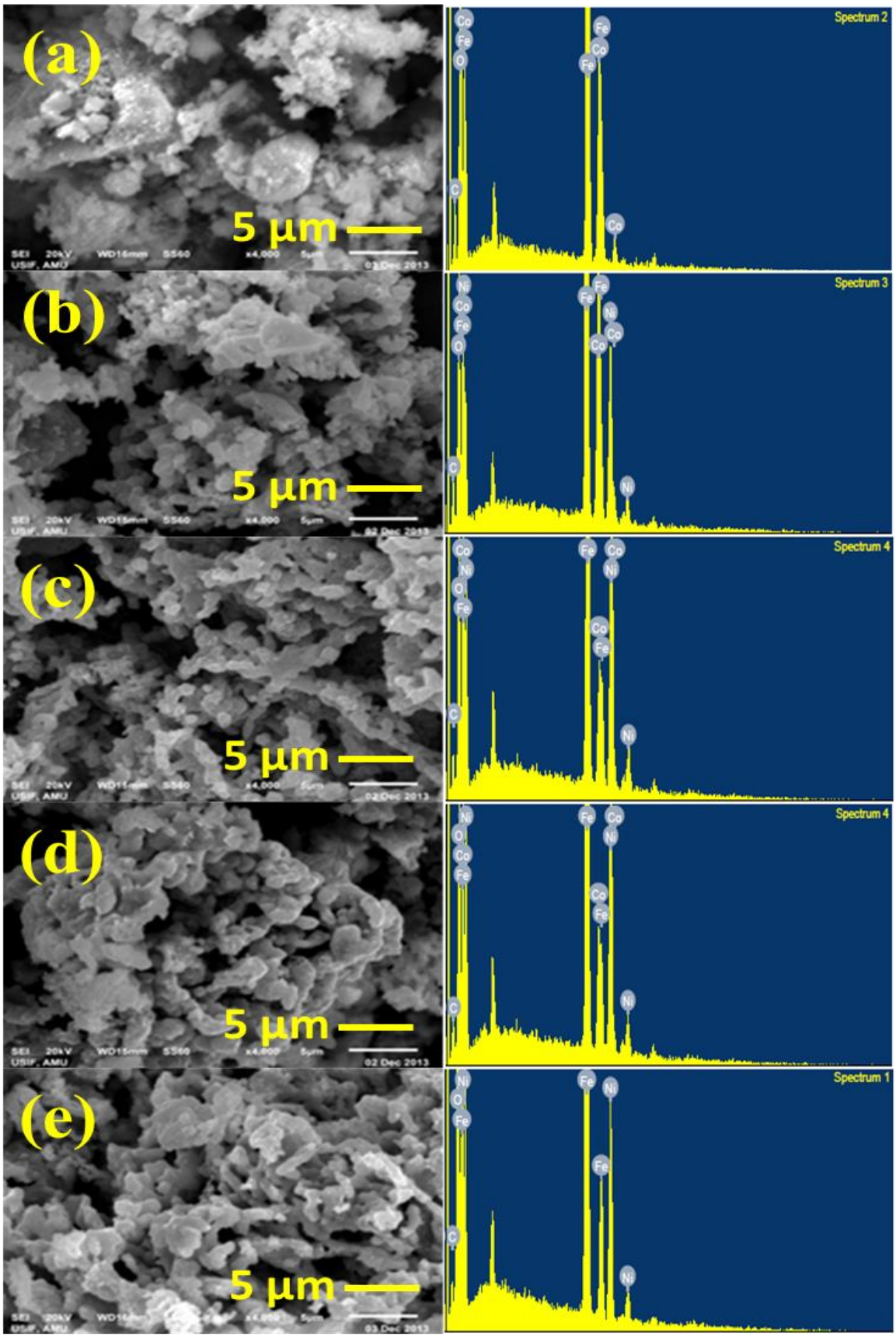

Figure 2.3. SEM images (left side) and EDS spectrum (right side) of $Ni_xCo_{1-x}Fe_2O_4$ (x = 0.0, 0.2, 0.5, 0.8, 1.0): (a) $CoFe_2O_4$ (b) $Ni_{0.2}Co_{0.8}Fe_2O_4$ (c) $Ni_{0.5}Co_{0.5}Fe_2O_4$ (d) $Ni_{0.8}Co_{0.2}Fe_2O_4$ (e) $NiFe_2O_4$.

Table 2.2. EDS analysis (weight % and atomic %) of $Ni_xCo_{1-x}Fe_2O_4$ at different compositions.

Comp-osition	x = 0.0		x = 0.2		x = 0.5		x = 0.8		x = 1.0	
Elem-ent	Wt. %	At. %	Wt. %	At. %	Wt. %	At. %	Wt. %	At. %	Wt. %	At. %
O	26.65	56.26	15.26	39.23	15.10	38.89	16.12	40.72	22.80	46.85
Fe	53.61	32.42	41.76	30.75	43.94	32.42	43.63	31.59	55.10	32.43
Ni	-	-	8.30	5.81	18.08	12.69	30.95	21.31	21.10	20.72
Co	19.74	11.32	34.67	24.20	22.88	16.00	9.30	6.38	-	-

2.2.4. Transmission electron microscopy (TEM) analysis

The HR-TEM images of magnetic NPs without **Fig. 2.4 (a)** and with **Fig. 2.4 (b)** immobilized YADH enzyme have been displayed along with their relevant size distributions. Nanoferrites which are not bound seemed to be very fine and uniformly distributed varying from 20 to 30 nm in diameter, respectively, with an overall mean diameter of 20.12 ± 5.74 nm. However, the nanoferrites remain discrete after binding and have a mean diameter of 18.84 ± 5.35 nm comparable to that of unbound ones. The variation on size between bare nanoferrites and the nanoferrites containing YADH complex has been obtained by statistical analysis of 50 NPs in total which were erratically selected from both images suggesting that there is no effect on the size of NPs after binding process. This is also apparent from the physical assessment of images without showing additional aggregation due to binding of YADH on nanoferrites.

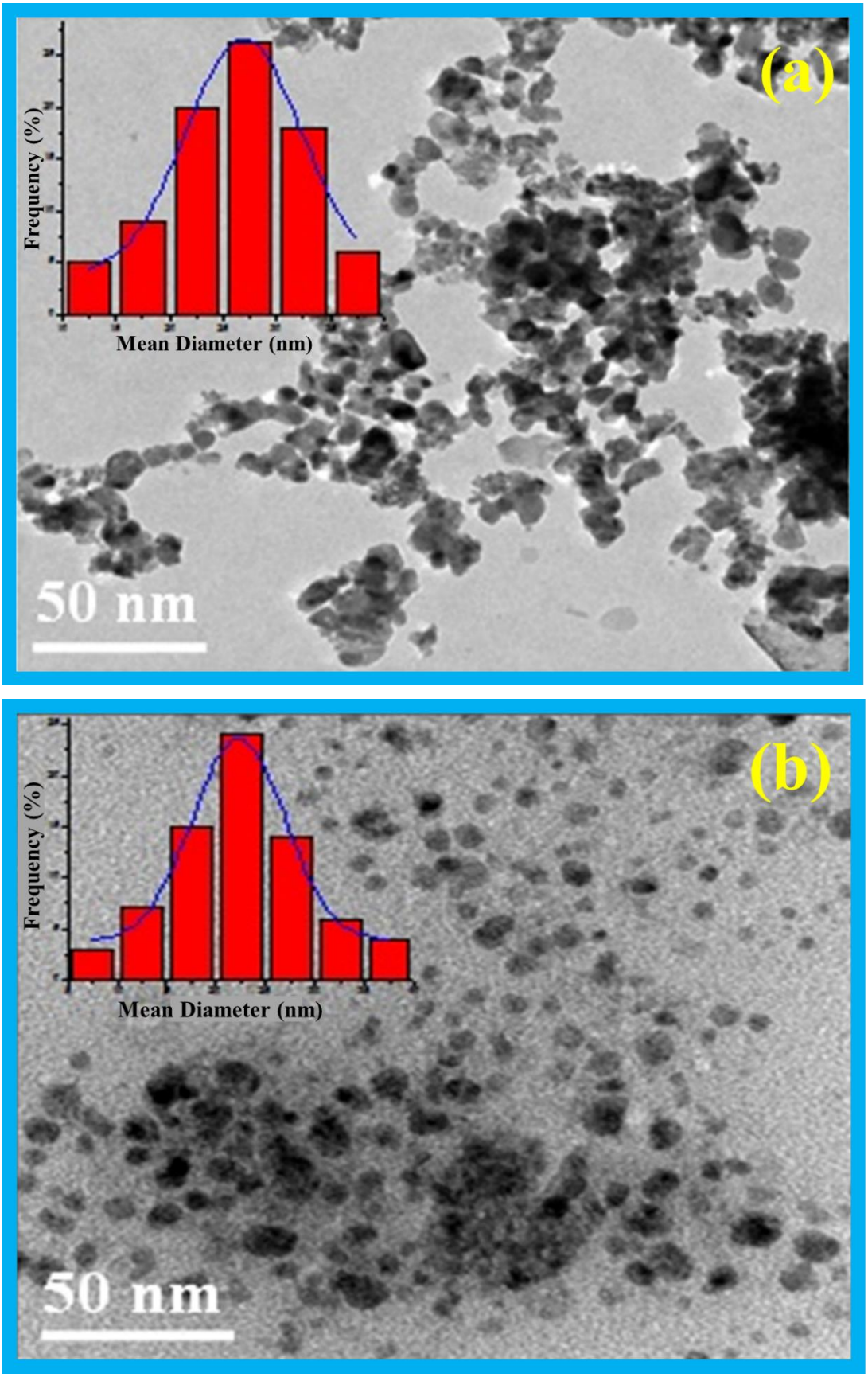

Figure 2.4. TEM images of magnetic Ni-Co nanoferrites without YADH (a) and with YADH (b) and their statistical analysis.

2.2.5. Vibrating sample magnetometer (VSM) analysis

The magnetic properties of the nanoferrites $Ni_xCo_{1-x}Fe_2O_4$ (x = 0.0, 0.2, 0.5, 0.8, 1.0) were studied on VSM at 300 K using magnetization *M* and applied field *H*, explained by Langevin equation:

$$M = Ms\ (Cothy - 1), \text{ and } Y = mH/kT$$

Where *Ms* is the saturation magnetization of NPs, '*m*' is the average magnetic moment of individual NP in the sample and *k* is Boltzmann constant.[61] The magnetic parameters such as saturation magnetization (*Ms*) and coercivity (*Hc*) were determined (**Table 2.3**) by plotting magnetization *vs* magnetic field (**Fig. 2.5**). The magnetic order is commonly due to the super exchange interaction mechanism taking place between the metal ions in the cubic system of ferromagnetic spinels. The magnetization '*M*' increases sharply on increasing the applied field in magnetic field range 0-2000 Oe, and saturates at about 2500 Oe showing that the nanoferrites have strong magnetic responses to a varying magnetic field. The hysteresis loop showed smooth change of magnetization with applied field in all the plots at room temperature. The saturation magnetization in a magnetic field decreases from 27 emu/g to 12.7 emu/g as Ni contents in place of Co in $CoFe_2O_4$ increases. The decrease in saturation magnetization with increase in Ni content is due to relatively high orbital contribution to the magnetic moment of Co^{2+} ions which induce large anisotropy.[62]

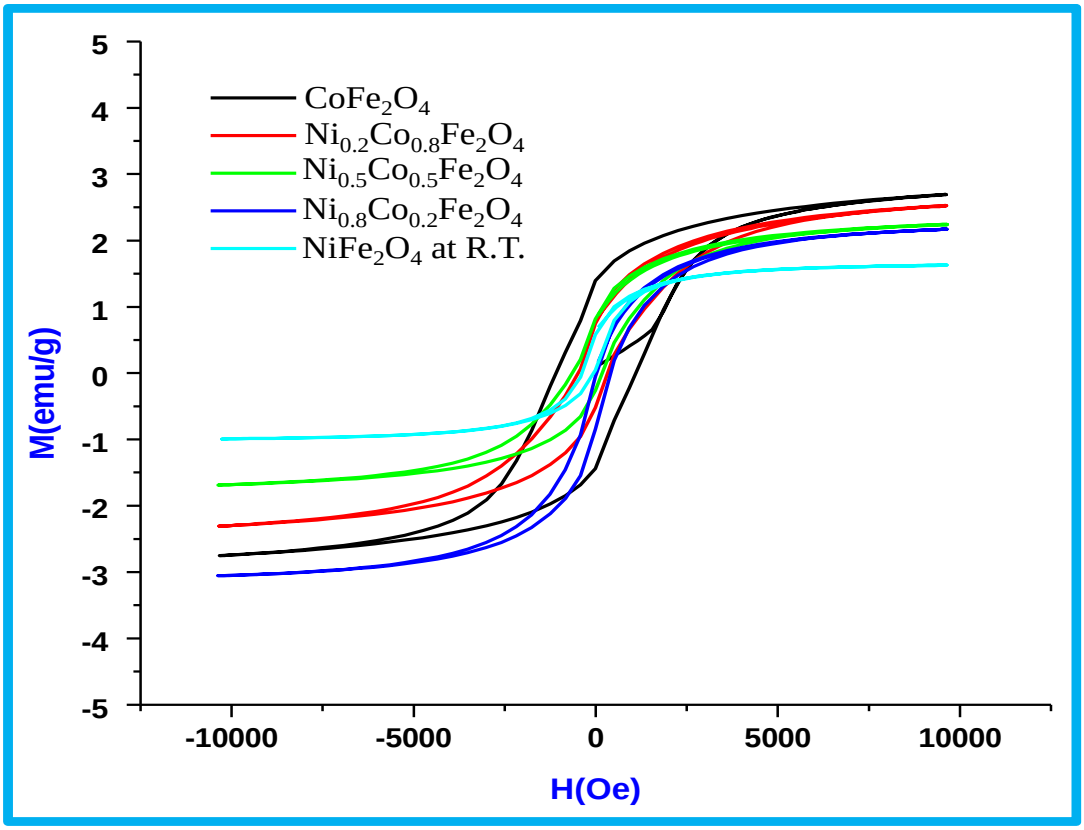

Figure 2.5. Magnetization curves for $Ni_xCo_{1-x}Fe_2O_4$ (x = 0.0, 0.2, 0.5, 0.8, 1.0).

Table 2.3. Magnetic data of nanocrystalline Ni-Co ferrites.

S.No.	Sample	Saturation magnetization (emu/g)	Coercivity (Oe)
1.	$CoFe_2O_4$	27.0	1.142
2.	$Ni_{0.2}Co_{0.8}Fe_2O_4$	25.5	0.017
3.	$Ni_{0.5}Co_{0.5}Fe_2O_4$	24.0	0.013
4.	$Ni_{0.8}Co_{0.2}Fe_2O_4$	19.2	0.002
5.	$NiFe_2O_4$	12.7	0.014

2.2.6. Properties of immobilized YADH

Immobilization of Ni-Co nanoferrites on YADH was done by covalent binding *via* carbodiimide activation. The binding efficiency of YADH on Ni-Co nanoferrites was 85.18 %.

2.2.6.1. Effect of pH on the activity of immobilized YADH

The pH activity profiles of soluble and immobilized YADH preparation are shown in **Fig. 2.6**. All immobilized YADH preparations showed no change in pH-optima but had a remarkable broadening in the pH activity profiles as compared to the native enzyme. The immobilized preparation however showed a marginal broadening of the activity

profile in acidic range and greater broadening of profile in alkaline range. When proportion of Ni increases in nanoferrites, the broadening of residual activity increased in alkaline range, immobilized YADH on $NiFe_2O_4$ retained 10.16 % and 45.71 % of initial activity at pH 3.0 and pH 12.0, respectively, whereas soluble enzyme retained 9.6 % and 16.7 % of the initial activity at these pH, respectively.

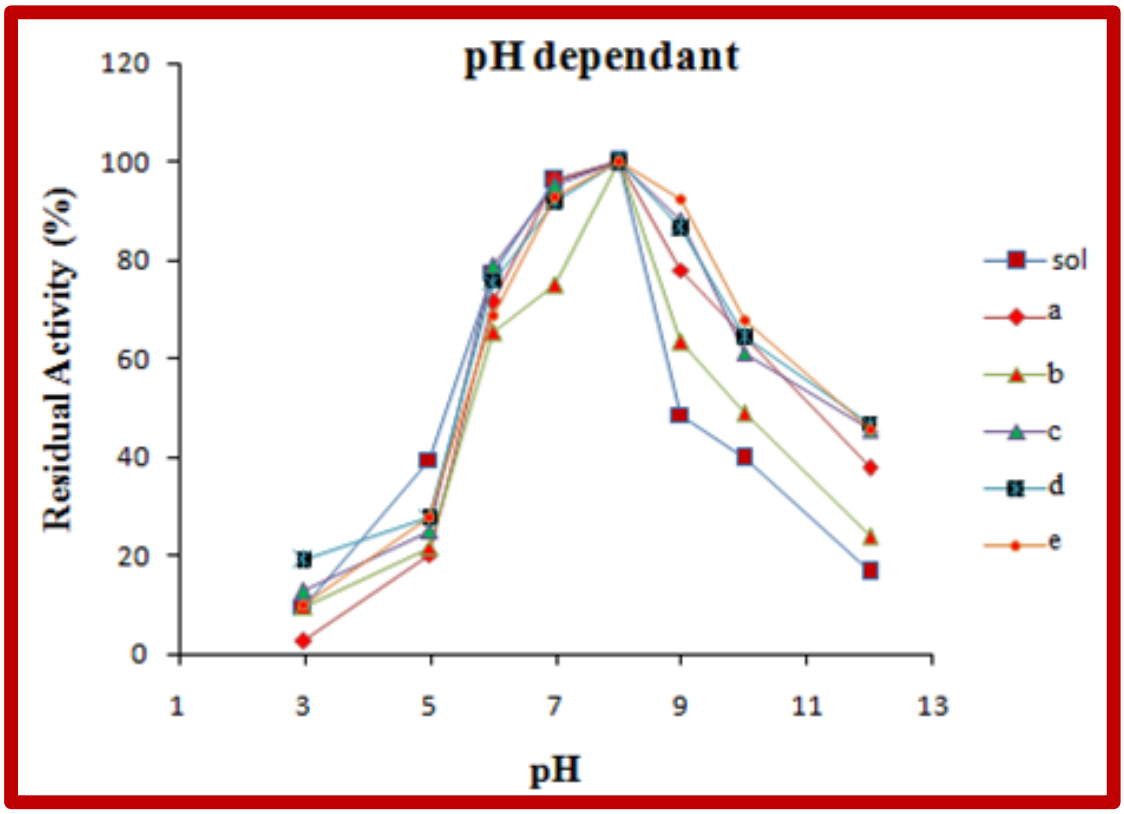

Figure 2.6. Effect of pH on the activity of soluble enzyme (sol) and immobilized YADH on $Ni_xCo_{1-x}Fe_2O_4$ (x = 0.0, 0.2, 0.5, 0.8, 1.0): (a) $CoFe_2O_4$ (b) $Ni_{0.2}Co_{0.8}Fe_2O_4$ (c) $Ni_{0.5}Co_{0.5}Fe_2O_4$ (d) $Ni_{0.8}Co_{0.2}Fe_2O_4$ (e) $NiFe_2O_4$.

2.2.6.2. Effect of temperature on the activity of immobilized YADH

The temperature activity profile of soluble and immobilized YADH preparation is shown in **Fig. 2.7**. There was no alteration in temperature-optima of the various immobilized enzyme preparations although there was a significant broadening in temperature-activity profiles for immobilized enzyme preparations. The temperature activity profile of both free and immobilized enzyme preparation showed increasing enzyme activity up to 45 ^{o}C. Immobilized YADH preparation significantly retained higher catalytic activity *i.e.* 60.45 % at 70 ^{o}C, while the soluble enzyme exhibited only 26 % of the initial enzyme activity.

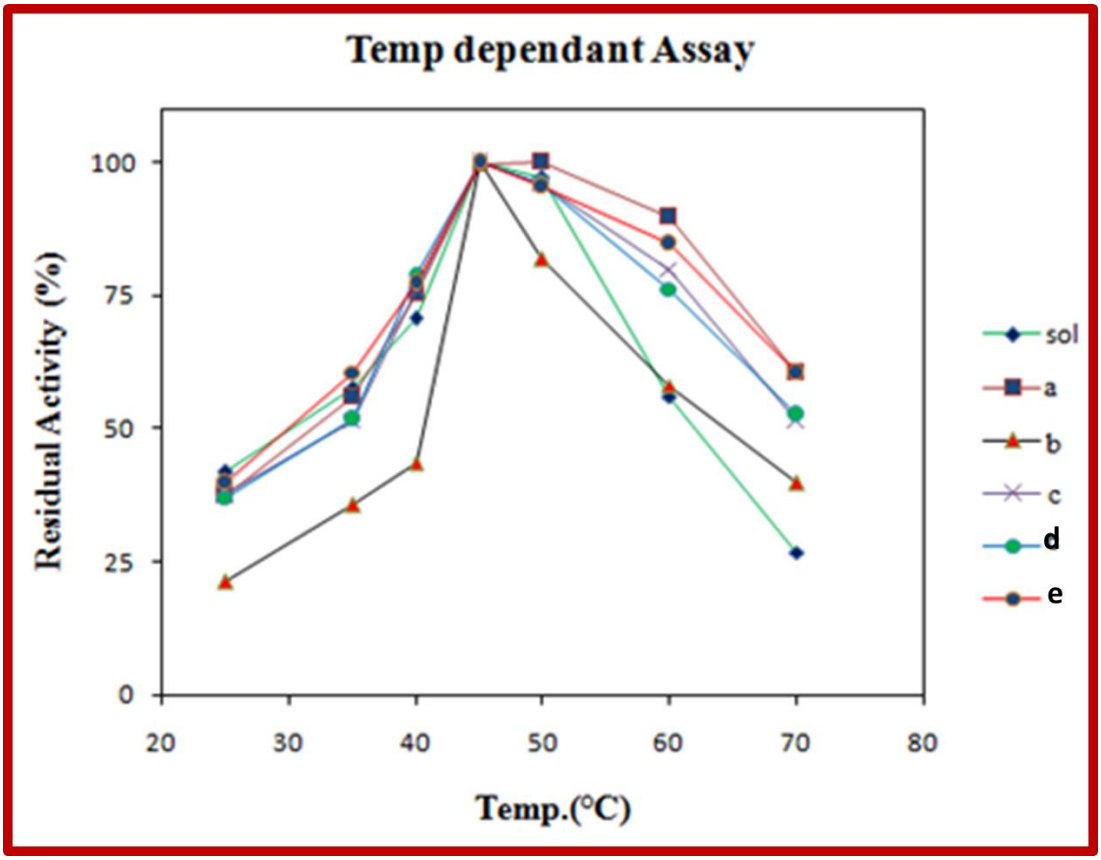

Figure 2.7. Effect of temperature on the activity of soluble enzyme (sol) and immobilized YADH on $Ni_xCo_{1-x}Fe_2O_4$ (x = 0.0, 0.2, 0.5, 0.8, 1.0): (a) $CoFe_2O_4$ (b) $Ni_{0.2}Co_{0.8}Fe_2O_4$ (c) $Ni_{0.5}Co_{0.5}Fe_2O_4$ (d) $Ni_{0.8}Co_{0.2}Fe_2O_4$ (e) $NiFe_2O_4$.

2.2.6.3. Thermal stability of immobilized YADH

The thermal stability profile on both soluble and immobilized YADH preparation after incubating at 60 ^oC for a period of 300 min is shown in **Fig. 2.8**. All the immobilized YADH preparation retained significantly higher catalytic activity even after 300 min of incubation at 60 ^oC. YADH immobilized on nanoferrites, $CoFe_2O_4$ showed nearly 45 % of the initial activity after 300 min exposure. Moreover, this retained activity was more pronounced as the proportion of Ni was increased in nanoferrites. YADH immobilized on $NiFe_2O_4$ exhibited 66 % catalytic activity after 300 min, whereas the soluble enzyme showed only marginal activity of 11 % after 300 min exposure under similar incubation condition. At high temperature soluble enzyme fraction loses its activity due to denaturation of enzyme. The improved thermal stability of immobilized YADH preparation was supposed to be aided by nanoferrites, which absorb considerable amount of heat and protect the enzyme from denaturation.

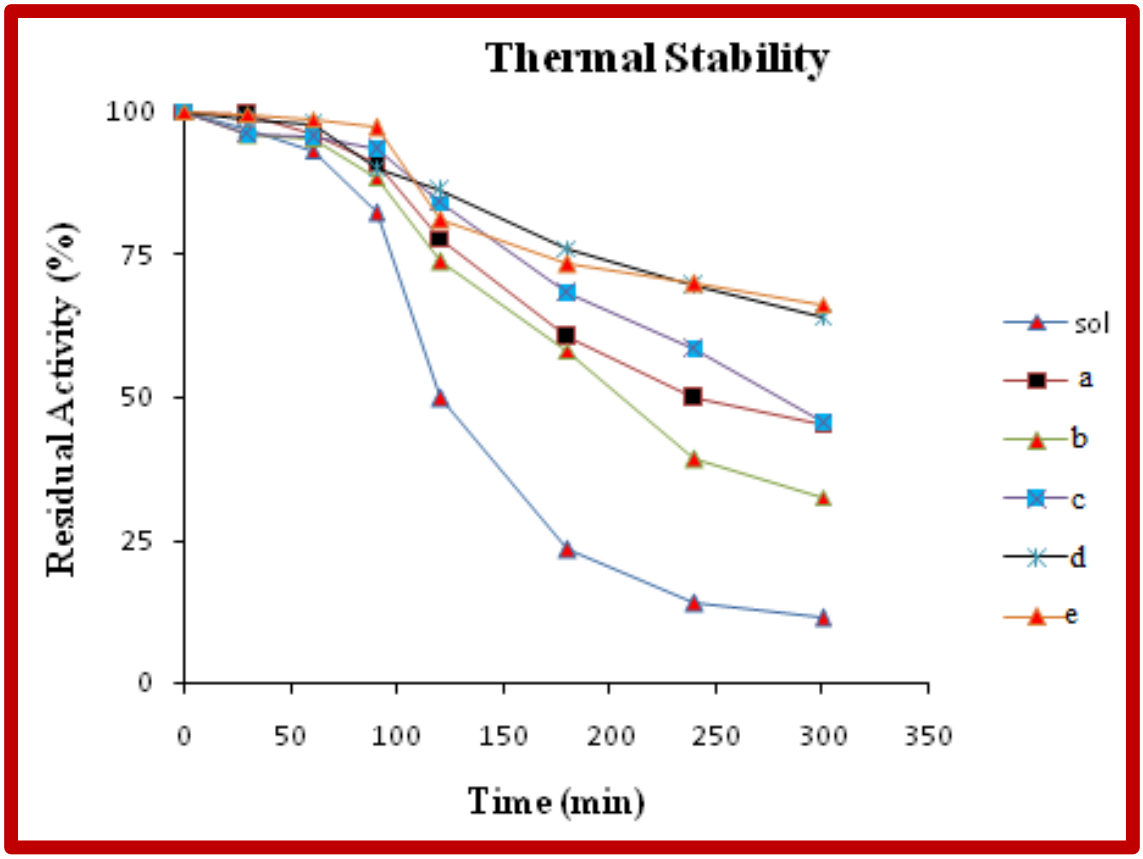

Figure 2.8. Thermal stability of soluble enzyme (sol) and immobilized YADH on $Ni_xCo_{1-x}Fe_2O_4$ (x = 0.0, 0.2, 0.5, 0.8, 1.0): (a) $CoFe_2O_4$ (b) $Ni_{0.2}Co_{0.8}Fe_2O_4$ (c) $Ni_{0.5}Co_{0.5}Fe_2O_4$ (d) $Ni_{0.8}Co_{0.2}Fe_2O_4$ (e) $NiFe_2O_4$.

2.2.6.4. Activity and kinetic parameters

Catalytic properties of the free and immobilized enzymes were evaluated by using EtOH as a substrate. The Michaelis-Menten constant, K_m and maximum activity, V_{max} of the free and immobilized enzymes were estimated at pH 8.0 and 37 ^oC. The apparent Michaelis-Menten constant for free and immobilized YADH enzyme were determined from double-reciprocal plots *i.e.* 1/V *vs* 1/[S] as shown in **Fig. 2.9**. From this plot the kinetic parameters K_m and V_{max} were determined (**Table 2.4**) as 154 mM and 315.55 μmol min^{-1}, respectively for the free YADH and 237 mM and 190.08 μmol min^{-1}, respectively for immobilized YADH. The immobilized enzymes has a higher K_m and lower V_{max} in comparison to the free enzyme. The higher K_m suggests that the enzyme has lower affinity for the substrate which may be due to the conformational changes in the enzyme introduced due to conjugation with the nanoferrites or the lower accessibility of substrate to the active site.

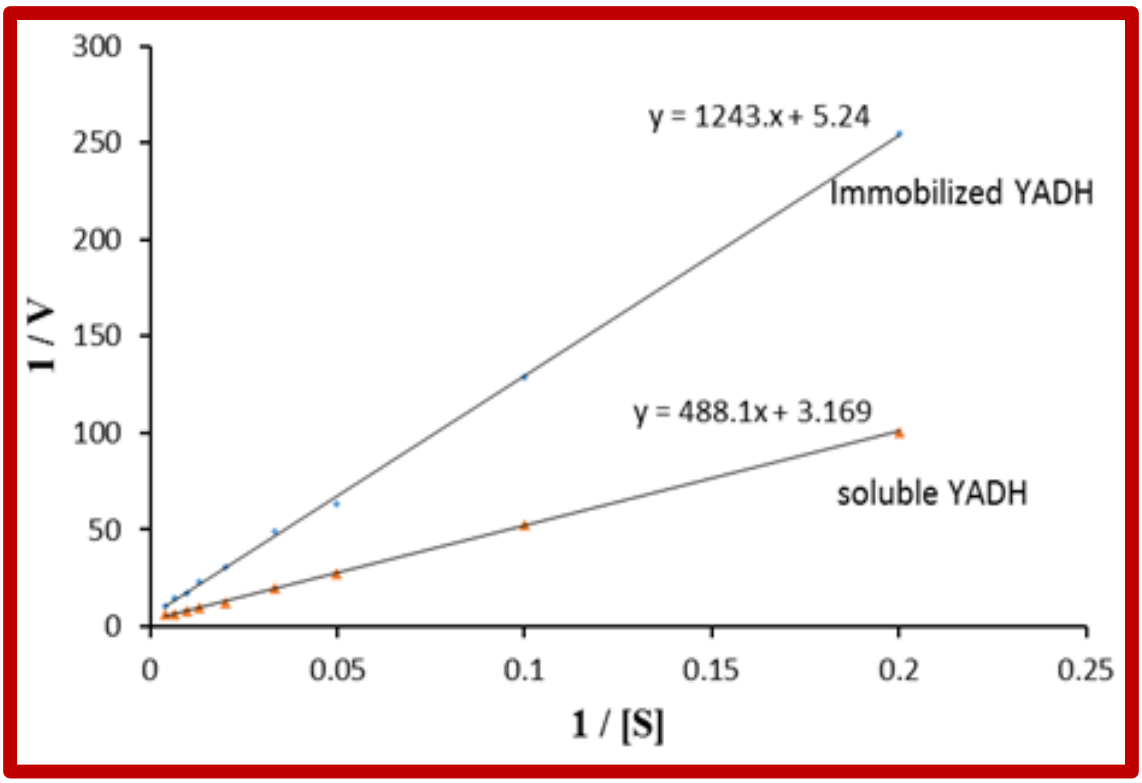

Figure 2.9. Double reciprocal plots for soluble and immobilized YADH.

Table 2.4. The kinetic parameters for free and immobilized YADH.

Alcohol dehydrogenase	K_m (mM)	V_{max} (µmol min^{-1})	V_{max} /K_m	Relative activity (%)
Free	154	315.55	0.0020	100
Immobilized	237	190.83	0.0008	40

2.2.6.5. Reusability of immobilized YADH

Reusability is one of the significant parameter to evaluate the property of immobilized enzyme at large scale. **Fig. 2.10**, shows the residual activity of immobilized enzyme upon subsequent uses. Immobilized YADH retained around 70 % of the initial activity even after its tenth repeated use as shown in **Table 2.5**. The results indicated that the immobilized YADH on the magnetic nanoferrites has a good durability and recovery.

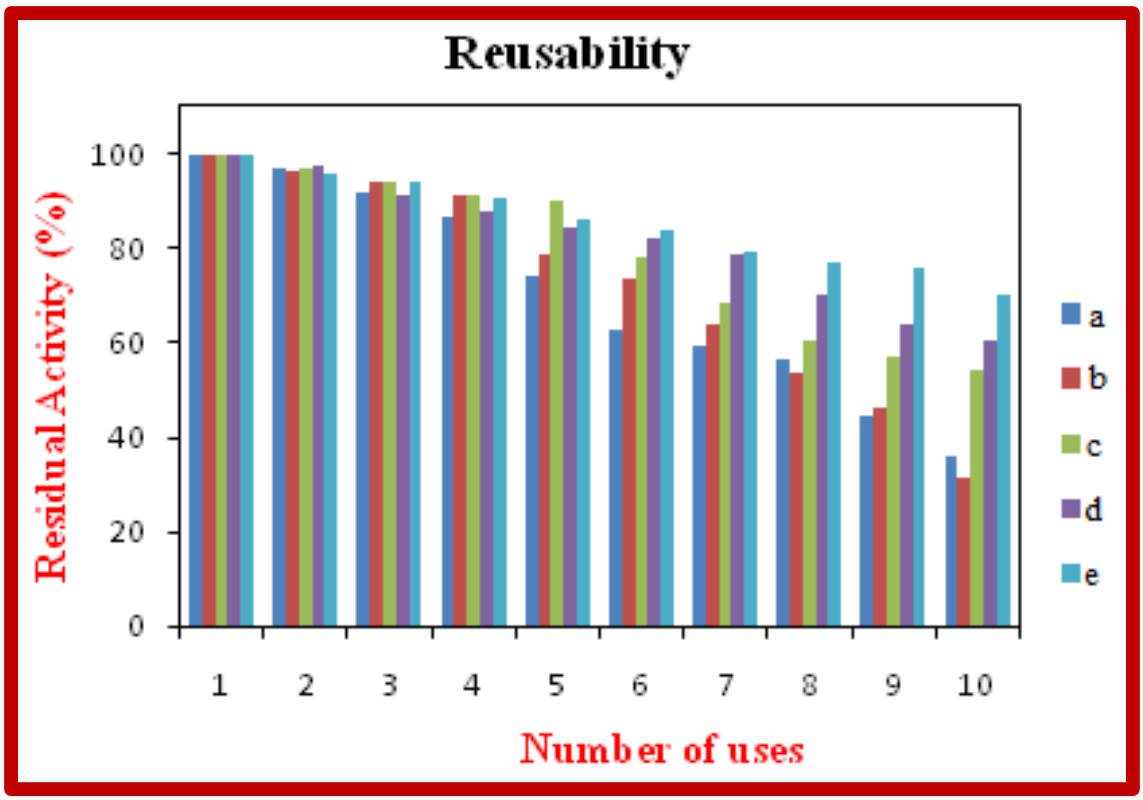

Figure 2.10. Reusability of the immobilized YADH on $Ni_xCo_{1-x}Fe_2O_4$ (x = 0.0, 0.2, 0.5, 0.8, 1.0): (a) $CoFe_2O_4$ (b) $Ni_{0.2}Co_{0.8}Fe_2O_4$ (c) $Ni_{0.5}Co_{0.5}Fe_2O_4$ (d) $Ni_{0.8}Co_{0.2}Fe_2O_4$ (e) $NiFe_2O_4$.

Table 2.5. Comparison of different systems of immobilization of YADH on magnetic NPs.

Methods	Activity retained after immobilization of YADH %	Optimum pH	Optimum temp.	References
SCAD/Fe_3O_4 NPs *via* glutaraldehyde	48.77	6.8-8.0	40 ºC	Ref.[63]
SCAD/Fe_3O_4-KCTS-Chitosan NPs *via* glutaraldehyde	65	7.4	30 ºC	Ref.[64]
YADH/Fe_3O_4 NPs *via* carbodiimide	62	5.0-6.0	50 ºC	Ref.[24]
YADH/Ni-Co nanoferrites *via* carbodiimide	70	8.0	45 ºC	This work

2.3. Experimental

2.3.1. Chemicals

Iron nitrate nonahydrate {$Fe(NO_3)_3 \cdot 9H_2O$}, nickel nitrate hexahydrate {$Ni(NO_3)_2 \cdot 6H_2O$}, cobalt nitrate hexahydrate {$Co(NO_3)_2 \cdot 6H_2O$}, hydrazine hydrate ($N_2H_4 \cdot H_2O$), sodium hydroxide (NaOH), 1-(3-dimethylaminopropyl)-3-ethylcarbodiimide hydrochloride ($C_8H_{17}N_3 \cdot HCl$, EDC), sodium chloride (NaCl), glycine ($C_2H_5NO_2$), sodium acetate (CH_3COONa), sodium phosphate (Na_3PO_4), ethanol (EtOH) and hydrochloric acid (HCl) were obtained from E. Merck (Germany).

2.3.2. Preparation of nickel and cobalt nanoferrites

$Ni_xCo_{1-x}Fe_2O_4$ (x = 0.0, 0.2, 0.5, 0.8, 1.0) were prepared by the sol-gel auto-combustion method in which metal nitrates were utilized as an oxidant while hydrazine hydrate was employed as a reducing agent. Stoichiometric proportion of nickel nitrate (99 %), cobalt nitrate (99.9 %), iron nitrate (99 %) and hydrazine hydrate (98.5 %) were mixed homogeneously in de-ionized water in a huge beaker. The solution obtained was further kept on vigorous stirring till the formation of a gel. On heating gel at 300 ^oC in an open atmosphere, the gel gets self-ignited and underwent a strong self-propagating combustion reaction with the evolution of a large volume of gases. The whole combustion process was completed after a few seconds. The resultant discrete product is of brown color and could be easily transformed into ash by slight touch. The product thus obtained is magnetic in nature and simply attracts to a magnet.

2.3.3. Covalent immobilization of YADH on magnetic Ni-Co nanoferrites

YADH was immobilized onto nanoferrites by using method described by Chen and Liao.[51] Each series of 2-30 mg magnetic nanoferrites were added to 2 mL buffer A (3 mM phosphate, pH 6.0, 100 mM NaCl). The reaction mixture was sonicated for 10 min after adding 0.5 mL of carbodiimide solution (0.05 g mL^{-1} in buffer A). Finally, 2.5 mL YADH (2 mg mL^{-1} in buffer A) was added and this reaction mixture was sonicated for 30 min. The YADH immobilized magnetic nanoferrites were recovered from the reaction mixture by placing the bottle on a permanent magnet. The magnetic particles settled within 1–2 min. The precipitates were washed with 3 mM phosphate buffer, pH 6.0 and 0.1 M Tris buffer, pH 8.0 and then used for further studies such as the characterization and measurements of activity and stability. The supernatants were

pooled and the amount of unimmobilized enzyme in the supernatants was determined by using Bicinchoninic assay using BSA as a standard.[52] The amount of enzyme immobilized on the nanoferrites was calculated by subtracting the amount of the unimmobilized enzyme from the total amount of enzyme used for immobilization.

2.3.4. Determination of YADH loading efficiency

The concentration of YADH enzyme was resolved according to Bicinconinic protein assay method[52] and loading efficiency of YADH was estimated from the following equation:

$$Loading\ efficiency\ (\%) = \frac{C_oV_o - C_iV_i}{C_oV_o} \times 100\ \%$$

Where C_o denotes the protein concentration and V_o is the volume of the YADH solution before immobilization, respectively. C_i is the protein concentration and V_i is volume of the filtrate which was left after immobilization, respectively. BSA was taken as a standard protein.

2.3.5. Characterization

The size, structure and magnetic properties of the resultant nanoferrites without and with immobilized YADH were characterized by FT-IR and spectra were recorded using Perkin Elmer 1725 instrument. Surface morphology and the particle size was obtained by recording SEM and HR-TEM micrographs by LEO 435-VF and JEOL TEM (JEM 2100F) instruments, respectively. The phase, particles size of the prepared nanoferrites were recorded *via* XRD data by PHILIPS PW1710 diffractometer with Cu Kα radiation at 1.54 Å in the range of $5^o \leq 2\theta \leq 70^o$ at 40 kV. The amount of YADH protein in the supernatant was determined by Bradford method with BSA as the standard using Lab Tech UV 2100 spectrophotometer (absorption at 280 nm).

2.3.6. Assay of YADH

The activity of soluble and immobilized YADH was determined spectrophotometrically using EtOH as substrate. The standard reaction mixture in a total volume of 1 mL contained 100 g of YADH, 0.3 mM NAD^+ and 0.1 M EtOH in 100 mM Tris-HCl buffer, pH 8.0. The reaction was initiated by the addition of EtOH,

followed by incubation at 37 ^{o}C for 3 min and subsequently measured the increase in absorbance at 340 nm due to formation of NADH.[53]

2.3.7. Effect of pH

Enzyme activity of soluble and immobilized YADH was assayed in the buffers of different pH (3.0-12.0). The used buffers were glycine-HCl (pH 3.0), sodium acetate (pH 5.0), sodium phosphate (6.0, 7.0), Tris-HCl (pH 8.0, 9.0) and glycine-NaOH (pH 10.0, 12.0). Concentration of each buffer was 0.1 M. The activity at pH 8.0 was taken as a control (100 %) for the calculation of remaining percent activity.

2.3.8. Effect of temperature

The activity of soluble and immobilized YADH was measured at different temperatures (25-70 ^{o}C) in 0.1 M Tris-HCl buffer, pH 8.0 for 3 min. The enzyme activity at 45 ^{o}C was taken as a control (100 %) for the calculation of remaining percent activity for soluble and immobilized enzyme.

2.3.9. Thermal stability of YADH

In order to explore the thermal stability of free and immobilized YADH, both the preparations were incubated at 60 ^{o}C for 300 min. After each 30 min of incubation, the enzyme was quickly chilled in crushed ice for 5 min to bring down to room temperature and then the residual enzyme activity was determined as described above. The residual activities were expressed in relative to the original activity assayed without heating.

2.3.10. Determination of kinetic constants

Kinetic parameters of free and immobilized YADH were determined in the standard assay conditions using Line-weaver Burk plot. The standard reaction mixture in a total volume of 1 mL contained 100 µg of YADH, 0.3 mM NAD^{+} and varying concentration of EtOH in 100 mM Tris-HCl buffer, pH 8.0. The kinetic constants were obtained from at least triplicate measurements of the initial rates at varying concentrations of EtOH (5-500 mM).

2.3.11. Reusability assay

The activity assay of immobilized enzyme was done in triplicates in order to investigate their reusability. After each assay, immobilized enzyme was washed with 0.1 M Tris-HCl buffer, pH 8.0 by centrifugation at 4000 rpm for 20 min. The pellet obtained was stored in assay buffer at 4 ^{o}C and this process was repeated for 10 successive days. The activity determined on the first day was considered as control (100 %) for the calculation of remaining activity after repeated uses.

2.4. Conclusion

The Ni-Co nanoferrites were synthesized by adopting auto-combustion synthetic technique involving cheaper and eco-friendly reactants followed by their characterization through different techniques. The ferromagnetic nature of the nanoferrites was confirmed by M-H hysteresis loops. The interaction of YADH enzyme complex immobilized on Ni-Co nanoferrites *via* carbodiimide activation, the probable mechanism and their mean diameter of 18.84 ± 5.35 nm was confirmed by FT-IR and HR-TEM, respectively. The comparison in average diameter of Ni-Co nanoferrites with and without YADH revealed that there is no observable change occurred. Ideal operating conditions were checked for pH and thermal stabilities. The optimum pH was 8.0 and the optimum temperature was 45 ^{o}C for immobilized YADH. The enzymatic activity of the immobilized enzyme molecules was retained after immobilization.

2.5. References

1 A. Sharma, Y. Qiang, J. Antony, D. Meyer, P. Kornacki and A. Paszczynski, *IEEE Trans. Magn.*, 2007, **43**, 2418–2420.

2 S. V Sonti and A. Bose, *J. Colloid Interface Sci.*, 1995, **170**, 575–585.

3 Y. Zhang, N. Kohler and M. Zhang, *Biomaterials*, 2002, **23**, 1553–1561.

4 A. Ito, M. Shinkai, H. Honda and T. Kobayashi, *J. Biosci. Bioeng.*, 2005, **100**, 1–11.

5 V. Holzapfel, M. Lorenz, C. K. Weiss, H. Schrezenmeier, K. Landfester and V. Mailänder, *J. Phys. Condens. Matter*, 2006, **18**, S2581–S2594.

6 A. Petri-Fink, M. Chastellain, L. Juillerat-Jeanneret, A. Ferrari and H. Hofmann, *Biomaterials*, 2005, **26**, 2685–2694.

7 I. Hilger, R. Hergt and W. A. Kaiser, *IEE Proc. - Nanobiotechnology*, 2005, **152**, 33–39.

8 J. B. Sundstrom, H. Mao, R. Santoianni, F. Villinger, D. M. Little, T. T. Huynh, A. E. Mayne, E. Hao and A. A. Ansari, *J. Acquir. Immune Defic. Syndr.*, 2004, **35**, 9–21.

9 M. Koneracká, P. Kopčanský, M. Antalík, M. Timko, C. N. Ramchand, D. Lobo, R. V Mehta and R. V Upadhyay, *J. Magn. Magn. Mater.*, 1999, **201**, 427–430.

10 A. K. Johnson, A. M. Zawadzka, L. A. Deobald, R. L. Crawford and A. J. Paszczynski, *J. Nanoparticle Res.*, 2008, **10**, 1009–1025.

11 H. P. Khng, D. Cunliffe, S. Davies, N. A. Turner and E. N. Vulfson, *Biotechnol. Bioeng.*, 1998, **60**, 419–424.

12 M. A. Ahmed, *J. Magn. Magn. Mater.*, 2010, **322**, 763–766.

13 W. Hummel and M. Kula, *Eur. J. Biochem.*, 1989, **13**, 1–13.

14 J. B. Jones, *Tetrahedron*, 1986, **42**, 3351–3403.

15 A. K. Williams and J. T. Hupp, *J. Am. Chem. Soc.*, 1998, **120**, 4366–4371.

16 H. Ooshima, Y. Genko and Y. Harano, *Biotechnol. Bioeng.*, 1981, **23**, 2851–2862.

17 B. Orlich, H. Berger, M. Lade and R. Schomacker, *Biotechnol. Bioeng.*, 2000, **70**, 638–646.

18 J. Jordan, C. S. S. R. Kumar and C. Theegala, *J. Mol. Catal. B Enzym.*, 2011, **68**, 139–146.

19 U. T. Bornscheuer, *Angew. Chemie - Int. Ed.*, 2003, **42**, 3336–3337.

20 K. M. Polizzi, A. S. Bommarius, J. M. Broering and J. F. Chaparro-Riggers, *Curr. Opin. Chem. Biol.*, 2007, **11**, 220–225.

21 C. Mateo, J. M. Palomo, G. Fernandez-Lorente, J. M. Guisan and R. Fernandez-Lafuente, *Enzyme Microb. Technol.*, 2007, **40**, 1451–1463.

22 R. Fernandez-Lafuente, *Enzyme Microb. Technol.*, 2009, **45**, 405–418.

23 P. V Iyer and L. Ananthanarayan, *Process Biochem.*, 2008, **43**, 1019–1032.

24 M. H. Liao and D. H. Chen, *Biotechnol. Lett.*, 2001, **23**, 1723–1727.

25 S. H. Huang, M. H. Liao and D. H. Chen, *Biotechnol Prog*, 2003, **19**, 1095–1100.

26 A. Kondo and H. Fukuda, *J Fermen Bioeng*, 1997, **84**, 337–341.

27 C. M. Niemeyer, *Angew. Chemie Int. Ed.*, 2001, **40**, 4128–4158.

28 C. Wilhelm, F. Gazeau, J. Roger, J. N. Pons, M. F. Salis, R. Perzynski and J. C. Bacri, *Phys. Rev. E*, 2002, **65**, 031404–(1–9).

29 Y. C. Lee, C. T. Chen, Y. T. Chiu and K. C. W. Wu, *ChemCatChem*, 2013, **5**, 2153–2157.

30 D. Brady and J. Jordaan, *Biotechnol. Lett.*, 2009, **31**, 1639–1650.

31 S. L. Hirsh, M. M. M. Bilek, N. J. Nosworthy, A. Kondyurin, C. G. dos Remedios and D. R. McKenzie, *Langmuir*, 2010, **26**, 14380–14388.

32 S. H. Chiou and W. T. Wu, *Biomaterials*, 2004, **25**, 197–204.

33 R. H. Y. Chang, J. Jang and K. C. W. Wu, *Green Chem.*, 2011, **13**, 2844–2850.

34 P. J. Halling and P. Dunnill, *Enzyme Microb. Technol.*, 1980, **2**, 2–10.

35 M. Y. Arica, H. Yavuz, S. Patir and A. Denizli, *J. Mol. Catal. B Enzym.*, 2000, **11**, 127–138.

36 H. Kobayashi and T. Matsunaga, *J. Colloid Interface Sci.*, 1991, **141**, 505–511.

37 M. T. Reetz, A. Zonta, V. Vijayakrishnan and K. Schimossek, *J. Mol. Catal. A Chem.*, 1998, **134**, 251–258.

38 S. Roath, *J. Magn. Magn. Mater.*, 1993, **122**, 329–334.

39 X. D. Tong, B. Xue and Y. Sun, *Biotechnol. Prog.*, 2001, **17**, 134–139.

40 T. M. Cocker, C. J. Fee and R. A. Evans, *Biotechnol. Bioeng.*, 1997, **53**, 79–87.

41 W. Schutt, C. Gruttner, U. Hafeli, M. Zborowski, J. Teller, H. Putzar and C. Schumichen, *Hybridoma*, 1997, **16**, 109–117.

42 F. Sauzedde, A. Elaissari and C. Pichot, *Macromol. Symp.*, 2000, **151**, 617–623.

43 W. Schütt, C. Grüttner, J. Teller, F. Westphal, U. Häfeli, B. Paulke, P. Goetz and W. Finck, *Artif. Organs*, 1999, **23**, 98–103.

44 S. R. Rudge, T. L. Kurtz, C. R. Vessely, L. G. Catterall and D. L. Williamson, *Biomaterials*, 2000, **21**, 1411–1420.

45 A. R. Varlan, J. Suls, P. Jacobs and W. Sansen, *Biosens. Bioelectron.*, 1995, **10**, 15–19.

46 T. N. Krogh, T. Berg and P. Højrup, *Anal. Biochem.*, 1999, **274**, 153–162.

47 R. V. Mehta, R. V. Upadhyay, S. W. Charles and C. N. Ramchand, *Biotechnol. Tech.*, 1997, **11**, 493–496.

48 W. Schöpp and M. Grunow, *Appl. Microbiol. Biotechnol.*, 1986, **24**, 271–276.

49 V. Bille, D. Plainchamp, S. Lavielle, G. Chassaing and J. Remacle, *Eur. J. Biochem.*, 1989, **180**, 41–47.

50 F. C. Cochrane, H. H. Petach and W. Henderson, *Enzyme Microb. Technol.*, 1996, **18**, 373–378.

51 D. H. Chen and M. H. Liao, *J. Mol. Catal. B Enzym.*, 2002, **16**, 283–291.

52 P. K. Smith, R. I. Krohn, G. T. Hermanson, A. K. Mallia, F. H. Gartner, M. D. Provenzano, E. K. Fujimoto, N. M. Goeke, B. J. Olson and D. C. Klenk, *Anal. Biochem.*, 1985, **150**, 76–85.

53 R. Haque, S. Anwar, M. F. Alam and H. Younus, *J. Proteins Proteomics*, 2012, **3**, 113–118.

54 N. Kasapoglu, B. Birsöz, A. Baykal, Y. Köseoglu and M. Toprak, *Cent. Eur. J. Chem.*, 2007, **5**, 570–580.

55 K. H. Wu, T. H. Ting, C. I. Liu, C. C. Yang and J. S. Hsu, *Compos. Sci. Technol.*, 2008, **68**, 132–139.

56 S. Maensiri, C. Masingboon, B. Boonchom and S. Seraphin, *Scr. Mater.*, 2007, **56**, 797–800.

57 S. Dey, A. Roy, D. Das and J. Ghose, *J. Magn. Magn. Mater.*, 2004, **270**, 224–229.

58 R. D. Waldron, *Phys. Rev.*, 1955, **99**, 1727–1735.

59 M. Monier, D. M. Ayad, Y. Wei and A. A. Sarhan, *Int. J. Biol. Macromol.*, 2010, **46**, 324–330.

60 V. Swarnalatha, R. A. Esther and R. Dhamodharan, *J. Mol. Catal. B Enzym.*, 2013, **96**, 6–13.

61 S. Ahmad, U. Riaz, A. Kaushik and J. Alam, *J. Inorg. Organomet. Polym. Mater.*, 2009, **19**, 355–360.

62 V. L. Mathe and A. D. Sheikh, *Phys. B Condens. Matter*, 2010, **405**, 3594–3598.

63 G. Y. Li, K. L. Huang, Y. R. Jiang, D. L. Yang and P. Ding, *Int. J. Biol. Macromol.*, 2008, **42**, 405–412.

64 G. Li, Z. Zhou, Y. Li, K. Huang and M. Zhong, *J. Magn. Magn. Mater.*, 2010, **322**, 3862–3868.

****

Chapter 3

Co-precipitation synthesis and characterization of Co doped SnO_2 NPs, HSA interaction via various spectroscopic techniques and their antimicrobial and photocatalytic activities

3.1. Introduction

Semiconductor metal oxide NPs with well-defined size, shape, optical and optoelectronic properties are the centre of ardent research activities because of their favourable potential in the area of medical applications.[1–4] NPs may conquer biocompatibility and bioactive functions through coating their surfaces with DNA, peptides and proteins. Among various metal oxides, SnO_2 is a wide band gap (3.6 eV) *n*-type semiconductor with many potential applications. The large band gap and high achievable carrier concentration (up to 6×10^{20} cm^3),[5] make SnO_2 an excellent candidate for a wide range of applications such as Li-ion batteries, transparent conducting electrodes (TCEs), solar cells, gas sensors *etc*.[6–13] The success of the material in many of its technological applications depends on the crystalline nature of SnO_2 as it has uniform nano-size pore structure.[14–16] Efforts towards the development of SnO_2 nanomaterials (NMs) with high sensitivity, excellent selectivity, quick response and recovery behaviour to gases has increased over years.

SnO_2 NPs is widely used to control air pollution and to detect toxic or smelling gases at low levels in air, domestic and industrial applications,[17–19] including this, the SnO_2 NPs have been successfully doped with rare earth ions (Tb^{3+}, Eu^{3+} and Ce^{3+}), and transition metal ion (Cu^{2+}). Recently, many elements such as Zn, La, Pt and Pd, have been proved to be effective dopants in improving sensor response or reaction speed and other characteristics of SnO_2 NMs.[20–22] As dopant, Co is known to inhibit the growth of crystallites and plays an important role in optical properties including absorption and luminescence.[23–25] SnO_2 has become of ample interest in the field of photocatalysis due to their different morphologies, high photochemical stability, strong oxidizing power, low-cost and non-toxic nature.[26] Different morphologies of SnO_2 NPs have been developed, for illustration, spherical,[27] ribbons,[28] hollow,[29] flowers,[30] and belts[31] and so on. Among all the shapes and morphologies, round shape NPs with excellent crystallinity have a great importance for a photocatalytic reaction because of their higher surface area and colloidal stability in aqueous solution than the TiO_2 or CeO_2 NPs.[32,33] The photocatalysis mainly relies upon charge separation between the photogenerated electron and hole pair. A quick recombination of the photogenerated electron and hole prevents augmentation of photocatalytic activity. Many strategies has been suggested to counter this challenge, such as semiconductor combination,[34] transition metal doping,[35] and metal deposition.[36] Certainly one of these methods,

transition metal doping appears to be most promising. We introduced Co doped SnO_2 NPs from co-precipitation method. Advantages of the applied method is a simple and rapid synthesis, easy to control of particle crystalline size morphology and composition and numerous prospects to customize the particle surface and overall homogeneity. The synthesized Co doped SnO_2 NPs is grafted with Co which take advantage of a hetero-junction for excellent photocatalysis. This approach magnifies the separation of photogenerated electron and hole in Co doped SnO_2 NPs. The Co in Co-doped SnO_2 NPs can facilitate an electron efficiently from the conduction band of SnO_2 to an oxygen molecule in solution, rendering it a novel material for photocatalytic reaction. In addition to photocatalytic activity, inorganic metal oxides (MOs) such as TiO_2, ZnO, and SnO_2 doped with transition metal ions have received much attention in antimicrobial applications because such materials can achieve effective disinfection without the formation of any harmful by-products.[37–43]

Human serum albumin (HSA) is the most studied serum albumin (SA) because of their primary structure, which is well known and its tertiary structure has been determined by X-ray crystallography. It is a single-chain, non-glycosylated globular protein consisting of 585 amino acid residues and 17 disulfide bridges assist in maintaining its familiar heart-like shape. Crystallographic data show that HSA contains three homologous α-helical domains (I, II and III): I (residues 1-195), II (196-383) and III (384-585), each of which includes 10 helices that are divided into six-helix and four-helix subdomains (A and B).[44] The principal regions of ligand binding sites in HSA are located in hydrophobic cavities in subdomains IIA and IIIA, called site I and site II, respectively.[45] There are nine distinct fatty acid binding sites, four thyroxine binding sites, several metal binding sites including albumin's N-terminus, and a site centred around residue Cys34. These multiple binding sites underline the exceptional ability of HSA to act as a major depot and transport protein, capable of binding, transporting and delivering an extraordinarily diverse range of endogenous and exogenous compounds in the bloodstream to their target organs.[46–51] Although the interaction of NPs with HSA has been reported previously, but there are no studies available on interaction of Co doped SnO_2 NPs with HSA. In continuation of the previous work on NPs,[52] herein displayed a report on synthesis of undoped and Co doped SnO_2 NPs using the co-precipitation technique to study their particle size, structure, morphology, elemental composition through XRD, SEM, EDS, HR-TEM and FT-IR analysis. The prime objective was to investigate the structural changes in HSA upon interaction with Co

doped SnO_2 NPs through various spectroscopic techniques and their antimicrobial and photocatalytic properties.

3.2. Results and discussion

3.2.1. Structural Analysis

XRD patterns for $Sn_{1-x}Co_xO_2$ (x = 0.00, 0.01, 0.03, 0.05) NPs demonstrated in the **Fig. 3.1**, showed the reflection planes: (110), (101), (211), (220), (310), (112) and (321) comparably close with the reported reflection planes of Co doped SnO_2 NPs.[53]

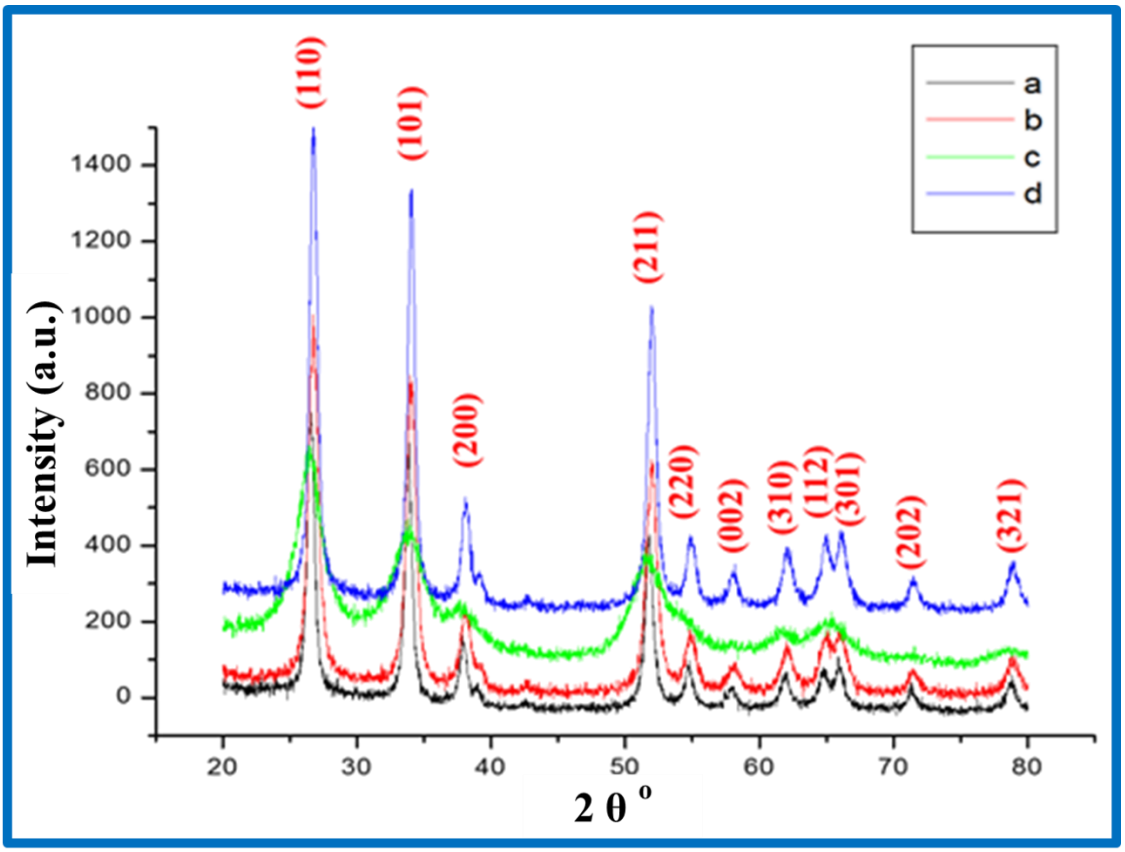

Figure 3.1. XRD patterns of $Sn_{1-x}Co_xO_2$ (x = 0.00, 0.01, 0.03, 0.05) NPs: (a) SnO_2 (b) $Sn_{0.99}Co_{0.01}O_2$ (c) $Sn_{0.97}Co_{0.03}O_2$ and (d) $Sn_{0.95}Co_{0.05}O_2$.

The d-spacing of peaks was confirmed with Joint Committee on Powder Diffraction Standards data (JCPDS card No. 77-0452) and the above mentioned reflection planes suggested a tetragonal-rutile type structures for all NPs having P*42/-mnm* spacegroup.[54] No additional phases such as the SnO_2 orthorhombic phase, metallic Co or other SnO (or) CoO based phases are observed. All the peaks in the diffraction pattern have been indexed and refinement of their lattice parameter was done by using Powder X

software. The variation in FWHM is in agreement with the crystallite size reckoned by Debye-Scherrer's formula:

$$D = \frac{0.9\lambda}{\beta COS\theta}$$

Where, λ is the wavelength of Cu Kα radiation, D is the particle size, β is the full width half maximum intensity and θ is the position of peak. The crystallite size was determined from main diffraction peak (110) and the calculation outputs are summarized in **Table 3.1**.

Table 3.1. Structural parameters of $Sn_{1-x}Co_xO_2$ (x = 0.00, 0.01, 0.03, 0.05) NPs.

Entry	$Sn_{1-x}Co_xO_2$ (x = 0.00, 0.01, 0.03,0.05) NPs	2θ	FWHM β	Crystallite size (nm)	Lattice parameter (a)
1	SnO_2	26.568	0.6727	13	4.7338
2	$Sn_{0.99}Co_{0.01}O_2$	26.751	0.8749	9	4.7354
3	$Sn_{0.97}Co_{0.03}O_2$	26.556	1.8949	4	4.7360
4	$Sn_{0.95}Co_{0.05}O_2$	26.771	0.7188	11.3	4.7368

3.2.2. Fourier transform infrared (FT-IR) spectroscopic studies

FT-IR spectra of $Sn_{1-x}Co_xO_2$ (x = 0.00, 0.01, 0.03, 0.05) NPs shows three peaks at around 671, 1628 and 3460 cm^{-1}. The signal at 671 cm^{-1} can be assigned to the stretching vibration of the O-Sn-O bond formed by oxolation reactions. A weak band at 1628 cm^{-1} is attributed to the deformation mode of O-H groups. The peak at 3460 cm^{-1} corresponds to the O-H vibrational mode.[55] The transmission band at 514 cm^{-1} is assigned to the Sn-O terminal bond of SnO_2 and that at 615 cm^{-1} is assigned to the O-Sn-O bridging bond.[56] The principal peak at 1629 cm^{-1} corresponds to the strong asymmetric stretching of C=O bond. The band observed at 2359 cm^{-1} is assigned to the existence of CO_2 molecule in air. Vibrational mode observed at 2923 cm^{-1} is due to C-H stretching vibration. The characteristic band at 3430 cm^{-1} corresponds to the stretching vibration of O-H groups. The two absorption bands are indicative of amide groups: amide I (1600-1700 cm^{-1}) and amide II (1500-1600 cm^{-1}). The amide I region is mainly due to C=O stretching, while the amide II region reflects in-plane N-H bending and C-N stretching (**Fig. 3.2**). In general, amide II is less sensitive to protein conformation changes (secondary or tertiary structure) but is useful for quantification of protein adsorption in aqueous solution due to its reduced interference from the absorbance of molecular water (≈1640 cm^{-1}) relative to amide I.[57–59] In **Fig. 3.3**, HSA

in the absence of NPs reveals the amide I peak at 1633 cm^{-1} and in the presence of undoped and Co doped SnO_2 NPs the amide I peak was shifted to 1643 and 1644 cm^{-1}, respectively. From the shift in peak position we endorsed that the conformation of HSA has been affected by the addition of undoped and Co doped SnO_2 NPs.

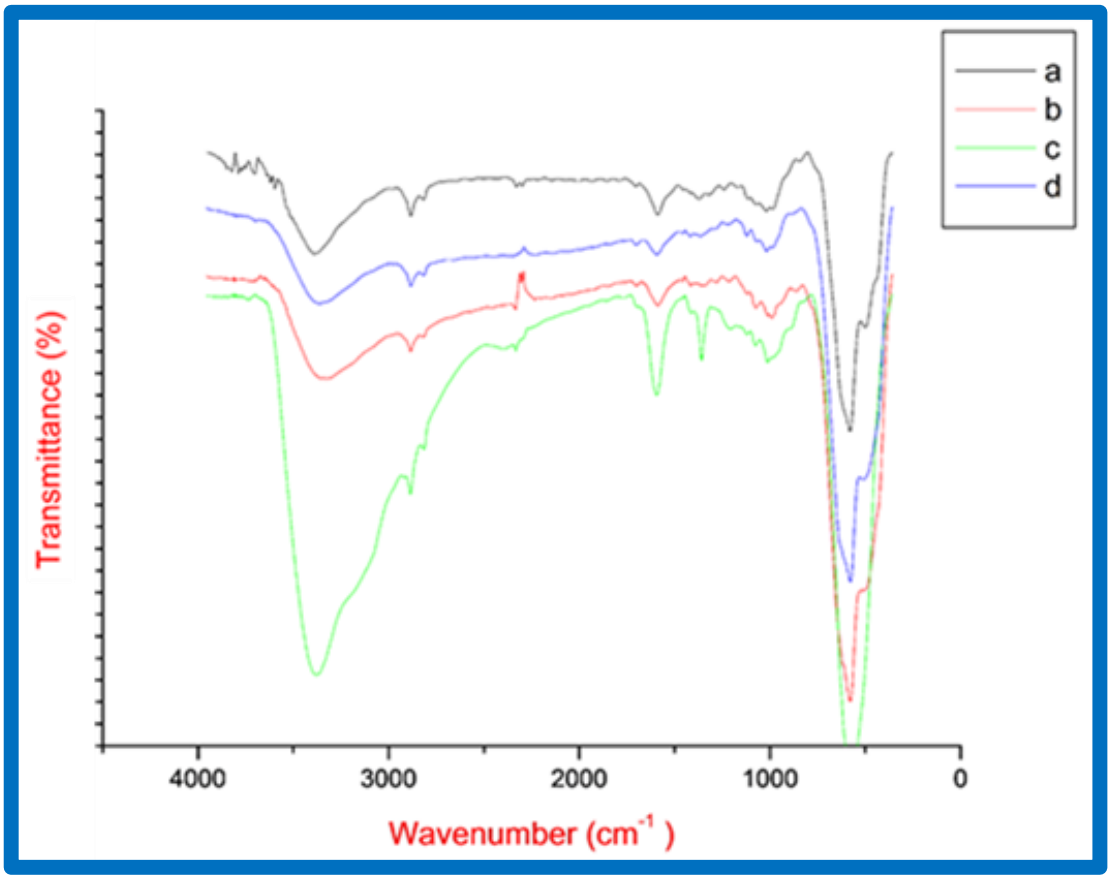

Figure 3.2. FT-IR spectra of $Sn_{1-x}Co_xO_2$ (x = 0.00, 0.01, 0.03, 0.05) NPs: (a) SnO_2 (b) $Sn_{0.99}Co_{0.01}O_2$ (c) $Sn_{0.97}Co_{0.03}O_2$ and (d) $Sn_{0.95}Co_{0.05}O_2$.

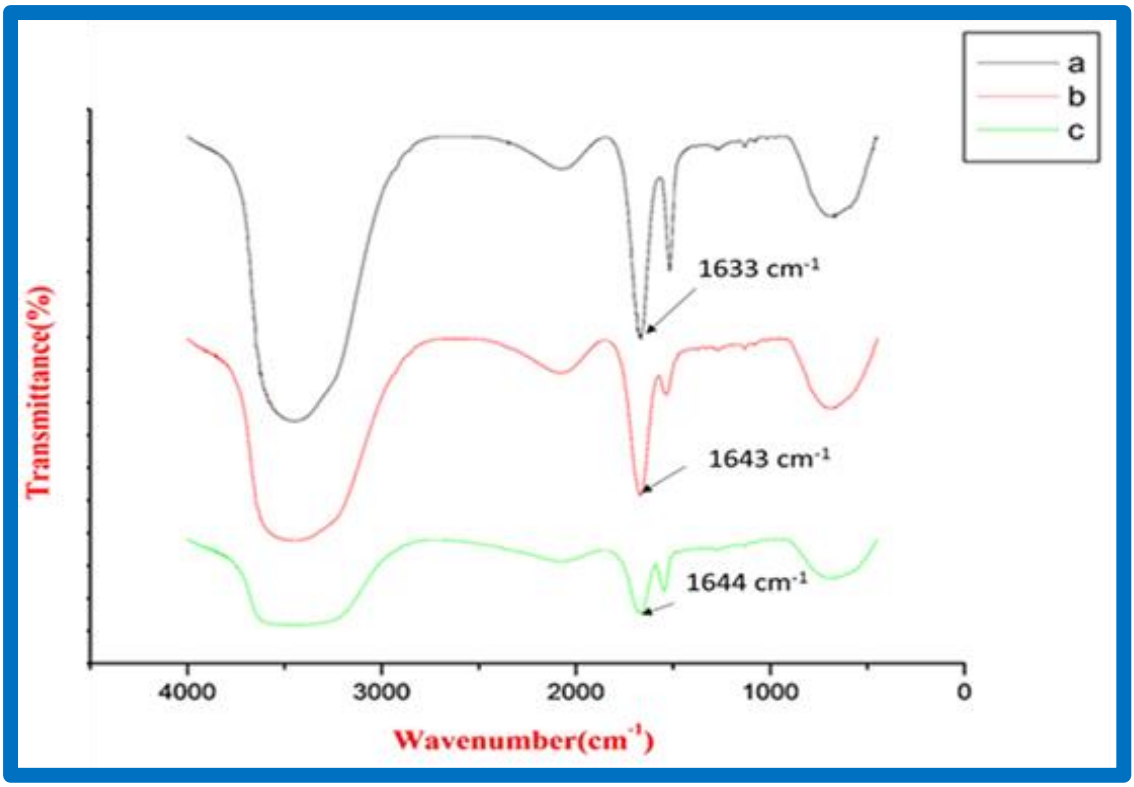

Figure 3.3. FT-IR spectra of (a) free HSA (b) HSA bound with undoped SnO_2 NPs and (c) HSA bound with Co doped SnO_2 NPs.

3.2.3. Surface morphology and compositional analysis

The SEM images and EDS spectra of the samples were taken at 3000 × magnification (**Fig. 3.4**) revealed the overall surface morphology of undoped and Co doped SnO_2 NPs. The undoped and Co doped SnO_2 NPs are not well distributed and are present in the form of aggregates. The compositions of different $Sn_{1-x}Co_xO_2$ (x = 0.00, 0.01, 0.03, 0.05) NPs have been analyzed by EDS for the various elements in terms of weight % and atomic % (**Table 3.2**) which revealed that Co, Sn and O are present approximately as per the expected stoichiometry.

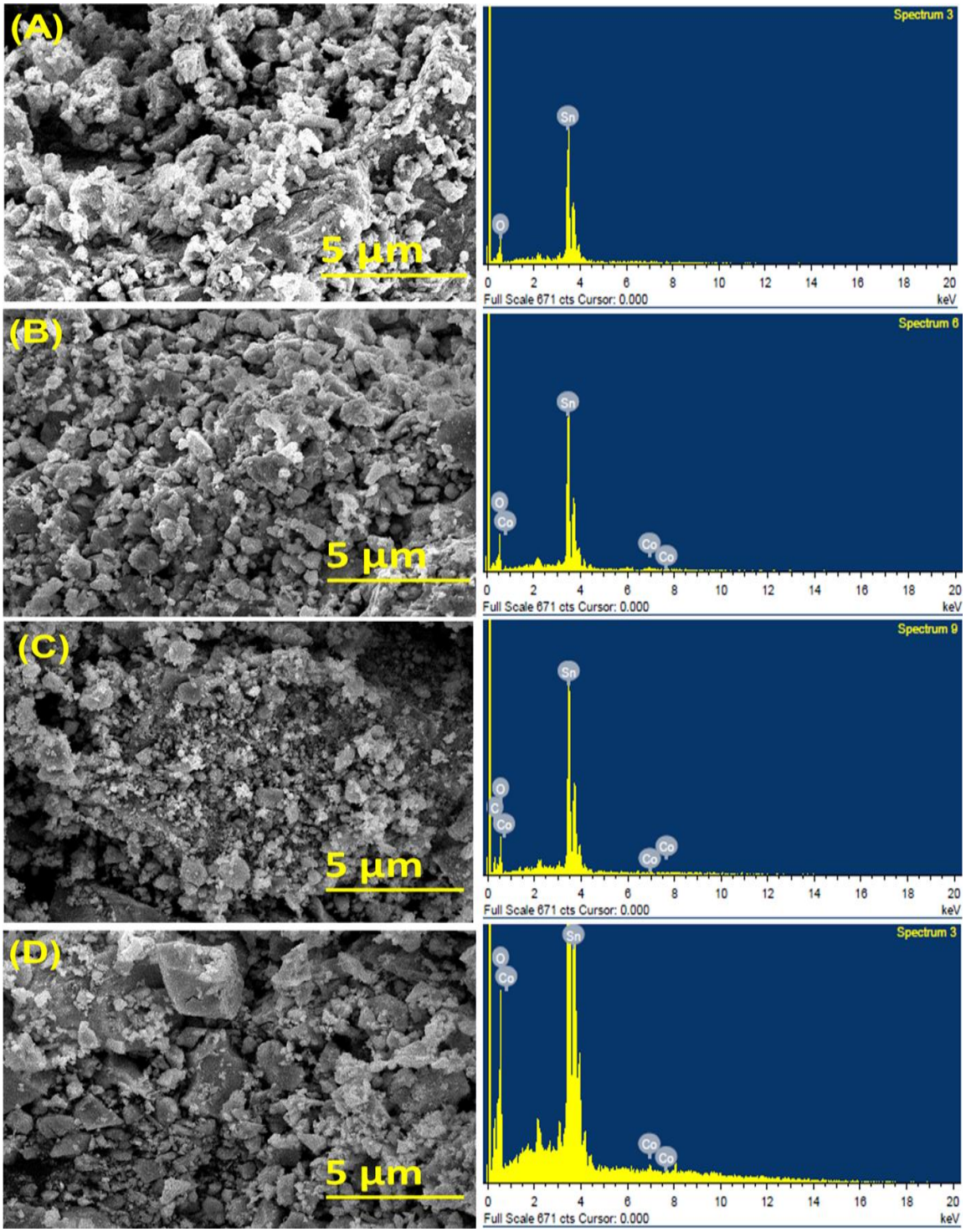

Figure 3.4. SEM images (left side) and EDS spectrum (right side) of $Sn_{1-x}Co_xO_2$ (x = 0.00, 0.01, 0.03, 0.05) NPs: (a) SnO_2 (b) $Sn_{0.99}Co_{0.01}O_2$ (c) $Sn_{0.97}Co_{0.03}O_2$ and (d) $Sn_{0.95}Co_{0.05}O_2$.

Table 3.2. EDS analysis (weight % and atomic %) of $Sn_{1-x}Co_xO_2$ (x = 0.00, 0.01, 0.03, 0.05) NPs at different compositions.

Composition	(x = 0.00)		(x = 0.01)		(x = 0.03)		(x = 0.05)	
Element	Wt. %	At. %	Wt. %	At. %	Wt. %	At. %	Wt. %	At. %
O	32.71	78.29	37.10	81.14	40.14	83.14	34.71	79.64
Sn	67.29	21.71	61.87	18.24	59.34	16.57	64.77	20.04
Co	-	-	1.03	0.61	0.52	0.29	0.52	0.32

3.2.4. Transmission electron microscopy (TEM) analysis

The HR-TEM images of Co doped SnO_2 NPs without and with HSA complex have been displayed in **Fig. 3.5 (a_1, a_2** and **b_1, b_2)**. Co doped SnO_2 NPs which are not bound seemed to be very fine and uniformly distributed varying from 30-40 nm in diameter, however, the Co doped SnO_2 NPs aggregated after binding clearly seen through the HR-TEM images. Furthermore, SAED pattern in **Fig. 3.5 (b_3)** clearly shown that crystallinity decreases of Co doped SnO_2 NPs after binding with HSA, which confirms the interaction of HSA to Co doped SnO_2 NPs.

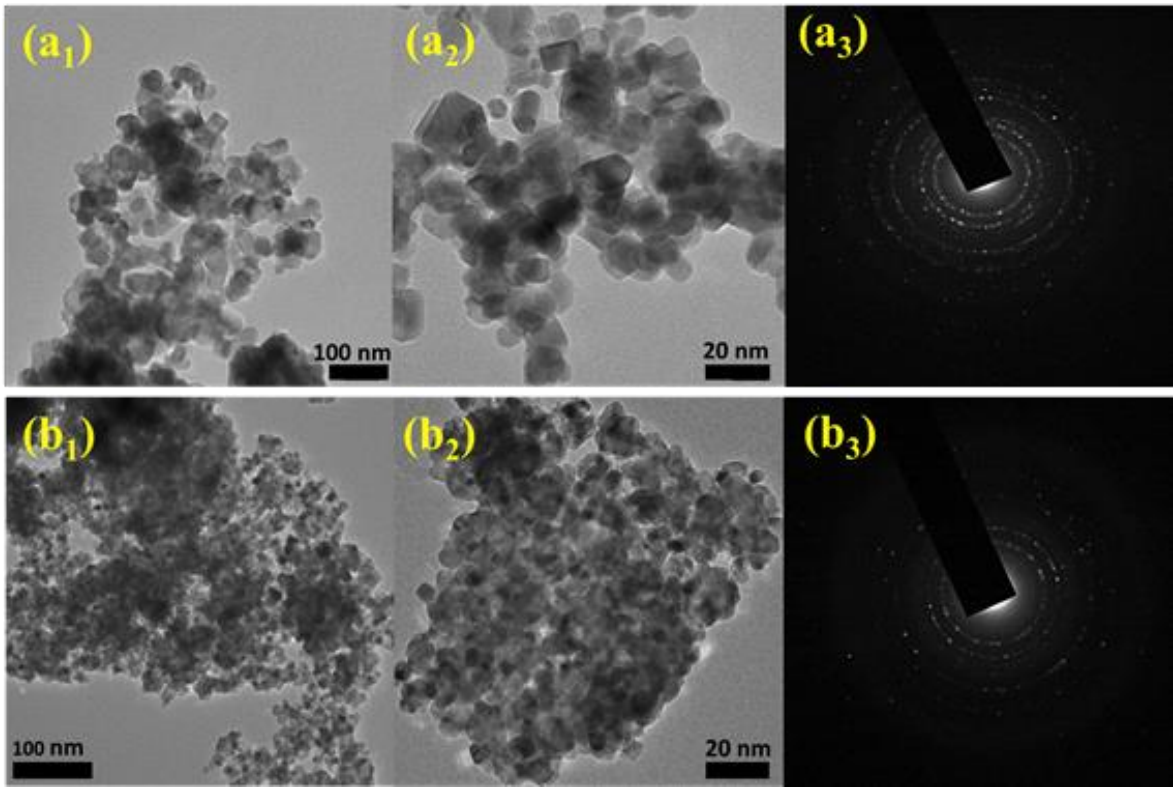

Figure 3.5. HR-TEM images of Co doped SnO_2 NPs without HSA (a_1, a_2) and with HSA (b_1, b_2) and their SAED pattern of Co doped SnO_2 NPs without HSA (a_3) and with HSA (b_3).

3.2.5. Steady state fluorescence measurements

Fluorescence spectroscopy is sensitive, rapid and easy method, employed to study protein-ligand interaction. Fluorescence spectroscopy provides information about the micro-environmental changes fluorophore of the protein and also provides the information about the binding mechanism of ligand to protein. HSA contains only one tryptophan residues (Trp 214) located in subdomain II A. **Fig. 3.6**, displays the fluorescence emission spectra of HSA in the presence of various concentrations of $Sn_{1-x}Co_xO_2$ (x = 0.00, 0.01, 0.03, 0.05) NPs.

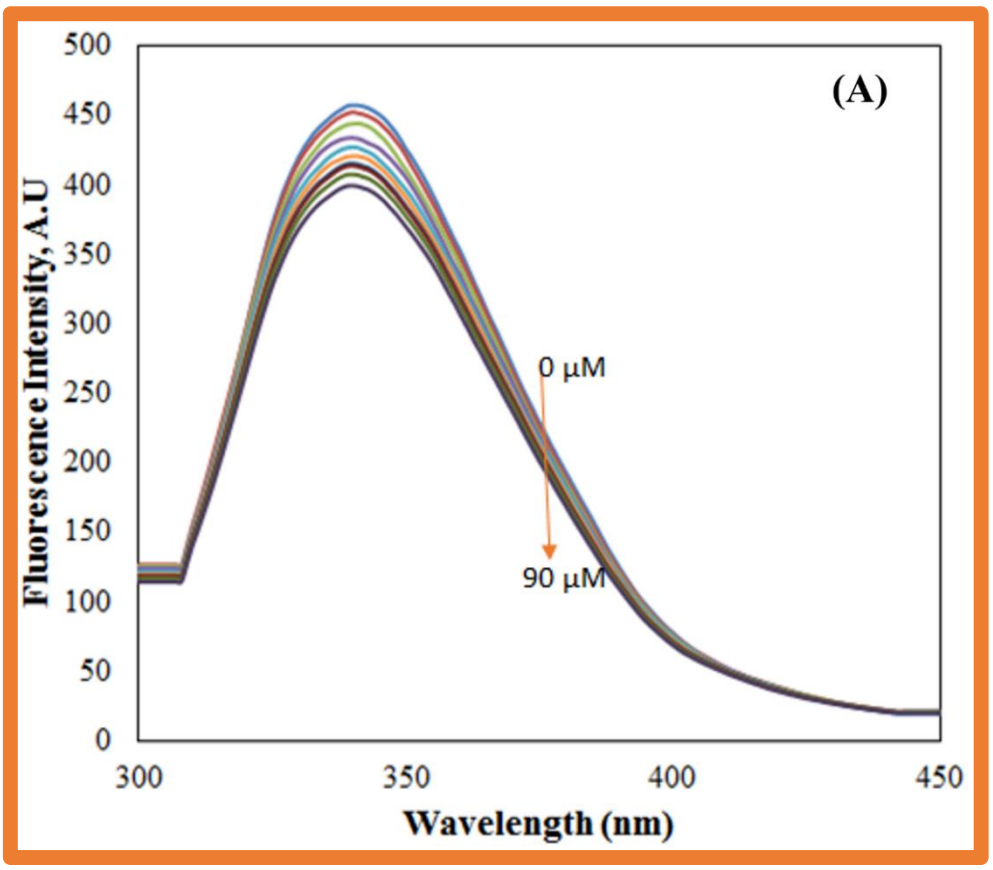

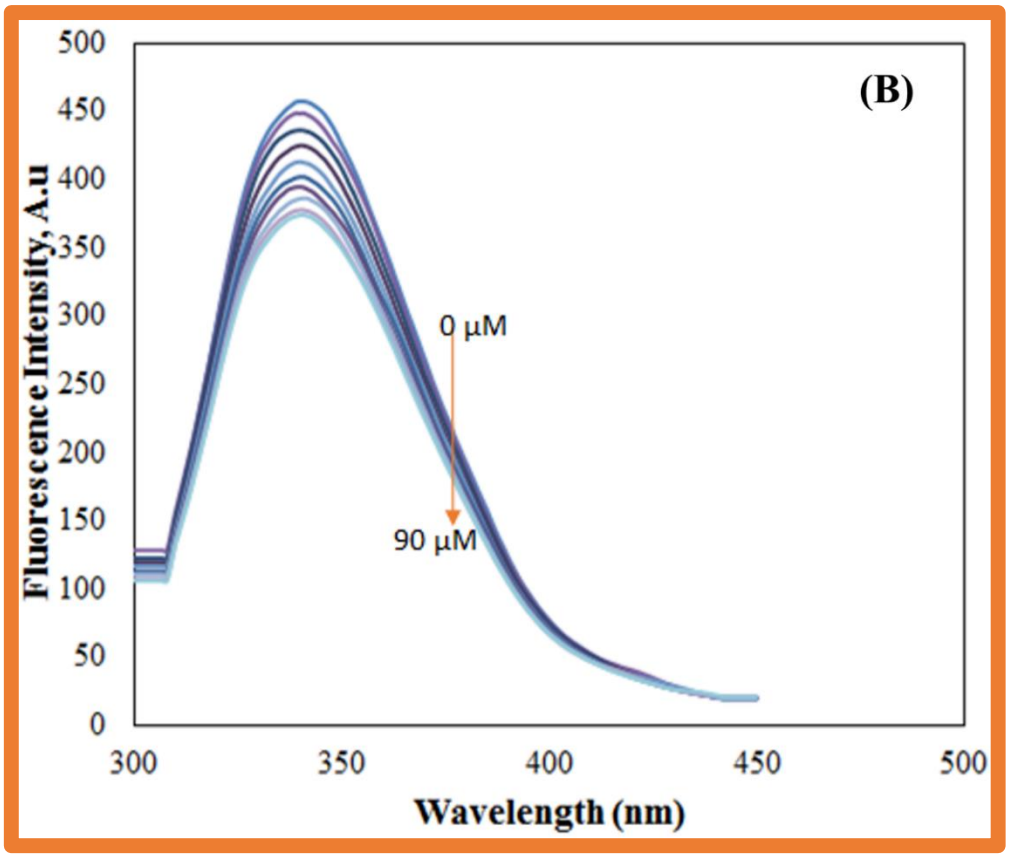

Figure 3.6. Fluorescence quenching spectra of HSA with increasing concentration of (a) undoped SnO_2 NPs and (b) Co doped SnO_2 NPs.

It is clear from **Fig. 3.6**, that there is quenching in fluorescence intensity on increasing the concentration of our formulation but more decrease in fluorescence intensity was observed in case of Co doped SnO_2 NPs.[60] The fluorescence quenching data were analyzed by Stern-Volmer equation:

$$\frac{F_0}{F} = K_{sv}[Q] + 1 = k_q\tau_0[Q] + 1 \quad (1)$$

Where, F_0 and F are the steady state fluorescence intensities in absence and presence of quencher, respectively, K_{sv} is the Stern-Volmer quenching constant and Q is the concentration of quencher, k_q is the bimolecular quenching constant and τ_0 is the life time of tryptophan in the absence of quencher. Life time of tryptophan for HSA (τ_0) is 5.6 ns.[61] Stern-Volmer plots are shown in **Fig. 3.7**. In order to establish the mechanism of quenching, k_q was calculated by using the following equation:

$$K_{sv} = k_q\tau_0 \quad (2)$$

The bimolecular quenching constant for doped and undoped NPs was calculated to be 1×10^{11} $M^{-1}s^{-1}$ which is greater than maximum collision quenching constant 2×10^{10} $M^{-1}s^{-1}$ suggests that the mechanism of quenching is static.

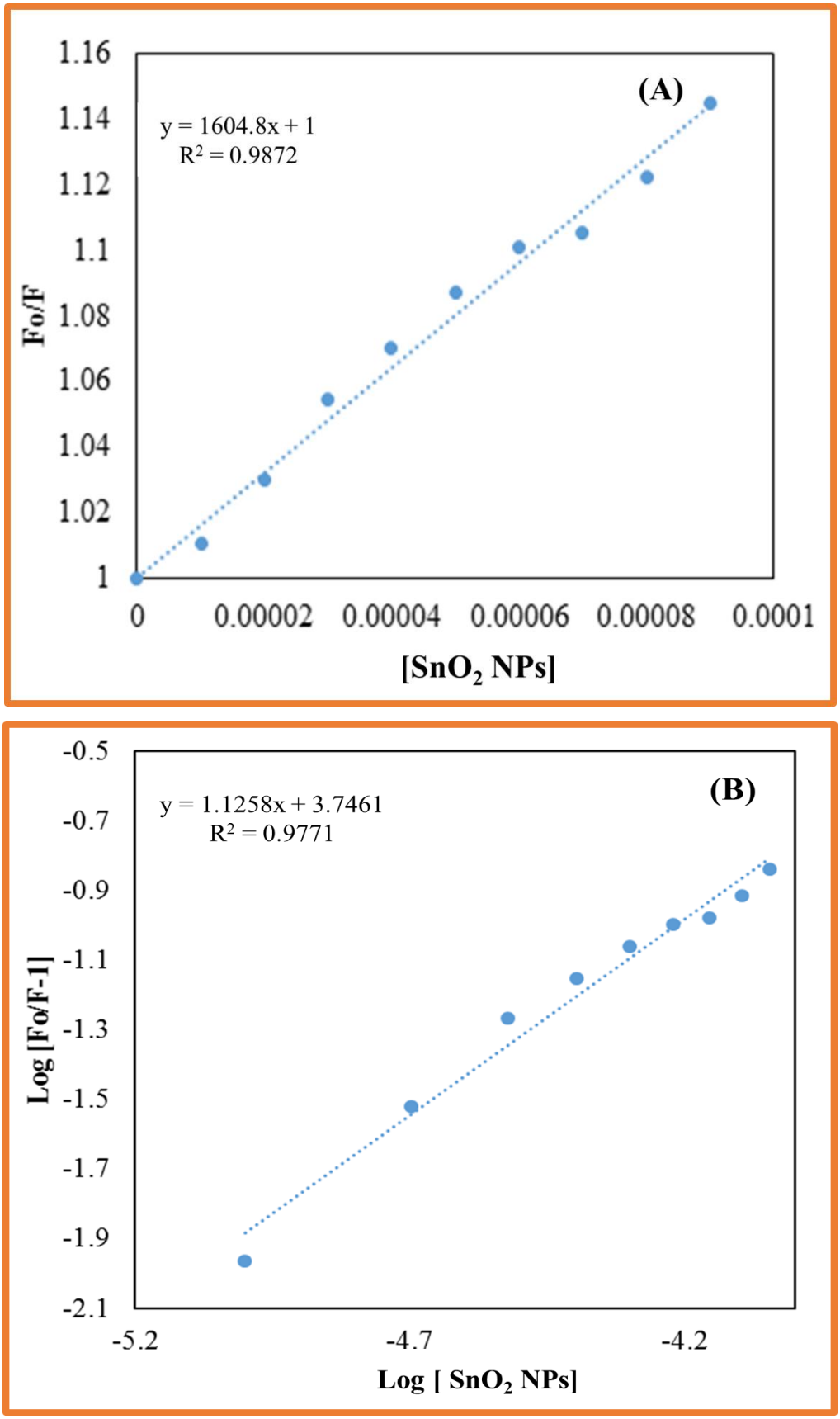

Figure 3.7. Stern-Volmer plot and modified Stern-Volmer plot of HSA with undoped SnO_2 NPs (A) and (B), respectively.

Value of binding constant and number of binding sites were obtained from the modified Stern-Volmer plot as shown in **Fig. 3.8**, by using the following equation:

$$\log\left(\frac{F_0 - F}{F}\right) = \log K_b + n\log[Q] \quad (3)$$

Where, F_0 and F are the steady state fluorescence intensities in the absence and presence of quencher, respectively, K_b is binding constant, n is the number of binding sites and Q is the concentration of quencher.

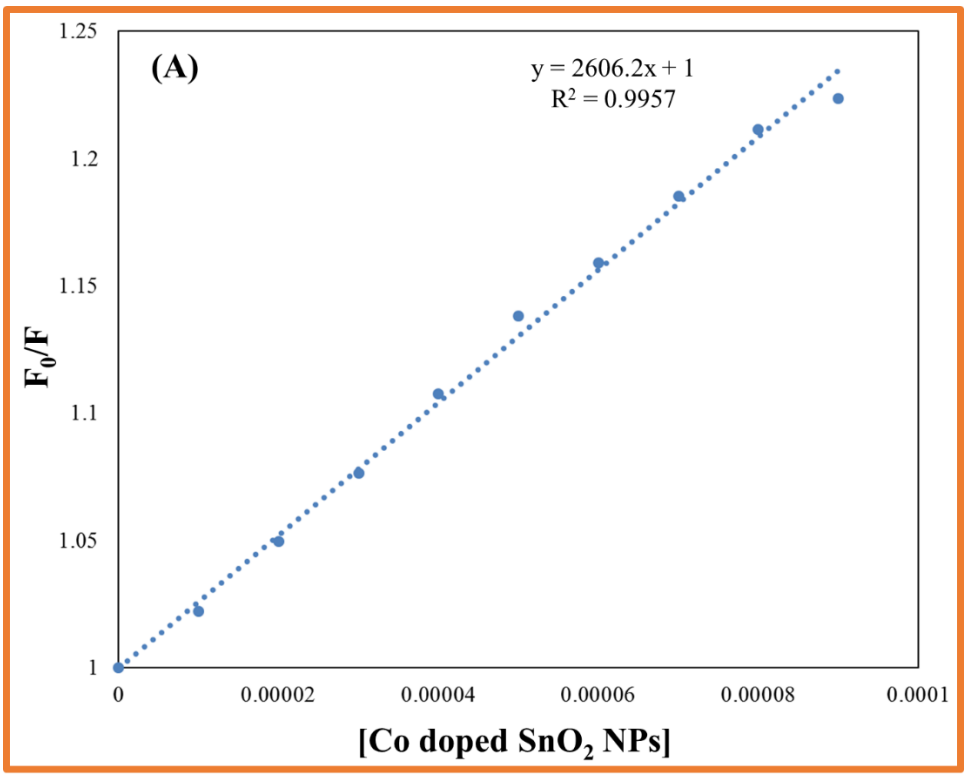

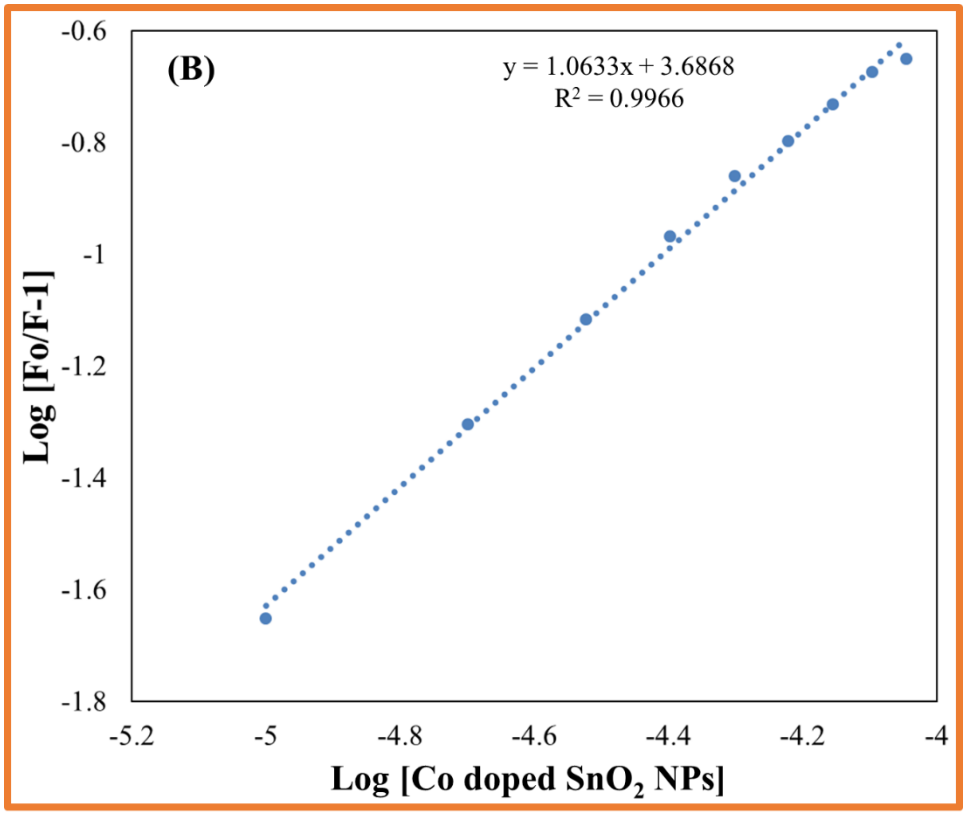

Figure 3.8. Stern-Volmer plot and modified Stern-Volmer plot of HSA with Co doped SnO_2 NPs (A) and (B), respectively.

Binding parameters are summarized in **Table 3.3**, the value of binding constant was found to be in order of 10^3 but more in case of Co doped SnO_2 NPs as compared to undoped SnO_2 NPs.

Table 3.3. Stern-Volmer quenching constants and binding parameters for HSA with undoped SnO_2 NPs and Co doped SnO_2 NPs at 298 K.

Condition	Temp. (K)	K_{sv} (M^{-1})	k_q ($M^{-1}s^{-1}$)	K_b (M^{-1})	n	ΔG^0 (kJ mol^{-1})	R^2
HSA-Co doped SnO_2 NPs	298	1.6×10^3	2.8×10^{11}	3.9×10^3	1.06	-21.10	0.98
HSA-undoped SnO_2 NPs	298	2.6×10^3	4.6×10^{11}	5.4×10^3	1.12	-21.34	0.99

3.2.6. UV-Visible spectroscopy measurements

UV absorption spectroscopy is an important tool to explore changes and complex formation in protein. UV-visible absorption spectra of HSA in absence and presence of undoped SnO_2 and Co doped SnO_2 NPs represented in **Fig. 3.9**. It is inferred from the

Fig. 3.9, that the absorption of HSA increases upon increasing the concentration of both doped and undoped SnO_2 NPs. But more increase in absorption was observed in case of Co doped SnO_2 NPs. Furthermore, it is clear that maximum peak position shifted towards shorter wavelength which indicates the complex formation between NPs and protein.

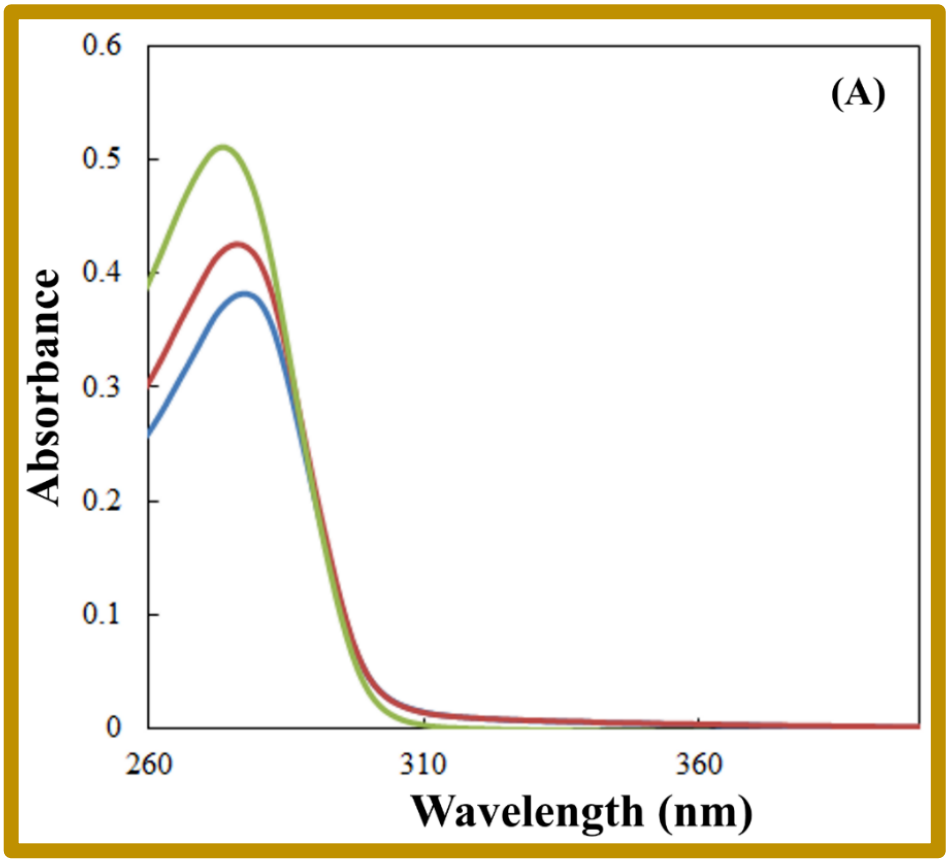

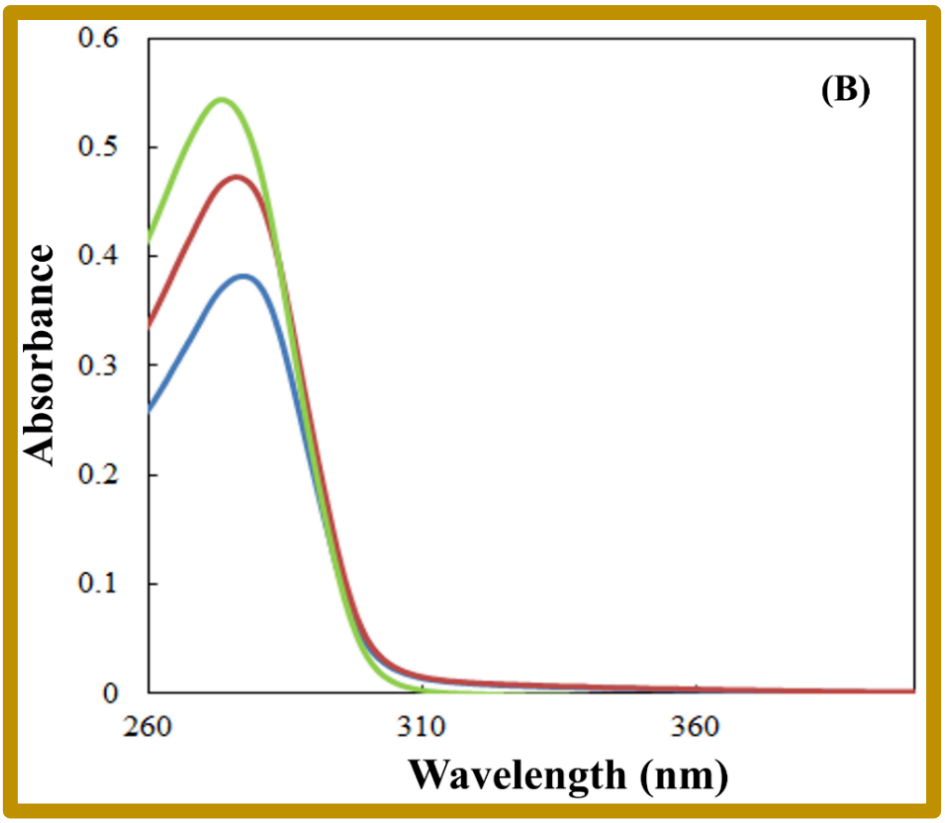

Figure 3.9. UV-Visible absorption spectra of HSA in absence and presence of (A) undoped SnO_2 NPs and (B) Co doped SnO_2 NPs.

3.2.7. Far UV-Circular dichroism (UV-CD) measurements: to monitor secondary structural changes in HSA

CD spectroscopy is very important tool in structural biology and protein chemistry.[62–64] To get further insight on the behaviour of both undoped SnO_2 NPs and Co doped SnO_2 NPs on the secondary structure of HSA, far UV-CD measurements were carried out. **Fig. 3.10**, shows that CD spectra of native HSA possess two negative bands at 208 nm and 222 nm, a characteristic feature of α-helical class of protein.[65] Both bands are contributed by n-π^* transfer of peptide bond of α-helix. On increasing the concentration of NPs, there was an increase in the value of both negative bands 208 nm and 222 nm without any shift which advocates that the structure of HSA remains α-helical. The increase in band intensity predicts that undoped SnO_2 NPs induced α-helical content in the HSA but more induction was in case of Co doped SnO_2 NPs (the α-helical content increases from 55.60 % to 56.20 % and 56.92 %, respectively, in case of undoped SnO_2 and Co doped SnO_2 NPs as obtained from K2D3 software).[66]

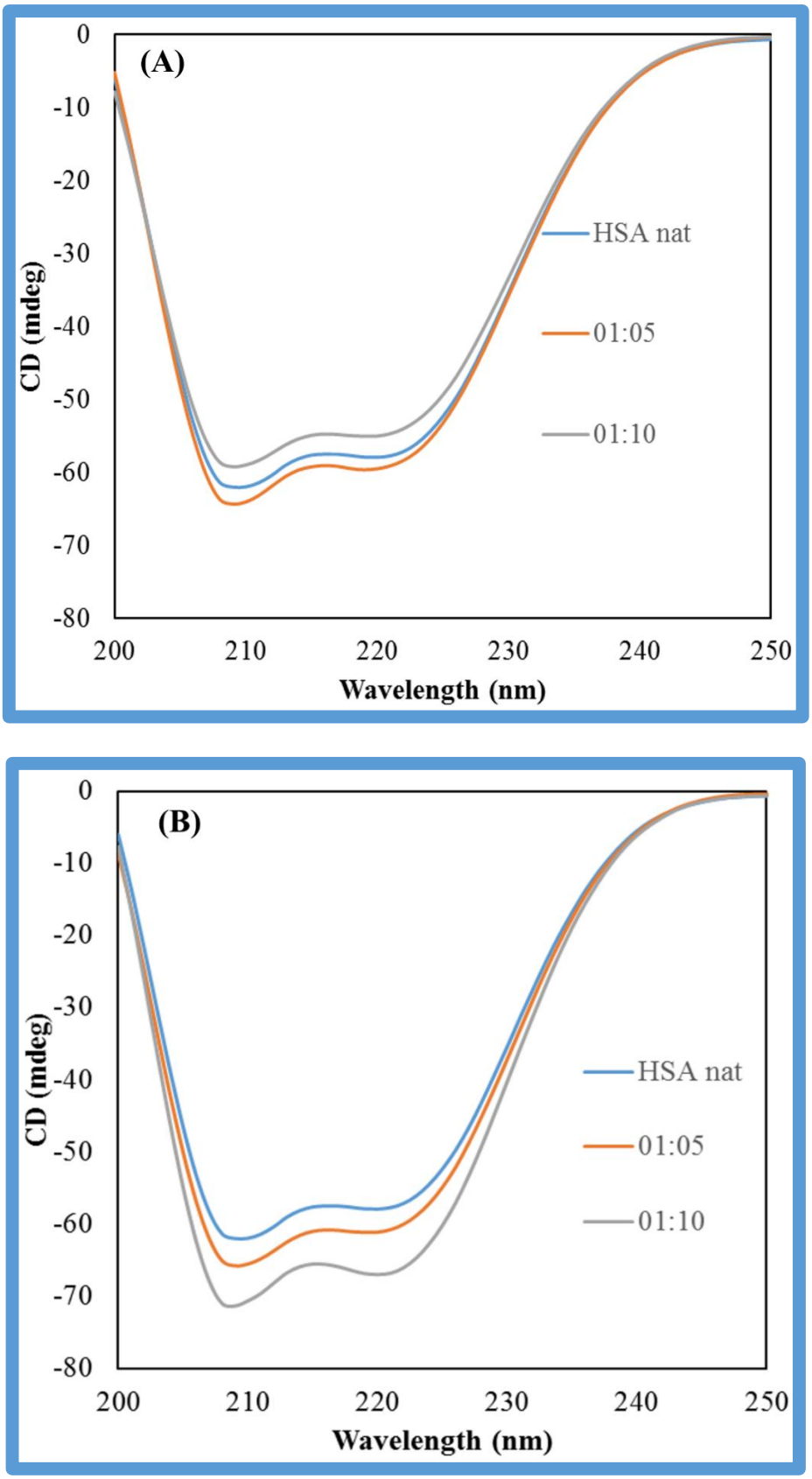

Figure 3.10. Far UV-CD spectra of (A) HSA bound with undoped SnO_2 NPs and (B) HSA bound with Co doped SnO_2 NPs.

3.2.8. Photocatalytic studies

Due to rapid development of industrialization, population growth and drought problems are the primary issues of the rising world, which upgraded expanded the interest of clean water. The recycling of waste water offers a potential solution. On the other hand, the vicinity of lethal organic components, for example, organic dyes, phenols and pesticides, in wastewater and the related ecological perils have as of late raised various concerns.[67–71] In this experiment, we have shown the photocatalytic activities of $Sn_{1-x}Co_xO_2$ (x = 0.00, 0.01, 0.03, 0.05) NPs on an organic pollutant model dye methylene blue (MB) under UV light. The UV spectral changes of MB dye at different irradiation times with undoped SnO_2 NPs and Co doped SnO_2 NPs. Time dependent UV-visible spectra of an aqueous MB solution in the vicinity of Co doped SnO_2 nanophotocatalyst under UV light irradiation at a regular time interval are shown in **Fig. 3.11**.

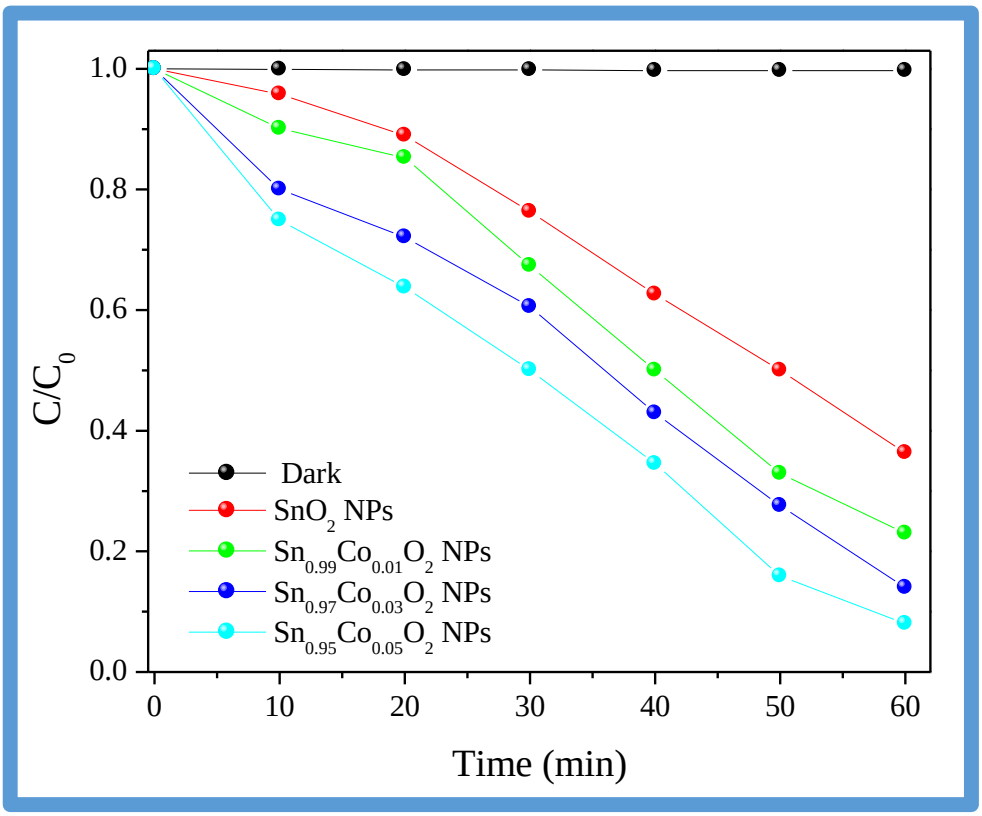

Figure 3.11. Photocatalytic degradation of MB dye under the irradiation of UV light over undoped SnO_2 NPs, Co doped SnO_2 NPs and without any catalysts.

Fig. 3.11, shows a gradual decrease in the intensity without the appearance of new absorption peaks, so the resultant intermediates formed during degradation did not absorb at analytical wavelength (upto 200-800 nm). $Sn_{0.95}Co_{0.05}O_2$ NPs have shown much higher photocatalytic activity than $Sn_{1-x}Co_xO_2$ (x = 0.00, 0.01, 0.03) NPs under

the UV light illumination, it shows homogeneity doping of Co. It is clearly revealed from **Fig. 3.12**, that $Sn_{0.95}Co_{0.05}O_2$ NPs exposed highest photocatalytic activity among these samples. Furthermore, the obtained data confirmed that MB dye is resistant to self-photocatalysis and for the same experiment with samples in the dark condition, a very little decrement in concentration of dye was shown due to the adsorption of dye on the catalyst (**Fig. 3.13**).

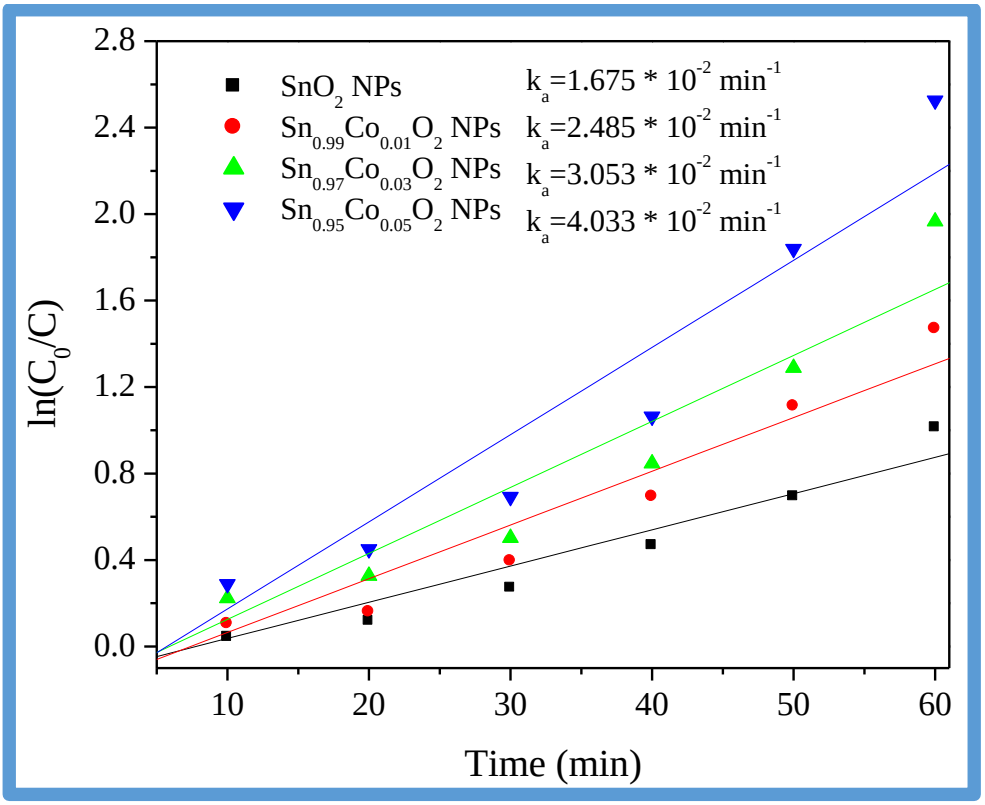

Figure 3.12. Plot of ln(C_0/C) as a function of UV irradiation time for photocatalysis of MB dye containing Co doped SnO_2 NPs and undoped SnO_2 NPs.

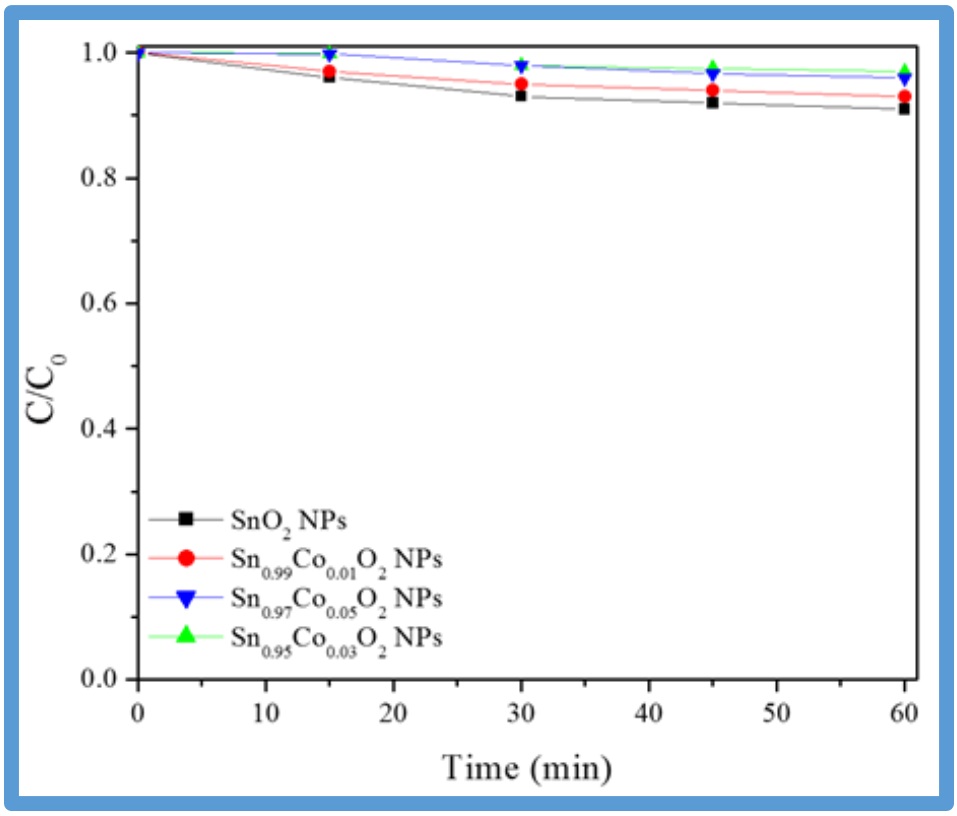

Fig. 3.13. Photocatalytic degradation of MB dye in the presence of undoped SnO_2 NPs and Co doped SnO_2 NPs in the dark condition.

Specifically, $Sn_{0.95}Co_{0.05}O_2$ NPs have shown highest photocatalytic degradation of MB dye under UV irradiation within 60 min *i.e.* ~92 % (**Fig. 3.14**). Whereas the lowest photocatalytic degradation of the parental SnO_2 NPs can be clearly seen through the **Fig. 3.14,** under UV light irradiation in 60 min.

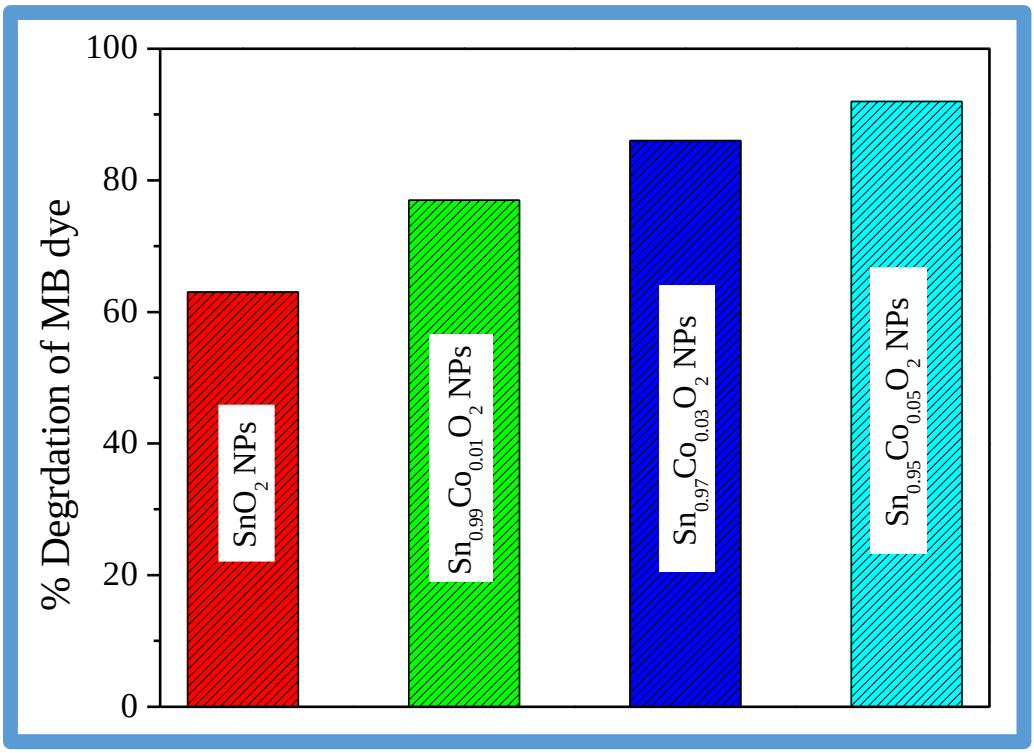

Figure 3.14. A comparison of % photodegradation of MB dyes in aqueous solution at different concentration of Co doping in SnO_2 NPs matrix.

Our study corroborates with the earlier reports of the experimental photocatalyst,[72] the photocatalytic degradation of MB dye can be explained on the basis of Langmuir-Hinshelwood[69] model *i.e.* pseudo first order where initial concentration C_0 is very small almost negligible $\ln(C_0/C) = kt$, where k is first order rate constant. As seen in **Fig. 3.12**, $Sn_{0.95}Co_{0.05}O_2$ NPs has shown highest rate constant (ca. 0.04033 min^{-1}) its 2.4 times higher than undoped SnO_2 NPs under UV light irradiation. When the paralleled all samples concentrations *i.e.* $Sn_{1-x}Co_xO_2$ (x = 0.00, 0.01, 0.03, 0.05) NPs find the photocatalytic and kinetic rate constant are of following order: $Sn_{0.95}Co_{0.05}O_2$ NPs > $Sn_{0.97}Co_{0.03}O_2$ NPs > $Sn_{0.99}Co_{.01}O_2$ NPs > SnO_2 NPs. At undoped SnO_2 NPs and lowest doping content of Co within SnO_2 NPs have shown lowest photocatalyst activity under UV light irradiation due to the less trapping site availability. As the doping content of Co gradually increases within SnO_2 NPs, the resultant formation of trapping site, efficient trapping and lower recombination rate increases the interfacial charge transfer.[67,71] The effects of photocatalyst (SnO_2 NPs and Co doped SnO_2 NPs) on the mineralization of MB dye were examined through the TOC (total organic carbon) analyzer. It has been pointed out the concentration of TOC and MB dye reduced in the long run with time, recommending the mineralization of MB dye as a consequence of

a decomposition of the aromatic intermediates. The TOC treatment efficiencies that are highest for $Sn_{0.95}Co_{0.05}O_2$ NPs and lowest for pure SnO_2 NP associated with MB solution, correspondingly, leaving some carbon that is non-mineralized (**Fig. 3.15**).

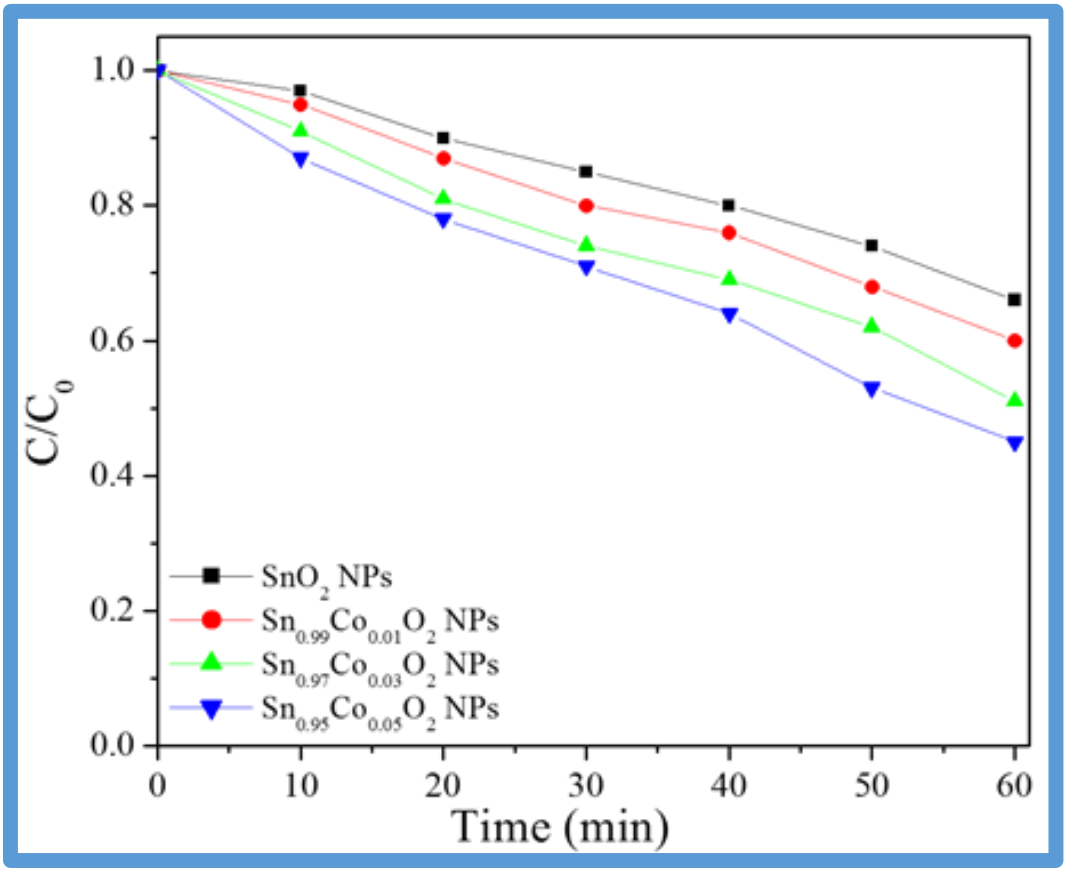

Fig. 3.15. TOC of MB dye over undoped SnO_2 NPs and Co doped SnO_2 NPs.

3.2.9. Antimicrobial activity of Co doped SnO_2 NPs

Researchers are increasingly turning their attention to nanomaterial and considering for new leads to develop better nano ranged antibacterial drugs against *Bacillus Cereus* (MC 2434).[73] In this study, we assessed the antibacterial activity of the $Sn_{1-x}Co_xO_2$ (x = 0.00, 0.01, 0.03, 0.05) NPs were investigated morphometric and qualitatively by the disk diffusion assay.[74] All the samples of Co doped SnO_2 NPs has shown the effective bacterial retardant behaviour except undoped SnO_2 NPs. Whereas $Sn_{0.95}Co_{0.05}O_2$ NPs has shown excellent antibacterial activity clearly visible in the **Fig. 3.16**.

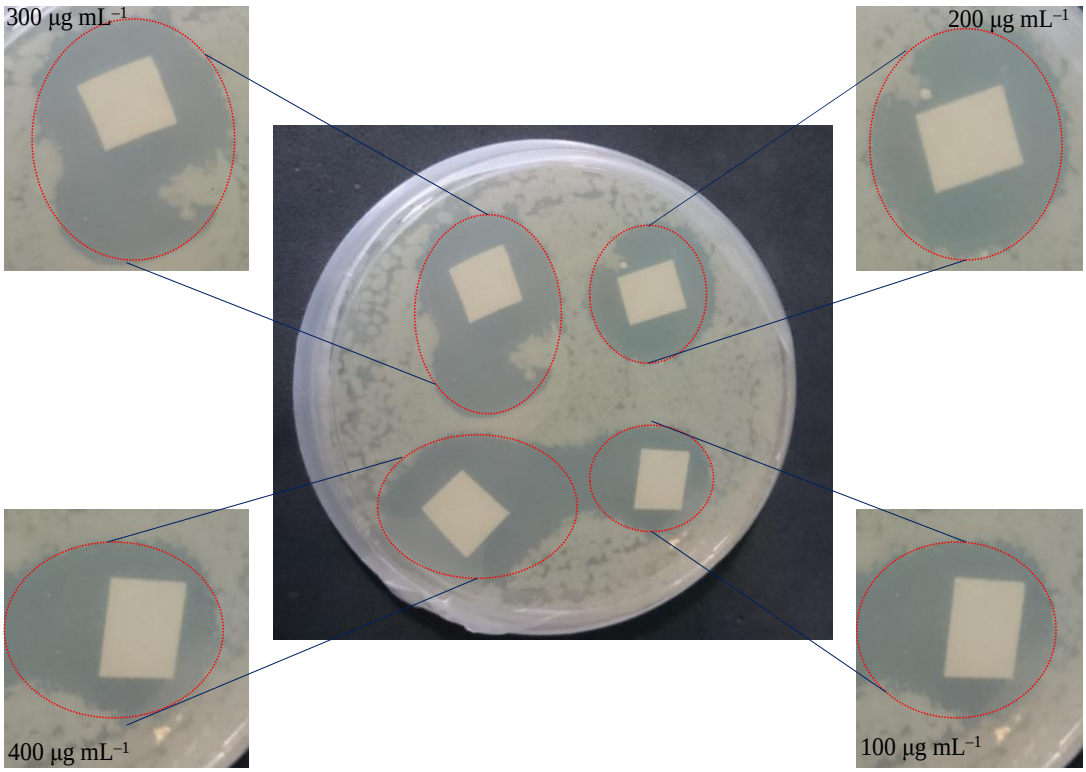

Figure 3.16. Zone of inhibition formed by $Sn_{0.95}Co_{0.05}O_2$ NPs at 100, 200, 300 and 400 µg mL^{-1} in disc diffusion test.

The interaction between modified surfaces of Co doped SnO_2 NPs and bacteria due to adsorption-desorption chemical-physical abilities towards the bacteria, main cause in different antibacterial activities.[75] The pristine SnO_2 NPs has shown least antibacterial activity might be due to the low concentration of SnO_2 NPs and difficult to diffuse into agar gel plate. However, as the highest doping concentration of Co into SnO_2 NPs, zones of inhibition are visible. As the doping concentration of Co gradually increases into SnO_2 NPs, zone of inhibition increases, so the antibacterial activity as a function of Co doping, shown in **Fig. 3.17**.

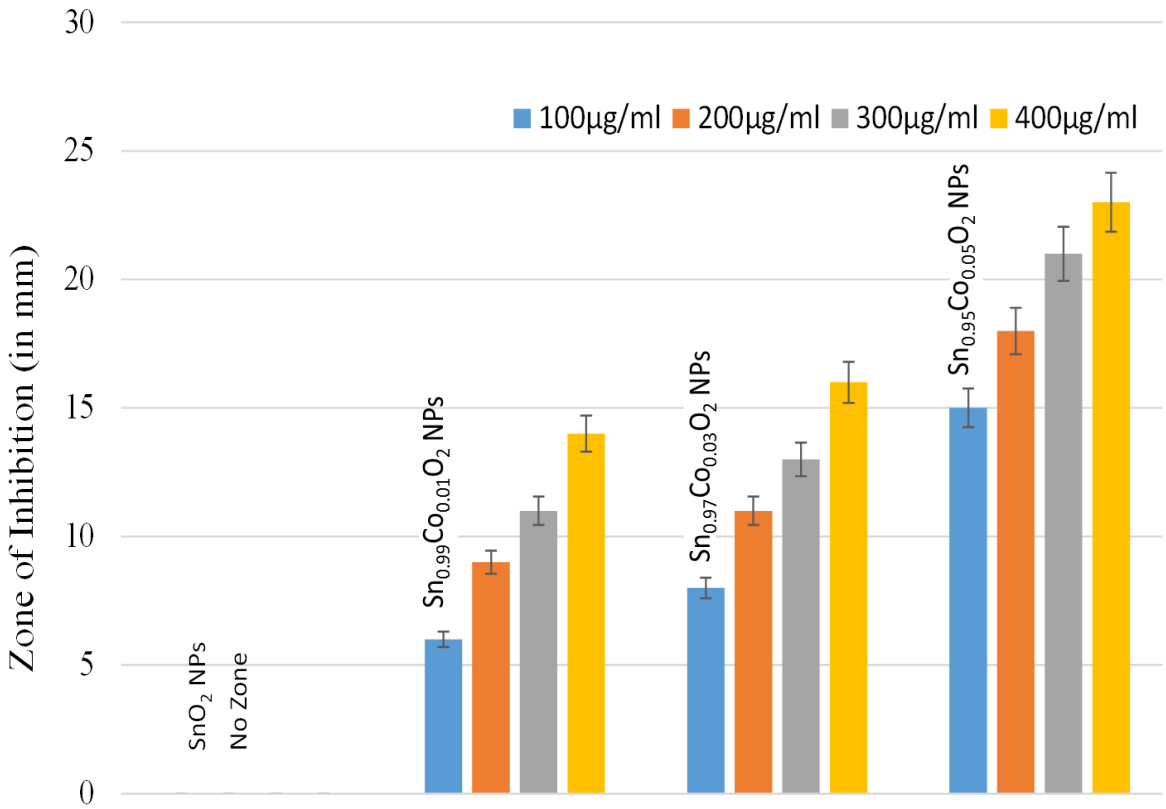

Figure 3.17. Comparative analysis of the antibacterial activity of undoped SnO_2 NPs and Co doped SnO_2 NPs at different concentration against *Bacillus Cereus* bacteria.

While the root cause of such differential activity is still to be completely explained, the plausible mechanisms could be involved in the interaction between Co doped SnO_2 NPs and bacterial species *Bacillus Cereus* (MC 2434): accumulation of NPs on the surface of bacteria due to adsorption-desorption chemical-physical or either in the cytoplasmic lipid membrane or cell membrane disruption due to inhibition of NPs and leading to cell death.[72,76] It is assumed that the prepared Co doped SnO_2 NPs penetrate into the cell wall of bacteria and due to surface reaction of NP on the cell wall surface produced reactive oxygen species (ROS) such as hydrogen peroxide (H_2O_2), superoxide anion $O_2^{\cdot -}$, hydroxyl radicals (OH_3), and organic hydro peroxides (OHPs), which leads to the cell damage due to the oxidative stress on the cell wall (**Fig. 3.18**).[75,77,78]

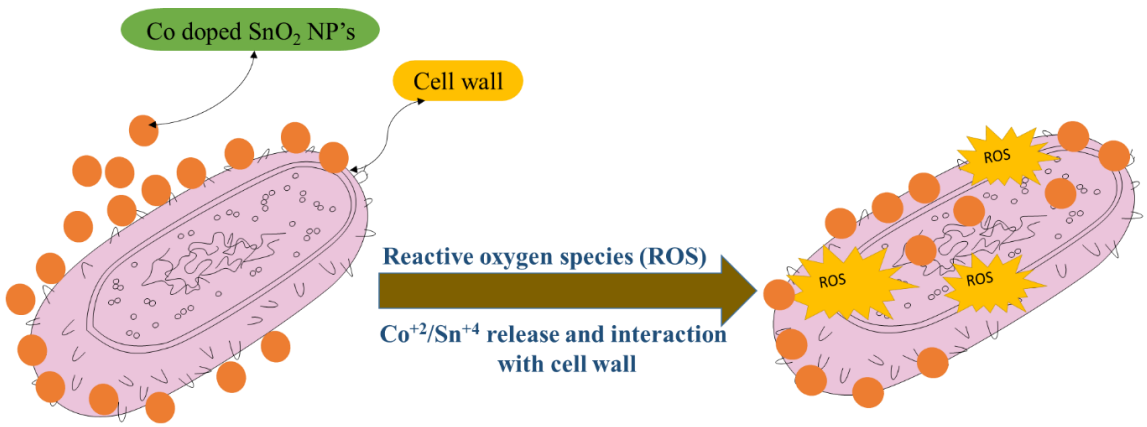

Figure 3.18. Schematic diagram of the mechanistic principles of the antibacterial action indicating ROS generation induced by Co doped SnO_2 NPs.

Furthermore, DNA inhibition by its replication due to high affinity of the NPs for phosphorus and nitrogen as well as binding with protein that inhibit cellular metabolism. The experimental observation of our study verify the prior discoveries of the antibacterial system of SnO_2 based NPs, whereas several researchers have generally involved ROS and cell membrane disruption.[74,78] By the by, the elaborate mode of action of Co doped SnO_2 NPs on pathogens is presumptively additional nuanced than heretofore elucidated, partaking multiple pathways that together end in necrobiosis.[79] Take along the nonspecific method of activity of SnO_2 based NPs against morbific microorganism and also the current methodology of chemically synthesized Co doped SnO_2 NPs gives a reasonable and clean route for the advancement of antimicrobial specialists.

3.3. Experimental

3.3.1. Chemicals

Tin chloride dihydrate ($SnCl_2{\cdot}2H_2O$), cobalt chloride dihydrate ($CoCl_2{\cdot}2H_2O$), ammonium hydroxide (NH_4OH), sodium chloride (NaCl), potassium chloride (KCl), sodium phosphate (Na_2HPO_4), potassium phosphate (KH_2PO_4) and methylene blue (MB) dye were purchased from Sigma-Aldrich (St. Louis, MO). Human serum albumin (A1887) was purchased from Sigma Aldrich, India. All chemicals were of analytical grade.

3.3.2. Synthesis of Co doped SnO_2 NPs

$Sn_{1-x}Co_xO_2$ (x = 0.00, 0.01, 0.03, 0.05) NPs were synthesized by co-precipitation technique. $SnCl_2{\cdot}2H_2O$ and $CoCl_2{\cdot}2H_2O$ were used as Sn and Co precursors, respectively. Primarily, $SnCl_2{\cdot}2H_2O$ was mixed in deionized water to make 0.1 M solution of Sn hydroxyl and proper amount of $CoCl_2{\cdot}6H_2O$ (0, 1, 3 and 5 wt %) was supplemented to the above solution. The solution was stirred for 20 min and a viscous sol was formed. Consequently, NH_4OH solution was added drop wise under vigorous stirring until the pH of the solution reached at 8.0. The dropping rate must be well regulated to maintain chemical homogeneity of the compound. The salts were then precipitated at 80 °C and kept at this temperature for several hours (h). The precipitate was filtered, thoroughly washed, and dried at 40 °C.

3.3.3. Interaction of Co doped SnO_2 NPs with HSA

HSA (100 μM) stock solution was prepared in 20 mM phosphate buffer (pH 7.4). Protein concentration was determined spectrophotometrically using $E_{1cm}^{\%}$ of 5.30 at 280 nm by using Perkin-Elmer Lambda double beam UV-visible spectrophotometer.[80,81] Nanoparticle solution (1 mM) was prepared in 20 mM phosphate buffer (pH 7.4) and diluted to various concentrations in the same buffer. All experiments were carried out in 20 mM phosphate buffer (pH 7.4) at 298 K.

3.3.4. pH determination

pH measurements were carried out on Mettler Toledo pH meter (Seven Easy S20-K) using Expert “Pro3 in 1” type electrode. The least count of the pH meter was 0.01 pH unit.

3.3.5. Photocatalytic measurements

The photocatalytic activity of $Sn_{1-x}Co_xO_2$ (x = 0.00, 0.01, 0.03, 0.05) NPs was measured against MB dye under UV light irradiation.[82] In the photocatalytic photodegradation experiment, 30 μg mL^{-1} of Co doped SnO_2 nanocatalyst was added to 100 mL dye solution (25 μg mL^{-1}). Before irradiation, the suspensions containing MB dye and Co doped SnO_2 NPs were magnetically stirred in the dark for 60 min to ensure the establishment of an adsorption/desorption equilibrium. The photocatalytic experiment was carried out at ambient condition in a tube-shaped glass vessel equipped with a

magnetic stirrer under a UV light installed horizontally 30 cm above the colloid surface. The glass vessel was illuminated by two 24 W UV lamp. The entire arrangement was put in a box covered with aluminium (Al) foil to prevent the passing of other lights inside the box. The suspensions at a fixed time interval (up to 60 min) 5 mL aliquots were periodically withdrawn and centrifuged to separate the nanocatalyst (SnO_2 and Co doped SnO_2) for analysis at a given irradiation time. The filtrate was analyzed by recording variations in the maximum absorption band (A668 nm) using a UV-vis spectrophotometer (Perkin Elmer Life and Analytical Sciences, CT, USA) in the wavelength range of $A_{200-800}$ nm. The photodegradation of the MB dye *via* photocatalytic activity of Co doped SnO_2 NPs was calculated according to the following equation:

$$\text{Photodegradation (\%)} = \frac{C_0 - C}{C_0}$$

Where, C_0 is the initial concentration of MB dye before photodegradation and C is the absorbance after different time intervals.

The total organic carbon (TOC) is measured through Shimadzu TOC-VCPN device at regular time interval subsequently after the degradation of dye in the presence of photocatalyst under UV illumination.

3.3.6. Antibacterial activity

The antibacterial activity of $Sn_{1-x}Co_xO_2$ (x = 0.00, 0.01, 0.03, 0.05) NPs was determined using agar-well diffusion method and analyzed against gram-positive bacteria (*Bacillus Cereus* MC 2434). Approximately 10^6 CFU mL^{-1} was inoculated on Luria-Bertani (LB) agar plates. Filter papers with a diameter of 1.5 cm sucked with 100, 200, 300 and 400 μg mL^{-1} of $Sn_{1-x}Co_xO_2$ (x = 0.00, 0.01, 0.03, 0.05) NPs were placed on the surface of seeded agar plate, respectively. After 24 h of incubation at 37 °C, the diameters of the inhibition zones were measured and optical images of the plates were taken.

3.3.7. Characterization

The size, structure and optical properties of the resultant NPs with and without HSA were characterized by FT-IR spectra which were recorded using Perkin Elmer FT-IR Spectrometer spectrum Two and values are given in cm^{-1}. Surface morphology and the particle size were obtained by recording SEM and HR-TEM micrographs by LEO 435-

VF and JEOL TEM (JEM 2100F) instruments, respectively. XRD data were recorded by PHILIPS PW1710 diffractometer with Cu Kα radiation at 1.540 Å in the range of $5^o \leq 2\theta \leq 70^o$, with an accelerating voltage of 40 kV with 30 mA. Fluorescence of HSA after interaction with Co doped SnO_2 NPs was measured using a spectrofluorometer (SL174, ELICO). CD spectra were analyzed using CD spectrometer (JASCO J-715). pH measurements were carried out on Mettler Toledo pH meter (Seven Easy S20-K) using Expert "Pro3 in 1" type electrode. The least count of the pH meter was 0.01 pH unit.

3.3.8. Steady state fluorescence quenching measurements

Fluorescence measurements were performed on a Shimadzu fluorescence spectrophotometer, model RF-5301 (Japan). The fluorescence spectra were measured at 25 ± 0.1 °C with a 1 cm path length cell. Excitation and emission slits were set at 3 and 5 nm, respectively. Intrinsic fluorescence was measured by exciting the protein solution at 295 nm and emission spectra were recorded in the range of 300-450 nm. The titration of undoped SnO_2 NPs and doped $Sn_{0.95}Co_{0.05}O_2$ NPs (0-90 μM) to HSA (6 μM) solution was carried out at 298 K. The fluorescence intensity at 340 nm (tryptophan) was used to calculate the binding constant (K_b).

3.3.9. UV-Visible absorption measurements

Absorbance measurements were carried out on Perkin-Elmer Lambda 25 double beam UV-visible spectrophotometer attached with Peltier temperature programmer 1 (PTP-1). Cuvette of cell length of 10 mm and scanning speed 1000 nm min^{-1} was used. The concentration of protein (5 μM) and 1:0, 1:5 and 1:10 molar ratio of HSA to undoped SnO_2 NPs and doped $Sn_{0.95}Co_{0.05}O_2$ NPs were used.

3.3.10. Circular dichroism (CD) measurements

Far UV-CD measurements (190-250 nm) were carried out on JASCO-J 813 spectropolarimeter equipped with a Peltier-type temperature controller at 298 K using a quartz cell of path length of 0.1 cm. Three scans were accumulated at a scan speed of 100 nm min^{-1}. 1:0, 1:10 and 1:20 molar ratio of complex HSA to undoped SnO_2 NPs and doped $Sn_{0.95}Co_{0.05}O_2$ NPs were taken. The percent α-helical and β-sheet contents

of the protein were calculated by using online K2D3 software,[83] using the CD values from 200-250 nm as extracted from the CD spectra.

3.4. Conclusion

The current study illustrates the nature of binding between HSA and Co doped SnO_2 NPs by using various spectroscopic techniques. Co-precipitation method was used to synthesize Co doped SnO_2 NPs of average size of ~35 nm with narrow size distribution as confirmed by HR-TEM analysis. Fluorescence spectra showed the quenching of fluorophores of HSA by the addition of Co doped SnO_2 NPs which indicates that the interaction between HSA and NPs. Since the results obtained from FT-IR spectroscopy revealed the prominent peaks of proteins, the complete coating of NPs by HSA can be confirmed. Besides, data of UV-visible and CD spectra suggested that the secondary structure of HSA underwent an increase in α-helix. We can infer that the binding of Co doped SnO_2 NPs to HSA could not only bring the conformational changes to HSA but also lead to more adverse influences on the physiological functions. Photocatalytic study shown that SnO_2 NPs can degradate MB dye. In order to enhance the photocatalytic activity of SnO_2, it can be doped/implanted with Co at different concentrations. It is clear from the observed data that the doping of Co in SnO_2 enhances the antimicrobial property of SnO_2, which is may be due to the large surface area and small particle size, lower band gap energy of NPs, and the production of ROS, especially generation of H_2O_2 on the surface area of the NPs that can penetrate the cell membrane and can cause damage to DNA and cellular proteins, leading to cell death.

3.5. References

1 C. M. Niemeyer, *Angew. Chemie Int. Ed.*, 2001, **40**, 4128–4158.

2 E. Katz and I. Willner, *Angew. Chemie Int. Ed.*, 2004, **43**, 6042–6108.

3 M. Agrawal, S. Gupta and M. Stamm, *J. Mater. Chem.*, 2011, **21**, 615–627.

4 P. Aggarwal, J. B. Hall, C. B. McLeland, M. A. Dobrovolskaia and S. E. McNeil, *Adv. Drug Deliv. Rev.*, 2009, **61**, 428–437.

5 P. Grosse, F. J. Schmitte, G. Frank and H. Köstlin, *Thin Solid Films*, 1982, **90**, 309–315.

6 Z. Peng, Z. Shi and M. Liu, *Chem. Commun.*, 2000, **21**, 2125–2126.

7 S. Ferrere, A. Zaban and B. A. Gregg, *J. Phys. Chem. B*, 1997, **101**, 4490–4493.

8 Y.-S. He, J. C. Campbell, R. C. Murphy, M. F. Arendt and J. S. Swinnea, *J. Mater. Res.*, 2011, **8**, 3131–3134.

9 S. Seal and S. Shukla, *JOM*, 2002, **54**, 35–38.

10 K. L. Chopra, S. Major and D. K. Pandya, *Thin Solid Films*, 1983, **102**, 1–46.

11 Y.-D. Wang, C.-L. Ma, X.-D. Sun and H.-D. Li, *Inorg. Chem. Commun.*, 2001, **4**, 223–226.

12 D. E. Williams, *Solid state gas sensors*, 1987, 71–123.

13 S. Zinatloo-Ajabshir, M. Salavati-Niasari and M. Hamadanian, *RSC Adv.*, 2015, **5**, 33792–33800.

14 L. Qi, J. Ma, H. Cheng and Z. Zhao, *Langmuir*, 1998, **14**, 2579–2581.

15 S. Zinatloo-Ajabshir, M. Salavati-Niasari and Z. Zinatloo-Ajabshir, *Mater. Lett.*, 2016, **180**, 27–30.

16 Z. Salehi, S. Zinatloo-Ajabshir and M. Salavati-Niasari, *RSC Adv.*, 2016, **6**, 26895–26901.

17 S. Zinatloo-Ajabshir and M. Salavati-Niasari, *Ceram. Int.*, 2014, **41**, 567–575.

18 Z. Salehi, S. Zinatloo-Ajabshir and M. Salavati-Niasari, *J. Mol. Liq.*, 2016, **222**, 218–224.

19 S. Zinatloo-Ajabshir and M. Salavati-Niasari, *J. Mater. Sci. Mater. Electron.*, 2015, **26**, 5812–5821.

20 H. Elhouichet, L. Othman, A. Moadhen, M. Oueslati and J. . Roger, *Mater. Sci. Eng. B*, 2003, **105**, 8–11.

21 M. Parthibavarman, V. Hariharan, C. Sekar and V. N. Singh, *J. Optoelectron.*

Adv. Mater., **12**, 1894–1898.

22 N. Van Hieu, H.-R. Kim, B.-K. Ju and J.-H. Lee, *Sensors Actuators B Chem.*, 2008, **133**, 228–234.

23 L. M. Fang, X. T. Zu, Z. J. Li, S. Zhu, C. M. Liu, L. M. Wang and F. Gao, *J. Mater. Sci. Mater. Electron.*, 2008, **19**, 868–874.

24 S. Zinatloo-Ajabshir and M. Salavati-Niasari, *New J. Chem.*, 2015, **39**, 3948–3955.

25 M. Salavati-Niasari, N. Mir and F. Davar, *Inorganica Chim. Acta*, 2010, **363**, 1719–1726.

26 P. Kamaraj, R. Vennila, M. Arthanareeswari and S. Devikala, *World J. Pharm. Sci.*, 2014, **3 (9)**, 382–388.

27 J. Peller, O. Wiest and P. V Kamat, *Environ. Sci. Technol.*, 2003, **37**, 1926–1932.

28 J. G. Zhou, H. T. Fang, J. M. Maley, J. Y. P. Ko, M. Murphy, Y. Chu, R. Sammynaiken and T. K. Sham, *J. Phys. Chem. C*, 2009, **113**, 6114–6117.

29 Z. R. Dai, J. L. Gole, J. D. Stout and Z. L. Wang, *J. Phys. Chem. B*, 2002, **106**, 1274–1279.

30 P. Wu, N. Du, H. Zhang, C. Zhai and D. Yang, *ACS Appl. Mater. Interfaces*, 2011, **3**, 1946–1952.

31 J. Xing, W. Q. Fang, Z. Li and H. G. Yang, *Ind. Eng. Chem. Res.*, 2012, **51**, 4247−4253.

32 A. K. Sinha, M. Pradhan, S. Sarkar and T. Pal, *Environ. Sci. Technol.*, 2013, **47**, 2339−2345.

33 M. S. Morassaei, S. Zinatloo-Ajabshir and M. Salavati-Niasari, *J. Mol. Liq.*, 2016, **220**, 902–909.

34 X. Dou, D. Sabba, N. Mathews, L. H. Wong, Y. M. Lam and S. Mhaisalkar, *Chem. Mater.*, 2011, **23**, 3938–3945.

35 S. Sun, G. Meng, G. Zhang and L. Zhang, *Cryst. Growth Des.*, 2007, **7 (10)**, 1988–1991.

36 G. S. Li, D. Q. Zhang and J. C. Yu, *Environ. Sci. Technol.*, 2009, **43**, 7079–7085.

37 Shamsuzamman, A. Ali, M. Asif, A. Mashrai and H. Khanam, *Eur. Chem. Bull.*, 2014, **3 (9)**, 939–945.

38 K. Rekha, M. Nirmala, M. G. Nair and A. Anukaliani, *Phys. B Condens. Matter*, 2010, **405**, 3180–3185.

39 B. Yu, K. M. Leung, Q. Guo, W. M. Lau and J. Yang, *Nanotechnology*, 2011,

22 (11), 115603.

40 M. G. Nair, M. Nirmala, K. Rekha and A. Anukaliani, *Mater. Lett.*, 2011, **65**, 1797–1800.

41 K. Gupta, R. P. Singh, A. Pandey and A. Pandey, *Beilstein J. Nanotechnol.*, 2013, **4**, 345–351.

42 A. H. Shah, E. Manikandan, M. B. Ahmed and V. Ganesan, *J. Nanomed. Nanotechnol.*, 2013, **4 (3)**, 1–6.

43 M. Dadkhah and M. Salavati-Niasari, *Electrochim. Acta*, 2014, **129**, 62–68.

44 X. M. He and D. C. Carter, *Nature*, 1992, **358**, 209–215.

45 G. Sudlow, D. J. Birkett and D. N. Wade, *Mol. Pharmacol.*, 1975, **11**, 824–832.

46 K. Aidas, J. M. H. Olsen, J. Kongsted and H. Ågren, *J. Phys. Chem.*, 2013, **117**, 2069–2080.

47 F. Samari, M. Shamsipur, B. Hemmateenejad, T. Khayamian and S. Gharaghani, *Eur. J. Med. Chem.*, 2012, **54**, 255–263.

48 X. Liu and Y. Du, *Eur. J. Med. Chem.*, 2010, **45**, 4043–4049.

49 N. Zaidi, E. Ahmad, M. Rehan, G. Rabbani, M. R. Ajmal, Y. Zaidi, N. Subbarao and R. H. Khan, *J. Phys. Chem. B*, 2013, **117**, 2595–2604.

50 N. Bijari, Y. Shokoohinia, M. R. Ashrafi-Kooshk, S. Ranjbar, S. Parvaneh, M. Moieni-Arya and R. Khodarahmi, *J. Lumin.*, 2013, **143**, 328–336.

51 N. Shahabadi, A. Khorshidi and N. H. Moghadam, *Spectrochim. Acta. A. Mol. Biomol. Spectrosc.*, 2013, **114**, 627–632.

52 M. Shakir, Z. Nasir, M. S. Khan, Lutfullah, M. F. Alam, H. Younus and S. I. Al-Resayes, *Int. J. Biol. Macromol.*, 2015, **72**, 1196–1204.

53 M. Parthibavarman, B. Renganathan and D. Sastikumar, *Curr. Appl. Phys.*, 2013, **13**, 1537–1544.

54 P. D. File, *Int. Cent. Diffr. data*, 2000, JCPDS file nos. 41–14445.

55 H. M. Xiong, K. K. Zhao, X. Zhao and Y. W. Wang, *Solid State Ionics*, 2003, **159**, 89–95.

56 O. N. Gavrilenko, E. V. Pashkova and A. G. Belous, *Russ. J. Inorg. Chem.*, 2007, **52**, 1835–1839.

57 T. J. Lenk, T. A. Horbett, B. D. Ratner and K. K. Chittur, *Langmuir*, 1991, **7 (8)**, 1755–1764.

58 P. Roach, D. Farrar and C. C. Perry, *J. Am. Chem. Soc.*, 2005, **127**, 8168–73.

59 J. R. Smith, M. T. Cicerone and C. W. Meuse, *Langmuir*, 2009, **25 (8)**, 4571–

4578.

60 T. Hu and Y. Liu, *J. Pharm. Biomed. Anal.*, 2015, **107**, 325–332.

61 D. P. Yeggoni, A. Rachamallu, M. Kallubai and R. Subramanyam, *J. Biomol. Struct. Dyn.*, 2015, **33 (6)**, 1336–1351.

62 P. Alam, F. Naseem, A. S. Abdelhameed and R. H. Khan, *J. Mol. Struct.*, 2015, **1099**, 149–153.

63 S. K. Chaturvedi, P. Alam, J. M. Khan, M. K. Siddiqui, P. Kalaiarasan, N. Subbarao, Z. Ahmad and R. H. Khan, *Int. J. Biol. Macromol.*, 2015, **80**, 375–384.

64 B. Ahmad, G. Muteeb, P. Alam, A. Varshney, N. Zaidi, M. Ishtikhar, G. Badr, M. H. Mahmoud and R. H. Khan, *Int. J. Biol. Macromol.*, 2015, **75**, 447–452.

65 P. Alam, G. Rabbani, G. Badr, B. M. Badr and R. H. Khan, *Cell Biochem. Biophys.*, 2015, **71 (2)**, 1199–1206.

66 S. K. Chaturvedi, E. Ahmad, J. M. Khan, P. Alam, M. Ishtikhar and R. H. Khan, *Mol. Biosyst.*, 2015, **11 (1)**, 307–316.

67 L. Ran, D. Zhao, X. Gao and L. Yin, *CrystEngComm*, 2015, **17**, 4225–4237.

68 T. Entradas, J. F. Cabrita, S. Dalui, M. R. Nunes, O. C. Monteiro and A. J. Silvestre, *Mater. Chem. Phys.*, 2014, **147 (3)**, 563–571.

69 M. Shoeb, B. R. Singh, M. Mobin, G. Afreen, W. Khan and A. H. Naqvi, *PLoS One*, 2015, **10**, e0135055.

70 B. R. Singh, M. Shoeb, W. Khan and A. H. Naqvi, *J. Alloys Compd.*, 2015, **651**, 598–607.

71 W. Wang, M. O. Tadé and Z. Shao, *Chem. Soc. Rev.*, 2015, **44**, 5371–5408.

72 D. Chandran, L. S. Nair, S. Balachandran, K. Rajendra Babu and M. Deepa, *J. Sol-Gel Sci. Technol.*, 2015, **76**, 582–591.

73 P. J. Rivero, A. Urrutia, J. Goicoechea and F. J. Arregui, *Nanoscale Res. Lett.*, 2015, **10**, 501.

74 P. Kongsong, L. Sikong, S. Niyomwas and V. Rachpech, *Sci. World J.*, 2014, **2014**, 869706.

75 J. P. Ruparelia, A. K. Chatterjee, S. P. Duttagupta and S. Mukherji, *Acta Biomater.*, 2008, **4 (3)**, 707–716.

76 A. Kubacka, M. S. Diez, D. Rojo, R. Bargiela, S. Ciordia, I. Zapico, J. P. Albar, C. Barbas, V. A. P. Martins dos Santos, M. Fernández-García and M. Ferrer, *Sci. Rep.*, 2014, **4**, 4134.

77 H. S. Guo, Y. N. Liu, Q. Qiao, H. Wei, C. X. Dong, J. Xue and K. B. Li, *Huan Jing Ke Xue*, 2015, **36 (5)**, 1700–1706.

78 A. Fakhri, S. Behrouz and M. Pourmand, *J. Photochem. Photobiol. B.*, 2015, **149**, 45–50.

79 N. Aziz, M. Faraz, R. Pandey, M. Shakir, T. Fatma, A. Varma, I. Barman and R. Prasad, *Langmuir*, 2015, **31**, 11605–11612.

80 K. Wallevik, *J. Biol. Chem.*, 1973, **248 (8)**, 2650–2655.

81 O. H. Lowry, N. J. Rosebrough, A. L. Farr and R. J. Randall, *J. Biol. Chem.*, 1951, **193 (1)**, 265–275.

82 J. A. Khan, M. Qasim, B. R. Singh, S. Singh, M. Shoeb, W. Khan, D. Das and A. H. Naqvi, *Spectrochim. acta. Part A, Mol. Biomol. Spectrosc.*, 2013, **109**, 313–321.

83 C. Louis-Jeune, M. A. Andrade-Navarro and C. Perez-Iratxeta, *Proteins*, 2011, **80 (2)**, 374–381.

****

Chapter 4

Silica supported NiO nanocomposite prepared via sol-gel technique and its excellent catalytic performance for one-pot multicomponent synthesis of benzodiazepine derivatives under microwave irradiation

4.1. Introduction

Metal oxide based nanocatalysts have attracted much attention in the fields of catalysis, separation, optoelectronics, active adsorbents for gases, magnetism, and microelectronics owing to their unique physical and chemical properties.[1–5] Catalysis is becoming a strategic field of science because it represents a new way in the area of nanotechnology to meet the challenges of energy and sustainability. These challenges are becoming the main concerns of the global vision of societal tasks and world economy. The societal pressure has been at the origin of the concept of nanoscience, which is an exponentially growing research field in modern science that involves the synthesis and application of nanoparticles (NPs) of different sizes and shapes.[6–9] The exciting prospect of nanoscience is its potential use in almost any conceivable domain. Every field from medicine and electronics to manufacturing and fashion stand to be benefitted from advances in nanotechnology.[10,11] Though nanoscale technology is multifaceted in its application, the use of nanomaterial as catalyst is perhaps the most intriguing. Further, the nanomaterial catalyzed reactions provide the advantages of high atom efficiency, simplified isolation of product, easy recovery and recyclability of the catalyst.[12–16]

Benzodiazepines and their polycyclic derivatives are a very important class of bioactive compounds. They are finding numerous new applications and are widely used as anti-convulsant, anti-inflammatory, analgesic, hypnotic, sedative and antidepressive agents.[17–19] Benzodiazepines are also valuable intermediates for the synthesis of fused ring compounds such as triazolo-, oxadiazolo-, oxazino-, and furano-benzodiazepines.[20–22] Due to their wide range of pharmacological activity and industrial applications, the development of mild and efficient protocols for their preparation continues to be a challenging endeavour in the synthetic organic chemistry.[19,23–36]

However, a large number of the modified methods reported in the literature, suffer from several drawbacks such as the use of a large amount of catalysts, unsatisfactory product yields and critical product isolation procedures. These disadvantages require a development of an efficient and practically useful process of preparation.[37] Generally, benzodiazepines are synthesized by the condensation of *o*-phenylenediamines with α,β-unsaturated carbonyl compounds, β-haloketones or ketones. Many reagents have been reported in the literature for this condensation including $Fe(ClO_4)_3 \cdot XH_2O$,[38] $Er(OTf)_3$,[39] PPA,[40] $NaBH_4$,[24] $MgO/POCl_3$,[25] $Yb(OTf)_3$,[26]

$InBr_3$,[30] and CH_3COOH under microwave conditions.[27] Silica composite materials containing different metal oxide particles like ZrO_2,[41] ZnO,[42,43] TiO_2,[44,45] Fe_3O_4,[46] NiO,[47,48] and CuO,[49–54] present a variety of interesting magnetic, electric, and catalytic properties, and have attracted considerable attention.

As a part of our research program in the field of nanomaterial's,[55–61] herein, we report first time to the best of our knowledge silica supported NiO nanocomposites (NiO@SiO_2 NCs) used as a nanocatalyst for the synthesis of benzodiazepines. The NiO@SiO_2 NCs has emerged as a promising heterogeneous solid catalyst for various organic transformations.[62,63] The catalyst possesses inherent environmentally benevolent properties such as non-toxicity, biocompatibility, physiological inertness, recyclability, inexpensiveness and thermal stability. The catalyst was prepared by employing sol-gel technique and the formation of NiO@SiO_2 NCs was evaluated by FT-IR, HR-TEM, XRD and SEM-EDS analysis.

4.2. Results and discussion

4.2.1. Characterization of catalyst (NiO@SiO_2 NCs)

To obtain a better understanding of the formation and evolution of NPs in silica matrix, FT-IR analysis of SiO_2 and NiO@SiO_2 NCs are carried out. For silica (SiO_2), the major characteristic peaks were broad asymmetric Si-O-Si stretching from 1200 to 1000 cm^{-1} and symmetric Si-O-Si stretching and bending modes lie near 809 and 468 cm^{-1}, respectively (**Fig. 4.1b**). The broad band at 3450 cm^{-1} was assigned to -OH stretching of free silanol groups of silica moiety. For FT-IR spectra of NiO@SiO_2 NCs, the dominant peak at around 1090 cm^{-1} together with less pronounced bands at 801 cm^{-1}, conforming to the vibration absorption of Si-O-Si groups, implying that the sample is mainly composed of silica network (**Fig. 4.1a**). In addition, band at 466 cm^{-1} is assigned to the stretching vibration of Ni-O bond[65] overlapping with the Si-O band at 468 cm^{-1}. Ni-O-Ni stretching mode is observed at 667 cm^{-1}.[66] A weak band at 1637 and 3436 cm^{-1} is assigned to the bending and stretching absorption of -OH groups, respectively.[52] Peaks at 2854 and 2925 cm^{-1} are ascribed to stretching vibration of C-H bond. The absorption band at 973 cm^{-1} in SiO_2 reveals the presence of non-bonded oxygen $Si–O^-$ or Si-OH[67] stretching vibration is shifted to 968 cm^{-1} in NiO@SiO_2 NCs that argues for formation of the Ni-O-Si bond.[68] However, some researchers[47,69] also attribute this band to vibration of the Si-OH bond. Considerably,

the band in the range 1240-1480 cm^{-1} assigned to the nitrate vibration which are sorely decreased at higher temperature showing the evolution of nitrogen compounds possibly in the form of nitrogen oxide.[70] Thus, it is assumed that the NiO NPs in silica matrix are prepared by the pyrogenic decomposition of nitrate.

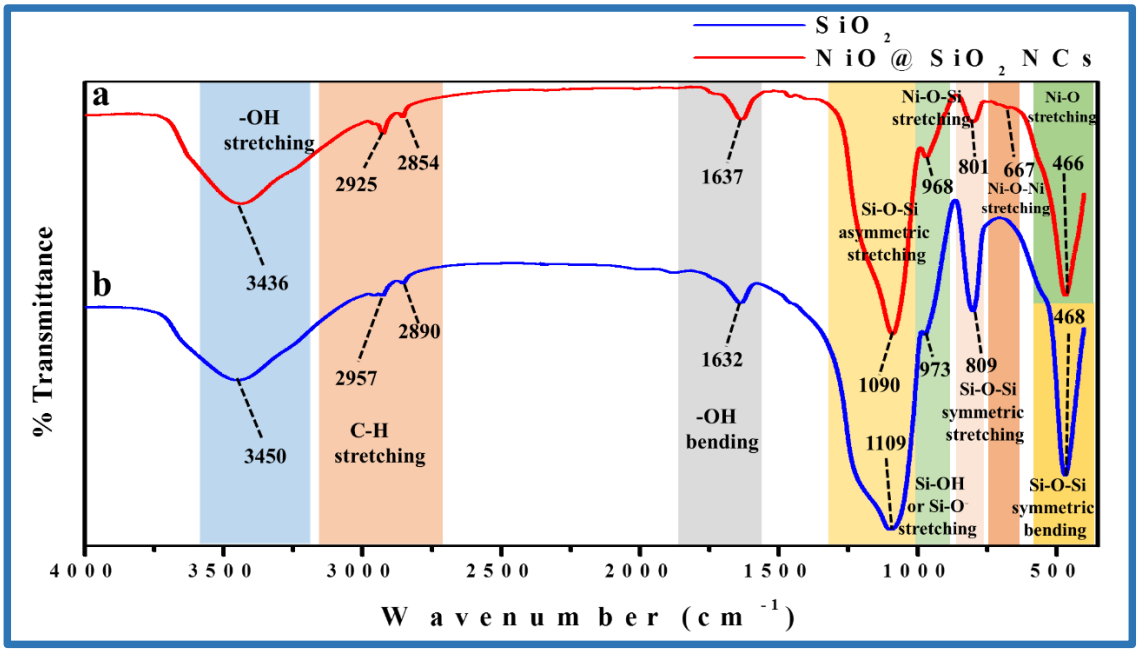

Figure 4.1. FT-IR spectra of (a) NiO@SiO_2 NCs and (b) SiO_2.

Formation of the catalytic system (NiO@SiO_2 NCs) was further confirmed by the powder XRD analysis (**Fig. 4.2**). XRD patterns showed reflection planes: (111), (200), (220), (311) and (222) comparably close with the reflection planes of NiO@SiO_2 NCs. The d-spacing of peaks was confirmed with joint Committee on Powder Diffraction Standards data (JCPDS No. 47-1049). The spectra of the sample is dominated by a broad peak (2θ = 23.1°) typical of amorphous silica presence. The patterns of NiO@SiO_2 NCs display characteristic NiO peaks centred at 2θ = 37.17°, 43.27° and 62.90°.[71,72] All the peaks in the diffraction pattern have been indexed and refinement of their lattice parameter was done by using Powder X software. The variation in FWHM is in agreement with the crystallite size reckoned by Debye-Sherrer's Formula:

$$D = \frac{0.9\,\lambda}{\beta COS\theta}$$

Where, λ is the wavelength of Cu Kα radiation, D is the particle size, β is the full width half maximum intensity and θ is the position of the peak. The calculation outputs are summarized in the **Table 4.1.**

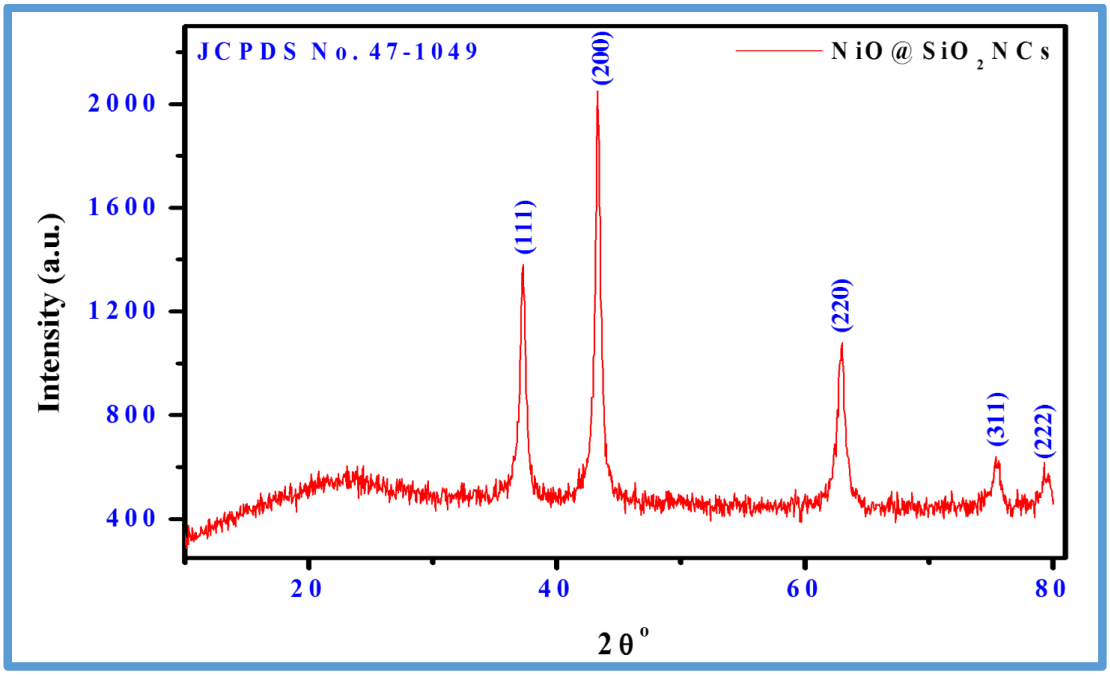

Figure 4.2. XRD patterns of NiO@SiO_2 NCs.

Table 4.1. Structural parameters of NiO@SiO_2 NCs.

Sample	2θ	FWHM (β)	Crystallite size (nm)
NiO@SiO_2 NCs	43.2	0.392	21.7

The SEM images of catalyst (NiO@SiO_2 NCs) before and after catalytic reaction were taken in **Fig. 4.3 (a** and **b)**. The SEM images revealed that the particles polydisperse in nature and show relatively diffused patterns. The successful incorporation of NiO was also confirmed by EDS analysis (**Fig. 4.4**). EDS spectrum showed the presence of Ni in addition to O and Si elements.

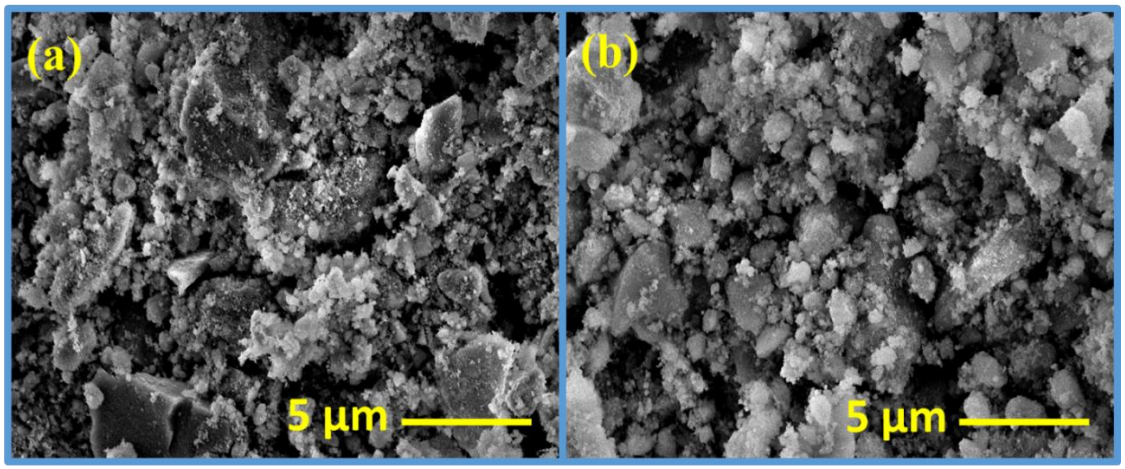

Figure 4.3. SEM images of (a) freshly synthesized NiO@SiO_2 NCs and (b) NiO@SiO_2 NCs after seven catalytic cycles.

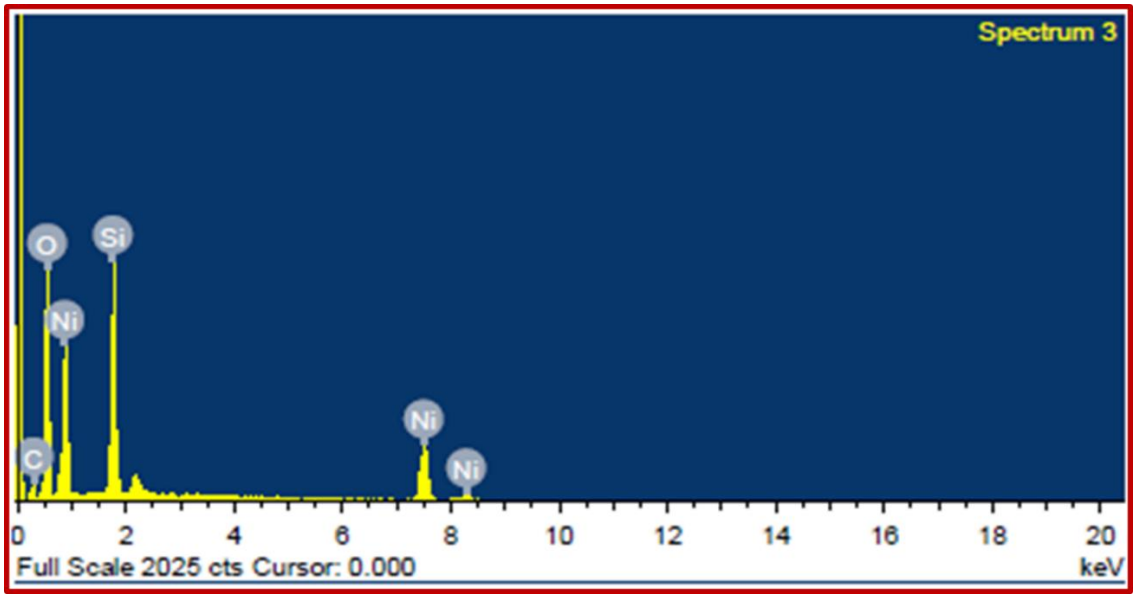

Figure 4.4. EDS spectrum of NiO@SiO_2 NCs.

Fig. 4.5 (a and **b)**, shows HR-TEM images of catalyst (NiO@SiO_2 NCs) calcined at 400 ^{o}C for 2 h. The HR-TEM images indicates clearly that the particle size is homogeneous and moderately small. From these images, it can be seen remarkably that the darker NiO NPs are surrounded by the lighter amorphous silica layer. The average particle size is around 20 nm in diameter which are in good agreement with the calculated results of XRD. **Fig. 4.5 (c** and **d)**, presents the particle size distribution histogram which is obtained by using an image-J processing software.

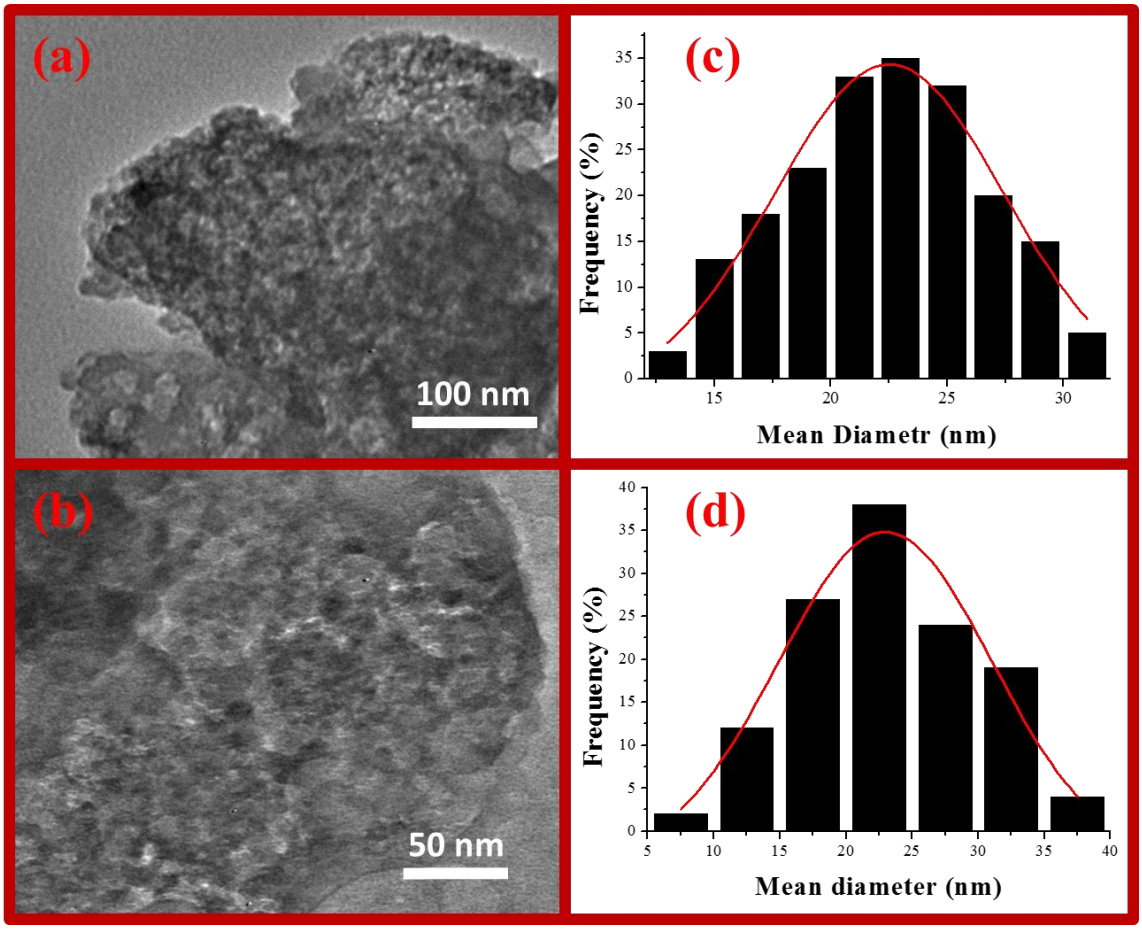

Figure 4.5. HR-TEM images of NiO@SiO_2 NCs (a and b) and their statistical analysis (c and d).

Furthermore, SAED pattern in **Fig. 4.6**, clearly shown that most of the NiO NPs in NiO@SiO_2 NCs are small crystallites and dispersed on support. Thus, SAED pattern supports the presence of both phases, NiO and SiO_2, within the prepared sample.

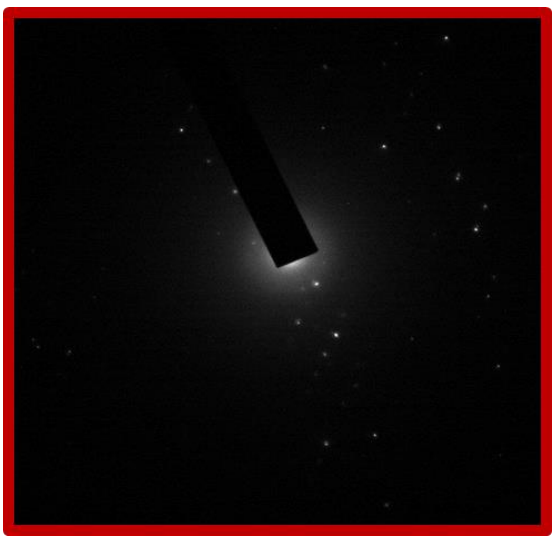

Figure 4.6. SAED pattern of NiO@SiO_2 NCs.

4.2.2. Optimization of reaction conditions

In order to explore the optimum conditions, we investigated the solvent effect, catalyst loading, effect of temperature, reaction time and recyclability of the catalyst on the model reaction **4e**. Initially, we optimized the catalytic efficiency of different catalysts such as $FeCl_3$, ZnO, NiO, Fe_3O_4, ZnS, $ZnCl_2$, MgO, $CuCl_2$, $NiCl_2$ and NiO@SiO_2 NCs (**Table 4.2**, entry **1-10**) applied for one-pot three component reaction of *o*-phenylenediamine **1** (1 mmol, 0.108 g), dimedone **2** (1 mmol, 0.140 g) and 4-(dimethylamino)benzaldehyde **3e** (1 mmol) in EtOH at 70 ^{o}C as a model reaction (**Table 4.2**). Among them NiO@SiO_2 NCs showed best catalytic activity when compared to other catalysts. Further, to improve the catalytic efficacy of NiO@SiO_2 NCs, the model reaction **4e** was examined at different concentrations (0.01-0.06 g) (**Table 4.2**, entries **11-16**) of the NiO@SiO_2 nanocatalyst under the microwave. Firstly, we have tested the model reaction **4e** with 0.01 g weight of the NiO@SiO_2 NCs to obtain 65 % yield of the product in 40 min (**Table 4.2**, entry **11**). By increasing the loading of the NiO@SiO_2 NCs from 0.02 to 0.05 g, improved in yield and reaction rate increased up to 70 % to 98 % with prominent fall in reaction time from 35 to 10 min (**Table 4.2**, entry **12-15**), respectively. It is significant to note that no progress was observed in the case of reaction rate and yield by increasing the amount of NiO@SiO_2 NCs beyond 0.05 g (**Table 4.2**, entry **16**). Based on these outcomes, 0.05 g of the NiO@SiO_2 NCs is sufficient for the reaction (**Scheme 4.1**) (**Fig. 4.7**).

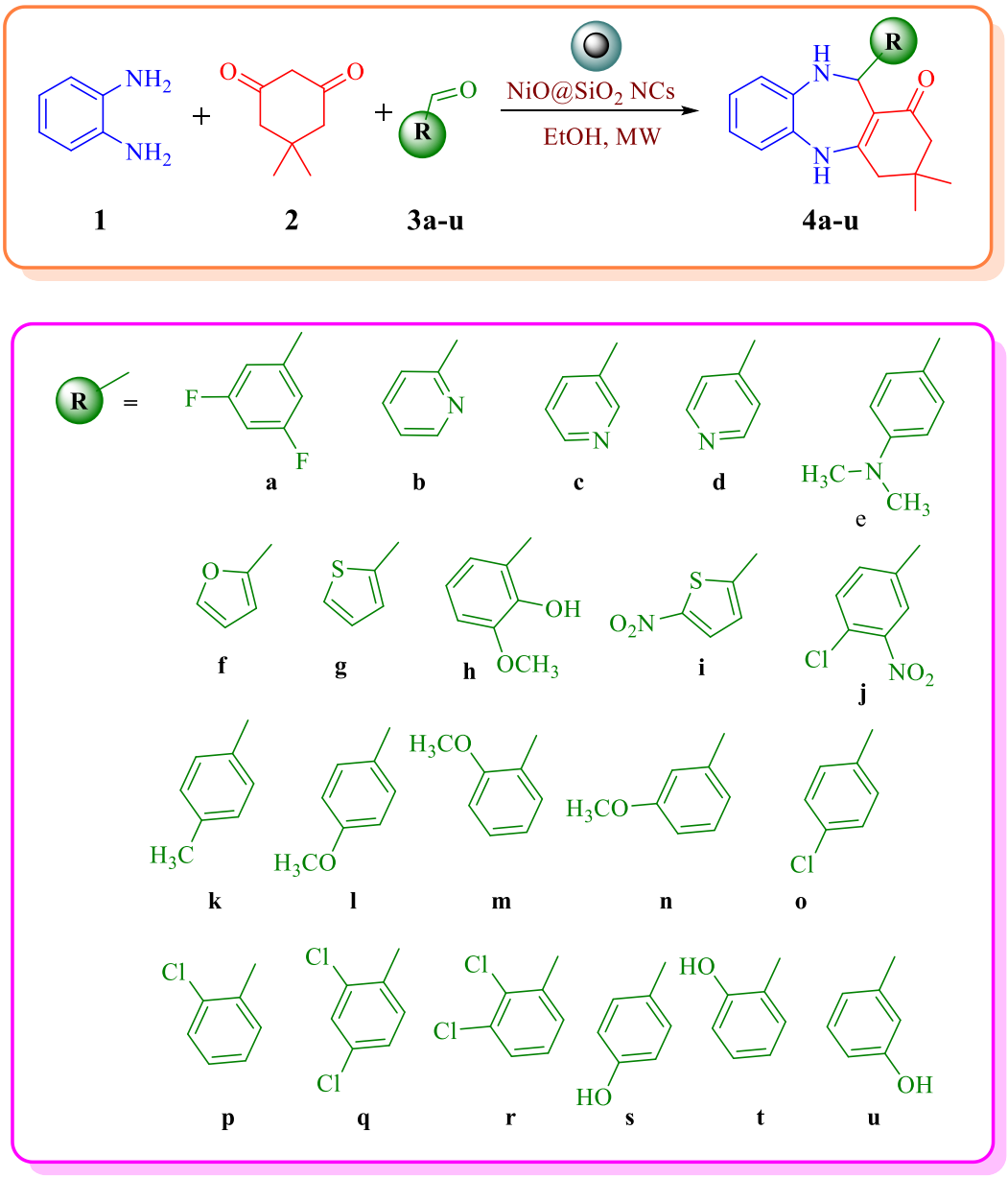

Scheme 4.1. NiO@SiO_2 NCs catalyzed benzodiazepine reaction.

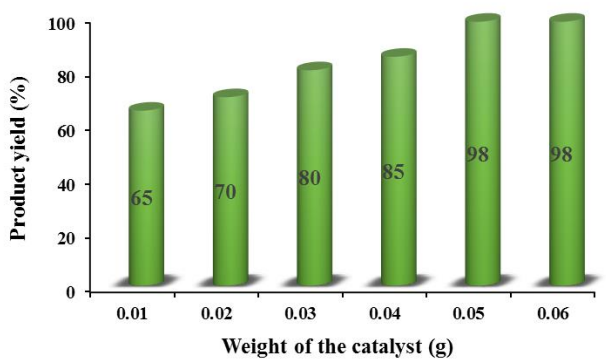

Figure 4.7. Effects of catalyst dose (0.01-0.06 g) on the production yield of benzodiazepine **4e** under microwave irradiation.

Table 4.2. Comparison of the catalytic efficiency of NiO@SiO_2 NCs with other catalysts **4e**[a].

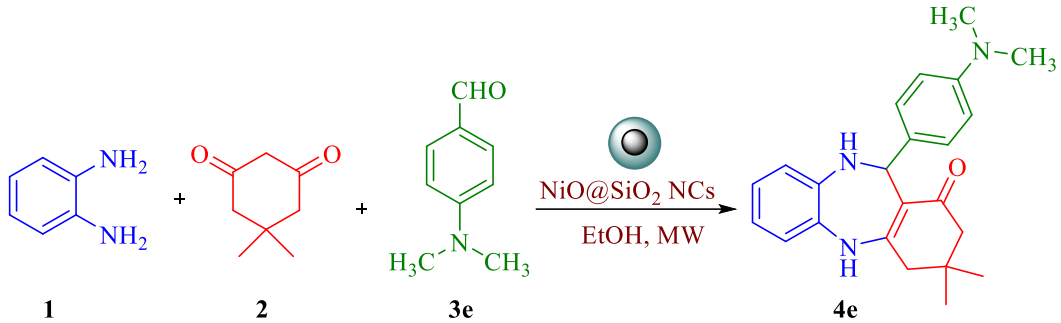

Entry	Catalyst	Catalyst loading (g)	Time (h)[b]	Yield[c] (%)
1.	$FeCl_3$	0.05	21	45
2.	ZnO	0.05	19	57
3.	NiO	0.05	15	43
4.	Fe_3O_4	0.05	17	61
5.	ZnS	0.05	12	59
6.	$ZnCl_2$	0.05	13	52
7.	MgO	0.05	10	48
8.	$CuCl_2$	0.05	9	35
9.	$NiCl_2$	0.05	14	26
10.	NiO@SiO_2 NCs	0.05	4	85
11.	NiO@SiO_2 NCs	0.01, MW	40 min	65
12.	NiO@SiO_2 NCs	0.02, MW	35 min	70
13.	NiO@SiO_2 NCs	0.03, MW	30 min	80
14.	NiO@SiO_2 NCs	0.04, MW	20 min	85
15.	NiO@SiO_2 NCs	0.05, MW	10 min	98
16.	NiO@SiO_2 NCs	0.06, MW	10 min	98

[a]Reaction condition: *o*-phenylenediamine **1** (1 mmol, 0.108 g), dimedone **2** (1 mmol, 0.140 g), and 4-(dimethylamino)benzaldehyde **3e** (1 mmol) in the presence of different catalyst in EtOH at 70 ^{o}C. [b]Reaction progress monitored by TLC. [c]Isolated yield of products.

Further, we also screened the model reaction **4e** by retaining *o*-phenylenediamine **1** (1 mmol, 0.108 g), dimedone **2** (1 mmol, 0.140 g), and 4-(dimethylamino)benzaldehyde **3e** (1 mmol) in various solvents and NiO@SiO_2 NCs used as a catalyst at different temperatures were displayed in the **Table 4.3**. First we accomplished the reaction in EtOH (5 mL) by loading NiO@SiO_2 NCs (0.05 g) at 50 ^{o}C for 24 h to obtain the 70 % yield of benzodiazepine **4e** (**Table 4.3**, entry **1**). To reduce the reaction time, we

executed the reaction at various temperatures such as 60, 65 and 70 ^{o}C with equal amount of catalyst yielding the benzodiazepine in 75 %, 80 % and 85% (**Table 4.3**, entry **2-4**) for 15 h, 10 h and 4 h, respectively. However, no further enhancement in the yield of product **4e** was observed when the reaction temperature was raised from 70 ^{o}C to 80 ^{o}C (**Table 4.3**, entry **5**). Therefore, 70 ^{o}C was chosen as the optimum temperature for the reaction. When the same reaction was carried out in *n*-Hexane, CH_2Cl_2, $CHCl_3$ and CH_3CN as solvents at 70 ^{o}C for a period of 15 h, 9 h, 7 h and 6 h, we obtained 75 %, 78 %, 73 % and 79 % yields (**Table 4.3**, entry **6, 8-10**), respectively. A moderate yield of 51 % (**Table 4.3,** entry **7**) was observed with CH_3COOH as solvent at 70 ^{o}C for 19 h. Low yields of 33 %, 35 % and 24% (**Table 4.3**, entry **11-13**) were obtained when we used DMF, DMSO and MeOH at 70 ^{o}C for 13 h. In order to further improve the protocol to make it more energy efficient we introduced microwaves (Anton Paar, Monowave 300). The use of microwaves enhanced the protocol extraordinarily with high yield of the product **4e** in very short time period using EtOH as solvent (**Table 4.3**, entry **14-17**) and no further increment was observed from 70 ^{o}C to 80 ^{o}C under microwave (**Table 4.3**, entry **18**) same as in conventional methods (**Table 4.3**, entry **5**). Based on the above results we suggested that EtOH is the most excellent solvent in comparison with other polar, non-polar, protic, and aprotic solvents and 70 ^{o}C as the optimum temperature in the case of NiO@SiO_2 NCs catalyzed reaction (**Scheme 4.1**) (**Fig. 4.8**).

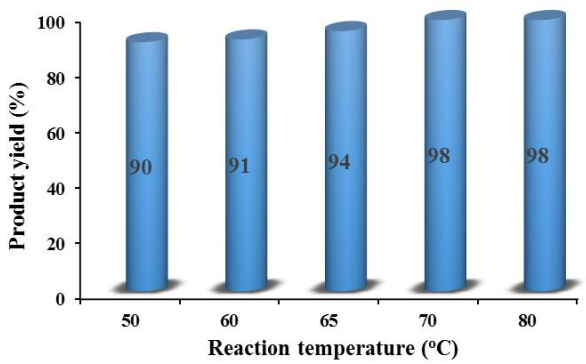

Figure 4.8. Effects of temperature with 0.05 g of the catalyst on the production yield of benzodiazepine **4e** under microwave irradiation.

Table 4.3. Effect of solvent and temperature on the model reaction **4e**[a].

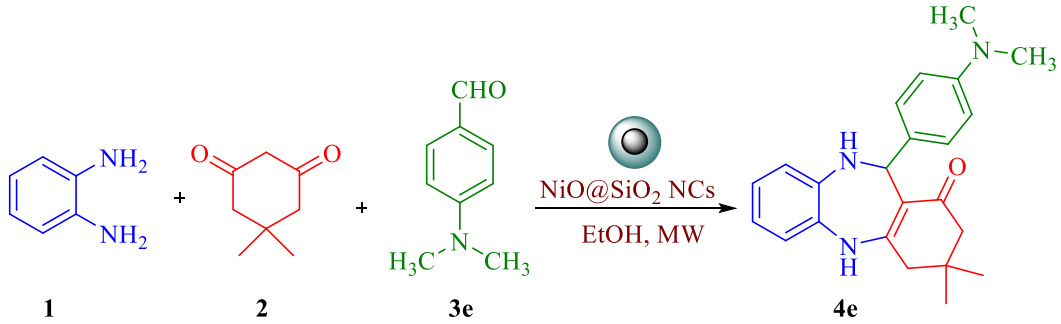

Entry	Catalyst loading (g)	Solvent	Time (h)	Temp. (°C)	Yield[b] (%)
1.	0.05	EtOH	24	50	70
2.	0.05	EtOH	15	60	75
3.	0.05	EtOH	10	65	80
4.	0.05	EtOH	4	70	85
5.	0.05	EtOH	4	80	85
6.	0.05	*n*-Hexane	15	70	75
7.	0.05	CH_3COOH	19	70	51
8.	0.05	CH_2Cl_2	9	70	78
9.	0.05	$CHCl_3$	7	70	73
10.	0.05	CH_3CN	6	70	79
11.	0.05	DMF	13	70	33
12.	0.05	DMSO	13	70	35
13.	0.05	MeOH	13	70	24
14.	0.05	EtOH, MW	55 min	50	90
15.	0.05	EtOH, MW	35 min	60	91
16.	0.05	EtOH, MW	20 min	65	94
17.	0.05	EtOH, MW	10 min	70	98
18.	0.05	EtOH, MW	10 min	80	98

[a]Reaction condition: *o*-phenylenediamine **1** (1 mmol, 0.108 g), dimedone **2** (1 mmol, 0.140 g), and 4-(dimethylamino)benzaldehyde **3e** (1 mmol) in the presence of $NiO@SiO_2$ NCs (0.05 g) in different solvents (5 mL) at various temperatures. [b]Isolated yield of products.

Having identified the optimal reaction conditions, it's necessary to evaluate the scope and efficiency of the reaction. For this purpose, *o*-phenylenediamine, aromatic aldehydes and dimedone were chosen to perform the reaction to yield the corresponding benzodiazepines (**4a-u**) and the results were displayed in **Table 4.4**. With regard to the aromatic aldehydes containing both electron donating and withdrawing substituents, they can be efficiently converted into benzodiazepines (**4a-u**) in high yields as shown in **Table 4.4**.

Table 4.4. Synthesis of benzodiazepine derivatives (**4a-u**) in the presence of NiO@SiO_2 NCs.

Entry	Product	Conventional Method		Microwave irradiation		M.p (°C)	
		Time (h)	Yield (%)	Time (min)	Yield (%)	Observed	Reported
4a	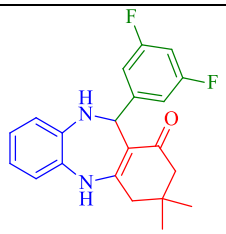	5	81	10	94	245-247	247-248[73]
4b	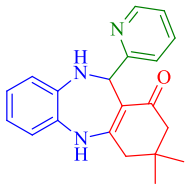	4.5	79	15	91	232-235	230-233[73]
4c	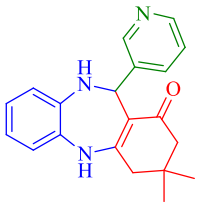	4	80	20	90	212-214	216-218[73]
4d	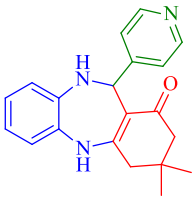	5.5	77	10	97	255-257	260-263[73]
4e	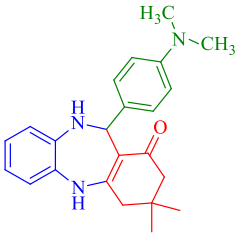	4	85	10	98	226-228	228-230[74]
4f	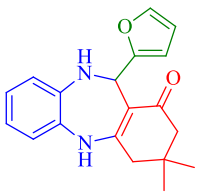	6	78	10	96	220-221	216-218[74]
4g	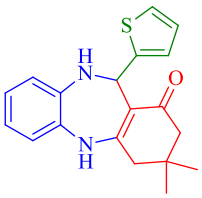	5	80	10	94	226-227	227-229[74]

Table 4.4. (*Continued*)

Entry	Product	Conventional Method		Microwave irradiation		M.p (°C)	
		Time (h)	Yield (%)	Time (min)	Yield (%)	Observed	Reported
4h	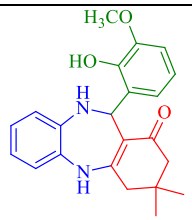	4	76	15	91	273-275	269-270[74]
4i	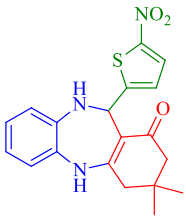	6.5	80	15	94	240-242	243-245[74]
4j	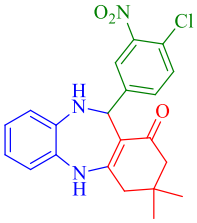	5	82	20	92	190-191	196-197[75]
4k	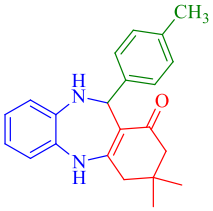	5.5	81	15	96	227-229	224-226[75]
4l	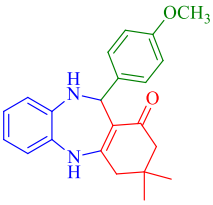	4.5	78	10	97	224-226	229-231[76]
4m	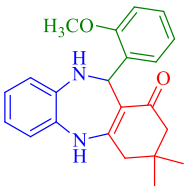	5	80	10	98	215-217	217-218[76]
4n	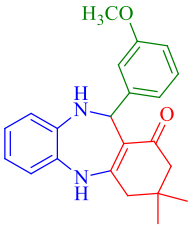	6	72	15	95	221-223	225-227[76]

Table 4.4. *(Continued)*

Entry	Product	Conventional Method		Microwave irradiation		M.p (°C)	
		Time (h)	Yield (%)	Time (min)	Yield (%)	Observed	Reported
4o	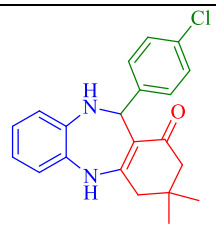	6	74	10	98	230-231	235-237[76]
4p	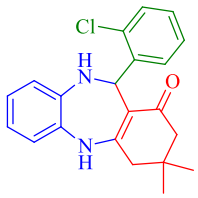	4	79	10	96	241-243	239-240[76]
4q	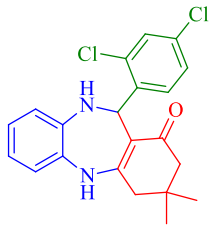	4.5	81	15	98	237-239	230-232[76]
4r	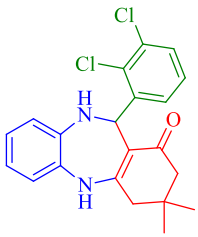	5	77	15	94	255-257	256-258[76]
4s	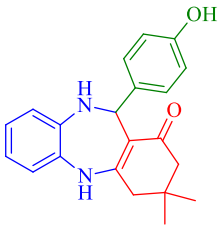	6	75	10	97	229-230	225[77]
4t	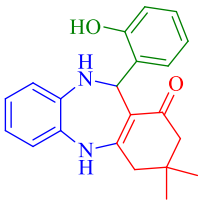	4	82	10	95	197-199	201-202[76]
4u	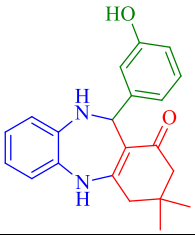	5.5	81	10	96	290-292	287-289[76]

4.2.3. Chemistry

The structural elucidation of the desired products (**4a-u**) was confirmed using FT-IR, ^{1}H NMR, ^{13}C NMR, MS and analytical data. The selected diagnostic bands in the IR spectra of synthesized compounds provide useful information for determining their structures. The analytical results for C, H and N were within ±0.4 % of the theoretical values. The FT-IR spectrum of the synthesized compounds (**4a-u**) exhibits a broad band at 3302-3351 and 3210-3268 cm^{-1}, were related to the stretching vibrations of amine protons (2 NH groups). The bands at 1058-1061, 742-749, 1612-1630, 715-718, and 1159-1168 cm^{-1} confirm the presence of C-O, C-Cl, C=C, C-S, C-F groups, whereas the strong bands at 1624-1642 cm^{-1} were attributed to the stretching vibrations of carbonyl groups (C=O stretching). Moreover, the absorption bands at 3071-3098, 1550–1572, 1372-1390 cm^{-1} are attributed to the aromatic ring in the products **4a-u** and the bands in the range 1633-1636 cm^{-1} confirm the presence of C=N in compounds **4b-d**. Characteristic peaks for the different functional groups such as methoxy, nitro and hydroxyl *etc*. have been deliberated in "Experimental section". In their ^{1}H NMR spectrum, each compound displayed the downfield singlet at around δ 6.32-7.99 was credited to aromatic protons, a broad singlet at around δ 5.01-6.30 and δ 6.98-8.87 has been ascribed to –NH proton (D_2O exchangeable) of benzodiazepine ring. Similarly, each compound exhibited two singlet bands for the *gem*-dimethyl groups at δ 0.94-1.12 and δ 1.01-1.26, as well as an AB quartet for the CH_2 protons at δ 2.07-2.24. Moreover, ^{1}H NMR spectrum of the compounds **4a-u** also contained a signal at δ 2.32-2.63 for CH_2–C=O protons, as well as a signal at δ 5.25-6.01 for CH proton of benzodiazepine ring. ^{13}C NMR spectra, displayed a series of signals resonating at around δ 110.8–168.7 which have been assigned to aromatic carbons, peaks resonating at around δ 52.3-66.1 and δ 133.2-145.8 corresponds to C-*C*H-NH and C=*C*-NH moiety of benzodiazepine ring, respectively. Similarly signals at δ 193.1-197.9 have been attributed to carbonyl group ($C{=}O_{dimethylcyclohex\text{-}2\text{-}enone}$) of compounds **4a-u**. Finally, the mass spectral analysis of the synthesized compounds **4a-u** (**Fig. 4.9-4.20**) displayed a molecular ion peak at the appropriate *m/z* value (**Scheme 4.2-4.6**).[74,77]

Fragmentation pattern I

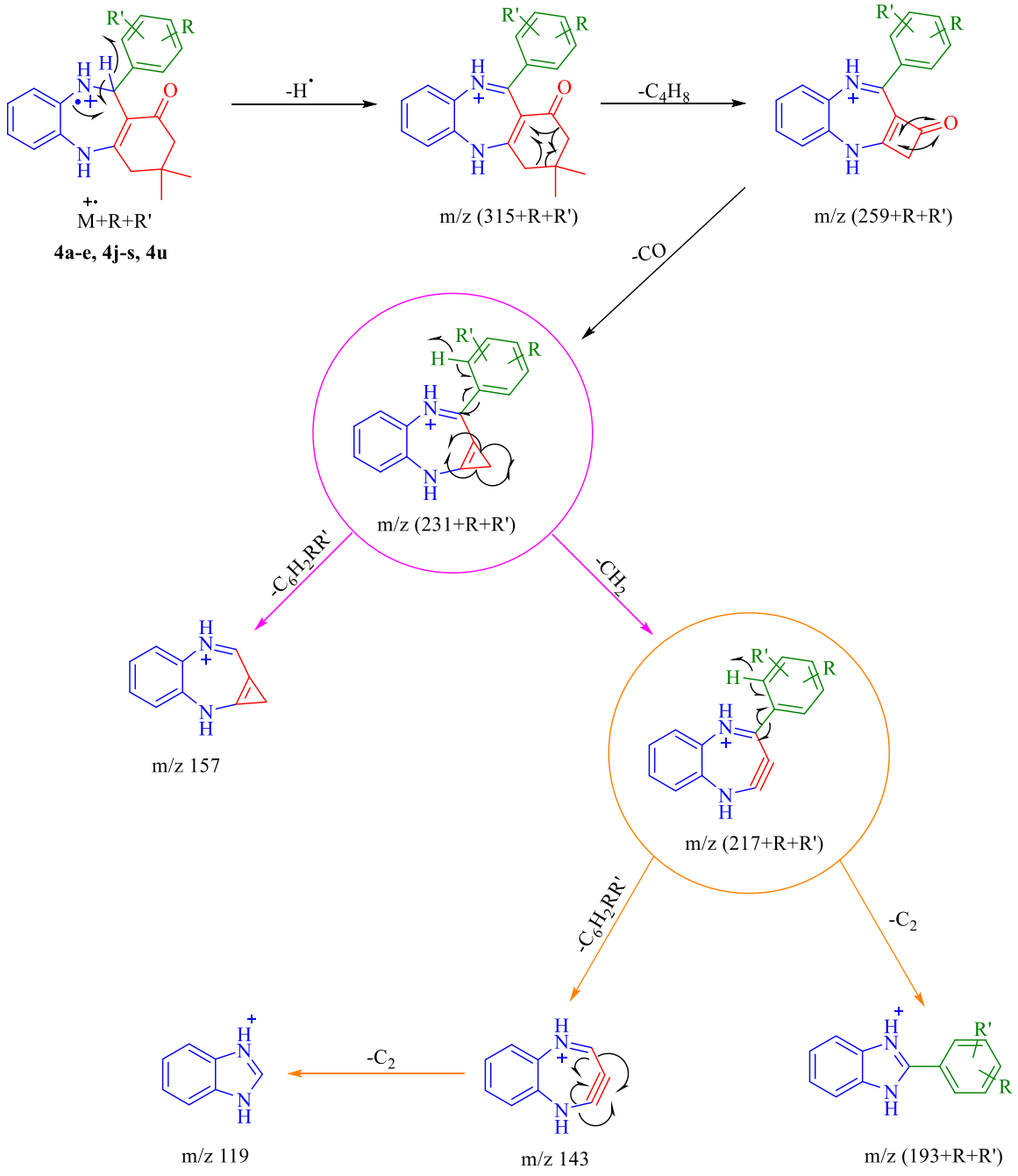

Scheme 4.2. Proposed fragmentation mechanisms of molecular ion [$M^{+\cdot}$] of compounds (**4a-e, 4j-s** and **4u**).

Fragmentation pattern II

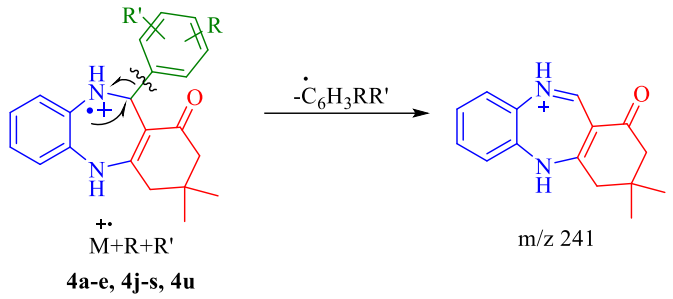

Fragmentation pattern III

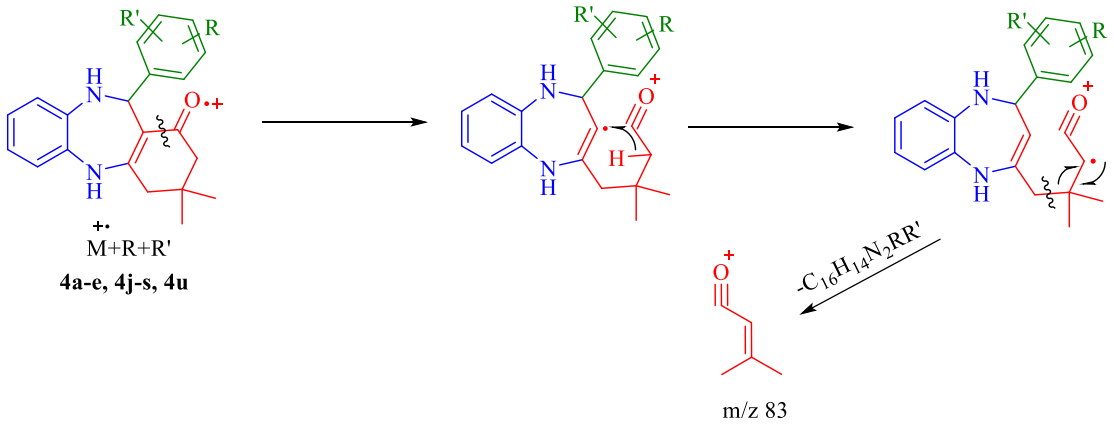

Scheme 4.3. Proposed fragmentation mechanisms of molecular ion [$M^{+\cdot}$] of compounds (**4a-e, 4j-s** and **4u**).

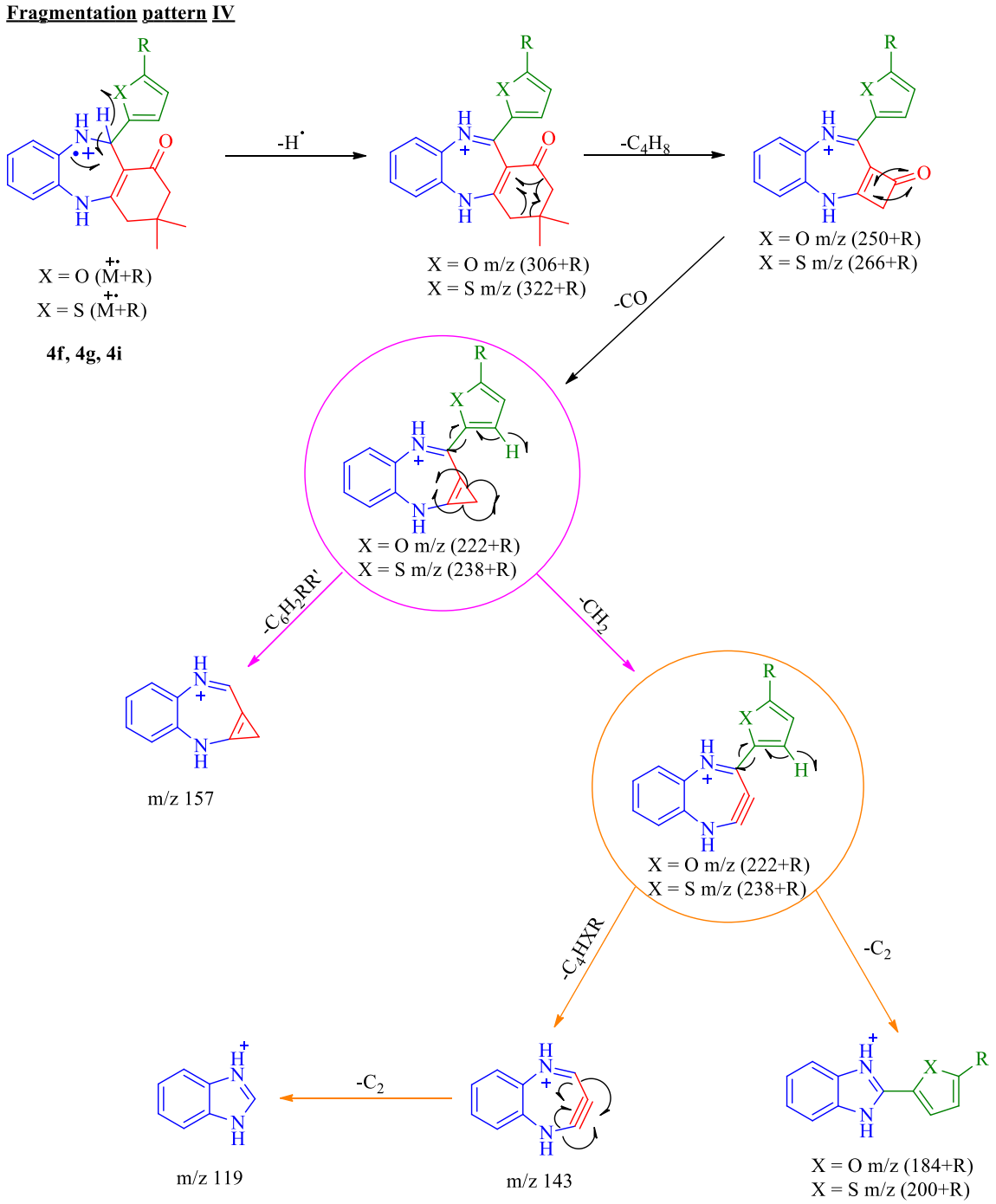

Scheme 4.4. Proposed fragmentation mechanisms of molecular ion [$M^{+\cdot}$] of compounds (**4f, 4g** and **4i**).

Fragmentation pattern V

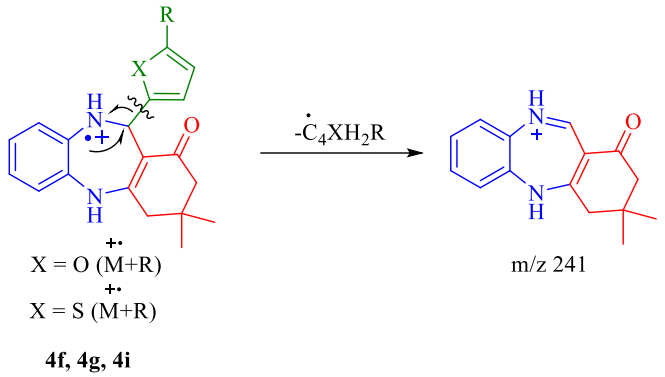

4f, 4g, 4i

Fragmentation pattern VI

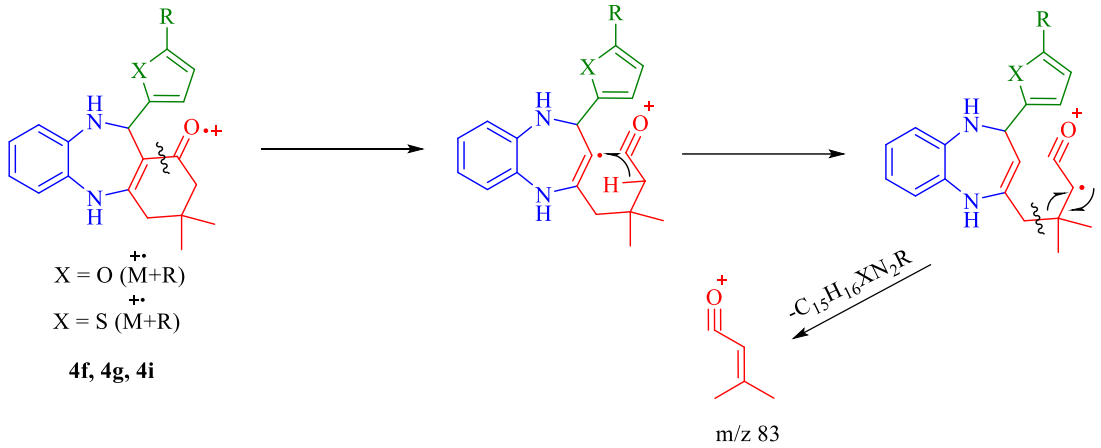

4f, 4g, 4i

Scheme 4.5. Proposed fragmentation mechanisms of molecular ion [$M^{+\cdot}$] of compounds (**4f, 4g** and **4i**).

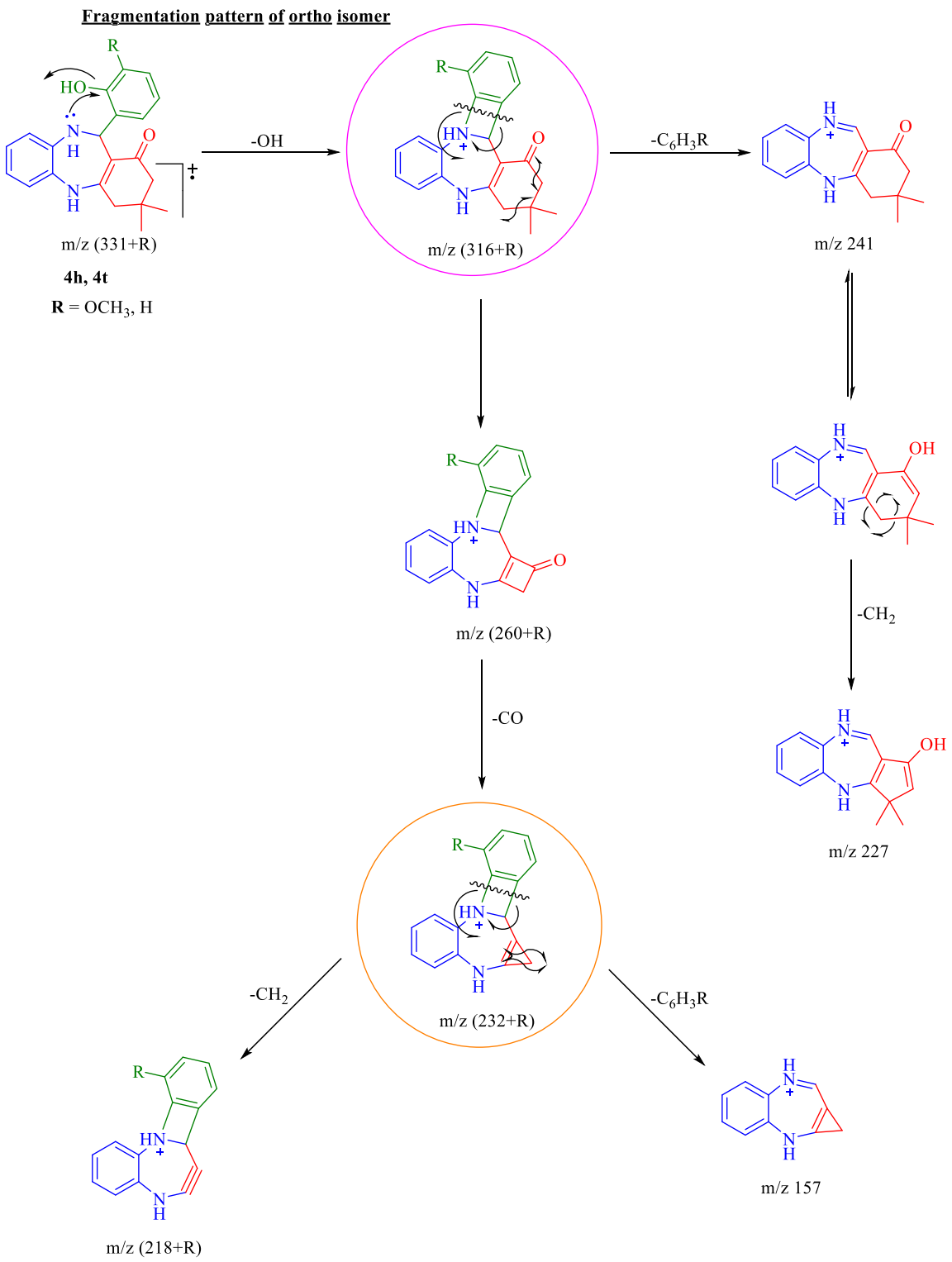

Scheme 4.6. Proposed fragmentation mechanisms of molecular ion [$M^{+\cdot}$] of compounds (**4h** and **4t**).

Based on the results of the current study, we have suggested here a plausible mechanism in **Scheme 4.7,** for one-pot three-component reaction of aromatic aldehydes, *o*-phenylenediamine and dimedone catalyzed by NiO@SiO_2 NCs in EtOH. The proposed mechanism is based on sequential Michael addition and Knoevenagel cyclization reactions. Initially, NiO@SiO_2 NCs activated carbonyl group of dimedone **2** undergo Michael addition reaction with *o*-phenylenediamine **1** to form imine intermediate **4**. The oxygen atoms of dimedone interact *via* lone pairs of electrons with the active sites of the catalyst surface, and the amino groups of *o*-phenylenediamine attack the carbonyl group of dimedone with elimination of H_2O leading to imine intermediate **4**. A 1,3-hydrogen shift then results in the formation of tautomeric enamine **5**.[64,76] The NH_2 group of enamine intermediate **5** would then react with the activated carbonyl group of aromatic aldehyde **6** to form the corresponding imine **7**, which would undergo an intramolecular cyclization to give the desired seven-membered benzodiazepine ring **4a-u**.

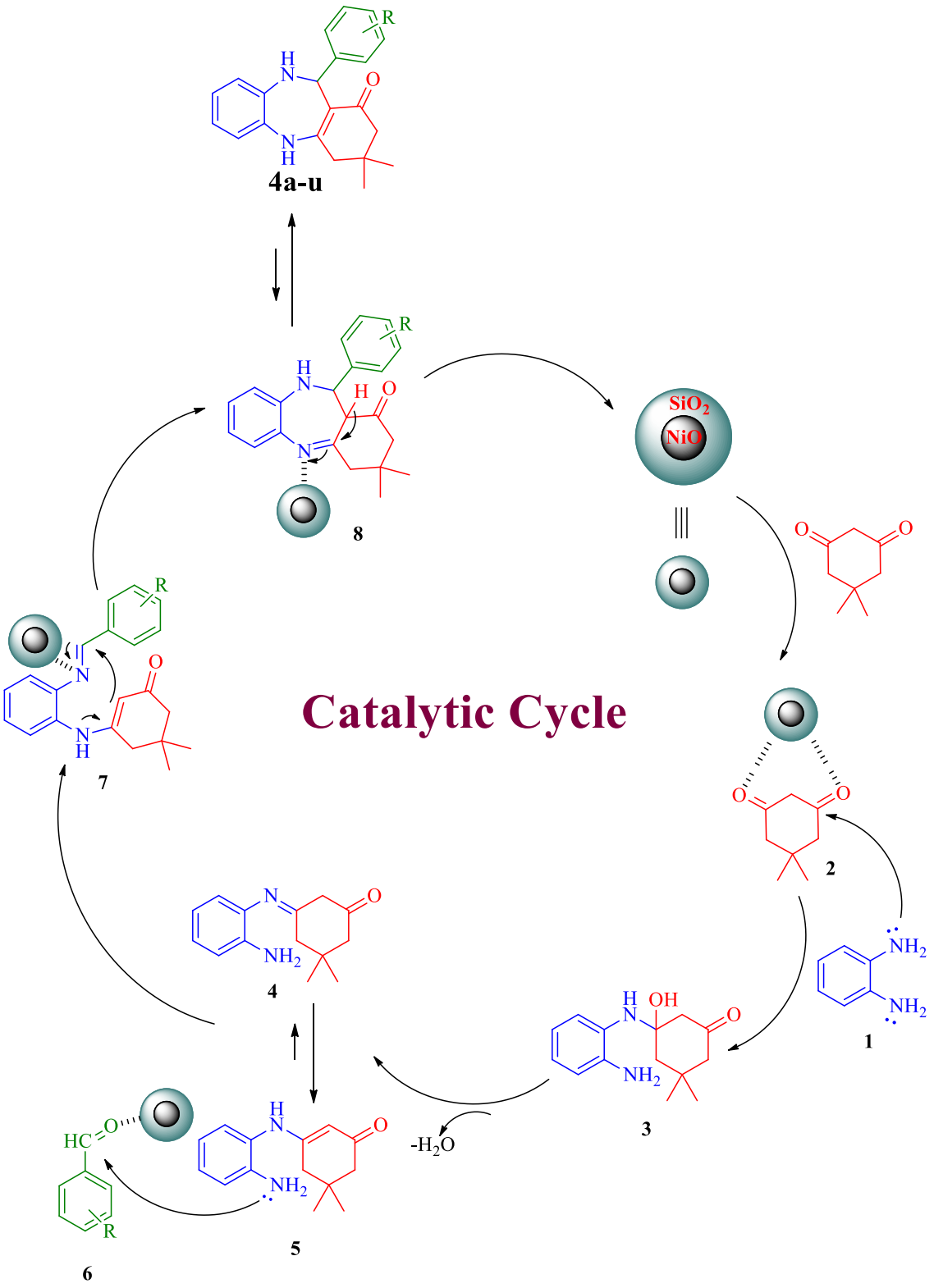

Scheme 4.7. Plausible reaction mechanism for the synthesis of benzodiazepines **4a-u**.

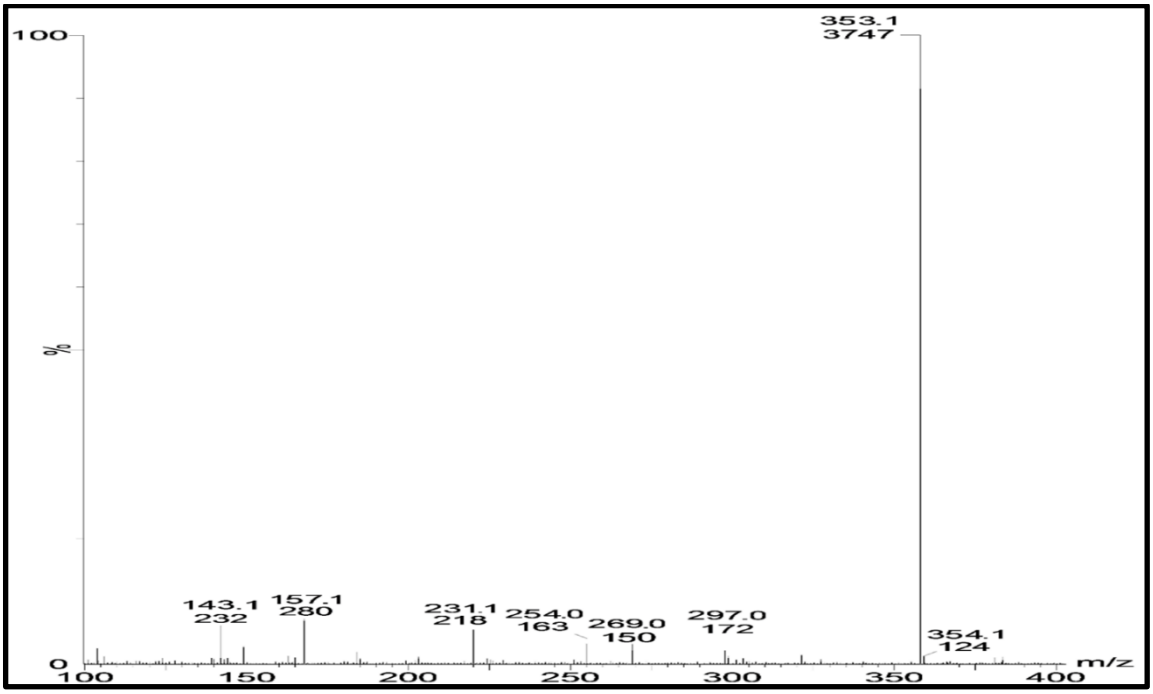

Figure 4.9. HRMS spectrum of 11-(3,5-difluorophenyl)-3,3-dimethyl-2,3,4,5,10,11-hexahydro-1H-dibenzo[b,e][1,4]diazepin-1-one **(4a)**.

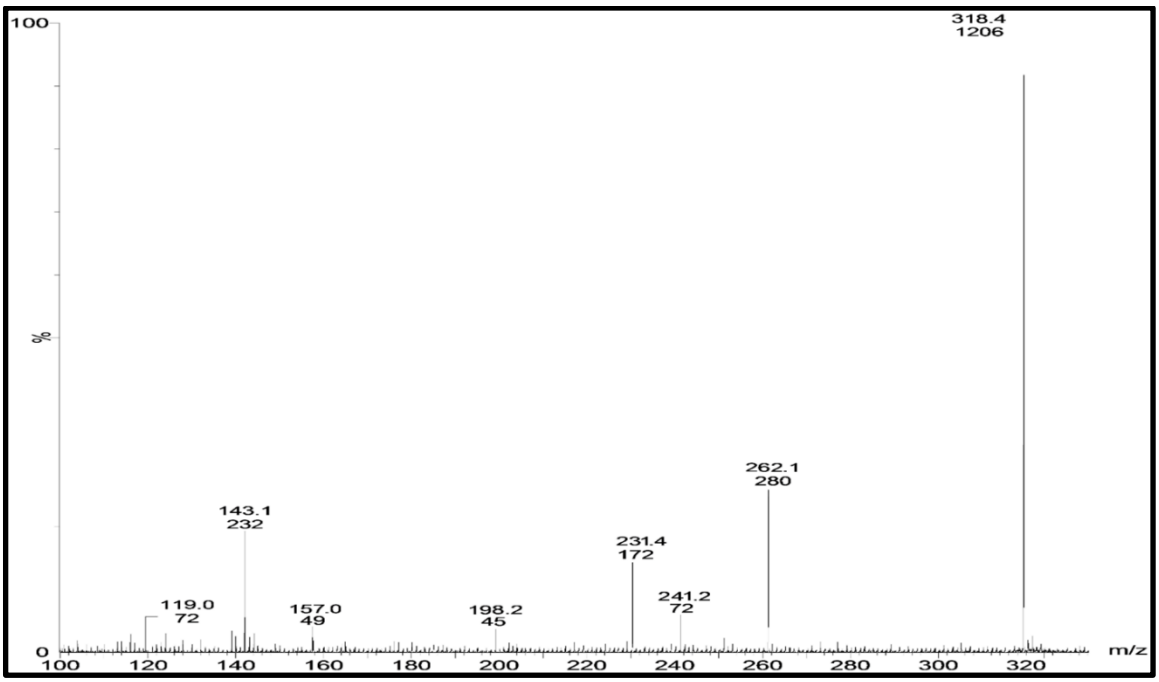

Figure 4.10. HRMS spectrum of 3,3-dimethyl-11-(pyridin-2-yl)-2,3,4,5,10,11-hexahydro-1H-dibenzo[b,e][1,4]diazepin-1-one **(4b)**.

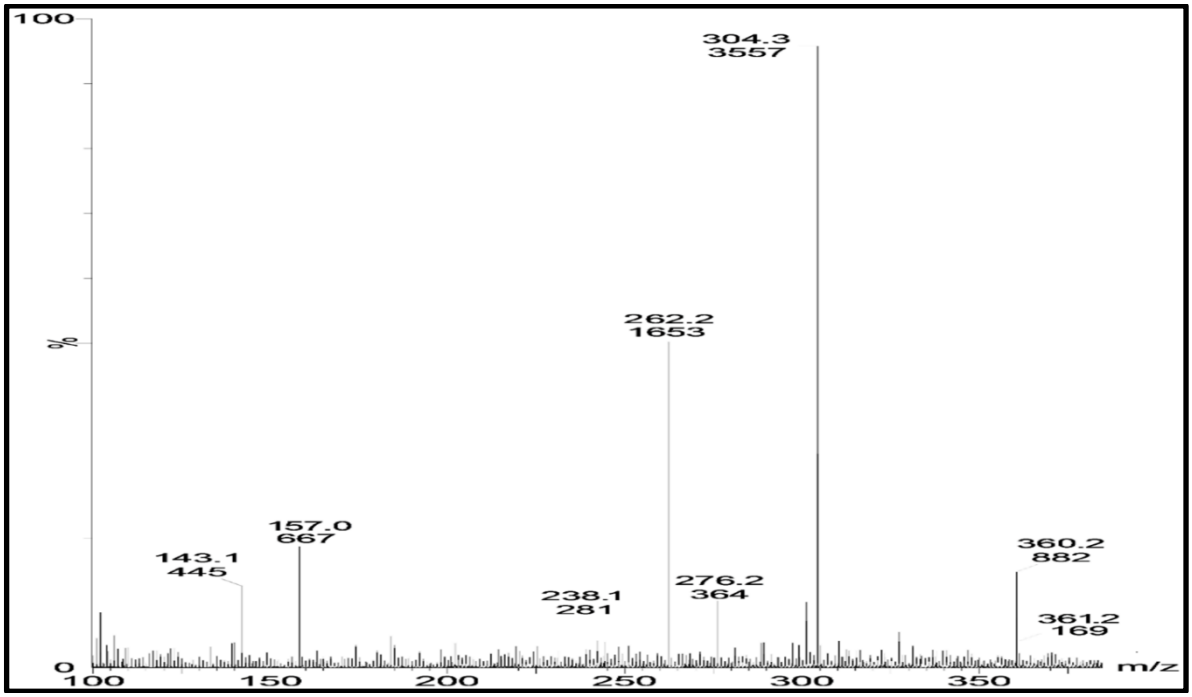

Figure 4.11. HRMS spectrum of 11-(4-(dimethylamino)phenyl)-3,3-dimethyl-2,3,4,5,10,11-hexahydro-1H-dibenzo[b,e][1,4]diazepin-1-one **(4e)**.

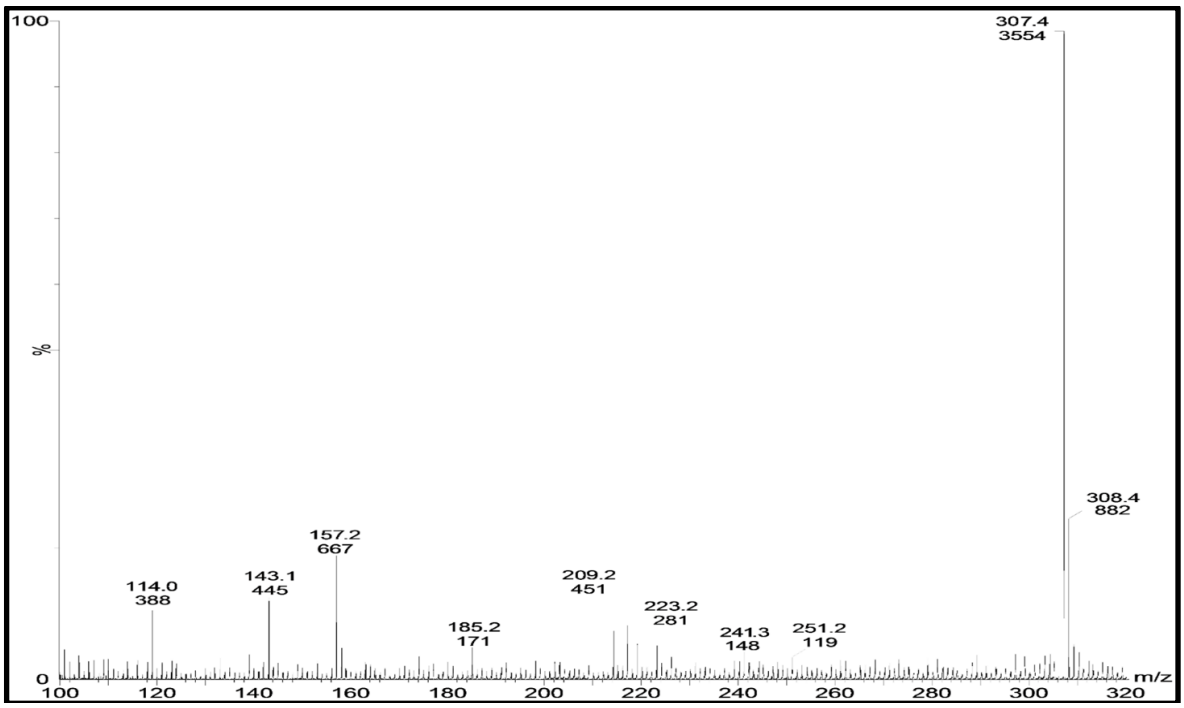

Figure 4.12. HRMS spectrum of 11-(furan-2-yl)-3,3-dimethyl-2,3,4,5,10,11-hexahydro-1H-dibenzo[b,e][1,4]diazepin-1-one **(4f)**.

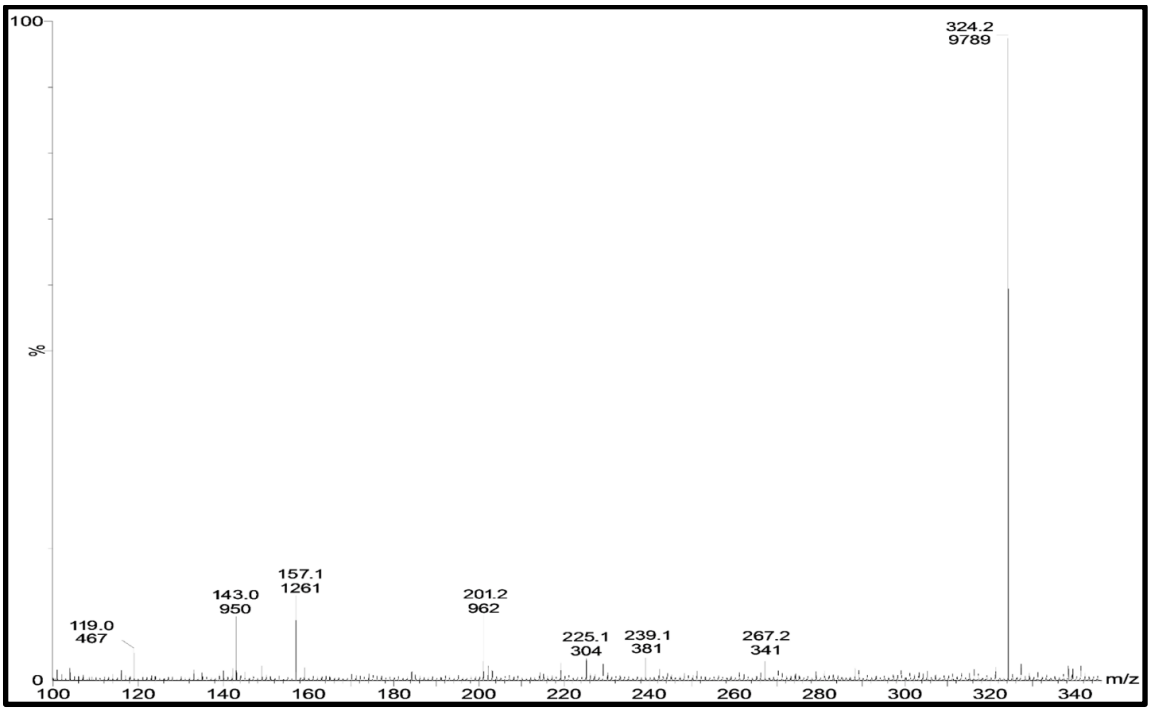

Figure 4.13. HRMS spectrum of 3,3-dimethyl-11-(thiophen-2-yl)-2,3,4,5,10,11-hexahydro-1H-dibenzo[b,e][1,4]diazepin-1-one **(4g)**.

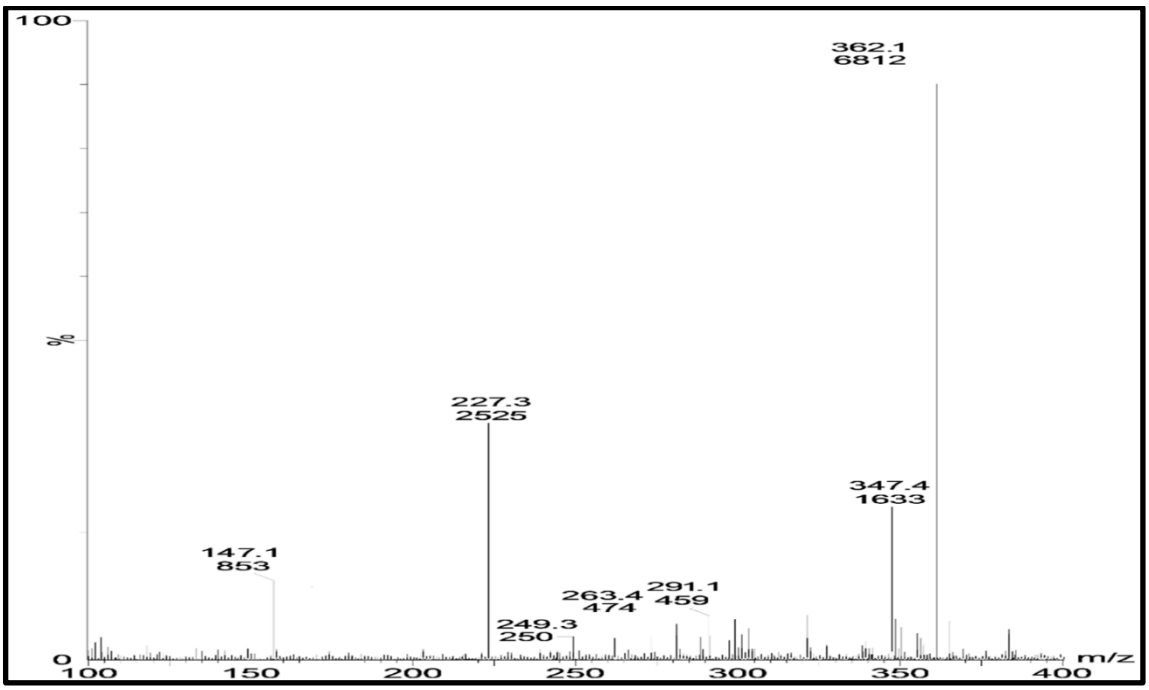

Figure 4.14. HRMS spectrum of 11-(2-hydroxy-3-methoxyphenyl)-3,3-dimethyl-2,3,4,5,10,11-hexahydro-1H-dibenzo[b,e][1,4]diazepin-1-one **(4h)**.

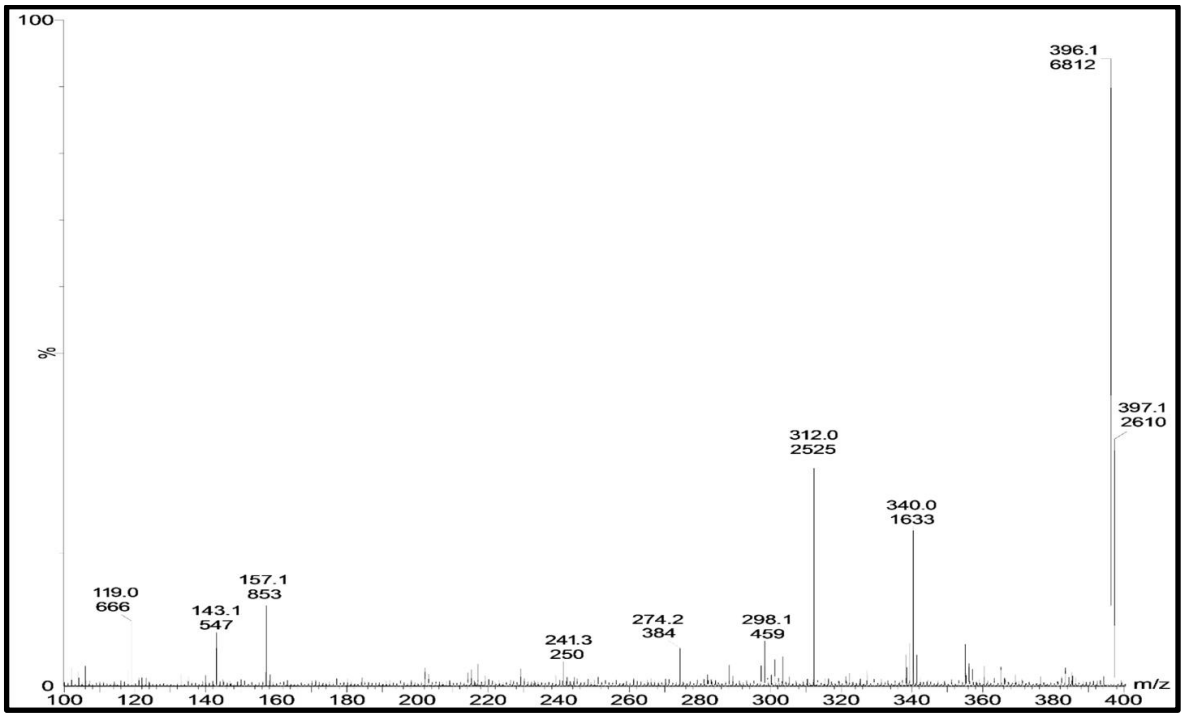

Figure 4.15. HRMS spectrum of 11-(4-chloro-3-nitrophenyl)-3,3-dimethyl-2,3,4,5,10,11-hexahydro-1H-dibenzo[b,e][1,4]diazepin-1-one **(4j)**.

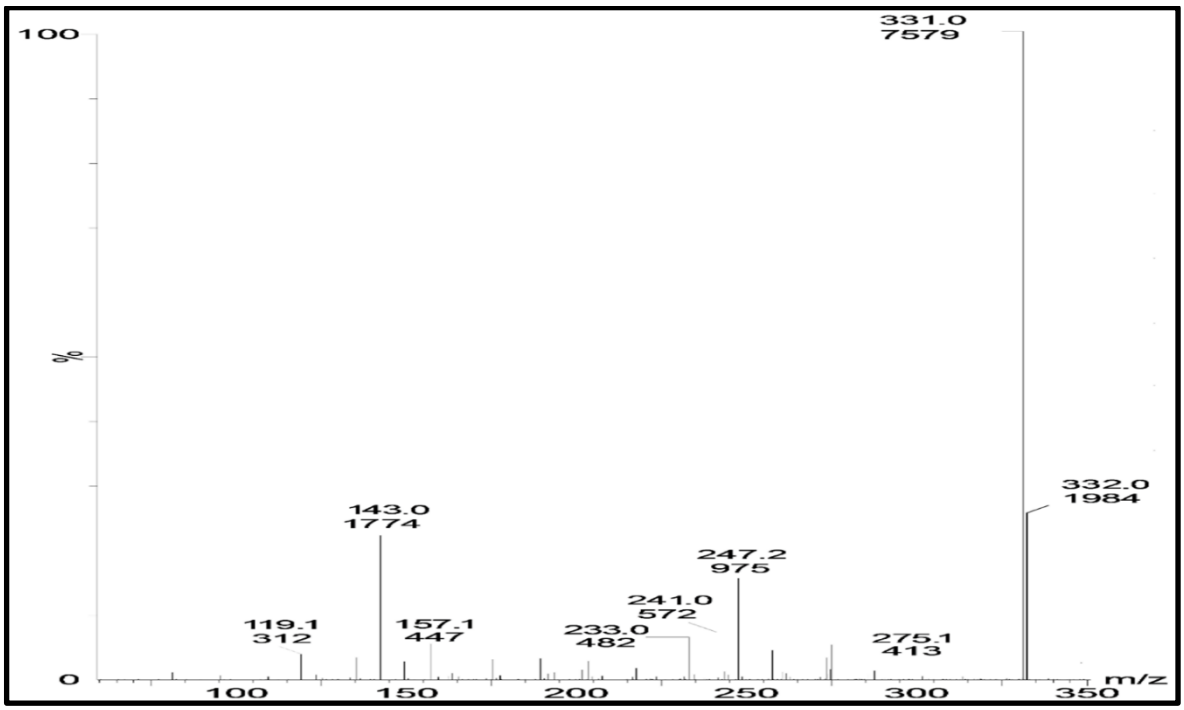

Figure 4.16. HRMS spectrum of 3,3-dimethyl-11-(*p*-tolyl)-2,3,4,5,10,11-hexahydro-1H-dibenzo[b,e][1,4]diazepin-1-one **(4k)**.

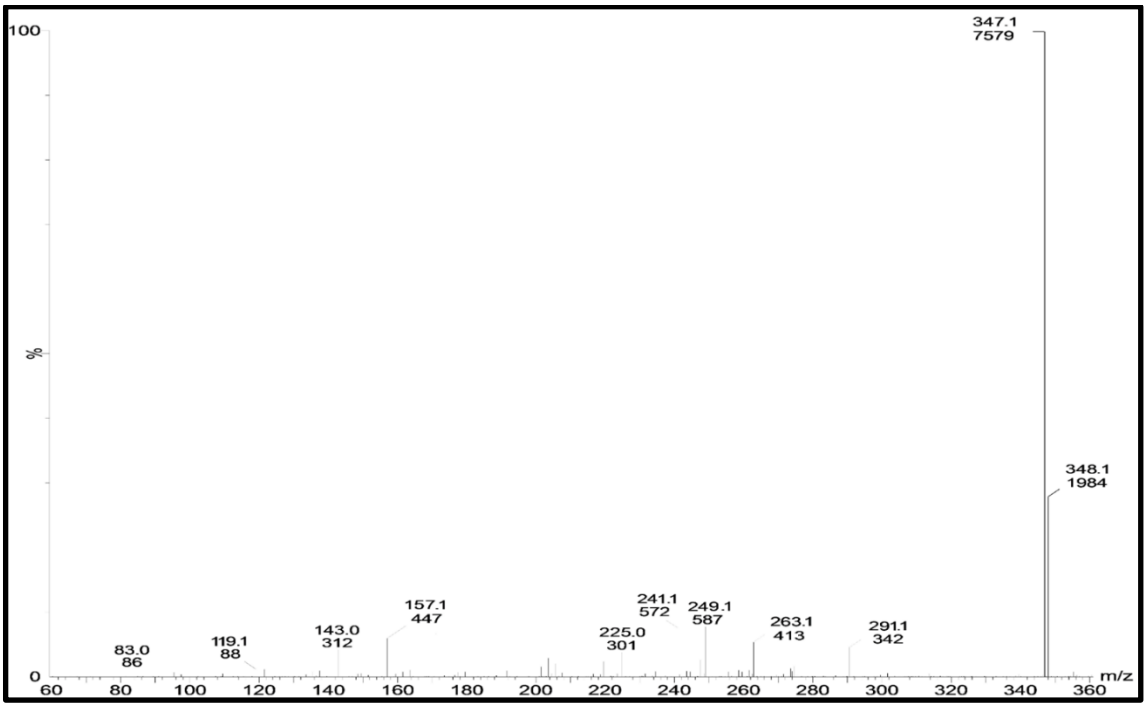

Figure 4.17. HRMS spectrum of 11-(4-methoxyphenyl)-3,3-dimethyl-2,3,4,5,10,11-hexahydro-1H-dibenzo[b,e][1,4]diazepin-1-one **(4l)**.

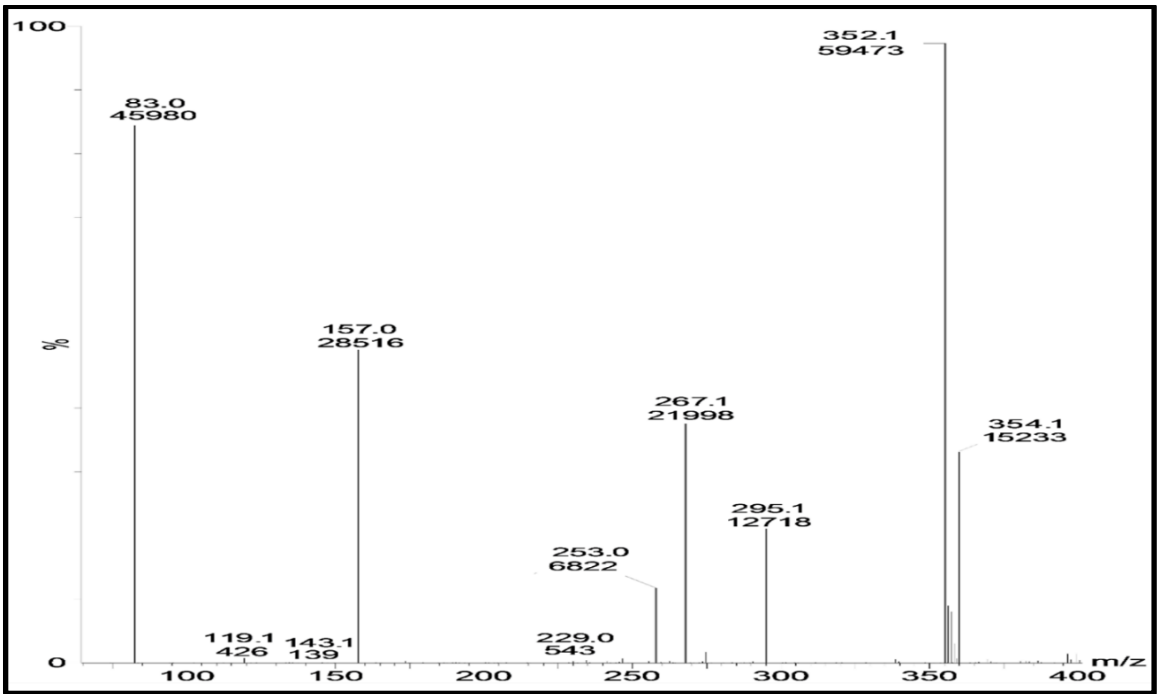

Figure 4.18. HRMS spectrum of 11-(4-chlorophenyl)-3,3-dimethyl-2,3,4,5,10,11-hexahydro-1H-dibenzo[b,e][1,4]diazepin-1-one **(4o)**.

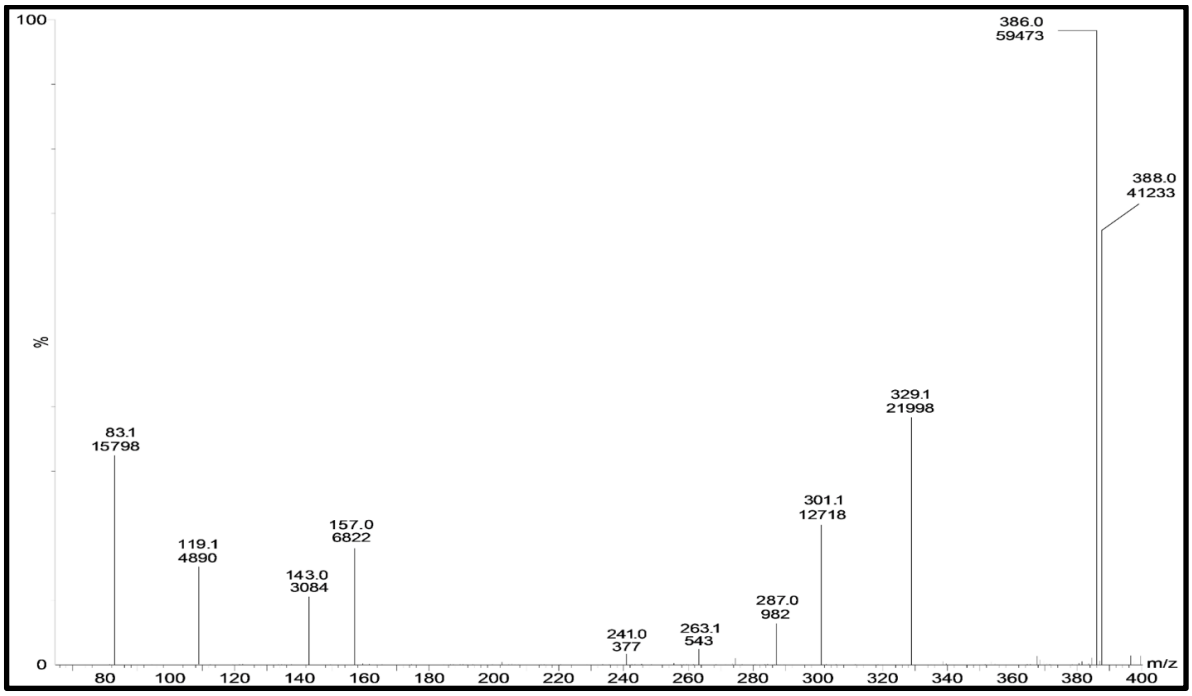

Figure 4.19. HRMS spectrum of 11-(2,4-dichlorophenyl)-3,3-dimethyl-2,3,4,5,10,11-hexahydro-1H-dibenzo[b,e][1,4]diazepin-1-one **(4q)**.

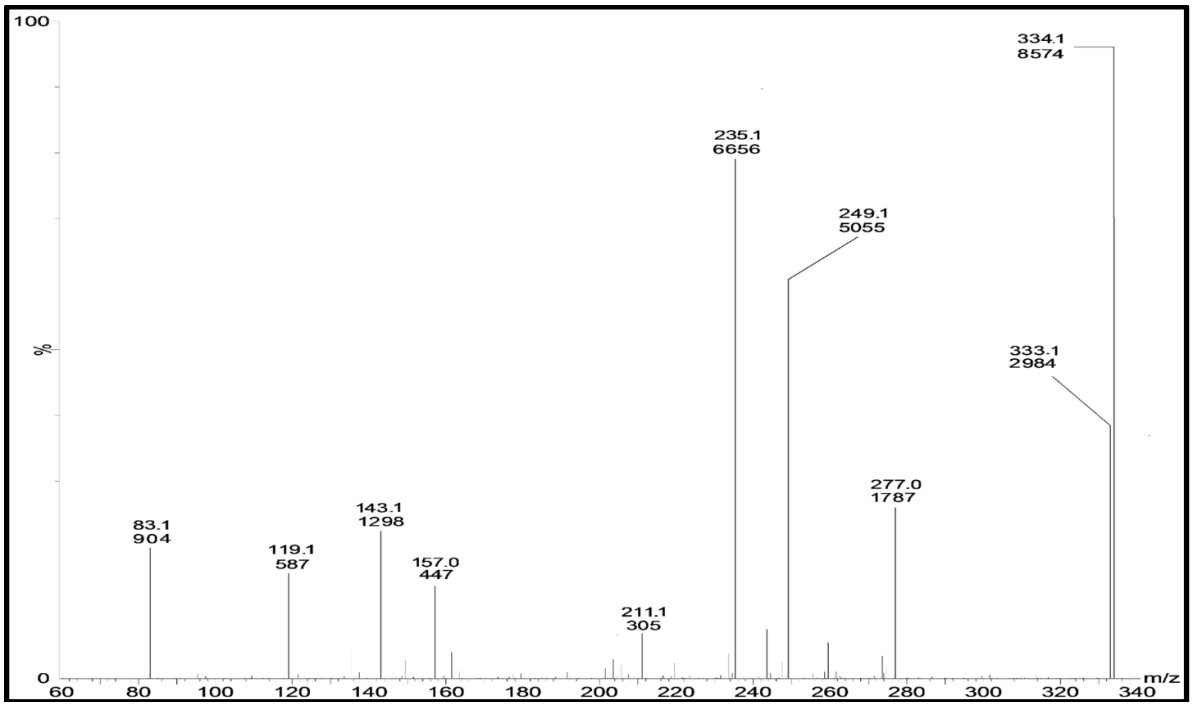

Figure 4.20. HRMS spectrum of 11-(3-hydroxyphenyl)-3,3-dimethyl-2,3,4,5,10,11-hexahydro-1H-dibenzo[b,e][1,4]diazepin-1-one **(4u)**.

4.2.4. Reusability of the catalyst

To establish the heterogeneous character of the catalyst, recycling experiments were carried out under microwave irradiation using selected model reaction **4e** in order to explore the extent of recyclability of our catalytic system (NiO@SiO_2 NCs) and reduce the cost of the process (**Scheme 4.8**).

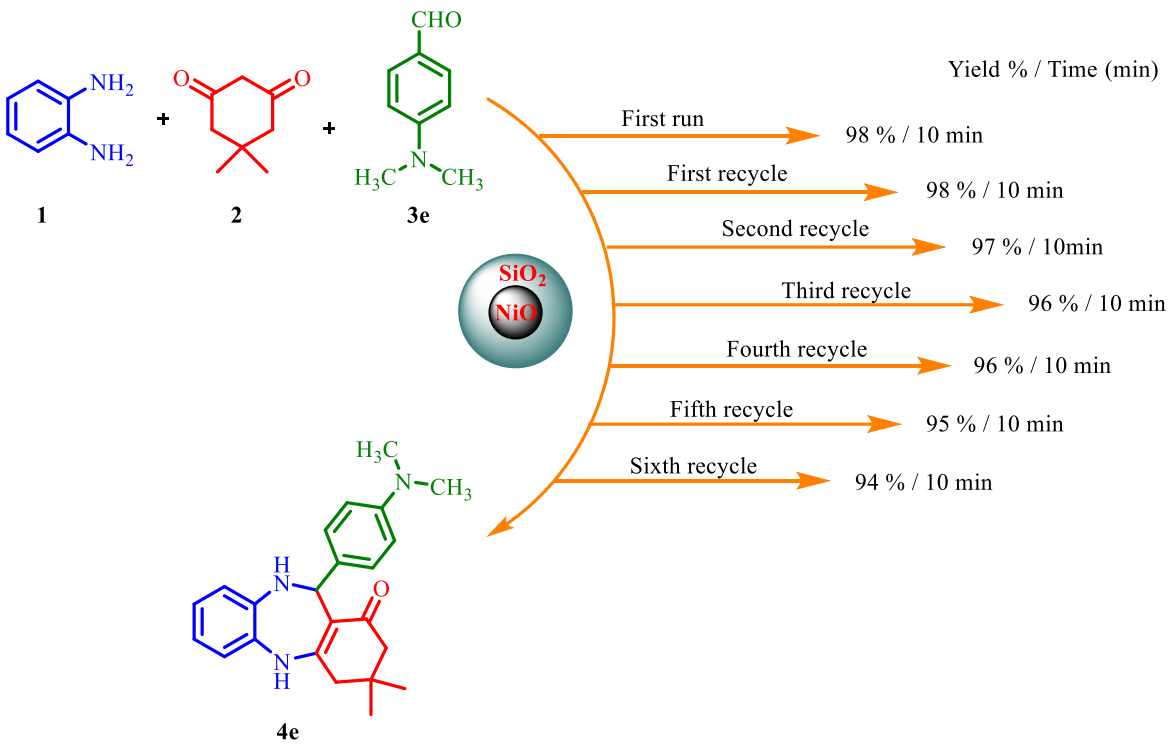

Scheme 4.8. Schematic representation of reusability of NiO@SiO_2 NCs for the model reaction **4e**.

After the first fresh run with 98% yield, the catalyst was recovered by simple filtration, washed with ethanol/ethylacetate and dried at 155 ^{o}C for 18 h and reused up to six more run with a minor loss in catalytic activity. The XRF analysis of the catalyst before (4.32 % w/w Ni) and after recycling experiments (4.25 % w/w Ni) revealed that the metal concentration remained unchanged with a very marginal reduction (within the experimental error of XRF analysis) (**Table 4.5**). This indicates that metal is tightly bound to the support and leaching of Ni(II) does not takes place during the course of reaction. The SEM image (**Fig. 4.3b**) of the catalyst after 7 runs showed no significant changes in the morphology indicating substantial retention of the catalytic activity throughout the recycling processes.

Table 4.5. Composition of NiO@SiO_2 NCs determined by XRF analysis.

Entry	Compound/element	Concentration (% w/w)	
		Fresh catalyst	Recycled catalyst (after 7 runs)
1.	SiO_2	82.51	83.22
2.	C	8.47	8.19
3.	Si	3.46	3.21
4.	Ni	4.32	4.25
5.	O	0.81	0.68
6.	Na	0.07	0.04
7.	others	0.13	0.09

4.3. Experimental

4.3.1. Materials and methods

All chemicals and reagents were purchased from Merck and Sigma-Aldrich (India) as 'analytical grade' and used without further purification. The microwave synthesis was performed in Anton Paar, Monowave 300 microwave synthesizer. Melting points were determined on a Biogen digital auto melting point apparatus. The IR spectra were recorded on KBr pellets with Perkin Elmer FT-IR Spectrometer spectrum Two and values are given in cm^{-1}. ^{1}H and ^{13}C NMR spectra were run in DMSO-d_6/$CDCl_3$ on a Bruker Avance-II 400 NMR Spectrometer (operating at 400 MHz for ^{1}H and at 100 MHz for ^{13}C NMR) with TMS as an internal standard and values are given in parts per million (ppm) (δ). Mass spectra were recorded on a Waters, Micromass Q-TOF micro YB361, UK. Elemental analysis of all the new compounds were recorded on Perkin Elmer 2400 CHN Elemental Analyzer. XRD of the catalyst were recorded in the 2θ range of 20-80° with a scan rate of 41 min^{-1} on a Shimadzu-6100 X-ray diffractometer with Ni-filtered Cu Kα radiation at a wavelength of 1.54060 Å. The SEM-EDS analysis was obtained using JEOL (JSM-6510) instrument. HR-TEM micrographs were recorded by JEOL TEM (JEM 2100F) instrument. Thin layer chromatography (TLC) glass plates (20×5 cm) were coated with silica gel G (Merck) using benzene-acetone (8:2) mixture as mobile phase and exposed to iodine vapors to check the homogeneity as well as the progress of the reaction. Sodium sulfate (anhydrous) was used as a drying agent.

4.3.2. Preparation of silica supported nickel oxide nanocomposites (NiO@SiO_2 NCs)

NiO@SiO_2 NCs were synthesized *via* sol-gel technique. For the synthesis of NiO@SiO_2 NCs, $Ni(NO_3)_2{\cdot}6H_2O$ is used as a precursor. 20 mL TEOS was mixed with ethyl alcohol (C_2H_5OH), ultrapure water (H_2O) and nitric acid (HNO_3) under vigorous stirring for 1 h to form a homogeneous solution. The overall molar ratio of TEOS:C_2H_5OH:H_2O:HNO_3 was 1:4:8:0.02. An aqueous solution of $Ni(NO_3)_2{\cdot}6H_2O$ was added into the above solution under vigorous stirring for 60 min. The prepared samples were aged for 24 h. Finally, the samples were evaporated and dried at 80 °C, followed by calcination at 400 °C for 3 h in air.

4.3.3. General procedure for the synthesis of benzodiazepine derivatives (4a-u) under microwave irradiation

A mixture of *o*-phenylenediamine **1** (1 mmol, 0.108 g), dimedone **2** (1 mmol, 0.140 g), aromatic aldehydes **3a-u** (1 mmol) and NiO@SiO_2 NCs (0.05 g) in EtOH (5 mL) was taken in a G30 vial and irradiated using microwaves with continuous stirring at 70 °C for 20-25 min. After completion of reaction (monitored by TLC for the purity), the reaction mixture was allowed to cool at room temperature and the catalyst was separated from the reaction mixture by filtration, and the residue was washed with EtOH to give benzodiazepine derivatives **4a-u**.[64] The recovered catalyst was reused for subsequent cycles without a significant loss in yield.

***11-(3,5-difluorophenyl)-3,3-dimethyl-2,3,4,5,10,11-hexahydro-1H-dibenzo[b,e][1,4]diazepin-1-one* (4a):**

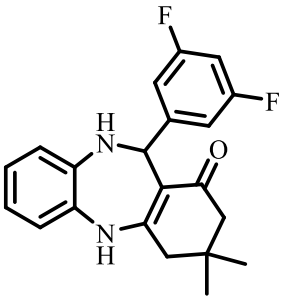

IR (KBr, ν cm^{-1}): 3082, 1559, 1386 (C-H, aromatic), 3302, 3218 (NH), 1615 (C=C), 1633 (C=O), 1168, 1159 (2×C-F); ^{1}H NMR (400 MHz, DMSO-d_6 + $CDCl_3$): δ 0.97 (3H, s, CH_3), 1.04 (3H, s, CH_3), 2.09 (2H, s, CH_2), 2.32 (2H, s, CH_2-C=O), 5.74 (1H, s, CH), 6.12 (s, 1H, NH, exchangeable with D_2O), 8.63 (s, 1H, NH, exchangeable with D_2O), 6.57-7.01 (m, 7H, C_6H_4, C_6H_3); ^{13}C NMR (100 MHz, DMSO-d_6 + $CDCl_3$): δ 28.3, 29.1, 35.5, 41.3, 52.6, 54.1, 106.7, 110.8, 116.2, 119.9, 125.1, 127.9, 132.7, 137.1, 138.5, 140.1, 142.5, 146.2, 157.3, 161.5,

195.0; Anal. Calcd for $C_{21}H_{20}F_2N_2O$; C, 71.17; H, 5.69; N, 7.90 found; C, 71.19; H, 5.70; N, 7.88; MS (EI): *m/z* 354 ($M^{+\cdot}$).

***3,3-dimethyl-11-(pyridin-2-yl)-2,3,4,5,10,11-hexahydro-1H-dibenzo[b,e][1,4]diazepin-1-one* (4b):**

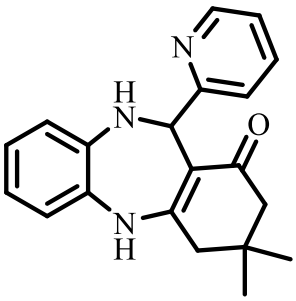

IR (KBr, ν cm^{-1}): 3084, 1556, 1384 (C-H, aromatic), 1634 (C=N), 3304, 3219 (NH), 1612 (C=C), 1630 (C=O); ^{1}H NMR (400 MHz, DMSO-d_6 + $CDCl_3$): δ 0.94 (3H, s, CH_3), 1.01 (3H, s, CH_3), 2.20 (2H, s, CH_2), 2.46 (2H, s, CH_2-C=O), 5.62 (1H, s, CH), 6.06 (s, 1H, NH, exchangeable with D_2O), 8.31 (s, 1H, NH, exchangeable with D_2O), 6.52-7.67 (m, 8H, C_6H_4, C_5H_4N); ^{13}C NMR (100 MHz, DMSO-d_6 + $CDCl_3$): δ 28.2, 29.4, 33.6, 42.3, 53.1, 55.3, 109.2, 117.4, 120.7, 122.1, 123.2, 125.9, 126.3, 128.1, 139.3, 141.5, 143.5, 150.2, 157.6, 196.7; Anal. Calcd for $C_{20}H_{21}N_3O$; C, 75.21; H, 6.63; N, 13.16 found; C, 75.19; H, 6.64; N, 13.14; MS (EI): *m/z* 319 ($M^{+\cdot}$).

***3,3-dimethyl-11-(pyridin-3-yl)-2,3,4,5,10,11-hexahydro-1H-dibenzo[b,e][1,4]diazepin-1-one* (4c):**

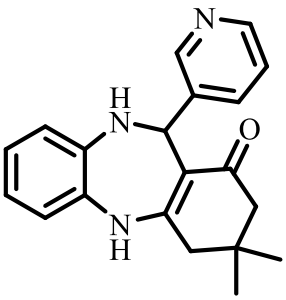

IR (KBr, ν cm^{-1}): 3081, 1553, 1381 (C-H, aromatic), 1633 (C=N), 3317, 3210 (NH), 1620 (C=C), 1627 (C=O); ^{1}H NMR (400 MHz, DMSO-d_6 + $CDCl_3$): δ 0.96 (3H, s, CH_3), 1.05 (3H, s, CH_3), 2.12 (2H, s, CH_2), 2.50 (2H, s, CH_2-C=O), 5.67 (1H, s, CH), 6.11 (s, 1H, NH, exchangeable with D_2O), 8.39 (s, 1H, NH, exchangeable with D_2O), 6.54-7.71 (m, 8H, C_6H_4, C_5H_4N); ^{13}C NMR (100 MHz, DMSO-d_6 + $CDCl_3$): δ 28.7, 29.1, 34.6, 41.2, 54.5, 57.1, 110.3, 116.1, 121.3, 124.2, 125.5, 126.3, 127.2, 130.0, 138.1, 142.8, 145.2, 153.1, 158.4, 194.6; Anal. Calcd for $C_{20}H_{21}N_3O$; C, 75.21; H, 6.63; N, 13.16 found; C, 75.23; H, 6.62; N, 13.17; MS (EI): *m/z* 319 ($M^{+\cdot}$).

***3,3-dimethyl-11-(pyridin-4-yl)-2,3,4,5,10,11-hexahydro-1H-dibenzo[b,e][1,4]diazepin-1-one* (4d):**

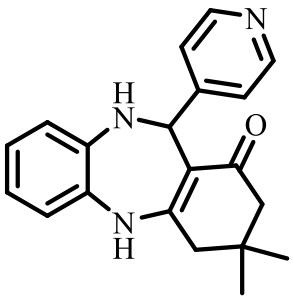

IR (KBr, ν cm^{-1}): 3086, 1558, 1380 (C-H, aromatic), 1636 (C=N), 3312, 3220 (NH), 1617 (C=C), 1624 (C=O); ^{1}H NMR (400 MHz, DMSO-d_6 + $CDCl_3$): δ 0.98 (3H, s, CH_3), 1.02 (3H, s, CH_3), 2.17 (2H, s, CH_2), 2.55 (2H, s, CH_2-C=O), 5.62 (1H, s, CH), 6.19 (s, 1H, NH, exchangeable with D_2O), 8.32 (s, 1H, NH, exchangeable with D_2O), 6.50-7.89 (m, 8H, C_6H_4, C_5H_4N); ^{13}C NMR (100 MHz, DMSO-d_6 + $CDCl_3$): δ 28.5, 29.2, 33.3, 43.1, 52.6, 56.9, 108.8, 118.5, 120.9, 123.0, 125.1, 127.7, 128.1, 131.1, 137.9, 143.4, 146.1, 155.6, 157.2, 197.4; Anal. Calcd for $C_{20}H_{21}N_3O$; C, 75.21; H, 6.63; N, 13.16 found; C, 75.17; H, 6.61; N, 13.15; MS (EI): *m/z* 319 ($M^{+\cdot}$).

***11-(4-(dimethylamino)phenyl)-3,3-dimethyl-2,3,4,5,10,11-hexahydro-1H-dibenzo[b,e][1,4]diazepin-1-one* (4e):**

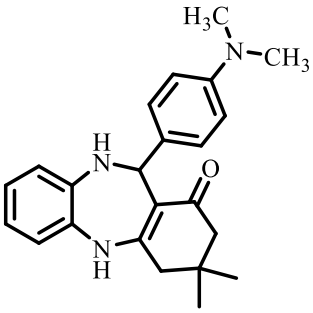

IR (KBr, ν cm^{-1}): 3078, 1560, 1389 (C-H, aromatic), 3320, 3225 (NH), 1622 (C=C), 1635 (C=O); ^{1}H NMR (400 MHz, DMSO-d_6 + $CDCl_3$): δ 1.04 (3H, s, CH_3), 1.07 (3H, s, CH_3), 2.15 (2H, s, CH_2), 2.49 (2H, s, CH_2-C=O), 5.59 (1H, s, CH), 6.01 (s, 1H, NH, exchangeable with D_2O), 8.59 (s, 1H, NH, exchangeable with D_2O), 2.55 {s, 6H, $N(CH_3)_2$}, 6.49-7.07 (m, 8H, C_6H_4, C_6H_4); ^{13}C NMR (100 MHz, DMSO-d_6 + $CDCl_3$): δ 28.6, 30.1, 34.1, 41.2, 42.4, 43.2, 54.6, 55.1, 108.6, 114.3, 115.1, 119.8, 124.4, 128.4, 129.2, 129.5, 130.7, 132.6, 134.3, 139.7, 144.6, 157.5, 194.3; Anal. Calcd for $C_{23}H_{27}N_3O$; C, 76.42; H, 7.53; N, 11.62 found; C, 76.44; H, 7.51; N, 11.59; MS (EI): *m/z* 361 ($M^{+\cdot}$).

***11-(furan-2-yl)-3,3-dimethyl-2,3,4,5,10,11-hexahydro-1H-dibenzo[b,e][1,4]diazepin-1-one* (4f):**

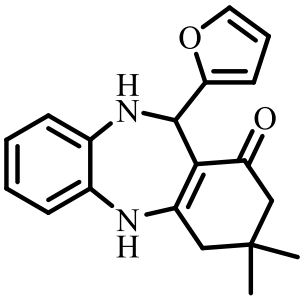

IR (KBr, ν cm^{-1}): 3085, 1550, 1378 (C-H, aromatic), 3326, 3231 (NH), 1621 (C=C), 1629 (C=O), 1058 (C-O); ^{1}H NMR (400 MHz, DMSO-d_6 + $CDCl_3$): δ 1.12 (3H, s, CH_3), 1.15 (3H, s, CH_3), 2.14 (2H, s, CH_2), 2.55 (2H, s, CH_2-C=O), 5.25 (1H, s, CH), 5.01 (s, 1H, NH, exchangeable with D_2O), 6.98 (s, 1H, NH, exchangeable with D_2O), 6.32-7.72 (m, 7H, C_6H_4, C_4H_3O); ^{13}C NMR (100 MHz, DMSO-d_6 + $CDCl_3$): δ 27.5, 29.3, 35.6, 45.1, 55.3, 57.8, 110.8, 111.1, 116.3, 117.3, 122.9, 123.1, 126.7, 131.2, 140.2, 143.8, 149.1, 158.4, 195.3; Anal. Calcd for $C_{19}H_{20}N_2O_2$; C, 74.00; H, 6.54; N, 9.08 found; C, 74.02; H, 6.52; N, 9.10; MS (EI): *m/z* 308 ($M^{+\cdot}$).

***3,3-dimethyl-11-(thiophen-2-yl)-2,3,4,5,10,11-hexahydro-1H-dibenzo[b,e][1,4]diazepin-1-one* (4g):**

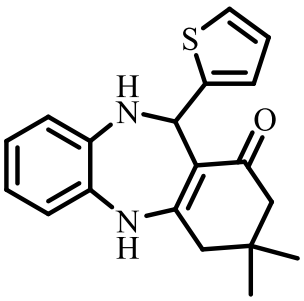

IR (KBr, ν cm^{-1}): 3092, 1562, 1381 (C-H, aromatic), 3315, 3255 (NH), 1627 (C=C), 1632 (C=O), 718 (C-S); ^{1}H NMR (400 MHz, DMSO-d_6 + $CDCl_3$): δ 1.06 (3H, s, CH_3), 1.13 (3H, s, CH_3), 2.19 (2H, s, CH_2), 2.52 (2H, s, CH_2-C=O), 5.69 (1H, s, CH), 6.07 (s, 1H, NH, exchangeable with D_2O), 8.62 (s, 1H, NH, exchangeable with D_2O), 6.53-7.49 (m, 7H, C_6H_4, C_4H_3S); ^{13}C NMR (100 MHz, DMSO-d_6 + $CDCl_3$): δ 27.9, 29.1, 31.7, 43.0, 53.2, 58.6, 112.0, 120.4, 123.9, 126.4, 127.4, 129.0, 130.7, 131.5, 132.3, 138.1, 142.5, 156.4, 194.8; Anal. Calcd for $C_{19}H_{20}N_2OS$; C, 70.34; H, 6.21; N, 8.63 found; C, 70.31; H, 6.22; N, 8.61; MS (EI): *m/z* 324 ($M^{+\cdot}$).

***11-(2-hydroxy-3-methoxyphenyl)-3,3-dimethyl-2,3,4,5,10,11-hexahydro-1H-dibenzo[b,e][1,4]diazepin-1-one* (4h):**

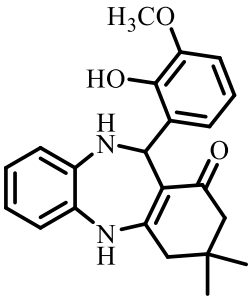

IR (KBr, ν cm^{-1}): 3089, 1561, 1384 (C-H, aromatic), 3311, 3239 (NH), 1625 (C=C), 1631 (C=O), 1059 (C-O), 3221 (O-H), 2825 (OCH_3); ^{1}H NMR (400 MHz, DMSO-d_6 + $CDCl_3$): δ 1.09 (3H, s, CH_3), 1.17 (3H, s, CH_3), 2.17 (2H, s, CH_2), 2.51 (2H, s, CH_2-C=O), 5.57 (1H, s, CH), 6.02 (s, 1H, NH, exchangeable with D_2O), 8.65 (s, 1H, NH, exchangeable with D_2O), 8.89 (1H, s, OH), 3.79 (3H, s, OCH_3), 6.47-6.99 (m, 7H, C_6H_4, C_6H_3); ^{13}C NMR (100 MHz, DMSO-d_6 + $CDCl_3$): δ 28.2, 29.9, 35.5, 47.4, 52.3, 56.1, 60.1, 109.9, 113.7, 125.3, 126.6, 127.5, 129.9, 131.2, 132.8, 133.1, 135.7, 139.8, 144.5, 159.2, 161.5, 197.6; Anal. Calcd for $C_{22}H_{24}N_2O_3$; C, 72.50; H, 6.64; N, 7.69 found; C, 72.48; H, 6.63; N, 7.71; MS (EI): *m/z* 364 ($M^{+\cdot}$).

***3,3-dimethyl-11-(5-nitrothiophen-2-yl)-2,3,4,5,10,11-hexahydro-1H-dibenzo[b,e][1,4]diazepin-1-one* (4i):**

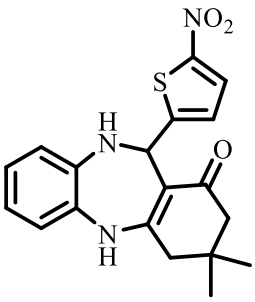

IR (KBr, ν cm^{-1}): 3098, 1572, 1390 (C-H, aromatic), 3341, 3255 (NH), 1630 (C=C), 1633 (C=O), 1535, 1355 (N-O), 715 (C-S); ^{1}H NMR (400 MHz, DMSO-d_6 + $CDCl_3$): δ 0.99 (3H, s, CH_3), 1.07 (3H, s, CH_3), 2.24 (2H, s, CH_2), 2.55 (2H, s, CH_2-C=O), 5.83 (1H, s, CH), 6.30 (s, 1H, NH, exchangeable with D_2O), 8.87 (s, 1H, NH, exchangeable with D_2O), 6.62-7.92 (m, 6H, C_6H_4, C_4H_2S); ^{13}C NMR (100 MHz, DMSO-d_6 + $CDCl_3$): δ 28.3, 29.7, 32.4, 45.1, 54.4, 61.1, 110.9, 121.7, 125.1, 128.7, 129.9, 132.2, 133.8, 135.6, 140.4, 142.7, 153.2, 159.5, 194.8 Anal. Calcd for $C_{19}H_{19}N_3O_3S$; C, 61.77; H, 5.18; N, 11.37 found; C, 61.79; H, 5.20; N, 11.36; MS (EI): *m/z* 369 ($M^{+\cdot}$).

***11-(4-chloro-3-nitrophenyl)-3,3-dimethyl-2,3,4,5,10,11-hexahydro-1H-dibenzo[b,e][1,4]diazepin-1-one* (4j):**

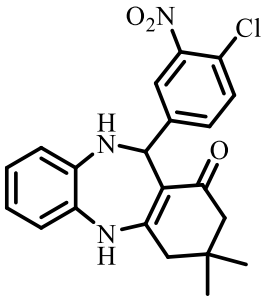

IR (KBr, ν cm^{-1}): 3095, 1569, 1389 (C-H, aromatic), 3317, 3245 (NH), 1628 (C=C), 1632 (C=O), 1533, 1341 (N-O), 742 (C-Cl); ^{1}H NMR (400 MHz, DMSO-d_6 + $CDCl_3$): δ 1.04 (3H, s, CH_3), 1.11 (3H, s, CH_3), 2.19 (2H, s, CH_2), 2.57 (2H, s, CH_2-C=O), 6.01 (1H, s, CH), 5.98 (s, 1H, NH, exchangeable with D_2O), 8.82 (s, 1H, NH, exchangeable with D_2O), 6.57-7.99 (m, 7H, C_6H_4, C_6H_3); ^{13}C NMR (100 MHz, DMSO-d_6 + $CDCl_3$): δ 27.7, 29.1, 34.2, 44.7, 56.2, 60.1, 107.2, 120.1, 121.7, 124.4, 127.1, 131.2, 133.3, 136.3, 139.2, 141.1, 143.2, 145.1, 149.2, 155.1, 196.2; Anal. Calcd for $C_{21}H_{20}ClN_3O_3$; C, 63.40; H, 5.07; N, 10.56 found; C, 63.42; H, 5.08; N, 10.54; MS (EI): *m/z* 397/399 ($M^{+\cdot}$).

***3,3-dimethyl-11-(p-tolyl)-2,3,4,5,10,11-hexahydro-1H-dibenzo[b,e][1,4]diazepin-1-one* (4k):**

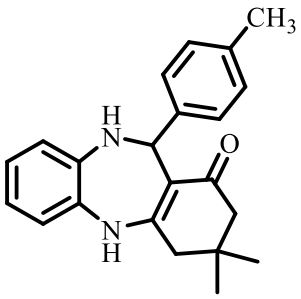

IR (KBr, ν cm^{-1}): 3092, 1571, 1385 (C-H, aromatic), 3321, 3251 (NH), 1629 (C=C), 1632 (C=O); ^{1}H NMR (400 MHz, DMSO-d_6 + $CDCl_3$): δ 1.07 (3H, s, CH_3), 1.13 (3H, s, CH_3), 2.07 (2H, s, CH_2), 2.51 (2H, s, CH_2-C=O), 2.29 (3H, s, CH_3), 5.78 (1H, s, CH), 5.89 (s, 1H, NH, exchangeable with D_2O), 8.61 (s, 1H, NH, exchangeable with D_2O), 6.49-7.18 (m, 8H, C_6H_4, C_6H_4); ^{13}C NMR (100 MHz, DMSO-d_6 + $CDCl_3$): δ 25.9, 28.3, 29.4, 35.2, 45.5, 54.4, 63.3, 112.2, 119.1, 122.6, 126.2, 129.9, 136.2, 137.1, 139.2, 139.9, 140.6, 142.5, 145.1, 149.5, 152.1, 197.9; Anal. Calcd for $C_{22}H_{24}N_2O$; C, 79.48; H, 7.28; N, 8.43 found; C, 79.50; H, 7.27; N, 8.45; MS (EI): *m/z* 332 ($M^{+\cdot}$).

***11-(4-methoxyphenyl)-3,3-dimethyl-2,3,4,5,10,11-hexahydro-1H-dibenzo[b,e][1,4]diazepin-1-one* (4l):**

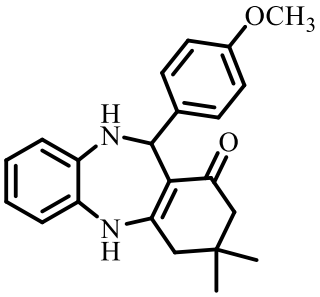

IR (KBr, ν cm^{-1}): 3078, 1558, 1378 (C-H, aromatic), 3345, 3255 (NH), 1626 (C=C), 1635 (C=O), 1057 (C-O), 2855 (OCH_3); ^{1}H NMR (400 MHz, DMSO-d_6 + $CDCl_3$): δ 1.05 (3H, s, CH_3), 1.11 (3H, s, CH_3), 2.15 (2H, s, CH_2), 2.58 (2H, s, CH_2-C=O), 5.62 (1H, s, CH), 5.92 (s, 1H, NH, exchangeable with D_2O), 8.59 (s, 1H, NH, exchangeable with D_2O), 3.57 (3H, s, OCH_3), 6.43-7.02 (m, 8H, C_6H_4, C_6H_4); ^{13}C NMR (100 MHz, DMSO-d_6 + $CDCl_3$): δ 27.7, 29.8, 33.1, 43.2, 56.7, 59.5, 61.8, 111.9, 119.6, 120.2, 121.5, 126.7, 129.3, 135.2, 139.5, 141.7, 142.3, 143.2, 144.3, 151.4, 168.7, 195.1; Anal. Calcd for $C_{22}H_{24}N_2O_2$; C, 75.83; H, 6.94; N, 8.04 found; C, 75.81; H, 6.93; N, 8.06; MS (EI): *m/z* 348 ($M^{+\cdot}$).

***11-(2-methoxyphenyl)-3,3-dimethyl-2,3,4,5,10,11-hexahydro-1H-dibenzo[b,e][1,4]diazepin-1-one* (4m):**

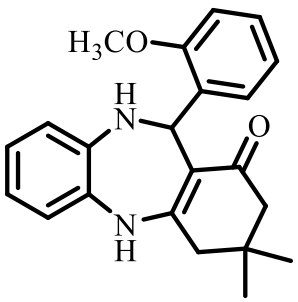

IR (KBr, ν cm^{-1}): 3071, 1560, 1373 (C-H, aromatic), 3342, 3252 (NH), 1627 (C=C), 1631 (C=O), 1061 (C-O), 2822 (OCH_3); ^{1}H NMR (400 MHz, DMSO-d_6 + $CDCl_3$): δ 1.02 (3H, s, CH_3), 1.17 (3H, s, CH_3), 2.21 (2H, s, CH_2), 2.61 (2H, s, CH_2-C=O), 5.91 (1H, s, CH), 5.83 (s, 1H, NH, exchangeable with D_2O), 8.65 (s, 1H, NH, exchangeable with D_2O), 3.81 (3H, s, OCH_3), 6.52-7.13 (m, 8H, C_6H_4, C_6H_4); ^{13}C NMR (100 MHz, DMSO-d_6 + $CDCl_3$): δ 28.3, 29.1, 35.4, 44.7, 55.5, 60.0, 62.2, 113.1, 121.6, 122.2, 126.4, 127.8, 131.2, 137.3, 140.6, 143.5, 144.5, 145.7, 146.2, 155.3, 167.5, 196.6; Anal. Calcd for $C_{22}H_{24}N_2O_2$; C, 75.83; H, 6.94; N, 8.04 found; C, 75.85; H, 6.96; N, 8.01; MS (EI): *m/z* 348 ($M^{+\cdot}$).

***11-(3-methoxyphenyl)-3,3-dimethyl-2,3,4,5,10,11-hexahydro-1H-dibenzo[b,e][1,4]diazepin-1-one* (4n):**

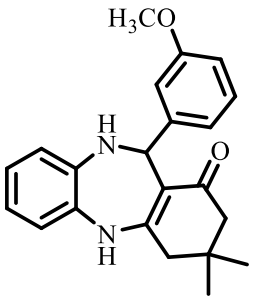

IR (KBr, ν cm^{-1}): 3079, 1565, 1372 (C-H, aromatic), 3339, 3268 (NH), 1623 (C=C), 1638 (C=O), 1058 (C-O), 2870 (OCH_3); ^{1}H NMR (400 MHz, DMSO-d_6 + $CDCl_3$): δ 1.09 (3H, s, CH_3), 1.15 (3H, s, CH_3), 2.19 (2H, s, CH_2), 2.59 (2H, s, CH_2-C=O), 5.80 (1H, s, CH), 5.78 (s, 1H, NH, exchangeable with D_2O), 8.61 (s, 1H, NH, exchangeable with D_2O), 3.59 (3H, s, OCH_3), 6.49-7.20 (m, 8H, C_6H_4, C_6H_4); ^{13}C NMR (100 MHz, DMSO-d_6 + $CDCl_3$): δ 27.6, 28.3, 34.2, 43.6, 56.6, 60.3, 61.2, 110.7, 122.6, 123.6, 125.2, 129.9, 133.6, 136.7, 142.8, 144.8, 145.8, 146.8, 147.1, 157.9, 168.4, 194.2; Anal. Calcd for $C_{22}H_{24}N_2O_2$; C, 75.83; H, 6.94; N, 8.04 found; C, 75.79; H, 6.95; N, 8.03; MS (EI): *m/z* 348 ($M^{+\cdot}$).

***11-(4-chlorophenyl)-3,3-dimethyl-2,3,4,5,10,11-hexahydro-1H-dibenzo[b,e][1,4]diazepin-1-one* (4o):**

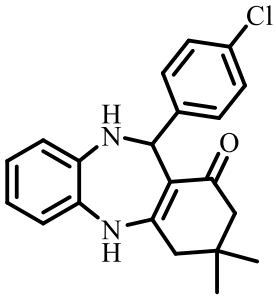

IR (KBr, ν cm^{-1}): 3081, 1562, 1380 (C-H, aromatic), 3341, 3262 (NH), 1629 (C=C), 1639 (C=O), 745 (C-Cl); ^{1}H NMR (400 MHz, DMSO-d_6 + $CDCl_3$): δ 1.12 (3H, s, CH_3), 1.22 (3H, s, CH_3), 2.16 (2H, s, CH_2), 2.55 (2H, s, CH_2-C=O), 5.83 (1H, s, CH), 5.75 (s, 1H, NH, exchangeable with D_2O), 8.58 (s, 1H, NH, exchangeable with D_2O), 6.50-7.17 (m, 8H, C_6H_4, C_6H_4); ^{13}C NMR (100 MHz, DMSO-d_6 + $CDCl_3$): δ 28.4, 30.2, 37.1, 48.2, 56.1, 62.2, 114.5, 121.6, 124.3, 129.5, 131.4, 136.4, 137.8, 138.2, 138.7, 139.9, 142.6, 145.8, 148.6, 152.4, 199.8; Anal. Calcd for $C_{21}H_{21}ClN_2O$; C, 71.48; H, 6.00; N, 7.94 found; C, 71.45; H, 6.01; N, 7.92; MS (EI): *m/z* 352/354 ($M^{+\cdot}$).

***11-(2-chlorophenyl)-3,3-dimethyl-2,3,4,5,10,11-hexahydro-1H-dibenzo[b,e][1,4]diazepin-1-one* (4p):**

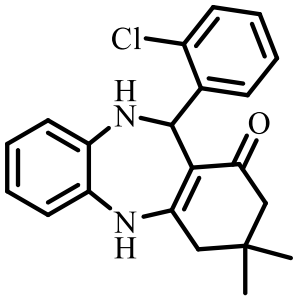

IR (KBr, ν cm^{-1}): 3078, 1564, 1375 (C-H, aromatic), 3337, 3265 (NH), 1612 (C=C), 1640 (C=O), 749 (C-Cl); ^{1}H NMR (400 MHz, DMSO-d_6 + $CDCl_3$): δ 1.10 (3H, s, CH_3), 1.19 (3H, s, CH_3), 2.14 (2H, s, CH_2), 2.59 (2H, s, CH_2-C=O), 5.98 (1H, s, CH), 5.71 (s, 1H, NH, exchangeable with D_2O), 8.67 (s, 1H, NH, exchangeable with D_2O), 6.47-7.23 (m, 8H, C_6H_4, C_6H_4); ^{13}C NMR (100 MHz, DMSO-d_6 + $CDCl_3$): δ 27.8, 29.9, 38.2, 47.6, 57.5, 65.8, 116.6, 120.5, 125.6, 128.4, 133.3, 137.8, 138.0, 138.6, 139.6, 140.2, 141.9, 147.7, 149.7, 154.8, 196.2; Anal. Calcd for $C_{21}H_{21}ClN_2O$; C, 71.48; H, 6.00; N, 7.94 found; C, 71.50; H, 5.99; N, 7.96; MS (EI): *m/z* 352/354 ($M^{+\cdot}$).

***11-(2,4-dichlorophenyl)-3,3-dimethyl-2,3,4,5,10,11-hexahydro-1H-dibenzo[b,e][1,4]diazepin-1-one* (4q):**

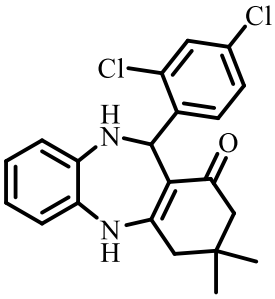

IR (KBr, ν cm^{-1}): 3091, 1571, 1381 (C-H, aromatic), 3326, 3254 (NH), 1621 (C=C), 1642 (C=O), 743 (C-Cl); ^{1}H NMR (400 MHz, DMSO-d_6 + $CDCl_3$): δ 1.09 (3H, s, CH_3), 1.21 (3H, s, CH_3), 2.12 (2H, s, CH_2), 2.61 (2H, s, CH_2-C=O), 5.95 (1H, s, CH), 5.26 (s, 1H, NH, exchangeable with D_2O), 8.71 (s, 1H, NH, exchangeable with D_2O), 6.48-7.52 (m, 7H, C_6H_4, C_6H_3); ^{13}C NMR (100 MHz, DMSO-d_6 + $CDCl_3$): δ 29.2, 30.6, 36.3, 47.2, 55.3, 66.1, 115.3, 122.4, 126.2, 127.6, 135.3, 137.8, 138.3, 140.3, 141.4, 145.2, 149.2, 149.9, 150.2, 154.6, 193.1; Anal. Calcd for $C_{21}H_{20}Cl_2N_2O$; C, 65.12; H, 5.20; N, 7.23 found; C, 65.10; H, 5.19; N, 7.25; MS (EI): *m/z* 386/388 ($M^{+\cdot}$).

***11-(2,3-dichlorophenyl)-3,3-dimethyl-2,3,4,5,10,11-hexahydro-1H-dibenzo[b,e][1,4]diazepin-1-one* (4r):**

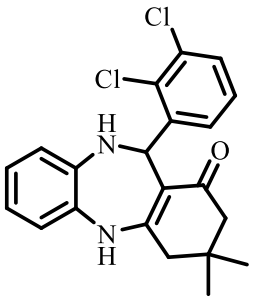

IR (KBr, ν cm^{-1}): 3085, 1560, 1389 (C-H, aromatic), 3348, 3261 (NH), 1623 (C=C), 1639 (C=O), 746 (C-Cl); ^{1}H NMR (400 MHz, DMSO-d_6 + $CDCl_3$): δ 1.05 (3H, s, CH_3), 1.18 (3H, s, CH_3), 2.09 (2H, s, CH_2), 2.63 (2H, s, CH_2-C=O), 5.97 (1H, s, CH), 5.12 (s, 1H, NH, exchangeable with D_2O), 8.69 (s, 1H, NH, exchangeable with D_2O), 6.56-7.45 (m, 7H, C_6H_4, C_6H_3); ^{13}C NMR (100 MHz, DMSO-d_6 + $CDCl_3$): δ 28.8, 29.7, 35.2, 48.1, 56.2, 64.2, 117.1, 121.3, 124.1, 125.6, 136.2, 137.7, 138.3, 143.5, 144.3, 145.4, 147.4, 150.1, 152.6, 156.2, 194.8; Anal. Calcd for $C_{21}H_{20}Cl_2N_2O$; C, 65.12; H, 5.20; N, 7.23 found; C, 65.15; H, 5.23; N, 7.21; MS (EI): *m/z* 386/388 ($M^{+\cdot}$).

***11-(4-hydroxyphenyl)-3,3-dimethyl-2,3,4,5,10,11-hexahydro-1H-dibenzo[b,e][1,4]diazepin-1-one* (4s):**

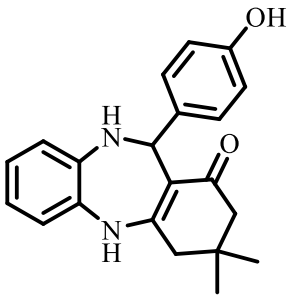

IR (KBr, ν cm^{-1}): 3083, 1558, 1383 (C-H, aromatic), 3345, 3257 (NH), 1625 (C=C), 1636 (C=O), 3226 (O-H); ^{1}H NMR (400 MHz, DMSO-d_6 + $CDCl_3$): δ 1.02 (3H, s, CH_3), 1.20 (3H, s, CH_3), 2.12 (2H, s, CH_2), 2.59 (2H, s, CH_2-C=O), 5.95 (1H, s, CH), 5.25 (s, 1H, NH, exchangeable with D_2O), 8.71 (s, 1H, NH, exchangeable with D_2O), 9.07 (1H, s, OH), 6.41-7.32 (m, 8H, C_6H_4, C_6H_4); ^{13}C NMR (100 MHz, DMSO-d_6 + $CDCl_3$): δ 27.9, 28.0, 32.3, 45.7, 53.9, 60.2, 112.2, 120.1, 120.7, 121.2, 125.5, 128.3, 131.3, 135.3, 137.2, 138.0, 141.2, 142.3, 147.7, 162.6, 194.1; Anal. Calcd for $C_{21}H_{22}N_2O_2$; C, 75.42; H, 6.63; N, 8.38 found; C, 75.45; H, 6.61; N, 8.35; MS (EI): *m/z* 334 ($M^{+\cdot}$).

***11-(2-hydroxyphenyl)-3,3-dimethyl-2,3,4,5,10,11-hexahydro-1H-dibenzo[b,e][1,4]diazepin-1-one* (4t):**

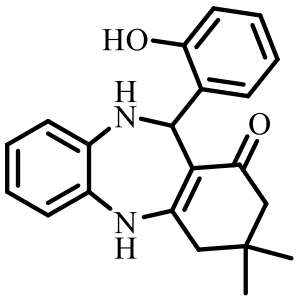

IR (KBr, ν cm^{-1}): 3088, 1561, 1380 (C-H, aromatic), 3347, 3261 (NH), 1621 (C=C), 1635 (C=O), 3229 (O-H); ^{1}H NMR (400 MHz, DMSO-d_6 + $CDCl_3$): δ 1.05 (3H, s, CH_3), 1.26 (3H, s, CH_3), 2.07 (2H, s, CH_2), 2.61 (2H, s, CH_2-C=O), 5.91 (1H, s, CH), 5.19 (s, 1H, NH, exchangeable with D_2O), 8.69 (s, 1H, NH, exchangeable with D_2O), 9.04 (1H, s, OH), 6.46-7.29 (m, 8H, C_6H_4, C_6H_4); ^{13}C NMR (100 MHz, DMSO-d_6 + $CDCl_3$): δ 28.1, 29.2, 35.4, 44.2, 56.9, 61.3, 116.7, 121.3, 122.0, 122.6, 124.6, 129.4, 130.1, 134.4, 135.1, 140.5, 143.2, 144.6, 145.2, 163.2, 196.3; Anal. Calcd for $C_{21}H_{22}N_2O_2$; C, 75.42; H, 6.63; N, 8.38 found; C, 75.40; H, 6.65; N, 8.39; MS (EI): *m/z* 334 ($M^{+\cdot}$).

***11-(3-hydroxyphenyl)-3,3-dimethyl-2,3,4,5,10,11-hexahydro-1H-dibenzo[b,e][1,4]diazepin-1-one* (4u):**

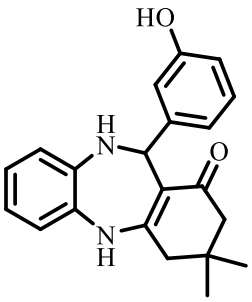

IR (KBr, ν cm^{-1}): 3084, 1556, 1377 (C-H, aromatic), 3351, 3259 (NH), 1628 (C=C), 1638 (C=O), 3225 (O-H); ^{1}H NMR (400 MHz, DMSO-d_6 + $CDCl_3$): δ 1.08 (3H, s, CH_3), 1.23 (3H, s, CH_3), 2.10 (2H, s, CH_2), 2.58 (2H, s, CH_2-C=O), 5.99 (1H, s, CH), 5.28 (s, 1H, NH, exchangeable with D_2O), 8.73 (s, 1H, NH, exchangeable with D_2O), 8.97 (1H, s, OH), 6.39-7.18 (m, 8H, C_6H_4, C_6H_4); ^{13}C NMR (100 MHz, DMSO-d_6 + $CDCl_3$): δ 27.5, 28.4, 34.2, 46.3, 55.1, 60.4, 115.8, 120.4, 121.3, 122.4, 125.7, 128.5, 133.0, 136.5, 137.0, 139.0, 143.2, 145.3, 148.3, 162.4, 195.2; Anal. Calcd for $C_{21}H_{22}N_2O_2$; C, 75.42; H, 6.63; N, 8.38 found; C, 75.44; H, 6.59; N, 8.37; MS (EI): *m/z* 334 ($M^{+\cdot}$).

4.4. Conclusion

In summary, a series of benzodiazepine derivatives (**4a-u**) in excellent yields were synthesized by using *o*-phenylenediamine (**1**), dimedone (**2**), and aromatic aldehydes (**3a-u**) in the presence of recyclable and reusable NiO@SiO_2 NCs under microwave irradiation. The catalyst does not need special precautions for preparation and can be stored at an ambient temperature without losing its catalytic activity. This new and efficient one-pot three-component protocol not only offers use of microwave at low temperature and substantial yield of products but also affords mild reaction conditions, shorter reaction times, high purity, operational simplicity, reusability of heterogeneous nano-based catalyst, high atom economy and easy workup. The protocol has several advantages over previously reported methods for the synthesis of benzodiazepines. The combination of heterogeneous catalysis and microwave irradiation has made possible development of efficient, rapid, and environmentally friendly synthetic methodologies in the future. The reusability of this catalyst was high and it can be reused seven times without any significant decrease from its initial activity. We hope that this synthetic approach provides a better scope for the synthesis of benzodiazepine analogues and will be a more practical substitute to the other existing methods.

4.5. References

1 T. Okuhara, N. Mizuno and M. Misono, eds. W. O. H. D.D. Eley and B. Gates, Academic Press, 1996, **41**, 113–252.

2 H. Bosch and F. Janssen, *Catal. Today*, 1988, **2**, 369–532.

3 M. A. Vannice and R. L. Garten, *J. Catal.*, 1979, **56**, 236–248.

4 S. Shylesh, V. Schünemann and W. R. Thiel, *Angew. Chem. Int. Ed. Engl.*, 2010, **49**, 3428–3459.

5 V. Polshettiwar, R. Luque, A. Fihri, H. Zhu, M. Bouhrara and J. M. Basset, *Chem. Rev.*, 2011, **111**, 3036–3075.

6 M. Dekker, D. L. Feldheim and C. A. Fross, *New York, NY, CRC Press*, 2002.

7 V. S. Murthy, R. K. Rana and M. S. Wong, *J. Phys. Chem. B*, 2006, **110**, 25619–25627.

8 J. Grunes, J. Zhu and G. A. Somorjai, *Chem. Commun.*, 2003, 2257–2260.

9 S. Reculusa, C. Poncet-Legrand, A. Perro, E. Duguet, E. Bourgeat-Lami, C. Mingotaud and S. Ravaine, *Chem. Mater.*, 2005, **17**, 3338–3344.

10 C. J. Murphy, *J. Mater. Chem.*, 2008, **18**, 2173–2176.

11 R. J. P. Corriu, A. Mehdi and C. Reye, *J. Mater. Chem.*, 2005, **15**, 4285–4294.

12 A. T. Bell, *Science (80-.).*, 2003, **299**, 1688–1691.

13 R. Schlögl and S. B. Abd Hamid, *Angew. Chemie Int. Ed.*, 2004, **43**, 1628–1637.

14 D. Astruc, F. Lu and J. R. Aranzaes, *Angew. Chem. Int. Ed. Engl.*, 2005, **44**, 7852–72.

15 G. A. Somorjai, F. Tao and J. Y. Park, *Top. Catal.*, 2008, **47**, 1–14.

16 R. A. Van Santen, *Acc. Chem. Res.*, 2009, **42**, 57–66.

17 V. H. Schütz., *Springer Verlag, Berlin-Heidelberg-New York*, 1982.

18 G. Sabitha, G. S. K. K. Reddy, K. B. Reddy, N. M. Reddy and J. S. Yadav, *Adv. Synth. Catal.*, 2004, **346**, 921–923.

19 R. Kumar, P. Chaudhary, S. Nimesh, A. K. Verma and R. Chandra, *Green Chem.*, 2006, **8**, 519–521.

20 M. Essaber, A. Baouid, A. Hasnaoui, A. Benharref and J.-P. Lavergne, *Synth. Commun.*, 1998, **28**, 4097–4104.

21 A. M. El-snyed, H. Abdel-ghany and A. M. M. El-snghier, *Synth. Commun.*, 1999, **29**, 3561–3572.

22 K. V. V. Reddy, P. S. Rao and D. Ashok, *Synth. Commun.*, 2000, **30**, 1825–1836.

23 J. A. L. Herbert and H. Suschitzky, *J. Chem. Soc., Perkin Trans.*, 1974, **1**, 2657–2661.

24 H. R. Morales, A. Bulbarela and R. Contreras, *Heterocycles*, 1986, **24**, 135–139.

25 M. S. Balakrishna and B. Kaboudin, *Tetrahedron Lett.*, 2001, **42**, 1127–1129.

26 M. Curini, F. Epifano, M. C. Marcotullio and O. Rosati, *Tetrahedron Lett.*, 2001, **42**, 3193–3195.

27 M. Pozarentzi, J. Stephanidou-Stephanatou and C. A. Tsoleridis, *Tetrahedron Lett.*, 2002, **43**, 1755–1758.

28 J. S. Yadav, B. V. S. Reddy, B. Eshwaraiah and K. Anuradha, *Green Chem.*, 2002, **4**, 592–594.

29 G. Sabitha, G. S. K. K. Reddy, K. B. Reddy, N. M. Reddy and J. S. Yadav, *Adv. Synth. Catal.*, 2004, **346**, 921–923.

30 J. S. Yadav, B. V. S. Reddy, S. Praveenkumar and K. Nagaiah, *Synthesis (Stuttg).*, 2005, **3**, 480–484.

31 D. V Jarikote, S. A. Siddiqui, R. Rajagopal, T. Daniel, R. J. Lahoti and K. V Srinivasan, *Tetrahedron Lett.*, 2003, **44**, 1835–1838.

32 S. K. De and R. A. Gibbs, *Tetrahedron Lett.*, 2005, **46**, 1811–1813.

33 R. Varala, R. Enugala, S. Nuvula and S. R. Adapa, *Synlett*, 2006, **7**, 1009–1014.

34 M. A. Pasha and V. P. Jayashankara, *Heterocycles*, **68**, 1017–1023.

35 B. M. Reddy, P. M. Sreekanth and P. Lakshmanan, *J. Mol. Catal. A Chem.*, 2005, **237**, 93–100.

36 J. S. Yadav, B. V. S. Reddy, G. S. G. Srinivasulu and A. C. Kunwar, *Arkivoc*, 2005, **3**, 221–227.

37 M. M. Heravi, S. Sadjadi, H. A. Oskooie, R. Hekmatshoar and F. F. Bamoharram, *J. Chinese Chem. Soc.*, 2008, **55**, 842–845.

38 M. M. Heravi and F. K. Behbahani, *J. Iran. Chem. Soc.*, 2007, **4**, 375–392.

39 M. Nardi, A. Cozza, A. De Nino, M. Oliverio and A. Procopio, *Synthesis (Stuttg).*, 2012, **44**, 800–804.

40 D.-I. Jung, T.-W. Choi, Y.-Y. Kim, I.-S. Kim, Y.-M. Park, Y.-G. Lee and D.-H. Jung, *Synth. Commun.*, 1999, **29**, 1941–1951.

41 A. J. Ruys and Y.-W. Mai, *Mater. Sci. Eng. A*, 1999, **265**, 202–207.

42 M. Kotecha, W. Veeman, B. Rohe and M. Tausch, *Microporous Mesoporous Mater.*, 2006, **95**, 66–75.

43 S. Chakrabarti, D. Das, D. Ganguli and S. Chaudhuri, *Thin Solid Films*, 2003,

441, 228–237.

44 O. K. Park and Y. S. Kang, *Colloids Surfaces A Physicochem. Eng. Asp.*, 2005, **257**–**258**, 261–265.

45 T. L. Hsiung, H. P. Wang and H. C. Wang, *Radiat. Phys. Chem.*, 2006, **75**, 2042–2045.

46 H. Xu, L. Cui, N. Tong and H. Gu, *J. Am. Chem. Soc.*, 2006, **128**, 15582–15583.

47 M. A. Ermakova, D. Y. Ermakov, S. V Cherepanova and L. M. Plyasova, *J. Phys. Chem. B*, 2002, **106**, 11922–11928.

48 A. Corrias, G. Mountjoy, G. Piccaluga and S. Solinas, *J. Phys. Chem. B*, 1999, **103**, 10081–10086.

49 G. Diaz, R. Perez-Hernandez, A. Gomez-Cortes, M. Benaissa, R. Mariscal and J. L. G. Fierro, *J. Catal.*, 1999, **187**, 1–14.

50 L. Armelao, D. Barreca, G. Bottaro, G. Mattei, C. Sada and E. Tondello, *Chem. Mater.*, 2005, **17**, 1450–1456.

51 G. Cordoba, R. Arroyo, J. L. G. Fierro and M. Viniegra, *J. Solid State Chem.*, 1996, **123**, 93–99.

52 Z. Wang, Q. Liu, J. Yu, T. Wu and G. Wang, *Appl. Catal. A Gen.*, 2003, **239**, 87–94.

53 S. Bennici, A. Gervasini, N. Ravasio and F. Zaccheria, *J. Phys. Chem. B*, 2003, **107**, 5168–5176.

54 V. S. Braga, F. A. C. Garcia, J. A. Dias and S. C. L. Dias, *J. Catal.*, 2007, **247**, 68–77.

55 Z. Nasir, M. Shakir, R. Wahab, M. Shoeb, P. Alam, R. H. Khan, M. Mobin and Lutfullah, *Int. J. Biol. Macromol.*, 2017, **94**, **Part A**, 554–565.

56 M. Shakir, Z. Nasir, M. S. Khan, Lutfullah, M. F. Alam, H. Younus and S. I. Al-Resayes, *Int. J. Biol. Macromol.*, 2015, **72**, 1196–1204.

57 A. Ali, M. Asif, H. Khanam, A. Mashrai, M. A. Sherwani, M. Owais and Shamsuzzaman, *RSC Adv.*, 2015, **5**, 75964–75984.

58 Shamsuzzaman, K. A. A. Abdul Baqi, A. Ali, M. Asif, A. Mashrai, H. Khanam, A. Sherwani, Z. Yaseen and M. Owais, *J. Mol. Struct.*, 2015, **1085**, 104–114.

59 M. Asif, A. Ali, A. Zafar, M. Farhan, H. Khanam, S. M. Hadi and Shamsuzzaman, *J. Photochem. Photobiol. B Biol.*, 2017, **166**, 104–115.

60 Shamsuzamman, A. Ali, M. Asif, A. Mashrai and H. Khanam, *Eur. Chem. Bull.*, 2014, **3 (9)**, 939–945.

61 A. Ansari, A. Ali, M. Asif and Shamsuzzaman, *New J. Chem.*, 2017, **41**, 16–41.

62 E. J. Park, J. H. Lee, K.-D. Kim, D. H. Kim, M.-G. Jeong and Y. D. Kim, *Catal. Today*, 2016, **260**, 100–106.

63 J. L. Rodríguez, M. A. Valenzuela, H. Tiznado, T. Poznyak and E. Flores, *J. Mol. Catal. A Chem.*, 2014, **392**, 39–49.

64 A. Maleki and M. Kamalzare, *Tetrahedron Lett.*, 2014, **55**, 6931–6934.

65 N. T. McDevitt and W. L. Baun, *Spectrochim. Acta*, 1964, **20**, 799–808.

66 A. M. Ali and R. Najmy, *Catal. Today*, 2013, **208**, 2–6.

67 R. M. Almeida, T. A. Guiton and C. G. Pantano, *J. Non. Cryst. Solids*, 1990, **121**, 193–197.

68 A. Ueno, H. Suzuki and Y. Kotera, *J. Chem. Soc. Faraday Trans. 1 Phys. Chem. Condens. Phases*, 1983, **79**, 127–136.

69 M. Kermarec, J. Y. Carriat, P. Burattin, M. Che and A. Decarreau, *J. Phys. Chem.*, 1994, **98**, 12008–12017.

70 J. R. Martínez, G. Ortega-Zarzosa, O. Domínguez-Espinós and F. Ruiz, *J. Non. Cryst. Solids*, 2001, **282**, 317–320.

71 G. A. El-Shobaky, N. R. E. Radwan, M. Samy El-Shall, A. M. Turky and H. M. A. Hassan, *Colloids Surfaces A Physicochem. Eng. Asp.*, 2007, **311**, 161–169.

72 Z. Gu and K. L. Hohn, *Ind. Eng. Chem. Res.*, 2004, **43**, 30–35.

73 N. N. Tonkikh, A. Strakovs, K. V Rizhanova and M. V Petrova, *Chem. Heterocycl. Compd.*, 2004, **40**, 949–955.

74 N. N. Kolos, E. N. Yurchenko, V. D. Orlov, S. V Shishkina and O. V Shishkin, *Chem. Heterocycl. Compd.*, 2004, **40**, 1550–1559.

75 H. Naeimi and H. Foroughi, *Chinese J. Catal.*, 2015, **36**, 734–741.

76 H. Naeimi and H. Foroughi, *New J. Chem.*, 2015, **39**, 1228–1236.

77 M. del R. Arellano, R. Martínez and E. Cortés, *J. Heterocycl. Chem.*, 1982, **19**, 321–326.

****

Chapter 5

Immobilization of glucose oxidase enzyme on silica coated Ni-Co ferrite nanocomposites as a magnetic support

5.1. Introduction

During the last decade, nanocrystalline ferrites have captivated attention in various fields including biomedical and environmental applications because of their small size, high specific surface area and low toxicity with strong magnetic properties extend the applications in intracellular uptake and separation,[1–5] drug delivery,[6] hyperthermia,[4,7] magnetic resonance imaging contrast enhancement,[4,8] enzyme and protein immobilization[9,10] and protein purification.[11] Various synthetic techniques have been embraced for the synthesis of nanoferrites such as mechanical milling, co-precipitation, thermal decomposition, sol-gel auto-combustion and hydrothermal methods.[1] Auto-combustion synthesis ensures numerous distinct advantages over co-precipitation and ceramic techniques as it does not involve any pH control or a consequent annealing step in the synthesis of phase pure and highly crystalline ferrite nanoparticle.[12]

Glucose oxidase (GOx) (E.C. 1.1.3.4) is an oxidoreductase and catalyzes the oxidation of *β*-D-glucose to D-glucono-*δ*-lactone by molecular oxygen, and the intermediate lactone, spontaneously hydrolyzes into gluconic acid and hydrogen peroxide by reducing the activation energy of the reaction (**Fig. 5.1**).[13,14]

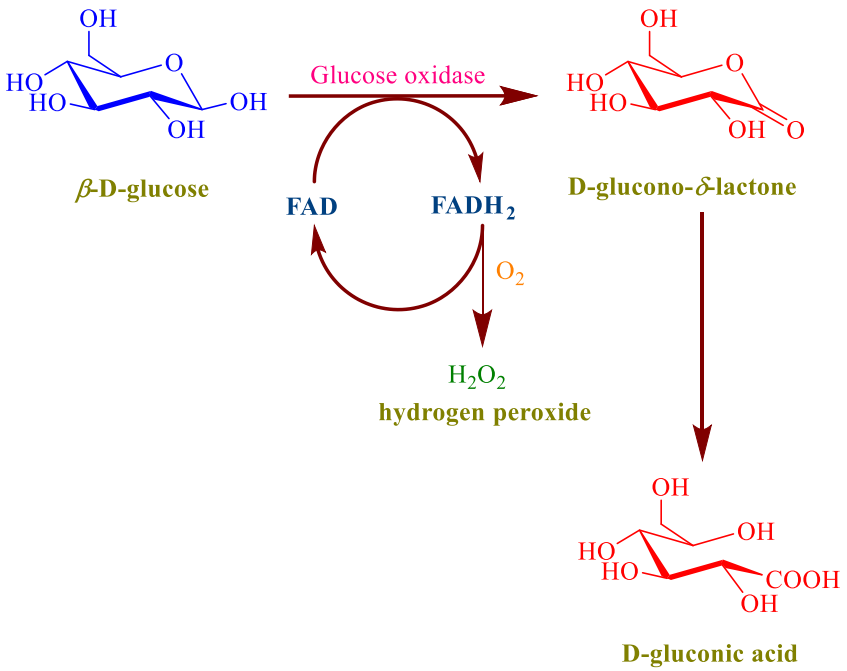

Figure 5.1. Representation of GOx reaction.

GOx has a wide range of application in various industries such as food, beverage, textile, clinical and biotechnology.[14–17] Generally, enzymes are

proteinaceous in nature and thermal stability is major concern when using in industrial applications. So, immobilization of enzymes on solid support is an important strategy by which we can improve operational stability, product recovery and reusability. There are several methods available by which we can immobilize various types of industrially important enzymes on different types of supports.[18] Among various ways, magnetic supports for biological and biomedical materials are of particular interest due to their inherent characteristics, including non-toxicity, large surface area, and capacity to generate required magnetic properties and their ability to be separated with magnets and recycled.[19–22]

In continuation of our research program in the field of nanomaterial's,[23–27] herein displayed a report on the synthesis of silica coated Ni-Co ferrite NCs, to study their particle size, structure, morphology and elemental composition through XRD, SEM, EDS, HR-TEM and FT-IR analysis. The main objective was to investigate the covalent interaction of GOx immobilized on silica coated Ni-Co ferrite NCs *via* glutaraldehyde activation. The covalent binding of GOx to silica coated Ni-Co ferrite NCs were confirmed by comparing the results of FT-IR spectroscopy and HR-TEM with that of unbounded nanocomposites. The relative assessment of operating parameters like kinetic constants, varying thermal and pH stability, and reusability of free GOx and immobilized GOx enzyme helped to determine optimum operating conditions.

5.2. Results and discussion

5.2.1. Structural Analysis

X-ray diffraction patterns for silica coated $Ni_xCo_{1-x}Fe_2O_4$ NCs (x = 0.0, 0.5, 1.0) demonstrated in the **Fig. 5.2**. All the spectra shows a hump around $2\theta \sim 23^o$, which corresponds to the amorphous matrix of SiO_2. The powder samples of $Ni_xCo_{1-x}Fe_2O_4/SiO_2$ NCs shows diffraction peaks at $2\theta \sim 30.10^o$ (220), 35.57^o (311), 43.16^o (400), 57.10^o (511) and 62.51^o (440), which could be easily indexed by comparing with JCPDS card No. 03-0864, to face centred cubic spinel structure of Ni-Co ferrite. The variation in FWHM is in agreement with the crystallite size reckoned by Debye-Scherrer's formula:

$$D = \frac{0.9\,\lambda}{\beta COS\theta}$$

Where, λ is the wavelength of Cu Kα radiation, D is the particle size, β is the full width half maximum intensity, and θ is the position of peak. The crystallite size was determined from main diffraction peak (311) and the calculation outputs are summarized in **Table 5.1**.

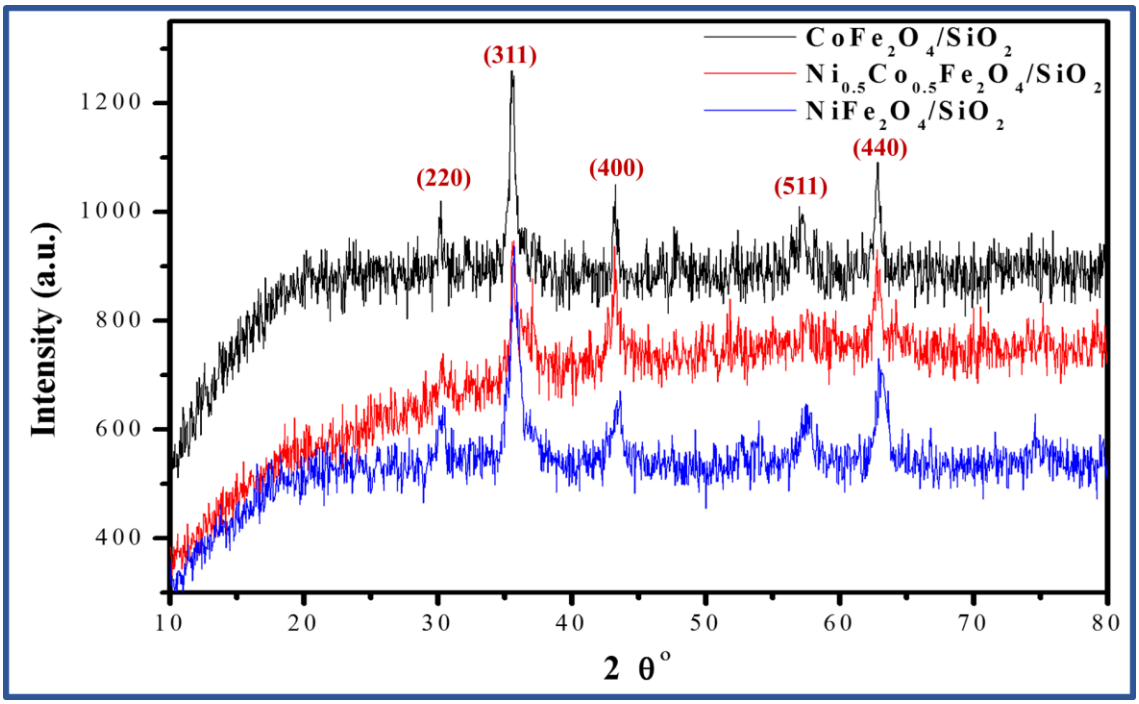

Figure 5.2. XRD patterns of silica coated Ni-Co ferrite NCs.

Table 5.1. Structural parameters of $Ni_xCo_{1-x}Fe_2O_4/SiO_2$ NCs.

S.No.	$Ni_xCo_{1-x}Fe_2O_4/SiO_2$ (x = 0.0, 05, 1.0) NCs	2θ	FWHM (β)	Crystallite Size (nm)
1.	$CoFe_2O_4/SiO_2$	35.57	0.48	17.37
2.	$Ni_{0.5}Co_{0.5}Fe_2O_4/SiO_2$	36.26	2.0	4.17
3.	$NiFe_2O_4/SiO_2$	35.62	0.66	12.64

5.2.2. Fourier transform infrared (FT-IR) spectroscopic studies

The FT-IR spectra presented in **Fig. 5.3**, enabled in assessing the pattern of the spinel structure in the silica coated Ni-Co ferrite NCs. In the prepared sample, strong absorption bands were observed at 467, 799, 1090 and 1631 cm^{-1}, which may be assigned to Si-O-Si symmetric bond stretching vibration, vibration mode of ring structure of SiO_2 tetrahedra,[30] stretching vibration of Si–O–Si asymmetric bond[31] and bending vibration of H–O–H absorbed in silica,[32] respectively. The characteristic absorption bands at 1090, 799 and 467 cm^{-1} indicate the formation of silica network.[33] The shoulder at 954 cm^{-1} was probably due to the contribution from Si–O–Fe

vibrations and from Si–O–H stretching vibrations. The presence of Si–O–Fe vibrations reflected some interactions between the highly secluded Fe^{3+} ions and the adjacent silica network. In addition, a band at 590 cm^{-1} may be attributed to the presence of cobalt ferrite.[34,35] These results correspond to the production of well crystallized silica coated Ni-Co ferrite NCs. Furthermore, FT-IR spectra of pure GOx and immobilized silica coated Ni-Co ferrite NCs are shown in **Fig. 5.4**. The absorption peak at 3421, 3423 and 3425 cm^{-1} in curves **b**, **c** and **d**, respectively, are accredited to the stretching vibrations of -OH adsorbed on the surface of the NCs (**Fig. 5.4**). APTES is absorbed on the magnetite NPs surfaces by Fe-O-Si bands, the coating of APTES is established by the presence of stretching vibration of CH_2 bonds on aminopropyl group appeared around at 2922 and 2850 cm^{-1} which confirmed the binding of APTES molecules at the surface of magnetite (**Scheme 5.1**).[36]

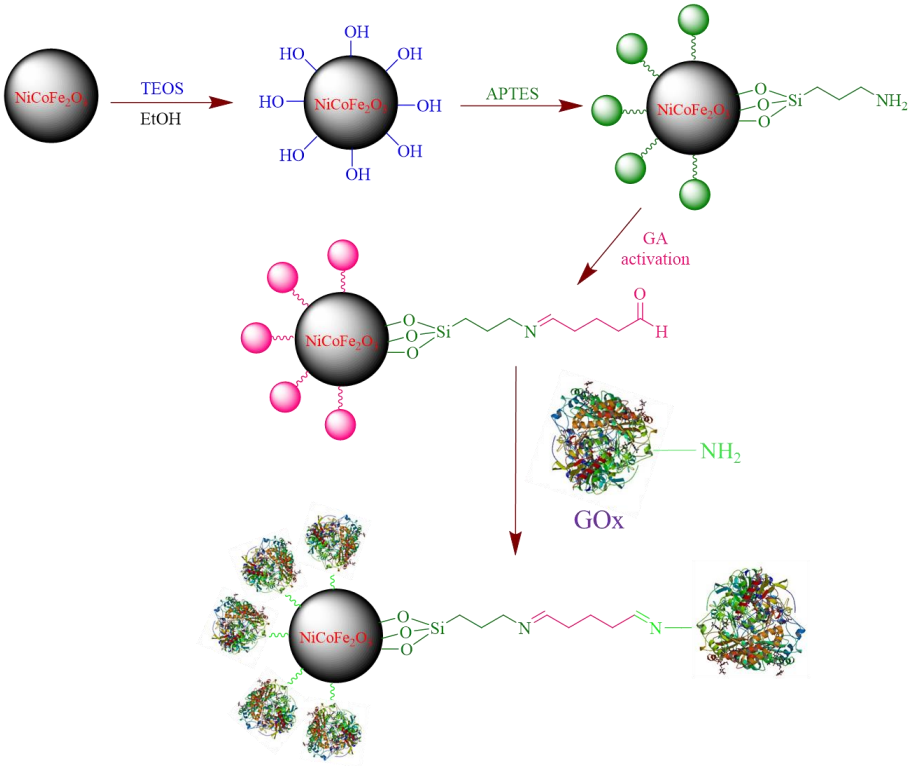

Scheme 5.1. Schematic diagram for the immobilization of glucose oxidase enzyme on silica coated Ni-Co ferrite NCs using glutaraldehyde as a cross-linker.

The maintenance of enzyme activity on the supporting materials is crucial because the secondary conformational variations of the enzyme can affect its activity markedly. Herein, FT-IR is utilized to check the secondary conformation variations of the polypeptide chain of GOx on the silica coated Ni-Co ferrite NCs. The two characteristic protein bands,[37–39] can be clearly observed around at 1675 and 1515 cm^{-}

[1] for the native GOx (**Fig. 5.4a**) and the GOx-encapsulated silica coated Ni-Co ferrite NCs (**Fig. 5.4b-d**). These spectral characteristics indicate that GOx has been successfully incorporated into the silica coated Ni-Co ferrite NCs and the secondary structure is maintained well in the immobilized GOx molecules.

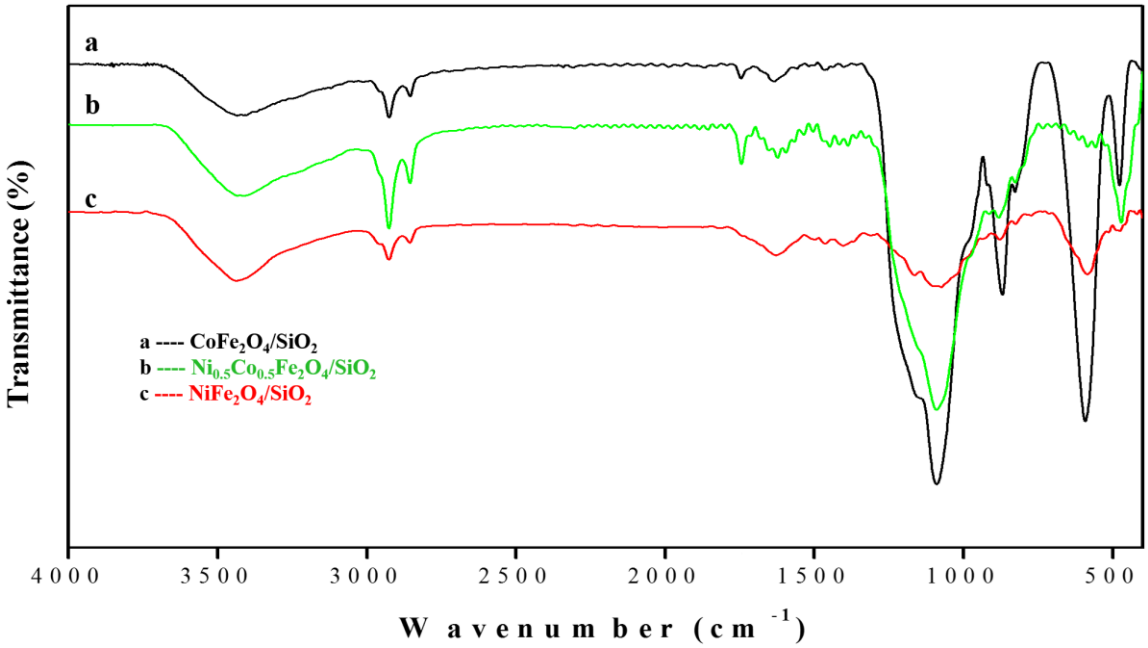

Figure 5.3. FT-IR spectra of silica coated Ni-Co ferrite NCs.

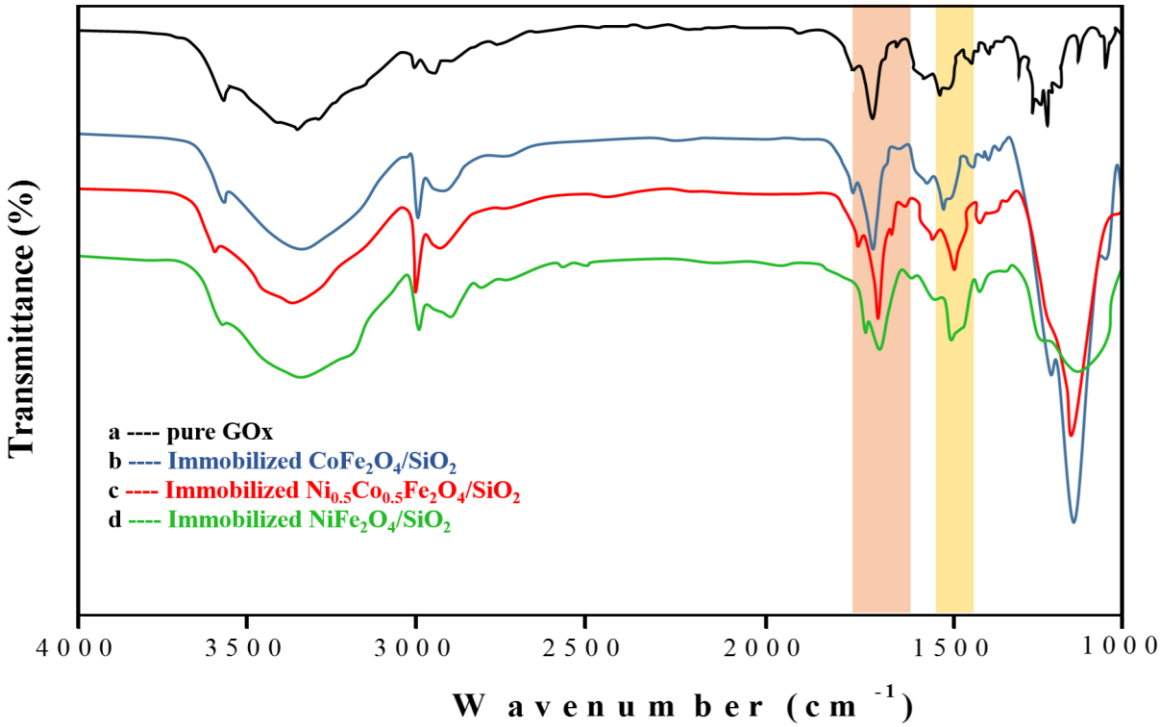

Figure 5.4. FT-IR spectra of pure GOx and immobilized silica coated Ni-Co ferrite NCs.

5.2.3. Surface morphology and compositional analysis

The SEM images and EDS spectra of the samples were taken at 4000 × magnification (**Fig. 5.5**). The SEM images of silica coated $Ni_xCo_{1-x}Fe_2O_4$ NCs (x = 0.0, 0.5, 1.0) exhibited that the particles are not properly distributed and show relatively diffused patterns of particles in the form of aggregates. The compositions of different samples, $Ni_xCo_{1-x}Fe_2O_4/SiO_2$ NCs (x = 0.0, 0.5, 1.0) have been examined by EDS for the different elements in relations of weight % and atomic % (**Table 5.2**) which represented that Si, Ni, Co, Fe and O are present nearly to the predicted stoichiometric proportions.

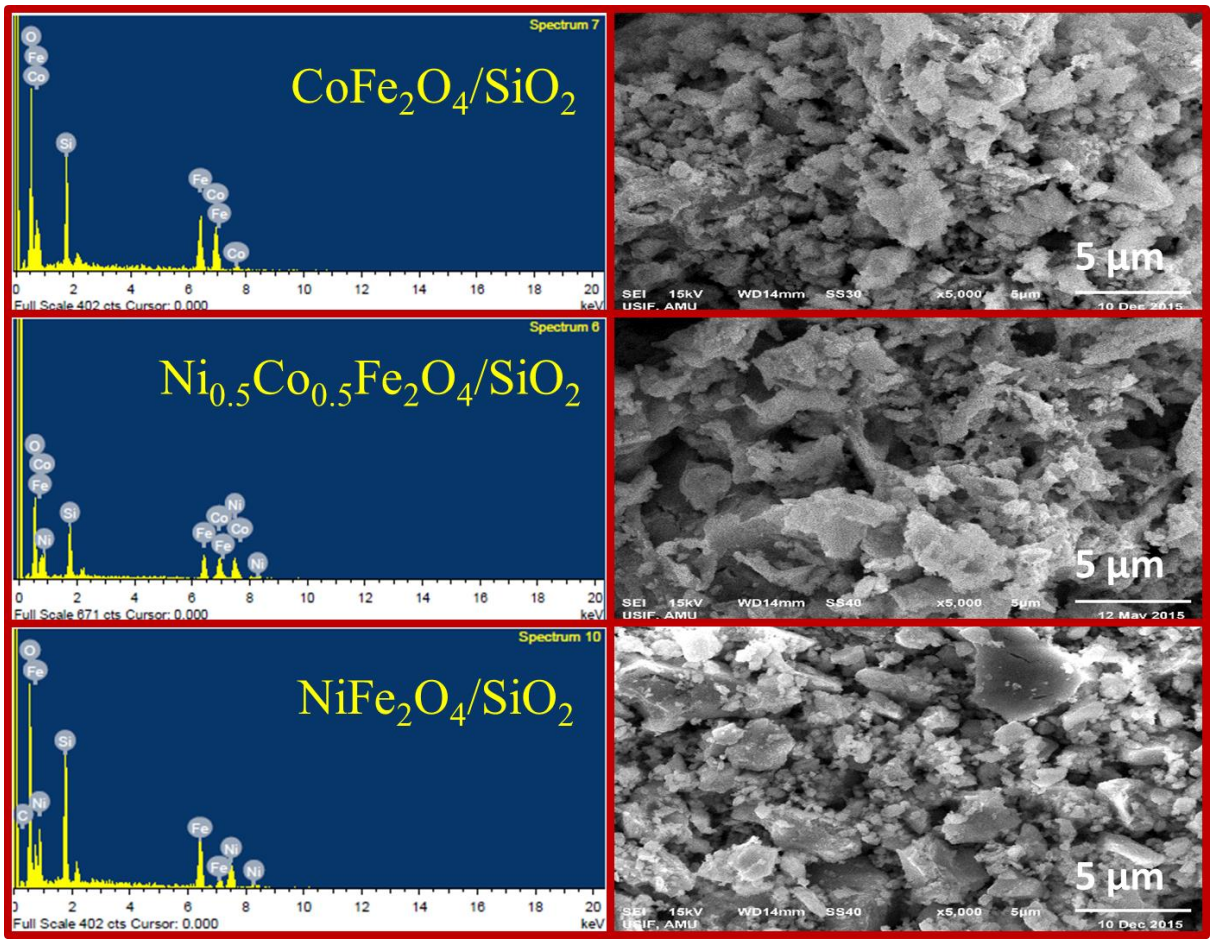

Figure 5.5. SEM images (right side) and EDS spectrum (left side) of silica coated Ni-Co ferrite NCs.

Table 5.2. EDS analysis (weight % and atomic %) of $Ni_xCo_{1-x}Fe_2O_4/SiO_2$ NCs at different compositions.

Composition	x = 0.0		x = 0.5		x = 1.0	
Elements	Wt. %	At. %	Wt. %	At. %	Wt. %	At. %
O	43.83	69.40	36.57	63.77	50.29	74.46
Si	12.55	11.32	11.09	11.02	13.27	10.86
Fe	22.04	10.00	15.29	7.64	19.14	7.88
Ni	-	-	17.97	8.51	17.30	6.77
Co	21.59	9.28	19.08	9.07	-	-

5.2.4. Transmission electron microscopy (TEM) analysis

The HR-TEM images of silica coated Ni-Co ferrite NCs without **Fig. 5.6 (a-c)** and with **Fig. 5.6 (d-f)** immobilized GOx enzyme have been displayed. Unimmobilized NCs appeared to be very well and uniformly distributed ranging from 20 to 30 nm in diameter. However, the NCs aggregated after immobilization which can be clearly visible through the HR-TEM images.

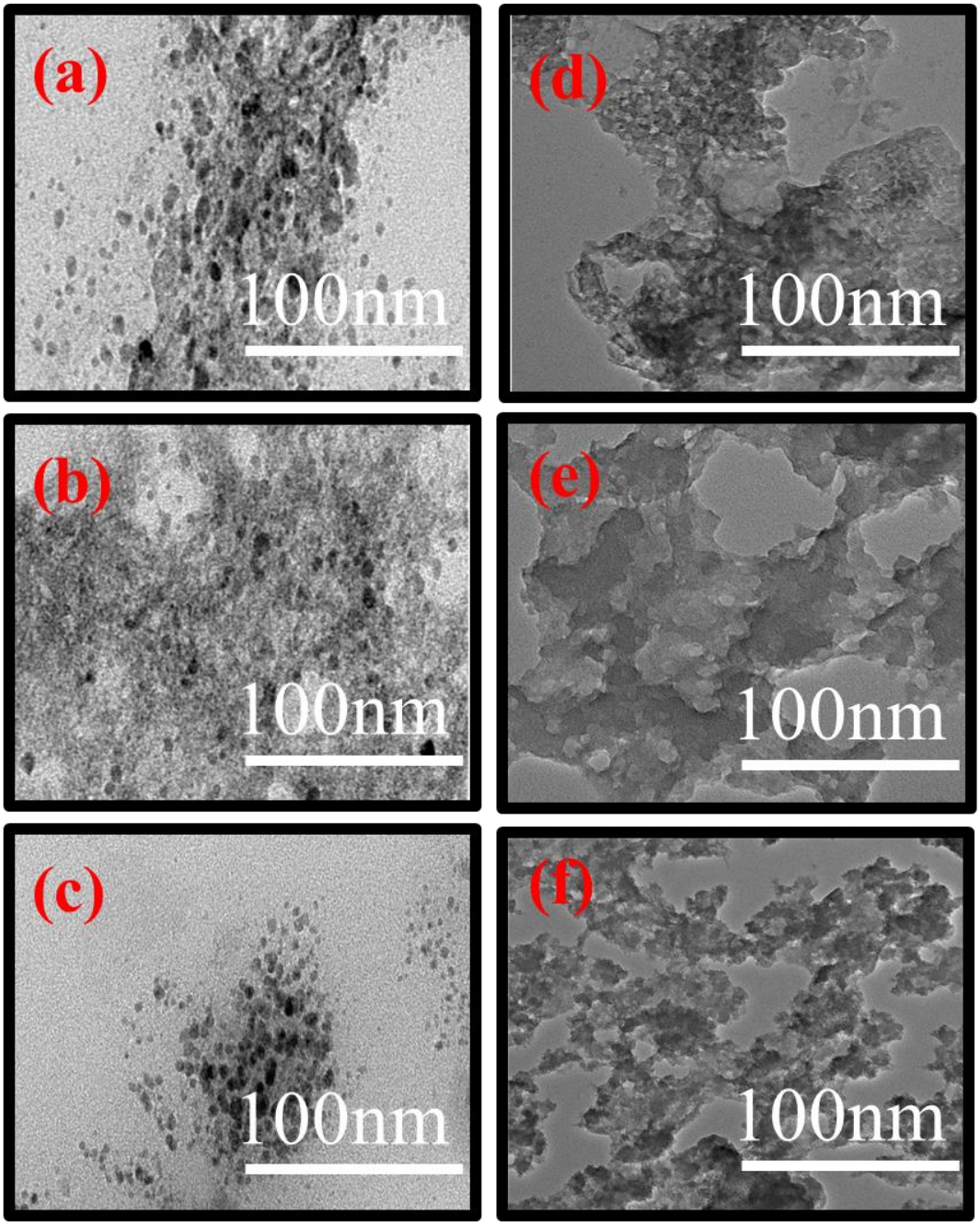

Figure 5.6. TEM images of (a) $CoFe_2O_4/SiO_2$ NCs (b) $NiCoFe_2O_4/SiO_2$ NCs (c) $NiFe_2O_4/SiO_2$ NCs (d) immobilized $CoFe_2O_4/SiO_2$ NCs (e) immobilized $NiCoFe_2O_4/SiO_2$ NCs (f) immobilized $NiFe_2O_4/SiO_2$ NCs.

5.2.5. Properties of immobilized GOx

Immobilization of silica coated Ni-Co ferrite NCs on GOx was done by covalent binding *via* glutaraldehyde activation. The binding efficiency of GOx on silica coated Ni-Co ferrite NCs was 85.184 %.

5.2.5.1. Effect of pH on the activity of immobilized GOx

The pH effect on the immobilization of GOx on $Ni_xCo_{1-x}Fe_2O_4/SiO_2$ NCs was investigated (**Fig. 5.7**). The activity of free enzyme is sensitive to pH and there is an optimal pH for a particular enzyme. The optimal pH for free GOx was observed at pH 5.5 and the deviation from optimal pH causes rapid decrease in enzyme activity. However, the optimal pH for immobilized GOx shifts to 6.0. The reason is probably that the immobilization of GOx on carrier causes the change of its micro-environment and therefore leads to the displacements in the pH activity profile. The broadening of residual activity increased in alkaline range, immobilized GOx on $NiFe_2O_4/SiO_2$ NCs retained 44.17 % and 59.84 % of initial activity at pH 3.0 and pH 10.0, respectively, whereas soluble enzyme retained 19.6 % and 7.71 % of the initial activity at these pH, respectively.

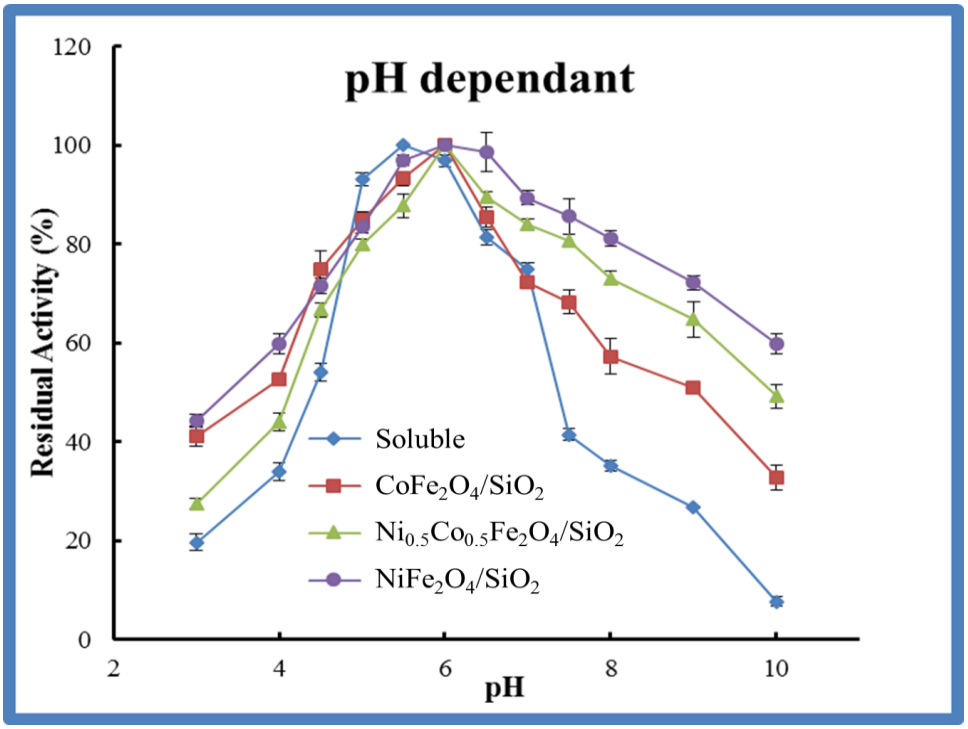

Figure 5.7. Effect of pH on the activity of soluble enzyme (sol) and immobilized GOx on SiO_2 coated Ni-Co ferrite NCs.

5.2.5.2. Effect of temperature on the activity of immobilized GOx

Temperature is one of the important parameter of an enzyme so every enzyme gives maximum catalytic efficiency at a particular temperature. Therefore, the relative activity of the soluble and immobilized GOx was investigated in the range of 25-65 ^oC. The temperature activity profile of soluble and immobilized GOx preparation is shown in **Fig. 5.8**. It was observed that maximum activity of soluble GOx was at 40

°C, whereas there is 5 °C shifts in optimum temperature in case of immobilized GOx.[40] This is might be due to presence of matrix which limits the diffusion of substrate to active sites of the enzyme. It was observed that the immobilized GOx preparations retained significant higher catalytic activity (60.09 %) in comparison with soluble GOx which retained only 26.23 % at 65 °C.

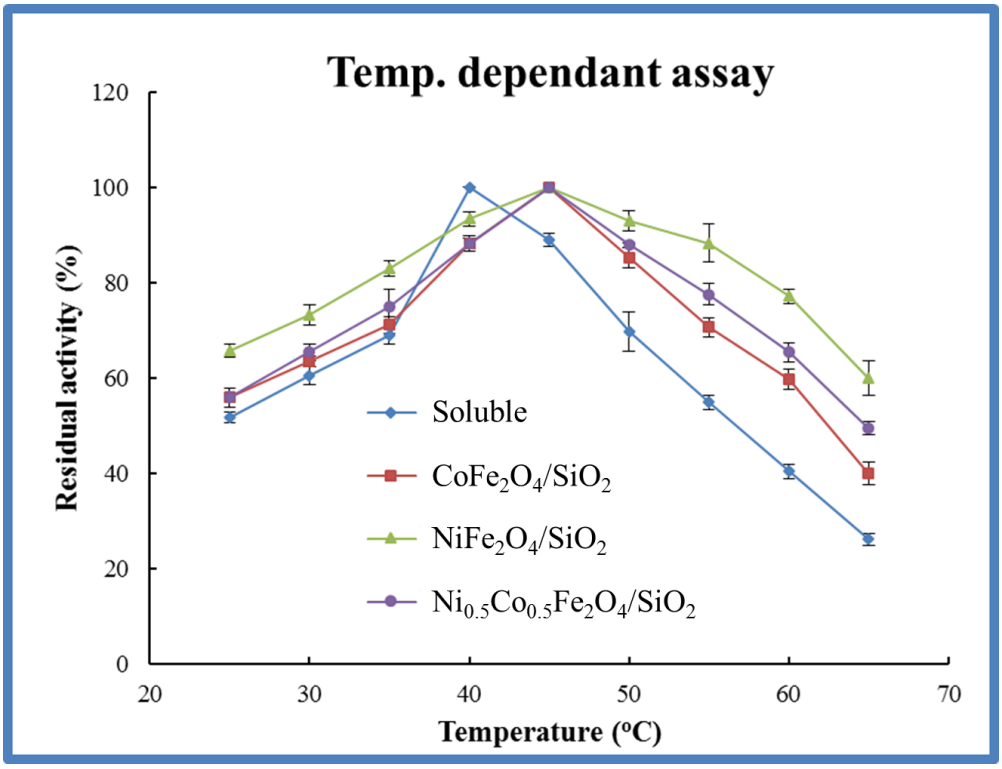

Figure 5.8. Effect of temperature on the activity of soluble enzyme (sol) and immobilized GOx on SiO_2 coated Ni-Co ferrite NCs.

5.2.5.3. Thermal stability of immobilized GOx

The thermal stability profile on both soluble and immobilized GOx preparation after incubation at 50 °C for a period of 240 min is shown in **Fig. 5.9**. It was observed that all the immobilized GOx preparation retained considerably higher catalytic activity even after 240 min of incubation at 50 °C. Soluble GOx showed almost no activity whereas GOx immobilized on $NiFe_2O_4/SiO_2$ NCs retained 59 % of its catalytic activity after incubation (240 min). Soluble enzyme segment losses its activity due to denaturation of enzyme at higher temperature. The improved thermal stability of immobilized GOx preparation was assumed to be supported by NCs, which absorb significant quantity of heat and resist the enzyme from denaturation.[41]

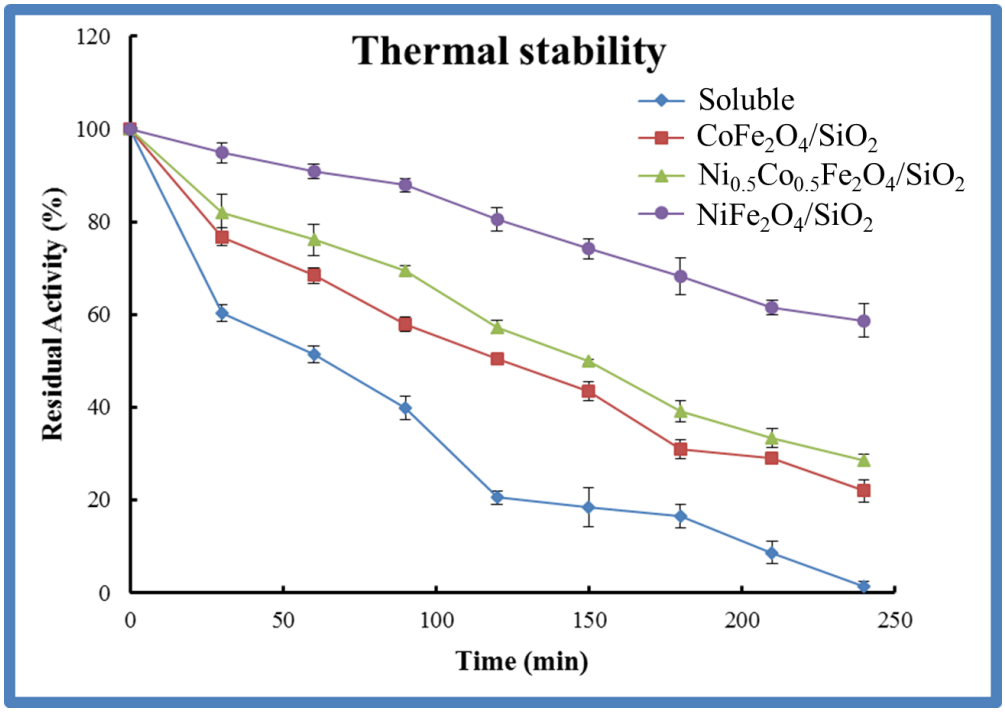

Figure 5.9. Thermal stability of soluble enzyme (sol) and immobilized GOx on SiO_2 coated Ni-Co ferrite NCs.

5.2.5.4. Kinetic parameter determination of immobilized GOx on silica coated Ni-Co ferrite NCs

The catalytic properties of free and immobilized enzymes were assessed by utilizing glucose as a substrate. It is evident from the Michaelis-Menten constant (K_m) for free and immobilized GOx on silica coated Ni-Co ferrite NCs were ascertained from double-reciprocal plots *i.e.* 1/V *vs* 1/[S] as shown in **Fig. 5.10**.

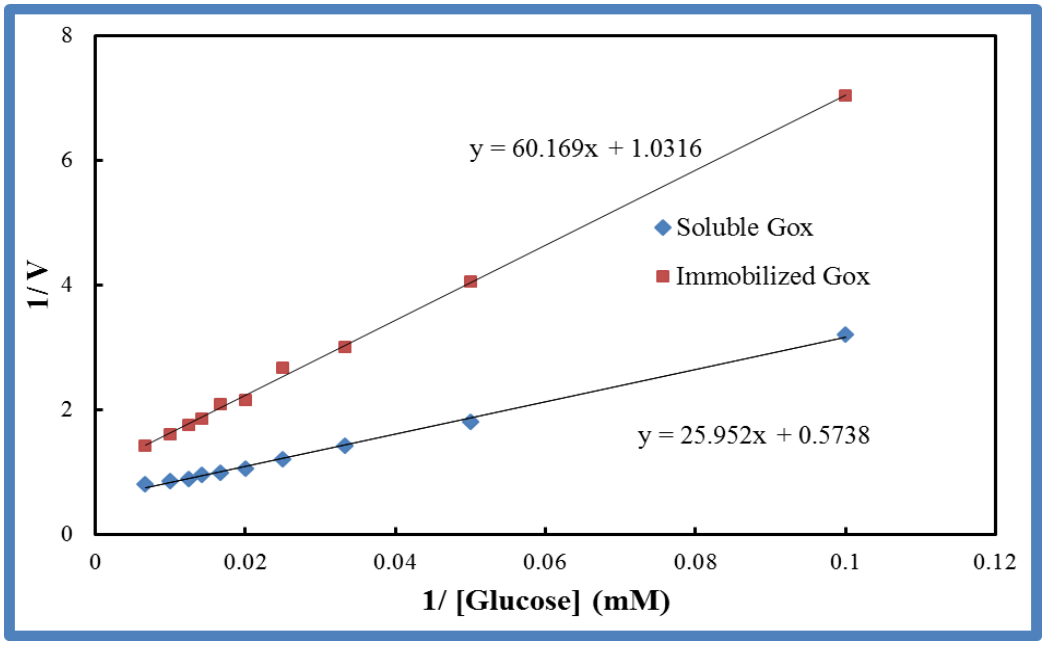

Figure 5.10. Double reciprocal plots for soluble and immobilized GOx.

From this plot the kinetic parameters K_m and V_{max} were calculated (**Table 5.3**) as 45.28 mM and 1745.22 µmol min^{-1}, respectively for the free GOx and 58.29 mM and 969.93 µmol min^{-1}, respectively for immobilized GOx. In comparison to the free enzyme the immobilized enzymes has a greater K_m and lower V_{max}. The enzyme has lower affinity for the substrate which might be due to the conformational changes in the enzyme occurred due to conjugation with the silica coated Ni-Co ferrite NCs or the lower accessibility of substrate to the active site can be predicted from the higher K_m value.

Table 5.3. The kinetic parameters for free and immobilized GOx.

Glucose oxidase	K_m (mM)	V_{max} (µmol min^{-1})	V_{max}/K_m	Relative activity (%)
Free	45.28	1745.22	0.039	100
Immobilized	58.29	969.93	0.017	43.58

5.2.5.5. Reusability of immobilized GOx

Reusability is one of the important parameter to assess the property of immobilized enzyme at large scale. The residual activity of immobilized enzyme on consequent uses is shown in **Fig. 5.11**. The initial activity of immobilized GOx retained after its tenth repeated use is around 69 %. The results implied that the immobilized GOx on the silica coated Ni-Co ferrite NCs possess good durability and recovery.

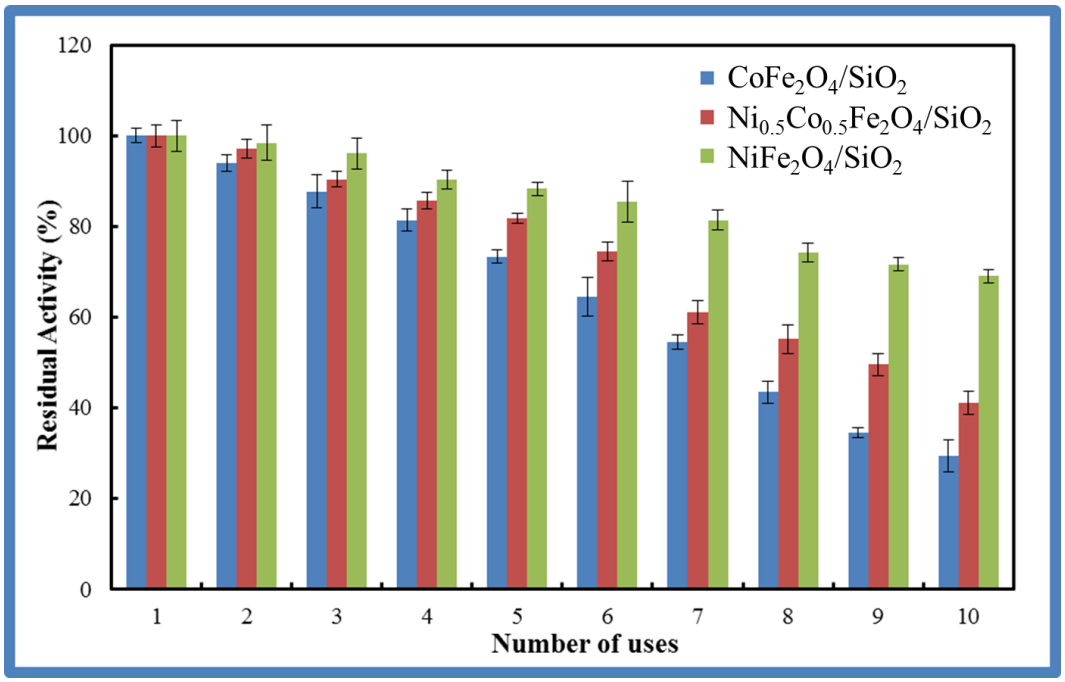

Figure 5.11. Reusability of the immobilized GOx on silica coated Ni-Co ferrite NCs.

5.3. Experimental

5.3.1. Chemicals

Iron nitrate nonahydrate {$Fe(NO_3)_3 \cdot 9H_2O$}, nickel nitrate hexahydrate {$Ni(NO_3)_2 \cdot 6H_2O$}, cobalt nitrate hexahydrate {$Co(NO_3)_2 \cdot 6H_2O$}, tetraethyl orthosilicate (TEOS), sodium hydroxide (NaOH), sodium chloride (NaCl), glycine ($C_2H_5NO_2$), sodium acetate (CH_3COONa), sodium phosphate (Na_3PO_4), ethanol (EtOH) and hydrochloric acid (HCl) were obtained from E. Merck (Germany). (3-Aminopropyl) triethoxy silane (APTES), dimethylformamide (DMF), 2-hydroxy-3,5-dinitrobenzoic acid (DNSA), glutaraldehyde (GA) and glucose oxidase (GOx) were procured from Sigma Aldrich (St. Louis, MO, USA). All reagents or chemicals used were of analytical grade.

5.3.2. Preparation of silica coated nickel-cobalt ferrite NCs ($Ni_xCo_{1-x}Fe_2O_4/SiO_2$ NCs)

Nanocrystalline silica coated $Ni_xCo_{1-x}Fe_2O_4$ (x = 0.0, 0.5, 1.0) NCs were prepared by sol-gel auto-combustion method. Firstly, TEOS diluted in EtOH was slowly added into deionized water, the molar ratio was fixed at 1:4:7 (TEOS:EtOH:H_2O).

Appropriate amount of acetic acid was added into the solution to maintain an acidic pH value of approximately 2.0. The precursor solution was stirred at 50 ^{o}C for 2 h when hydrolysis of TEOS took place and a resultant transparent viscous sol (Sol A) was obtained. Solution B was prepared by dissolving $Ni(NO_3)_2$, $Co(NO_3)_2$, $Fe(NO_3)_3$ and citric acid in deionized water. The molar ratio of citric acid to metal ions was fixed at 1:1. An appropriate amount of ammonia was added into the solution to adjust the pH value to about 7.0. Sol A and Sol B were then mixed to form a homogeneous transparent aqueous solution. The solution was evaporated at about 70 ^{o}C until a transparent sol was obtained, then the resulting sol was heated at 110 ^{o}C for 24 h to allow the dried gel formation. Self-propagation manner was found when the dried gel was ignited at 250 ^{o}C in the air. The as-burnt Ni-Co ferrite/SiO_2 NCs were reddish-brown and voluminous.

5.3.3. Immobilization of GOx on silica coated Ni-Co ferrite NCs

5.3.3.1. Activation of NCs

For the activation of silica coated Ni-Co ferrite NCs, firstly these formulations are silanized with APTES then activated with coupling agent GA. 30 mg of each series of silica coated Ni-Co ferrite NCs were treated with 5 mL of 70 % EtOH solution in ultra sonicator for the period of 30 min and after that 0.25 mL APTES and 0.25 mL DMF was added. The solution was kept on shaking (300 rpm) for 4 h and nanocomposites were collected with magnet after washing with 10 mM phosphate buffer saline (PBS) of pH 7.3 three times. Then 10 mL (2 mg mL^{-1}) of nanocomposites suspension in 10 mM PBS (pH 7.3) mix with 400 µL of 0.5 % GA and whole reaction was kept of shaking (300 rpm) at 30 ^{o}C for 1 h, then washed several times with PBS. The activated carriers are redispersed in the 5 mL of PBS for further uses.

5.3.3.2. Immobilization of GOx with activated silica coated Ni-Co ferrite NCs

For the immobilization of GOx with activated silica coated Ni-Co ferrite NCs: 4 mg of GOx was mixed with 6 mL (3 mg mL^{-1}) of resuspended activated NCs in 100 mM PBS (pH 6.0) at 4 ^{o}C for 12 h with occasional shaking. The carriers were washed with the same buffer solution to remove free GOx by placing whole solution on permanent magnet. By using Bicinconinic methods (BCA), the amount of GOx enzyme loaded onto the NCs was evaluated by subtracting the residual protein content in the solution

from the initial protein content and the content of immobilized protein was quantified. The stock solutions of GOx-silica coated Ni-Co ferrite NCs were stored at 4 ºC until used.

5.3.4. Determination of GOx loading efficiency

The concentration of GOx enzyme was concluded according to Bicinconinic protein assay method[28] and loading efficiency of GOx was predicted from the following equation:

$$Loading\ efficiency\ (\%) = \frac{C_oV_o - C_iV_i}{C_oV_o} \times 100\ \%$$

Where, C_o denotes the protein concentration and V_o is the volume of the GOx solution before immobilization, respectively. C_i is the protein concentration and V_i is the volume of the filtrate which was left after immobilization, respectively. Bovine serum albumin (BSA) was considered as a standard protein.

5.3.5. Characterization of silica coated Ni-Co ferrite NCs

The size, structure and magnetic properties of the resultant silica coated Ni-Co ferrite NCs without and with immobilized GOx were characterized by FT-IR and spectra were recorded using Perkin Elmer FT-IR Spectrometer spectrum Two and values are given in cm^{-1}. Surface morphology and the particle size was obtained by recording SEM and HR-TEM micrographs by LEO 435-VF and JEOL TEM (JEM 2100F) instruments, respectively. XRD data were recorded by PHILIPS PW1710 diffractometer with Cu Kα radiation at 1.540 Å in the range of $5^o \leq 2\theta \leq 70^o$ at 40 kV.

5.3.6. Assay of GOx

The standard activity for soluble and immobilized GOx were analyzed by using DNSA as a chromogenic substrate.[29] The standard reaction mixture in a total volume of 2 mL contained 8 µg of GOx, and 5 mM of glucose in 100 mM PBS of pH 6.0. The reaction started after addition of glucose to reaction mixture at room temperature with continuous stirring for 10 min. After 10 min, 2 mL of DNSA was added to mixture and boil at 100 ºC for another 10 min to develop the color and the absorbance was recorded at 576 nm. An appropriate reaction blanks were used for both the soluble and immobilized GOx, *i.e.* for the soluble enzyme all components of the reaction

mixture were present in blank except the enzyme, and for the immobilized enzyme all components of the reaction mixture including silica coated Ni-Co ferrite NCs were present in the blank except the immobilized enzyme.

5.3.7. Effect of pH on GOx activity

Enzymatic activities of soluble and immobilized GOx were tested in the buffers of different pH (3.0-10.0). The buffers used for determining pH were glycine-HCl (pH 3.0), sodium acetate (pH 5.0), sodium phosphate (6.0, 7.0) and Tris-HCl (pH 8.0-10.0). The concentration of each buffers were 0.1 M. The enzyme activity at pH 5.5 and 6.0 were chosen as a control (100 %) for the soluble and immobilized GOx, respectively, for the calculation of remaining percent activity.

5.3.8. Effect of temperature on GOx activity

The activity of soluble and immobilized GOx was evaluated at variable temperatures (25-65 °C) in standard reaction assay condition as described above. The enzyme activity at 40 and 45 °C was chosen as a control (100 %) for the calculation of remaining percent activity for soluble and immobilized GOx, respectively.

5.3.9. Thermal stability of GOx

The preparations of free and immobilized GOx, were incubated at 50 °C for 240 min in order to investigate their thermal stability. After each 30 min interval of incubation, appropriate amount of enzyme was picked and put in crushed ice for 3 min, then activity was determined by using standard reaction condition. The residual activity was expressed in relative to the original activity assessed without heating.

5.3.10. Determination of kinetic constants

For the determination of kinetic parameters *i.e.* velocity maximum (V_{max}) and Michaelis-Menten constant (K_m) of soluble and immobilized GOx, were used with varying concentration of glucose in standard reaction condition by double reciprocal plot. The standard reaction mixture in a total volume of 2 mL comprises of 8 µg of GOx and varying concentration of EtOH in 100 mM PBS buffer, pH 6.0. The kinetic constants were attained from at least triplicate measurements of the initial rates at variable concentrations of glucose (10-150 mM).

5.3.11. Reusability assay

In order to explore the reusability of immobilized enzyme their activity assay was done in triplicates. Immobilized enzyme was thoroughly washed with 100 mM PBS buffer, pH 6.0 by centrifugation at 4000 rpm for 20 min after each assay. The resultant pellet was stored in assay buffer at 4 °C and this procedure was repeated for 10 continuous days. For the calculation of remaining activity after repeated uses the activity determined on the first day was considered as control (100 %).

5.4. Conclusion

Silica coated Ni-Co ferrite NCs were synthesized by employing sol-gel auto-combustion synthetic route comprising inexpensive and environmental friendly reactants followed by their characterization through various techniques. GOx enzyme was bound to the silica coated Ni-Co ferrite NCs *via* glutaraldehyde activation. The probable mechanism for the interaction of GOx enzyme complex immobilized on silica coated Ni-Co ferrite NCs was confirmed by FT-IR analysis. After immobilization, enzyme activity was enhanced to some level at the pH range of 7.0-9.0 and at the temperature range of 45-60 ^{o}C. Due to the conformational changes and restrained accessibility, the enzyme's affinity to substrate decreased upon immobilization. Studies revealed that the immobilized GOx is found to be more stable as compared to free GOx. The kinetic parameters, involving maximum reaction velocity and Michaelis constants, were also determined. The reusability of the immobilized GOx complex was determined and was able to retain 69 % of its initial activity after 10 recycles. The unique and excellent immobilization approach developed in this study provides immense benefits for several industrial applications, not merely for GOx, but similarly for other enzymes and biomolecules.

5.5. References

1 A. Sharma, Y. Qiang, J. Antony, D. Meyer, P. Kornacki and A. Paszczynski, *IEEE Trans. Magn.*, 2007, **43**, 2418–2420.

2 S. V Sonti and A. Bose, *J. Colloid Interface Sci.*, 1995, **170**, 575–585.

3 Y. Zhang, N. Kohler and M. Zhang, *Biomaterials*, 2002, **23**, 1553–1561.

4 A. Ito, M. Shinkai, H. Honda and T. Kobayashi, *J. Biosci. Bioeng.*, 2005, **100**, 1–11.

5 V. Holzapfel, M. Lorenz, C. K. Weiss, H. Schrezenmeier, K. Landfester and V. Mailänder, *J. Phys. Condens. Matter*, 2006, **18**, S2581–S2594.

6 A. Petri-Fink, M. Chastellain, L. Juillerat-Jeanneret, A. Ferrari and H. Hofmann, *Biomaterials*, 2005, **26**, 2685–2694.

7 I. Hilger, R. Hergt and W. A. Kaiser, *IEE Proc. - Nanobiotechnology*, 2005, **152**, 33–39.

8 J. B. Sundstrom, H. Mao, R. Santoianni, F. Villinger, D. M. Little, T. T. Huynh, A. E. Mayne, E. Hao and A. A. Ansari, *J. Acquir. Immune Defic. Syndr.*, 2004, **35**, 9–21.

9 M. Koneracká, P. Kopčanský, M. Antalík, M. Timko, C. N. Ramchand, D. Lobo, R. V Mehta and R. V Upadhyay, *J. Magn. Magn. Mater.*, 1999, **201**, 427–430.

10 A. K. Johnson, A. M. Zawadzka, L. A. Deobald, R. L. Crawford and A. J. Paszczynski, *J. Nanoparticle Res.*, 2008, **10**, 1009–1025.

11 H. P. Khng, D. Cunliffe, S. Davies, N. A. Turner and E. N. Vulfson, *Biotechnol. Bioeng.*, 1998, **60**, 419–424.

12 M. A. Ahmed, *J. Magn. Magn. Mater.*, 2010, **322**, 763–766.

13 D. L. Nelson and M. M. Cox, *New York*, 2005.

14 S. B. Bankar, M. V Bule, R. S. Singhal and L. Ananthanarayan, *Biotechnol. Adv.*, 2009, **27**, 489–501.

15 T. Du, B. Liu, X. Hou, B. Zhang and C. Du, *Appl. Surf. Sci.*, 2009, **255**, 7937–7941.

16 G. Irena, B. Jolanta and Z. Karolina, *Appl. Surf. Sci.*, 2009, **255**, 8293–8298.

17 G. K. Kouassi, J. Irudayaraj and G. McCarty, *Biomagn. Res. Technol.*, 2005, **3**, 1–10.

18 A. A. Laskar, M. F. Alam and H. Younus, *Int. J. Biol. Macromol.*, 2017, **96**, 798–806.

19 W. D. Callister and D. G. Rethwisch, *Mater. Sci. Eng. an Introd. 6th ed. New York John Wiley Sons*, 2003, 129–130.

20 R. C. O'handley, *Modern magnetic materials*, Wiley, 2000.

21 K. M. S. Youssef, C. C. Koch and P. S. Fedkiw, *Corros. Sci.*, 2004, **46**, 51–64.

22 I. Z. Vass, Z. Deák, K. Paul, S. Kovács and I. Vass, *Acta Biol. Szeged.*, 2015, **59**, 225–245.

23 Z. Nasir, M. Shakir, R. Wahab, M. Shoeb, P. Alam, R. H. Khan, M. Mobin and Lutfullah, *Int. J. Biol. Macromol.*, 2017, **94**, **Part A**, 554–565.

24 M. Shakir, Z. Nasir, M. S. Khan, Lutfullah, M. F. Alam, H. Younus and S. I. Al-Resayes, *Int. J. Biol. Macromol.*, 2015, **72**, 1196–1204.

25 A. Ali, M. Asif, H. Khanam, A. Mashrai, M. A. Sherwani, M. Owais and Shamsuzzaman, *RSC Adv.*, 2015, **5**, 75964–75984.

26 Shamsuzamman, A. Ali, M. Asif, A. Mashrai and H. Khanam, *Eur. Chem. Bull.*, 2014, **3 (9)**, 939–945.

27 Shamsuzzaman, K. A. A. Abdul Baqi, A. Ali, M. Asif, A. Mashrai, H. Khanam, A. Sherwani, Z. Yaseen and M. Owais, *J. Mol. Struct.*, 2015, **1085**, 104–114.

28 P. K. Smith, R. I. Krohn, G. T. Hermanson, A. K. Mallia, F. H. Gartner, M. D. Provenzano, E. K. Fujimoto, N. M. Goeke, B. J. Olson and D. C. Klenk, *Anal. Biochem.*, 1985, **150**, 76–85.

29 G. L. Miller, *Anal. Chem.*, 1959, **31**, 426–428.

30 I. K. Battisha, *Indian J. Pure Appl. Phys.*, 2002, **40**, 122–131.

31 H. Ono and T. Katsumata, *Appl. Phys. Lett.*, 2001, **78**, 1832–1834.

32 P. D. Maniar, A. Navrotsky, E. M. Rabinovich, J. Y. Ying and J. B. Benziger, *J. Non. Cryst. Solids*, 1990, **124**, 101–111.

33 A. V. Rao, P. B. Wagh, D. Haranath, P. P. Risbud and S. D. Kumbhare, *Ceram. Int.*, 1999, **25**, 505–509.

34 L. A. García Cerda and S. M. Montemayor, *J. Magn. Magn. Mater.*, 2005, **294**, e43–e46.

35 J. M. D. Coey, *Phys. Rev. Lett.*, 1971, **27**, 1140–1142.

36 M. Yamaura, R. L. Camilo, L. C. Sampaio, M. A. Macêdo, M. Nakamura and H. E. Toma, *J. Magn. Magn. Mater.*, 2004, **279**, 210–217.

37 Q.-G. Xiao, X. Tao and J.-F. Chen, *Ind. Eng. Chem. Res.*, 2007, **46**, 459–463.

38 A. Gole, P. Chaudhari, J. Kaur and M. Sastry, *Langmuir*, 2001, **17**, 5646–5656.

39 D. Jung, C. Streb and M. Hartmann, *Int. J. Mol. Sci.*, 2010, **11**, 762–778.

40 M. F. Alam, A. A. Laskar, M. Zubair, U. Baig and H. Younus, *J. Mol. Catal. B Enzym.*, 2015, **119**, 78–84.

41 U. Baig, M. A. Gondal, M. F. Alam, A. A. Laskar, M. Alam and H. Younus, *New J. Chem.*, 2015, **39**, 6976–6986.

****

LIST OF ABBREVIATIONS AND SYMBOLS

2θ	Angle of incidence of X-rays diffracting planes
A	Absorbance
Å	Angstrom
eV	Electronvolt
FT-IR	Fourier transform infrared
g	Gram
h or hrs	Hours
Hz	Hertz
mg	Milligram
mL	Millilitre
mmol	Millimole
XRD	X-ray diffraction
SEM	Scanning electron microscopy
TEM	Transmission electron microscopy
HR-TEM	High resolution transmission electron microscopy
VSM	Vibrating sample magnetometer
YADH	Yeast alcohol dehydrogenase
GOx	Glucose oxidase

NPs	Nanoparticles
NCs	Nanocomposites
EDS	Energy dispersive X-ray
XPS	X-ray photoelectron spectroscopy
UV-Vis	UV-Visible
DTA	Differential thermal analysis
TGA	Thermogravimetric analysis
IR	Infrared
nm	Nanometres
HSA	Human serum albumin
MB	Methylene blue
ROS	Reactive oxygen species
TEOS	Tetraethyl orthosilicate
min	Minutes
EtOH	Ethanol
APTES	(3-Aminopropyl) triethoxy silane
HOMO	Highest occupied molecular orbital
LUMO	Lowest unoccupied molecular orbital
NSMs	Nanostructured materials

μ	Microns
K_BT	Thermal energy
$g\ mol^{-1}$	Gram per mole
$g\ cm^{-3}$	Gram per cubic centimetre
$cm^3\ mol^{-1}$	Cubic centimetres per mole
χ	Magnetic susceptibility
mA	Milliampere
hkl	Diffraction reflection indices
FWHM	Full width-at-half maximum
DLS	Dynamic light scattering
BSE	Back-scattered electrons
μm	Micrometre
λ_{max}	Wavelength of maximum absorption
$kcal\ mol^{-1}$	Kilocalorie per mole
$MoSe_2$	Molybdenum diselenide
Li_2CO_3	Lithium carbonate
TCE	Trichloroethylene
HRP	Horse radish peroxidase
NP-PC	Nanoparticle-protein corona

NMR	Nuclear magnetic resonance spectroscopy
FNPs	Ferrite nanoparticles
BSA	Bovine serum albumin
M	Magnetization
Ms	Saturation magnetization
k	Boltzmann constant.
Hc	Coercivity
pH	Potential of hydrogen
K_m	Michaelis-Menten constant
V_{max}	Velocity maximum
mM	Millimolar
EDC	1-(3-Dimethylaminopropyl)-3-ethylcarbodiimide hydrochloride
NaOH	Sodium hydroxide
HCl	Hydrochloric acid
µg	Microgram
TCEs	Transparent conducting electrodes
NMs	Nanomaterials
MOs	Metal oxides
SA	Serum albumin

JCPDS	Joint committee on powder diffraction standards data
SAED	Selected area (electron) diffraction
K_{sv}	Stern-Volmer quenching constant
Q	Concentration of quencher
k_q	Bimolecular quenching constant
τ_0	Life time
ns	Nanosecond
K_b	Binding constant
CD	Circular dichroism
TOC	Total organic carbon
OHPs	Organic hydro peroxides
OH_3	Hydroxyl radicals
KCl	Potassium chloride
NaCl	Sodium chloride
NH_4OH	Ammonium hydroxide
wt	Weight
$CHCl_3$	Chloroform
CH_2Cl_2	Dichloroform
DMF	N, N-Dimethylformamide

DMSO	*Dimethyl sulfoxide*
MeOH	*Methanol*
D_2O	*Deuterium oxide*
XRF	*X-ray fluorescence*
$CDCl_3$	*Deuterated chloroform*
TMS	*Tetramethylsilane*
ppm	*Parts per million*
GA	*Glutaraldehyde*
DNSA	*2-Hydroxy-3,5-dinitrobenzoic acid*
PBS	*Phosphate buffer saline*
rpm	*Revolutions per minute*
µL	*Microliter*
BCA	*Bicinchoninic acid assay*

LIST OF PUBLICATIONS

- ***Study on immobilization of yeast alcohol dehydrogenase on nanocrystalline Ni-Co ferrites as magnetic support***
  Mohammad Shakir, **Zeba Nasir**, Mohd Shoeb Khan, Lutfullah, Md. Fazle Alam, Hina Younus, Saud Ibrahim Al-Resayes
  Int. J. Biol. Macromolec., 2015, **72**, 1196-1204.

- ***Co-precipitation synthesis and characterization of Co doped SnO_2 NPs, HSA interaction via various spectroscopic techniques and their antimicrobial and photocatalytic activities***
  Zeba Nasir, Mohammad Shakir, Rizwan Wahab, Mohd Shoe, Parvez Alamd, Rizwan Hasan Khan, Mohammad Mobin, Lutfullah
  Int. J. Biol. Macromolec., 2017, **94**, 554-565.

- ***Silica supported NiO nanocomposite prepared via sol-gel technique and its excellent catalytic performance for one-pot multicomponent synthesis of benzodiazepine derivatives under microwave irradiation***
  Zeba Nasir, Mohammad Shakir, Lutfullah *et al.*
  (Communicated)

- ***Immobilization of glucose oxidase enzyme on silica coated Ni-Co ferrite nanocomposites as a magnetic support***
  Zeba Nasir, Mohammad Shakir, Lutfullah *et al.*
  (Communicated)

International Journal of Biological Macromolecules 94 (2017) 554–565

Contents lists available at ScienceDirect

International Journal of Biological Macromolecules

journal homepage: www.elsevier.com/locate/ijbiomac

Co-precipitation synthesis and characterization of Co doped SnO_2 NPs, HSA interaction *via* various spectroscopic techniques and their antimicrobial and photocatalytic activities

Zeba Nasir[a], Mohammad Shakir[a], Rizwan Wahab[b], Mohd Shoeb[c], Parvez Alam[d], Rizwan Hasan Khan[d], Mohammad Mobin[c], Lutfullah[a,*]

[a] Department of Chemistry, Aligarh Muslim University, Aligarh 202 002, UP, India
[b] Department of Zoology, College of Science, King Saud University, Riyadh 11451, Saudi Arabia
[c] Department of Applied Chemistry, Z.H. College of Engg. & Tech., Aligarh Muslim University, Aligarh 202 002, UP, India
[d] Interdisciplinary Biotechnology unit, Aligarh Muslim University, Aligarh 202 002, UP, India

ARTICLE INFO

Article history:
Received 7 August 2016
Received in revised form 17 October 2016
Accepted 18 October 2016
Available online 19 October 2016

Keywords:
Co doped SnO_2 NPs
HSA
Photocatalysis
Antimicrobial
Fluorescence spectroscopy

ABSTRACT

$Sn_{1-x}Co_xO_2$ (x = 0.00, 0.01, 0.03, 0.05) nanoparticles (NPs) of average size ~30–40 nm were synthesized by co-precipitation method. The interaction of Co doped SnO_2 NPs with human serum albumin (HSA) and their photocatalytic and antimicrobial properties were studied. The structural analysis and morphology of Co doped SnO_2 NPs were analysed *via* X-ray diffraction (XRD), scanning electron microscopy (SEM), energy dispersive X-ray spectroscopy (EDS), high resolution transmission electron microscopy (HRTEM) and Fourier transform infrared spectroscopy (FT-IR). Besides the structural and morphological analysis, the interaction of Co doped SnO_2 NPs with HSA were studied by UV–vis, Circular dichroism (CD) and fluorescence spectroscopy. Fluorescence quenching results suggest that Co doped SnO_2 NPs interact with an HSA molecule through static mechanism. CD indicates that α-helicity of HSA increases due to the interaction of Co doped SnO_2 NPs. The photocatalytic activities of the NPs with increased doping concentration were evaluated through a degradation process in the presence of methylene-blue (MB) dye under UV light irradiation, which exhibited that the surface area of NPs with increased doping concentration plays a major role in improving the photocatalytic activity. The antimicrobial effect of undoped and Co-doped SnO_2 NPs was determined using agar-well diffusion method and analyzed against gram-positive bacteria (*Bacillus Cereus* MC 2434). In our results, we have found that as the doping concentration increases into NPs, zone of inhibition increases, which could be ascribed to the production of ROS and large surface area of the NPs.

© 2016 Elsevier B.V. All rights reserved.

1. Introduction

Metal and semiconductor oxide NPs with well-defined size, shape, optical and optoelectronic properties are the centre of ardent research activities because of their favourable potential in the area of medical applications [1–4]. Nanoparticles may conquer biocompatibility and bioactive functions through coating their surfaces with DNA, peptides and proteins. Among various metal oxide, SnO_2 is a wide band gap (3.6 eV) n-type semiconductor with many potential applications. The large band gap and high achievable carrier concentration (up to 6×10^{20} cm^3) [5], make SnO_2 an excellent candidate for a wide range of applications such as lithium-ion batteries, transparent conducting electrodes, solar cells, gas sensors *etc* [6–13]. Its success in many of its technological applications depends on the crystalline nature of SnO_2 as it has uniform nano-size pore structure [14–16]. Efforts towards the development of SnO_2 nanomaterials (NMs) with high sensitivity, excellent selectivity, quick response and recovery behaviour to gases has increased over years.

SnO_2 NPs is widely used to control air pollution and to detect toxic or smelling gases at low levels in air, domestic and industrial applications [17–19]. SnO_2 NPs have been successfully doped with rare earth ions (Tb3þ, Eu3þ, and Ce3þ), and transition metal ion (Cu2þ). Recently, many elements such as Zn, La, Pt and Pd, have been proved to be effective dopants in improving sensor response

* Corresponding author.
E-mail address: lutfullah786@gmail.com (Lutfullah).

http://dx.doi.org/10.1016/j.ijbiomac.2016.10.057
0141-8130/© 2016 Elsevier B.V. All rights reserved.

International Journal of Biological Macromolecules 72 (2015) 1196–1204

Contents lists available at ScienceDirect

International Journal of Biological Macromolecules

journal homepage: www.elsevier.com/locate/ijbiomac

Study on immobilization of yeast alcohol dehydrogenase on nanocrystalline Ni-Co ferrites as magnetic support

Mohammad Shakir[a,*], Zeba Nasir[a], Mohd Shoeb Khan[a], Lutfullah[a], Md. Fazle Alam[b], Hina Younus[b], Saud Ibrahim Al-Resayes[c]

[a] Department of Chemistry, Aligarh Muslim University, Aligarh 202002, India
[b] Interdisciplinary Biotechnology unit, Aligarh Muslim University, Aligarh 202002, UP, India
[c] Department of Chemistry, College of Science, King Saud University, Riyadh, Saudi Arabia

ARTICLE INFO

Article history:
Received 26 July 2014
Received in revised form 20 October 2014
Accepted 21 October 2014
Available online 25 October 2014

Keywords:
Nanoferrites
Auto-combustion
Alcohol dehydrogenase
Immobilization

ABSTRACT

The covalent binding of yeast alcohol dehydrogenase (YADH) enzyme complex in a series of magnetic crystalline Ni-Co nanoferrites, synthesized via sol-gel auto combustion technique was investigated. The structural analysis, morphology and magnetic properties of Ni-Co nanoferrites were determined by X-ray diffraction (XRD), scanning electron microscopy (SEM), energy dispersive X-ray spectroscopy (EDS), vibrating-sample magnetometer (VSM), high resolution transmission electron microscopy (HRTEM) and Fourier transform infrared spectroscopy (FTIR). The comparative analysis of the HRTEM micrographs of bare magnetic nanoferrite particles and particles immobilized with enzyme revealed an uniform distribution of the particles in both the cases without undergoing change in the size which was found to be in the range 20–30 nm. The binding of YADH to Ni-Co nanoferrites and the possible binding mechanism have been suggested by comparing the FTIR results. The binding properties of the immobilized YADH enzyme were also studied by kinetic parameters, optimum operational pH, temperature, thermal stability and reusability. The immobilized YADH exhibits enhanced thermal stability as compared to the free enzyme over a wide range of temperature and pH, and showed good durability after recovery by magnetic separation for repeated use.

© 2014 Elsevier B.V. All rights reserved.

1. Introduction

Nanocrystalline ferrites have fascinated much interest in various fields including biomedical and environmental applications during the last decade because of their small size, high specific surface area and low toxicity with strong magnetic properties extending applications in intracellular uptake and separation [1–5], drug delivery [6], hyperthermia [4,7], magnetic resonance imaging contrast enhancement [4,8], enzyme and protein immobilization [9,10] and protein purification [11]. A number of synthetic routes have been adopted for the synthesis of nanoferrites such as mechanical milling, co-precipitation, thermal decomposition, sol-gel, auto-combustion and hydrothermal methods [1]. Auto-combustion synthesis provides numerous distinct advantages over co-precipitation and ceramic techniques as it does not involve any pH control or a consequent annealing step in the synthesis of phase pure and highly crystalline ferrite nanoparticle [12].

Although alcohol dehydrogenase which catalyzes the oxidation of alcohols and the reduction of carbonyl compounds attracted the attention of chemists due to its potential applications in the production of various starting materials and intermediates in chemical industry viz., the synthesis of chiral compounds, regeneration of coenzymes NAD(P) and NAD(P)H and biosensors [13–15] but the poor stability limits its practical applications [16,17]. Therefore, the efforts have been directed towards the immobilization of bioactive materials onto insoluble organic and inorganic supports which not only offered a path to enhance stability and reusability, but also altered the catalytic properties, enzymatic activity or selectivity in some cases [18–23]. Magnetic supports for biological and biomedical materials are of particular interest amongst various supports due to their inherent characteristics, including non toxicity, large surface area, and capacity to generate required magnetic properties and their ability to be separated with magnets and recycled. A number of techniques have been adopted for immobilization where physical adsorption technique is one of the most widely used techniques in which the enzymes and the supports interact via van der Waals, ionic, covalent and hydrogen bonding [9,24–31]. The use of physical adsorption technique is encouraged as it is simple

* Corresponding author. Tel.: +91 9837430035.
E-mail address: shakir078@yahoo.com (M. Shakir).

http://dx.doi.org/10.1016/j.ijbiomac.2014.10.045
0141-8130/© 2014 Elsevier B.V. All rights reserved.